Vascular Patterning and Its Application in Cancer and Choroidal Neovascularization

Abbas Shirinifard

Submitted to the faculty of the University Graduate School
in partial fulfillment of the requirements
for the degree
Doctor of Philosophy
in the Department of Physics,
Indiana University

March 2012

Accepted by the Graduate Faculty, Indiana University, in partial fulfillment of the requirements for the degree of Doctor of Philosophy.

Doctoral Committee

Prof. James A. Glazier, Ph.D.

Prof. John M. Beggs, Ph.D.

Prof. John P. Carini, Ph.D.

Prof. Joe Pomerening, Ph.D.

Date of Oral Examination

September 6th, 2011

To my wonderful wife and best friend, Mona, for her support, patience and encouragement.

Acknowledgements

This work would not have been completed without help and support of many individuals. I would like to thank everyone who has helped me along the way. First and foremost I offer my sincerest gratitude to my advisor, Professor James A. Glazier, who has supported me throughout my thesis with his patience and knowledge.

I would like to thank my research committee members, Dr. John Beggs, Dr. John Carini and Dr. Joe Pomerening, for their valuable suggestions and guidance.

I would like to acknowledge the CompuCell3D development team, Dr. Maciej Swat, Benjamin Zaitlen, Randy Heiland and Dr. Mitja Hmeljak, for their patience and support. I also thank my collaborator in the cancer evolution project, Dr. Gilberto Thomas, for his invaluable contribution.

I am very grateful to the biologists in Glazier's team, Dr. Sherry Clendenon and Dr. Scott Gens, for sharing their expertise, providing irreplaceable insight and helping with imaging projects to make my computational models closer to reality.

I would like to thank Dr. Roeland Merks from Centrum Wiskunde & Informatica, for many fruitful discussions and his valuable insights in angiogenesis modeling.

I owe thanks to my collaborators in choroidal neovascularization project, Dr. Fereydoon Family and Dr. Hans Grossniklaus from Emory University and Dr. Yi Jiang from Los Alamos National Laboratory, for their guidance, encouragement, and enthusiasm. I would like to Dr. Thomas J. Gast for his biological and clinical insights and guidance.

I wish to thank lab members and staff at Physics Department, Mike Hosek, Dr. Dragos Amarie, Dr. Abdelkrim Alileche and David Sprinkle, for introducing experimental techniques and helping me to setup my experiments.

I extend special thanks to my collaborator from the TIVS Center, Dr. Maria Bondesson and Dr. Catherine McCollum from University of Houston, for providing invaluable time-lapse images of angiogenesis in zebrafish embryos.

My deepest gratitude goes to my wife, Mona, who has made this work possible, my parents, Abolhassan and Fereshte, and to my sister and brothers for the support and love they provided me through my entire life, and to my American parents, James and Harriet Kulis, for sharing their love with my family and providing the support and encouragement. I specially thank my extended family and friends, Maryam Khoushabeh Adeh and Bagher Tarighat, for providing support throughout this endeavor.

Finally, I extend my thanks to the agencies whose financial support made this research possible: the United States National Institutes of Health (under grants RM01 GM077138 and RM01 GM076692), the United States Environmental Protection Agency (under grants RD83500101 and R834289), the Indiana University College of Arts and Sciences Office of the Vice President of Research, the Indiana University Biocomplexity Institute and the Lilly Foundation for their support of my Biocomplexity Graduate Student Fellowship.

Preface

My research primarily addresses the interface between physics and biology, focusing on the mechanisms of growth and patterning of capillaries and how they interact with their micro-environment and other tissues. These interactions are important during development, wound healing, Age-Related Macular Degeneration (*AMD*) and tumor growth.

Chapter 1 briefly reviews basic processes during the initial stages of vascular patterning and introduces a multi-cell computer simulation of vascular patterning. I analyze the instabilities responsible for vascular pattering both analytically and with multi-cell simulations using the Glazier-Graner-Hogeweg model. My analysis of vascular patterning shows that interactions between cells introduce a key patterning mechanism, which is missing in comparable continuum models. As a result, vascular patterning in continuum models is qualitatively wrong.

My analysis predicts that vascular patterning obeys a simple scaling law during its initial stages. To verify the predicted scaling law, I ran *in vitro* experiments and tried to alter the diffusive properties of growth factors like the short-diffusion isoforms of vascular endothelial growth factor-A. While endothelial cell death in my experiments prevented me from verifying the predicted scaling law *in vitro,* I did develop novel *in vitro* tissue engineering devices for assaying angiogenesis and for *in vitro* construction of viable capillaries [Patent Application, 2010]. I briefly discuss characteristics of these new *in vitro* methods.

Chapter 2 presents a three-dimensional (3D) multi-cell simulation of simplified vascular tumors [published in *PLoS One*, *2009*] that I developed using the results of my instability analysis. In this model, the endothelial cells in the pre-existing vasculature chemotax and proliferate in response to pro-angiogenic factors originating from hypoxic tumor cells. The tumor-induced vasculature increases the growth rate of the vascularized solid tumor compared to an avascular tumor and produces a range of biologically reasonable complex morphologies. Based on this work, I plan to extend my simulations to describe specific vascular tumor types and host tissues and to study the evolution of tumor progression.

Chapter 3 presents a 3D multi-cell simulation of choroidal neovascularization (*CNV*) in the retina, a major cause of vision loss in patients with AMD [*PLoS Comp. Bio.*, 2012]. I developed these simulations in close collaboration with Dr. Hans Grossniklaus and Dr. Fereydoon Family of Emory University.

Normally, an acellular layer called Bruch's membrane (*BrM*) separates the vasculature supplying photoreceptors from the retina. In CNV, blood vessels pass through BrM and spread in one of the three distinct patterns: in a layer between BrM and retinal pigment epithelium (*RPE*) (*occult CNV*), in a layer between the RPE and the photoreceptors (*classic CNV*) or in a distinctive combination of occult and classic (*type 3*). In all three cases, the resulting disruption of photoreceptors severely and irreversibly degrades vision, often leading to complete loss of central vision in affected eyes. However, while capillaries often penetrate BrM, in healthy eyes they do not spread or develop into CNV. The mechanisms determining CNV initiation and whether CNV progresses or not are poorly understood, impending the development of effective treatments and preventive therapies. My three-dimensional multi-cell simulations of normal and aged retinas successfully recapitulate the three types of CNV, the histopathology of exudative (wet) AMD and explain why vascular penetration does not lead to CNV in healthy eyes. Health and different types of CNV appears to depend on the viability of the RPE-RPE junctional structures and the adhesion of the RPE to BrM and the photoreceptors.

Chapter 4 discusses my plans to refine and extend my current studies. I am currently collaborating with Dr. Gilberto Thomas to apply my computational techniques to study the role of somatic evolution in tumor progression. In our current cancer evolution model, we study the evolution of cell behaviors due to controlled and emergent environmental variations. I am specifically interested in evolutionary mechanisms leading to disruption of cell-cell adhesion, which enable cancer cells to invade tissues and metastasize. I will briefly describe our current model and preliminary results.

My research shows that multi-cell simulation of angiogenesis provides an effective and efficient framework to capture the complex interplay between capillaries and their microenvironment in both homeostasis and pathological conditions. As an application of these techniques, in collaboration with the Texas-Indiana Virtual STAR Center, I am building a refined 3D model of intersegmental blood-vessel formation in zebrafish embryos to predict the low-dosage effects of toxins on angiogenesis during development.

Abbas Shirinifard

Title: Vascular Patterning and Its Application in Cancer and Choroidal Neovascularization

My research primarily addresses the interface between physics and biology, focusing on the mechanisms of growth and patterning of capillaries and how they interact with their micro-environment and other tissues. These interactions are important during development, wound healing, Age-Related Macular Degeneration (*AMD*) and tumor growth. Endothelial cells, which line the inner walls of blood vessels, self-organize into quasi-random networks of solid vascular cords *in vitro* and *in vivo*. The physical mechanisms of network formation are a current subject of debate. I have analyzed the instabilities responsible for vascular pattering both analytically and with multi-cell simulations using the Glazier-Graner-Hogeweg model. Using the results of my analysis, I have developed a 3D multi-cell simulation of simplified vascular tumors in which the endothelial cells in the pre-existing vasculature chemotax and proliferate in response to pro-angiogenic factors originating from hypoxic tumor cells. The tumor-induced vasculature increases the growth rate of the vascularized solid tumor compared to an avascular tumor and produces a range of biologically reasonable complex morphologies. I have also simulated choroidal neovascularization (*CNV*) in the retina, a major cause of vision loss in patients with AMD. The mechanisms determining CNV initiation and whether it progresses or not are poorly understood, impending the development of effective treatments and preventive therapies. My 3D multi-cell simulations of normal and aged retinas successfully recapitulate the three types and histopathology of CNV and

explain why vascular penetration does not lead to CNV in healthy eyes. My research shows that multi-cell simulation of angiogenesis is an effective and efficient framework to capture the complex interplay between capillaries and their microenvironment in both homeostasis and pathological conditions. As an application of these techniques, in collaboration with the Texas-Indiana Virtual STAR Center, I am building a refined 3D model of intersegmental blood vessel formation in zebrafish embryos to predict the low-dosage effects of toxins on angiogenesis during development.

Doctoral Committee

Prof. James A. Glazier, Ph.D.

Prof. John M. Beggs, Ph.D.

Prof. John P. Carini, Ph.D.

Prof. Joe Pomerening, Ph.D.

Table of Content

List of Figures

List of Tables

Chapter I: Vascular Patterning

Abstract

Endothelial cells, which line the inner walls of blood vessels, self-organize into quasi-random networks of solid vascular cords *in vitro* and *in vivo*. The physical mechanisms of network formation are a current subject of debate and are important during development, wound healing, Age-Related Macular Degeneration and tumor growth. During *vasculogenesis*, vascular endothelial cells begin randomly and nearly homogeneously distributed in tissues like the limb-bud and aggregate to form a non-directional, multiply connected random network (called a capillary plexus) resembling random, three-dimensional (*3D*) chicken-wire. Later remodeling of this capillary plexus during *angiogenesis* results in the familiar branched hierarchical *vascular tree*. Although patterning mechanisms during vasculogenesis and angiogenesis are closely related biologically, most computational models describe sprouting at the level of the blood vessel, ignoring how cell behavior drives branch splitting during sprouting. Merks *et al.* [1] have developed a cell-based Glazier–Graner–Hogeweg model (*GGH*) (also called Cellular Potts Model) that simulates the initial patterning before the vascular cords form lumens, based on plausible behaviors of endothelial cells. In this model, the endothelial cells secrete a chemoattractant, which attracts other endothelial cells. As in the classic Keller–Segel model, chemotaxis by itself causes cells to aggregate into isolated clusters. However, including experimentally observed VE-cadherin–mediated contact inhibition of chemotaxis in the simulation causes randomly distributed cells to organize into networks and cell aggregates to sprout, reproducing aspects of both de novo and sprouting blood-

vessel growth. In this chapter, I discuss my continuum partial-differential-equation (*PDE*) analysis that shows that the finite size of the cells gives rise to a novel type of instability mechanism, which results in patterns with asymptotically-fixed cord-widths. I discuss the two patterning instabilities responsible for my results: the cord-thinning and the cord-thickening instabilities. I use a renormalization-like argument to show that the cord-width scales linearly with the diffusion length of the principal chemoattractant when the two instabilities reach a dynamical equilibrium. I also briefly review current *in vitro* angiogenesis assays and present *in vitro* techniques that I developed during my experimental attempts to test the predicted scaling law.[1]

I.1 Contact-inhibited Chemotaxis in Vascular Patterning

I.1.1 *Introduction*

Blood-vessel development is essential for myriad biological phenomena in healthy and diseased individuals, including wound healing and tumor growth [2]. Blood vessels form either *de novo*, via *vasculogenesis* or by sprouting or splitting of existing blood vessels via *angiogenesis*.

In vasculogenesis, dispersed *endothelial cells* (*ECs*; the cells lining the inner walls of fully-formed blood vessels) organize into a *primary vascular plexus* of solid cords which then remodel into a vascular network. ECs elongate parallel to the cords, with typical final aspect ratios of ten to one. Because the early stages of vasculogenesis

---

[1] Portions of this chapter were published in PLoS Comp. Bio., 2008.

depend on a single cell type, vasculogenesis is relatively easy to reproduce *in vitro*. When cultured *in vitro* on *Matrigel*, a commercial product mimicking the extracellular matrix (*ECM*; the mixture of proteins, growth-factors and carbohydrates surrounding cells *in vivo*), even in the absence of other cell types or positional cues, ECs organize into cords which form large-scale, honey-comb-like patterns, with cords of ECs surrounding regions devoid of ECs. This network slowly reorganizes, with the size of the polygonal, cell-free *lacunae,* gradually increasing. This observation suggests that ECs have *autonomous* patterning ability, rather than following morphogen pre-patterns. The standard Matrigel assay produces artifact that I discuss in the section I.4, below.

The sprouting or splitting of existing blood vessels during angiogenesis is more complex. In the first step of angiogenesis, a vessel dilates and releases plasma proteins that induce a series of changes in EC behavior. The ECs which will form the sprout next detach from each other and from the surrounding smooth-muscle cells, destabilizing the vessel. These detached ECs proliferate, migrate out of the vessel and organize into a sprout. EC proliferation continues in the sprout and is fastest just behind the leading *tip cell*, which is selected using a lateral-inhibition mechanism mediated by *delta-like ligand 4* (*Dll4*) and *Notch1* [3]. Finally, the sprout forms a lumen (become a hollow tube), secretes a basal lamina and surrounds itself with pericytes that stabilize the sprout to form a mature new vessel [4].

Two fundamental questions concerning vasculogenesis and angiogenesis and their relation to each other are: 1) Does blood-vessel formation require external patterning cues (*pre-patterns* of morphogens) to define the precise position of the ECs, or can ECs organize into vascular patterns autonomously, with external cues merely initiating and fine-tuning vascular morphogenesis? 2) Do vasculogenesis and angiogenesis require the same or different cell behaviors, molecular signals and biomechanics?

I.1.2 *Experimental Background*

Despite the biomedical importance of angiogenesis and vasculogenesis, existing experiments are sufficiently ambiguous that even the fundamental mechanisms guiding patterning are uncertain. Experiments suggest a central role for chemotaxis in both *de novo* and sprouting blood-vessel growth [5,6]. ECs respond to, and often produce, a wide range of chemoattractants and chemorepellants, including the many isoforms of vascular-endothelial growth factor A (*VEGF-A*) [6], the chemokine SDF-1 [7,8], which ECs secrete [7], fibroblast growth factor 2 (*FGF-2*), which induces ECs in developing vessels to secrete VEGF [9], Slit-2, which can act either as a chemoattractant or a chemorepellant depending on the receptor to which it binds [9], and the chemorepelling semaphorins [10].

Which of these molecules (if any) govern vascular patterning is still unclear. The Torino Group (*e.g.*, [11,12]) argued that one of many types of VEGF-A was the short-range autocrine chemoattractant that their chemotaxis-based blood-vessel-growth model required, since ECs express receptors for VEGF (*VEGFR-2*), chemotax towards sources of VEGF under favorable conditions, and secrete VEGFs. However, experiments suggest that cell-autonomous secretion of VEGF is essential only for vascular maintenance, not for angiogenesis *per se*: mice genetically-engineered to lack the VEGF gene only in their ECs have normal vascular density and patterning, but impaired vascular homeostasis and EC survival [13]. A plausible, alternative cell-autonomous chemoattractant to guide EC aggregation is the chemokine SDF-1/CXCL12, which ECs both secrete and respond to [8].

However, based on experiments that suggest that ECs can follow stresses in the ECM (see, e.g., [14] for review), Manoussaki and Murray [15], and Namy *et al.* [16] proposed that mechanical interactions rather than, or in addition to, chemical interactions govern vasculogenesis. Further complicating this picture, Szabo and coworkers [17] showed that non-vascular glia or muscle cells cultured on rigid, plastic culture dishes in continuously-shaken medium can form linear structures. Such culture conditions should reduce both the formation of chemoattractant gradients or migration along stress lines in the ECM. In the absence of ECM, they hypothesized that cells preferentially move towards elongated structures. Szabo and coworkers [17] proposed two mechanisms for such cell behavior: cells could align to surrounding cells, or they would mechanotactically follow stress fields in the cytoskeleton of neighboring cells. The molecular mechanisms of such cell behaviors remain unclear as is the relevance of these results to ECs.

Angiogenesis and vasculogenesis also require a number of local, contact-dependent (*juxtracrine*) signals: Tip-cell selection during angiogenic sprouting depends on Delta-notch signaling [3], while binding of *Eph receptors* to *ephrin ligands* amplifies ECs' response to SDF-1 [8]. All ECs express vascular-endothelial-cadherin (*VE-cadherin*), a homophilic, trans-membrane cell-adhesion molecule, which appears to play a crucial role in vascular patterning [18,19]. Besides its role in cell-cell adhesion, VE-cadherin has a signaling function that determines how ECs respond to VEGF-A. When ECs bind to other ECs through their VE-cadherin, VEGF-A reduces their motility and proliferation. In the absence of VE-cadherin binding, VEGF-A activates pathways related to actin polymerization and the cell cycle, enhancing cell motility and proliferation in sub-confluent monolayers, and causes preferential extension of pseudopods in directions with higher VEGF-A concentrations [20]. Merks *et al.* hypothesize that VE-cadherin-binding acts locally to prevent extension of pseudopods in the direction of cell-cell contacts for all critical chemoattractants, not only to VEGF-A. VE-cadherin −/− double-knock-out mice develop abnormal vascular networks in the yolk sac [18], with ECs forming isolated vascular islands instead of wild-type polygonal vascular networks. These mice also have defective angiogenic sprouting, suggesting that both vasculogenesis and angiogenesis require VE-cadherin. VE cadherin −/− ECs still form strong adhesive junctions, so loss of VE-cadherin-mediated signaling rather than loss of intercellular adhesion seems to be responsible for the knock-out phenotype [18].

I.1.3 *Computational Background*

A number of models and simulations replicate features of *in vitro* vascular patterning and can help partially reconstruct minimal sets of behaviors ECs require to self-organize into polygonal, vascular patterns [11,12,15,16,21-23]. Because of the experiments we discussed above, and others which have demonstrated that sprouting angiogenesis and vasculogenesis both require chemotaxis (see, *e.g.*, [7,8]), most models of vasculogenesis assume that intercellular signaling occurs via a diffusible chemoattractant. Using continuum models deriving from the fluid-dynamic Burgers' equation, Preziosi and coworkers (called the *Torino Group*) showed that simulated ECs secreting a chemoattractant that attracts surrounding ECs could self-organize into polygonal patterns similar to the patterns in EC cultures and in vivo [11,12,24,25]. However, their work assumed that endothelial cells accelerate in chemical gradients, which is not plausible in the highly viscous, non-inertial environment of the ECM. Microfluidic evidence indicates that mammalian cells (HL60) rapidly reach a flow-dependent, constant velocity [26] in chemoattractant gradients, rather than continuously accelerating. Merks *et al.* have previously suggested that [21] a linear force-velocity relation is the most appropriate model of ECs' experimental response, with the velocity of ECs proportional to the strength of the gradient of the chemoattractant. However, in simulations of this simple model, isotropic ECs form well-separated rounded clusters instead of networks. Merks *et al.* also have shown that adding one of a number of mechanisms (including cell adhesion [27] and cell elongation [21]) to chemotactic aggregation suffices to produce quasi-polygonal networks.

In the mechanical models of Manoussaki and Murray [15], and Namy *et al.* [16] ECs pull on the elastic ECM and aggregate by *haptotactically* migrating along the resulting ECM stress lines. Surprisingly, the mathematical form of the chemical and mechanical models is practically identical. Because these mechanical models assume that ECs exert radially-symmetric stresses on the ECM, modeling stress fields and EC haptotaxis or EC secretion and response to a chemoattractant, results in the same cell movement. Since simulations of the two mechanisms are identical, distinguishing between the effects of chemical and mechanical mechanisms would require additional experiments.

A separate set of simulations addresses angiogenesis. Many models of sprouting blood-vessel growth introduce blood-vessel-level phenomenology by hand through high-level rules for branching [28,29]. Attempts to derive blood-vessel sprouting and splitting from the underlying behavior of ECs include Levine and coworkers' [30] model of the onset of angiogenic sprouting as a reinforced random walk, where the ECs degrade the ECM, which locally enhances EC motility and produces paths of degraded ECM, and Bauer and Jiang's [31] cell-based model of blood-vessel sprouting along externally generated morphogen gradients, which assumes that branch splitting results from ECM inhomogeneities. Neither model can explain both EC assembly and blood-vessel sprouting.

Could the behavior of the individual ECs also explain aspects of blood-vessel sprouting? Because the same genetic machinery regulates both patterning during angiogenesis and vasculogenesis [4], a common set of mechanisms is plausible. Manoussaki [32] extended her mechanical model of vasculogenesis to describe angiogenesis by adding long-range, chemotactic guidance cues. In her simulations, ECs migrate from an aggregate towards a chemoattractant source and cell-traction-driven migration contract the sprout into a narrow, vessel-like cord.

In our chemotaxis-based multi-cell model, ECs can produce networks both from dispersed ECs and EC clusters without requiring long-range guidance cues. Instead, in our model, long-range signals only steer the self-organized vessels, a more biologically-realistic mechanism. Extending simulations that Merks *et al.* have briefly introduced elsewhere [33], we show that VE-cadherin-mediated contact inhibition of chemotactic pseudopod projections, in combination with secretion of a diffusing, rapidly decaying chemoattractant by ECs, suffices to reproduce aspects of both *de novo* and sprouting blood-vessel growth (Figure I.1). In these simulations ECs: a) secrete a chemoattractant and b) preferentially extend pseudopods up gradients of the chemoattractant, unless, c) contact inhibition locally prevents chemotactic pseudopod extension. Thus, cell-cell binding suppresses the extension of chemotactic pseudopods, while unbound cell surfaces in contact with the ECM continue to extend pseudopods towards sources of chemoattractant [23]. Although this model is based on contact-inhibited autocrine chemotaxis mechanism, the model can represent any self-generated attraction field which rapidly decays with distance and a taxis response which is inhibited or reduced when cells are too close to each other.

I.1.4 *Multi-Cell Models of Vascular Patterning*

We modeled endothelial cell behavior at a mesoscopic level using the Glazier-Graner-Hogeweg (*GGH*) model, also known as the Cellular Potts Model (*CPM*) [34-37]. Intercellular junctions and cell junctions to the ECM determine adhesive (or binding) energies. The GGH algorithm (see, section I.3) models pseudopod protrusions by iteratively displacing cell interfaces, with a preference for displacements which reduce the local *Effective Energy* of the configuration. In addition to interface displacements that reduce the effective energy, active cell motility also allows displacements that increase the effective energy. The likelihood of these active displacements increases with the *cell-motility* parameter *T*. Further constraints regulate cell volumes, surface areas, and chemotaxis.

Merks *et al.* described chemoattractant diffusion and degradation macroscopically, using a continuum approximation. In analogy to the Torino Group's continuum model of *de novo* blood-vessel growth [11,24], ECs secrete a diffusing chemoattractant at a rate α, which degrades in the ECM at a rate ε (*e.g.*, due to proteolytic enzymes or by binding to ECM components), obeying:

$$\frac{\partial C(\vec{x})}{\partial t} = \alpha\left(1-\delta\left(\tau\left(\sigma(\vec{x})\right),\mathrm{ECM}\right)\right) - \epsilon\, C(\vec{x})\,\delta\left(\tau\left(\sigma(\vec{x})\right),\mathrm{ECM}\right) + D\nabla^2 C(\vec{x}), \qquad (1.1)$$

where $\delta\left(\tau\left(\sigma(\vec{x})\right),\mathrm{ECM}\right)=0$ inside cells and is $\delta\left(\tau\left(\sigma(\vec{x})\right),\mathrm{ECM}\right)=1$ in the ECM. Merks *et al.* used a two-dimensional (2D) GGH to be able to compare the results to experimental yolk-sac cultures, where the vascular patterns are essentially monolayers. Merks et al. set the chemoattractant's secretion rate by cells $\alpha = 10^{-3}\ s^{-1}$, its decay rate $\varepsilon = \alpha$, and its diffusion constant in ECM to a slow $D = 10^{-13}\ \mathrm{m}^2\ \mathrm{s}^{-1}$. These parameter values produce steeper gradients than those for VEGF-A_{165}, the chemoattractant which Gamba *et al.* suggested was responsible for vasculogenesis, which has a diffusion coefficient of $D \sim 10^{-11}\ \mathrm{m}^2\ \mathrm{s}^{-1}$ [12]. This D produces a long diffusion length of ~ 200 μm, which makes it impractical as a source of chemotactic guidance. The diffusion coefficient of SDF-1/CXCL12 is in the range of $1.7 \times 10^{-13}\ \mathrm{m}^2\ \mathrm{s}^{-1}$ [38]. I will show below that the long-term behaviors of most pattern characteristics scale with the diffusion length, with prefactors depending on the chemotaxis strength, cell motility and cell-cell adhesion.

In the simplest implementation of chemotaxis in the GGH, cell velocity is proportional to the strength of the chemical gradient, $\vec{v}_{\mathrm{cell}} \propto \vec{\nabla} C$, in general agreement with experiments; see, *e.g.*, [21]. To model preferential protrusions of pseudopods at the boundary between cells and ECM due to contact-inhibited chemotaxis, *i.e.* chemotaxis only at cell-ECM interfaces, not at cell-cell interfaces, we add to the basic $\Delta\mathcal{H}_{\mathrm{GGH}}$ a Savil-

Hogeweg term ($\Delta\mathcal{H}_{\text{chemotaxis}}$) that favors extensions and retractions of pseudopods up concentration gradients of a chemoattractant [39]:

$$\begin{aligned}
&\Delta\mathcal{H}_{\text{chemotaxis}} = \big(\mu(\sigma_{\text{target}}) - \mu(\sigma_{\text{source}})\big)\big(C(\vec{i}_{\text{target}}) - C(\vec{i}_{\text{source}})\big),\\
&\Delta\mathcal{H}_{\text{chemotaxis}} = 0 \text{ at EC} - \text{EC boundaries,}\\
&\Delta\mathcal{H}_{\text{total}} = \Delta\mathcal{H}_{\text{chemotaxis}} + \Delta\mathcal{H}_{\text{GGH}},
\end{aligned} \tag{1.2}$$

where $\mu(\sigma)$ is the degree of chemotactic response of the cell with index σ and $C(\vec{i}\,)$ is chemoattractant concentration at lattice site $\vec{i}$.

In simulations of this model, ECs either sparsely distributed or packed in a cluster self-organize into capillary-like networks (Figure I.1), resembling aspects of both sprouting angiogenesis and *de novo* vasculogenesis. I start the simulation with two separate groups of identical cells, one distributed randomly in the lower left quadrant and the other in a cluster in the top-right quadrant. During first three simulated hours, the randomly dispersed cells self-organize into one-cell-diameter vascular cords and small clusters a few cells in diameter, while cells from the large cluster form initial sprouts at the periphery of the cluster. After 9 hours, the thin cords in Figure I.1B reorganize into mostly two-cell diameter vascular cords. The initial sprouts in Figure I.1B form thick irregular vascular cords (Figure I.1C). After 4 simulated days, both group of cells form practically capillary-like networks independent of their initial spatial clustering. This simulation clearly shows that the long-term morphometric properties of the resulting capillary-like network are independent of the initial spatial clustering of cells.

In the next sections, I discuss key patterning instability mechanisms and their scaling dependence on the rates of diffusion and decay of the chemoattractant.

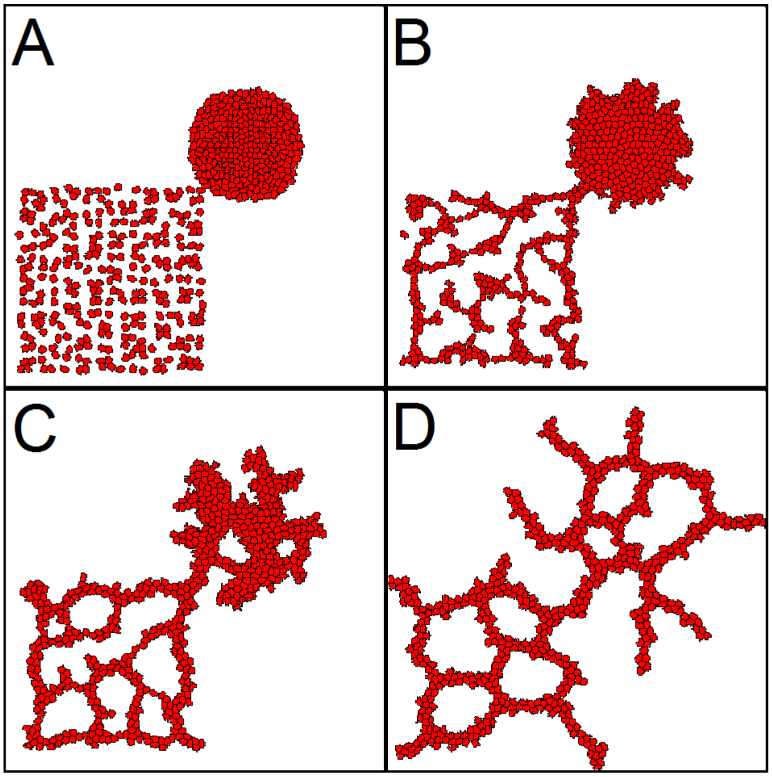

Figure I.1. Formation of capillary-like networks from randomly distributed cells (*de novo* vasculogenesis) and cells in a cluster (sprouting angiogenesis). A) The simulation starts with two separate groups of identical cells distributed randomly in a rectangular region (lower left quadrant) and in a dense cluster (top-right quadrant). B) 3 simulated hours: The randomly dispersed cells initially self-organize into one-cell diameter vascular cords and small clusters of a few cells. Cells in the dense cluster form initial sprouts at the periphery of the cluster. C) 9 simulated hours: The thin cords (B) from the dispersed cells reorganize into mostly two-cell-diameter vascular cords. The initial sprouts (B) from the dense cluster form thick irregular vascular cords. D) 4 simulated days: The groups of cells form indistinguishable capillary-like networks independent of their initial spatial clustering. See Video S1-1 and Appendix A for the simulation code.

I.2 Analysis of Vascular Patterning and Instabilities and Wavelength Selection

I.2.1 *Cord Thinning: The Sprouting Instability*

Starting from a circular cluster of ECs, the chemoattractant field rapidly assumes a saturated, quasi-Gaussian profile as shown in Figure I.2A. Due to contact inhibition of filopodial protrusions inside the cluster, only those parts of cells which lie on the boundary of the cluster in contact with the medium contribute to chemotaxis. The inward-directed chemotactic movement of the boundary compresses the cluster and increases the internal pressure of its cells, resulting in formation of finger-like sprouts, reminiscent of viscous fingering instability [40]. To analyze this sprouting instability, I have developed a continuum PDE model of the linear (small amplitude) fingering instability which appears in Figure I.2A and performed a linear stability to calculate its most unstable modes (Figure I.2B).

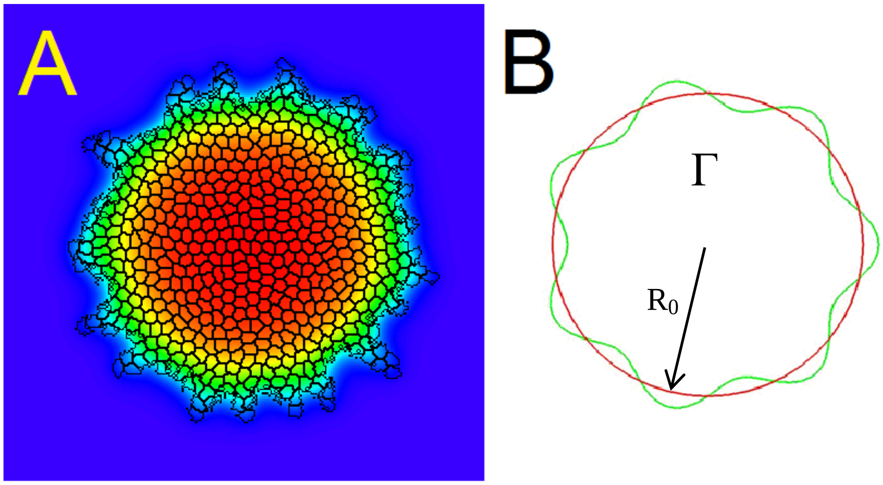

Figure I.2. Fingering instability and its continuum representation. A) Nearly circular cluster of ECs develops finger-like sprouts after ~ 3 hours. Red represents the highest concentration of the chemoattractant and dark blue represents zero concentration. B) Schematic of the linear-stability analysis: The red line shows the boundary of an unperturbed circular cell cluster Γ which has a radius of R_0. The green boundary shows a sinusoidally perturbed boundary of the cell cluster; *wavenumber* $k = 7$, *wavelength* $\lambda = 2\pi R_0 / k$.

My analysis assumes that the cell size is much smaller than the other relevant length scales (*e.g.* the cluster diameter) and model the cluster of cells in Figure I.2A as a bounded domain Γ (Figure I.2B) in $\mathbb{R}^2$. I assumed that Γ behaves like a continuum fluid and its boundary is free to move in $\mathbb{R}^2$. As discussed before, cells have a nearly constant speed when chemotaxing up a constant gradient [21]. I represent this chemotactic movement of a cell in a gradient field by:

$$\vec{F}_{\text{chemotaxis}} \propto \oint_{\text{cell boundary}} \vec{\nabla} C ds, \tag{1.3}$$

so:

$$\vec{F}_{\text{chemotaxis}} \propto \vec{v}_{\text{cell}}, \tag{1.4}$$

where $\vec{F}_{\text{chemotaxis}}$ represents the total effect of preferential formation of pseudopods in response to the gradient of chemoattractant near the cell boundary. Thus, in my continuum model, the net force acting on the boundary of Γ in the absence of surface tension is:

$$\vec{F}_{net} \equiv \vec{\nabla} C + p \hat{\boldsymbol{n}}, \tag{1.5}$$

where $\hat{\boldsymbol{n}}$ is the normal vector and p is the pressure.

Since chemical diffusion is much faster than cell diffusion due to cell motility, I can approximate the chemical concentration field using a stationary diffusion equation:

$$D\nabla^2 C\left(\vec{x}\right)+\alpha\left(1-\delta\left(\tau\left(\sigma\left(\vec{x}\right)\right),\mathrm{ECM}\right)\right)-\epsilon\, C\left(\vec{x}\right)\delta\left(\tau\left(\sigma\left(\vec{x}\right)\right),\mathrm{ECM}\right)=0, \tag{1.6}$$

where $\delta\left(\tau\left(\sigma\left(\vec{x}\right)\right),\mathrm{ECM}\right)=0$ inside Γ. Although this quasi-static approximation simplifies the analysis, the spatial discontinuities of the secretion and decay terms introduce new classes of complexity. The diffusion equation inside Γ is a Poisson equation, while the diffusion equation outside of Γ is a Helmholtz equation.

Fortunately, the stationary diffusion equations are analytically soluble for a sinusoidally perturbed circular domain. Using the separation-of-variables method, the general solutions of the diffusion equations inside and outside Γ are:

$$C_{inside}(r,\theta)=\sum_{i=1}^{\infty}C^{(i)}_{inside}(r,\theta)=\frac{-\alpha r^2}{4D}+A_0+A_0'\ln(r)+\sum_{n=1}^{\infty}(A_n r^n+A_n' r^{-n})\cos(n\theta+\phi_n), \tag{1.7}$$

and

$$C_{outside}(r,\theta)==\sum_{i=1}^{\infty}C^{(i)}_{outside}(r,\theta)=\sum_{n=0}^{\infty}\left(B_n K_0\left(\frac{r}{\ell_D}\right)+B_n' I_0\left(\frac{r}{\ell_D}\right)\right)\cos(n\theta+\varphi_n), \tag{1.8}$$

where $C^{(i)}_{inside}(r,\theta)$ and $C^{(i)}_{outside}(r,\theta)$ are *i*-th perturbative solutions and $K_0(r)$ and $I_0(r)$ are zeroth-order Bessel functions of the second kind. Consider a perturbation of form:

$$R_k(\theta)=R_0+\delta\cos(k\theta);\ k\geq 2, \tag{1.9}$$

where R_0 is the radius of the unperturbed domain and δ is the perturbation amplitude. We exclude the case, $k=1$ which translates the unperturbed domain by δ to the right (on the positive $\hat{x}$ direction). On the boundary of Γ and at the origin, $C(r,\theta)$ and its gradient are continuous and finite. Moreover, because the size of the domain which secretes the chemoattractant is finite and compact and the field decays everywhere else, the $C(r,\theta)$ is zero at infinity. Combining all the continuity and boundary conditions, the first-order perturbative solutions inside and outside Γ:

$$C_{inside}^{(1)}(r,\theta)=\frac{-\alpha r^2}{4D}+\frac{\alpha R_0\left[R_0K_1\left(\frac{R_0}{\ell_D}\right)+2\ell_DK_0\left(\frac{R_0}{\ell_D}\right)\right]}{4D}+\cos(k\theta)r^kA_k;$$
$$A_k=\frac{\delta\alpha K_k\left(\frac{R_0}{\ell_D}\right)\left[R_0K_0\left(\frac{R_0}{\ell_D}\right)+R_0K_2\left(\frac{R_0}{\ell_D}\right)+2\ell_DK_1\left(\frac{R_0}{\ell_D}\right)\right]}{4R_0^kDK_1\left(\frac{R_0}{\ell_D}\right)K_{k+1}\left(\frac{R_0}{\ell_D}\right)}, \tag{1.10}$$

and,

$$C_{outside}^{(1)}(r,\theta)=\frac{\alpha R_0\ell_DK_0\left(\frac{r}{\ell_D}\right)}{2DK_1\left(\frac{R_0}{\ell_D}\right)}+\cos(k\theta)K_k\left(\frac{r}{\ell_D}\right)B_k;$$
$$B_k=\frac{\delta\alpha\left[R_0K_0\left(\frac{R_0}{\ell_D}\right)+R_0K_2\left(\frac{R_0}{\ell_D}\right)+2\ell_DK_1\left(\frac{R_0}{\ell_D}\right)\right]}{4R_0^kDK_1\left(\frac{R_0}{\ell_D}\right)K_{k+1}\left(\frac{R_0}{\ell_D}\right)}, \tag{1.11}$$

where A_k and B_k are constants which are linear in δ. I use these solutions to calculate the net forces $\vec{F}_{net}(r,\theta)$ on the boundary of the perturbed cluster:

$$\vec{F}_{net}(r,\theta)|_{r=R_0+\delta\cos(k\theta)} \equiv \vec{\nabla}C + p\,\hat{\boldsymbol{n}},$$

(1.12)

where $\hat{\boldsymbol{n}}$ is the normal vector and p is the pressure. Since I approximate the cell cluster as an incompressible fluid, $p = \langle p \rangle$ where $\langle p \rangle$ is the average pressure:

$$\langle p \rangle = \frac{1}{2\pi R_0} \oint (\vec{\nabla}C + p\,\hat{\boldsymbol{n}}) \cdot \hat{\boldsymbol{n}}\, ds.$$

(1.13)

To prove the existence of a net outward force on the sprouting tips, I calculate the total force on each sprouting tip $\vec{F}_{total}$ which I normalized by the surface area of the sprouting tip:

$$\vec{F}_{total} = \frac{\int_{-\pi/2k}^{\pi/2k} \vec{F}_{net}(r,\theta)ds}{\int_{-\pi/2k}^{\pi/2k} \delta\cos(k\theta)ds}.$$

(1.14)

Since the gradient of the chemical field is continuous at the boundary, I can use either (1.10) or (1.11) to calculate the first-order gradient $\vec{\nabla}C^{(1)}(r,\theta)$:

$$\hat{\boldsymbol{r}} \cdot \vec{\nabla}C^{(1)}(r,\theta)|_{r=R_0+\delta\cos(k\theta)} = \frac{-\alpha\left(R_0+\delta\cos(k\theta)\right)}{2D} + \cos(k\theta)kR_0^{k-1}A_k$$
$$\hat{\boldsymbol{\theta}} \cdot \vec{\nabla}C^{(1)}(r,\theta)|_{r=R_0+\delta\cos(k\theta)} = -R_0^{-1}k\sin(k\theta)K_k\left(\frac{r}{\ell_D}\right)B_k.$$

(1.15)

In the absence of surface tension, I insert equations (1.10) to (1.13) to calculate the mean pressure:

$$\langle p \rangle = \frac{\alpha R_0}{2D},$$

(1.16)

and insert the result into equation (1.12) to calculate the first-order net force $\vec{F}^{(1)}_{net}(r,\theta)$ due to chemotaxis:

$$\hat{r}.\vec{F}^{(1)}_{net}(r,\theta)\,|_{r=R_0+\delta\cos(k\theta)} = \frac{-\alpha\delta\cos(k\theta)}{2D} + \cos(k\theta)kR_0^{k-1}A_k.$$

(1.17)

Azimuthal component of the net force does not contribute to the total force by symmetry. For radial component of $\vec{F}_{total}$ we have:

$$\begin{aligned}
\hat{\boldsymbol{r}} \cdot \vec{F}^{(1)}_{total} &= \frac{\int_{-\pi/2k}^{\pi/2k} \vec{F}^{(1)}_{net}(r,\theta)ds^{(0)}}{\int_{-\pi/2k}^{\pi/2k} \delta\cos(k\theta)ds^{(0)}} \\
&= \frac{-\alpha}{2D} + kR_0^{k-1}\delta^{-1}A_k \\
&= \frac{-\alpha}{2D} + \frac{\alpha k K_k\left(\frac{R_0}{\ell_D}\right)\left[R_0K_0\left(\frac{R_0}{\ell_D}\right) + R_0K_2\left(\frac{R_0}{\ell_D}\right) + 2\ell_D K_1\left(\frac{R_0}{\ell_D}\right)\right]}{4R_0DK_1\left(\frac{R_0}{\ell_D}\right)K_{k+1}\left(\frac{R_0}{\ell_D}\right)},
\end{aligned}$$

(1.18)

where $ds^{(0)} = R_0 d\theta$ is the zeroth-order line element of the boundary of a sprouting tip. To relate wavenumber, *k*, to the wavelength of perturbation I define:

$$\lambda \equiv 2\pi R_0 / k,$$

(1.19)

and consider $\lambda / 2$ to be the width of the sprouting tip in Figure I.2B. Figure I.3 shows the radial total force $\hat{r} \cdot \vec{F}^{(1)}_{total}$ acting on a sprouting tip as a function of the wavelength λ

for a fixed small perturbation amplitude $\delta / R_0 = 0.1$ and three values of δ / ℓ_D:Red ($\delta / \ell_D = 1$), Green ($\delta / \ell_D = 0.5$) and Yellow ($\delta / \ell_D = 0.1$). Figure I.3 show that: 1) An outward-pushing total force is always present at the sprouting tip ($F_{\text{total}} > 0$), 2) Shorter wavelengths are more unstable, 3) The rate of growth of unstable modes increases as the ratio of the perturbation amplitude to the diffusion length of the chemoattractant decreases (*i.e.* the sprouting instability is strong when $\delta / \ell_D \ll 1$). Figure I.3 shows not only that no wavelength selection exists in the linear perturbation regimes but that the continuum model is more unstable to shorter wavelength perturbations. Thus, the cord-thinning instability would favor sprouting tips with infinitely small widths.

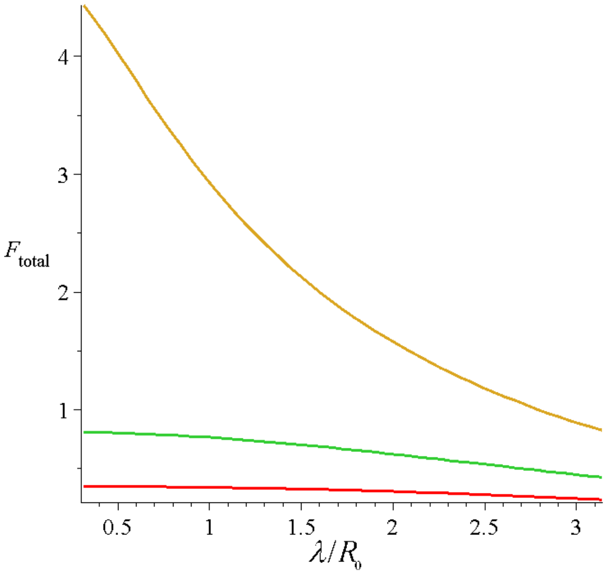

Figure I.3. Total force as a function of the interface perturbation wavelength λ for a fixed small perturbation amplitude $\delta / R_0 = 0.1$ and three values of δ / ℓ_D: Red ($\delta / \ell_D = 1$), Green ($\delta / \ell_D = 0.5$), Yellow ($\delta / \ell_D = 0.1$). $\lambda / R_0 = \pi$ corresponds to a perturbed circular domain with only two sprouts (a circular domain transformed into an ellipse); the total number of sprouts increases as λ decreases. A net outward-pushing force is always present at sprout tips ($F_{\text{total}} > 0$) and shorter wavelengths are more unstable than longer wavelengths. The rate of growth of unstable modes is higher when the perturbation amplitude is small compared to the diffusion length of the chemoattractant ($\delta / \ell_D \ll 1$).

The cord thinning instability in the continuum model is unable to explain the observed asymptotic mean cord-width in simulations. Assume that the domain Γ is composed of incompressible cells of radius r_0. The finite cell size imposes a cutoff wavelength $\lambda_c \simeq 4r_0$ on minimum width of a sprout. Based on the analysis above, λ_c is the most unstable mode available to the cluster and λ_c is independent of ℓ_D (see Figure I.3). **Thus, for all diffusion lengths, cord thinning mechanism promotes one-cell wide cords. It is unable to explain by itself formation of cords thicker than one cell (Figure I.1) and the dependence of the cord-width on the diffusion length observed in my simulations.**

Although the linear analysis of the continuum model does not completely describe the vascular patterning instabilities, it sheds light on general behavior of the unbalanced chemotaxis forces in the multi-cell simulations and the relevant scales at which they act. In summary, the sprouting instability acts to thin the cords in *GGH* model simulations until the cord-width reaches the intrinsic lower cutoff imposed by the cell size.

I.2.2 *Cord Thickening: The Folding Instability Mechanism*

The finite cell size also introduces another wavelength-changing instability resulting from cell-cell interactions. To explain this cell-scale *folding* instability, I numerically solve the stationary diffusion equation (1.6) and calculate $\vec{F}_{total}$ (1.20) acting on individual cells for a simple cell distribution (Figure I.4).

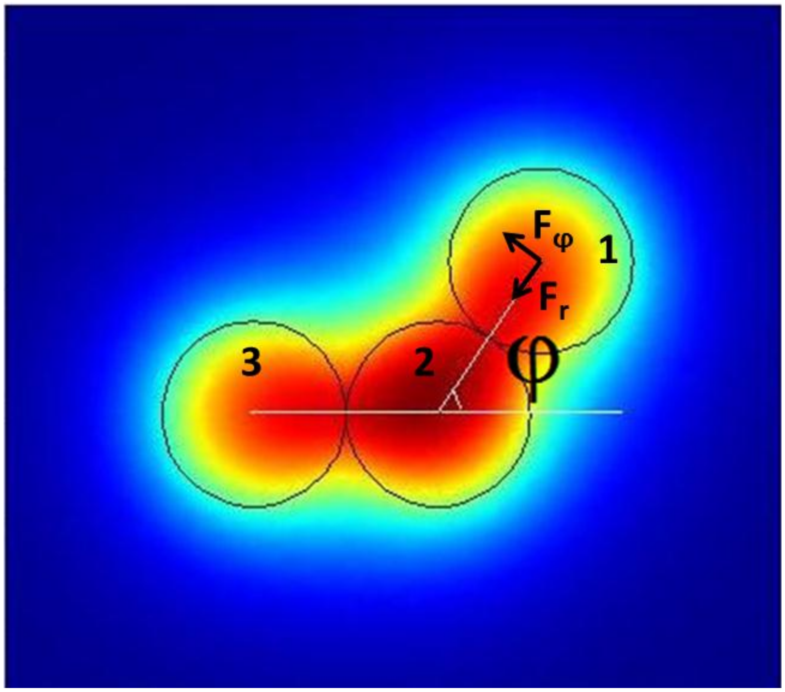

Figure I.4. Chemoattractant concentration for a simple distribution of three cells. Each cell is represented with a circular domain of a fixed radius. The plot shows the solution of the stationary diffusion equation (1.6) for three cells (labeled 1 to 3) defining an angle φ. I vary φ from 0° to 120° and calculate $\vec{F}_{\text{total}}$ acting on individual cells as a function of φ. F_φ is the azimuthal component and F_r the radial component of $\vec{F}_{\text{total}}$.

In this simplified cell-scale model, I represent an individual finite volume cell as a circular domain. I calculate $\vec{F}_{total}$ for three circular domains which are connected to each other and make an angle φ between 0° and 120°, as in Figure I.4. For $\varphi = 0$ the three circles form a line and for $\varphi = 120$ they form compact equilateral triangle. Below (section I.2.3), I relate the size of the circular domains to the cord-widths.

The total force acting on a single cell normalized by the cell volume is:

$$\vec{F}_{\text{total}} = \frac{1}{2\pi R_0^2} \oint_{\text{cell boundary}} (\vec{\nabla} C + p\,\hat{\boldsymbol{n}})\,ds, \tag{1.20}$$

since pressure is constant within a cell, $\oint_{\text{cell boundary}} p\,\hat{\boldsymbol{n}}\,ds = 0$, so:

$$\vec{F}_{\text{total}} = \frac{1}{2\pi R_0^2} \oint_{\text{cell boundary}} \vec{\nabla} C\,ds. \tag{1.21}$$

Figure I.5A shows $\hat{\boldsymbol{\varphi}} \cdot \vec{F}_{\text{total}}$ acting on cell 1 as a function of φ for three values of R_0 / ℓ_D and Figure I.5B shows the corresponding radial component of $\hat{\boldsymbol{r}} \cdot \vec{F}_{\text{total}}$ for each curve in Figure I.5A. The azimuthal component of $\vec{F}_{\text{total}}$ is always positive, which tends to increase φ, folding in-line cells ($\varphi = 0°$) into a compact configuration with $\varphi = 120°$. The folding rate at a given φ is higher for smaller values of R_0 / ℓ_D, reaching its maximum rate when ℓ_D is much greater than R_0 (Figure I.5A, black line). The radial component of $\vec{F}_{\text{total}}$ is always negative, which pulls the cells towards each other radially, preventing cells from dispersing and keeping them in a cluster. This clustering force is higher for smaller values of R_0 / ℓ_D. Due to the symmetry of the three-cell configuration (Figure I.4): 1) $\vec{F}_{\text{total}}$ acts on cell 3 just as it acts on cell 1, 2) $\vec{F}_{\text{total}}$ acting on cell 2 has no azimuthal component and only acts radially. Thus, $\vec{F}_{\text{total}}$ acting on individual cells always promotes folding and widening of clusters. However, the rate of thickening decreases as the cluster size increases (cord width), increasing the ratio R_0 / ℓ_D (*i.e.* cord thickening).

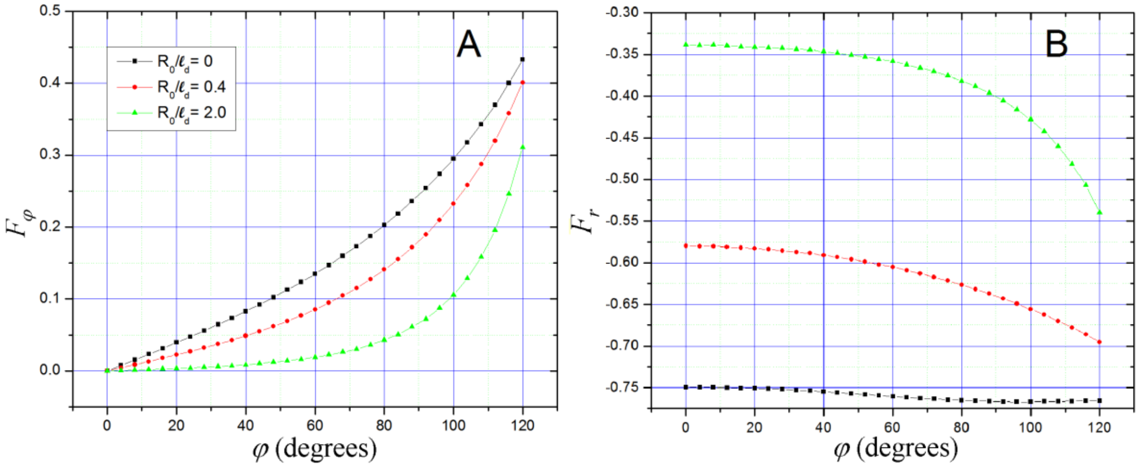

Figure I.5. $\vec{F}_{\text{total}}$ acting on cell 1 as a function of φ for three values of R_0 / ℓ_D. A) The azimuthal component of $\vec{F}_{\text{total}}$ (F_φ) is always. B) The radial component of $\vec{F}_{\text{total}}$ (F_r) is always negative. The clustering force is higher for smaller values of R_0 / ℓ_D. $\vec{F}_{\text{total}}$ only depends on R_0 / ℓ_D for a given φ (see section I.2.4 for more details).

I.2.3 *Dynamical Equilibrium between Cord-Thinning and Cord-Thickening Instabilities*

As I showed earlier (sections I.2.1-2), the folding instability (cord-thickening) and sprouting instability (cord-thinning instability) act in opposite directions on the cord width. The folding instability increases R_0 / ℓ_D and the sprouting instability decreases R_0 / ℓ_D for a given ℓ_D. These instabilities explain the self-organization of both the randomly distributed cells (lower left quadrant) in Figure I.1A into thin cords and of the dense cluster of cells (top-right quadrant) in Figure I.1A into thick cords (Figure I.1C). **Since this self-organization produces a pattern with a long-term stable cord width (as observed in Figure I.1D), the two instabilities must reach a dynamical**

equilibrium. In this section, I will characterize the behavior of these instabilities in more detail.

In general, sprouting and folding rates in the simulations are nonlinear functions of the chemotaxis strength, cell motility, cell-cell and cell-ECM adhesion. These nonlinear dependencies make analytical calculation of the instability rates in a simulation impossible. However, I can use GGH simulations to explore key characteristics of the two instabilities and then use my analysis to estimate the rates.

Pressure gradients in a long cord maintain simultaneous cell flows towards the cord ends and center (in opposite direction), corresponding to cord-thinning and cord-thickening mechanism. Figure I.6 shows spatially binned time-averaged pressure gradients and cell velocity fields at the tip of a finger-like sprout in a simulation after the two instabilities have reached dynamical equilibrium (axes measured in pixels unit). Pressure gradients and cell velocity fields fluctuate significantly when the cord-width is less than 3 cell diameter. To reduce these fluctuations, I use a relatively long diffusion length to produce a thick cord at equilibrium (10-cell diameter in width, Figure I.6A). Figure I.6B shows the *x*-component of the velocity field at about $x = 310$ (vertical black line) and Figure I.6C shows the *x*-component of the velocity field at about $y = 150$ (horizontal black line). The average pressure is high and almost constant along the midline of the cord ($x < 290$, $y \sim 150$). The pressure gradually decreases towards the tip (*e.g.* along black horizontal line in Figure I.6A). This longitudinal pressure gradient produces a relatively slow outward flow towards the tip (a positive velocity, Figure I.6B-C). This outward flow corresponds to the cord-thinning instability. Inward forces at the boundary of the cord (due to contact-inhibited chemotaxis) produce two relatively fast inward flows (negative velocities close to the boundaries of the cord in Figure I.6B-C). These inward flows correspond to the cord-thickening instability. At dynamical equilibrium, the outward flow cancels the inward flows, maintaining a fixed cord-width. Due to nonlinearities in the GGH model, changes in the simulation parameters can affect these flows differently. For example, an increase in T (fluctuation amplitude) generally increases cell motility, which could increase or decrease the cord width. In fact an increase in T increases the outward flow more than inward flow, producing thinner cords. This differential effect occur because cells moving away from the tip often have high velocities close to the practical maximum cell velocity in the GGH (0.1 pixel/MCS), so an increase in T does not significantly increase their velocity. However, an increase in T does significantly increase the cell motilities in the interior of the cord, increasing outward flow rate which results in thinner cords.

Numerical analysis of large-amplitude perturbations (large δ in equation 1.9) (data not shown) shows that the most unstable wavelength corresponds to a mode that transforms an initially circular domain to infinitely-long ellipse (*i.e.* $k = 2$). To estimate outward and inward flow rates at equilibrium, I use equation (1.18) to calculate total forces that acts to transform a circular domain into an ellipse (representing the cord-thinning mechanism) and use equation (1.21) to calculate angular component of the total force that acts to transform in-line cells (Figure I.4, $\varphi = 0°$) into a compact configuration with $\varphi = 120°$ (representing the cord-thickening mechanism). Figure I.7 shows the estimated folding and sprouting rates as a function of R_0 / ℓ_D. The blue line shows $\vec{F}_{\text{total}}$

as a function of R_0/ℓ_D for the fixed wavenumber $k=2$ and the small perturbation amplitude $\delta/R_0=0.1$. The red shows $2\times\hat{\boldsymbol{\varphi}}\cdot\vec{F}_{\text{total}}$ (angular component of the total force) as a function of R_0/ℓ_D at a fixed angle ($\varphi=60°$). The angular component of the total force for non-zero φ, represents the cord-thickening inward flows. The folding instability balances the sprouting instability where $R_0/\ell_D\cong 0.6$, *i.e.*, cord width = $2R_0\cong 1.2\ell_D$. This estimated cord-width agrees with widths observed in the GGH simulations which range from $1.5\ell_D$ to $2.2\ell_D$. A more accurate estimate of the equilibrium cord width would require detailed characterization of nonlinear interdependences among chemotaxis strength, pressure and cell motility in the GGH model.

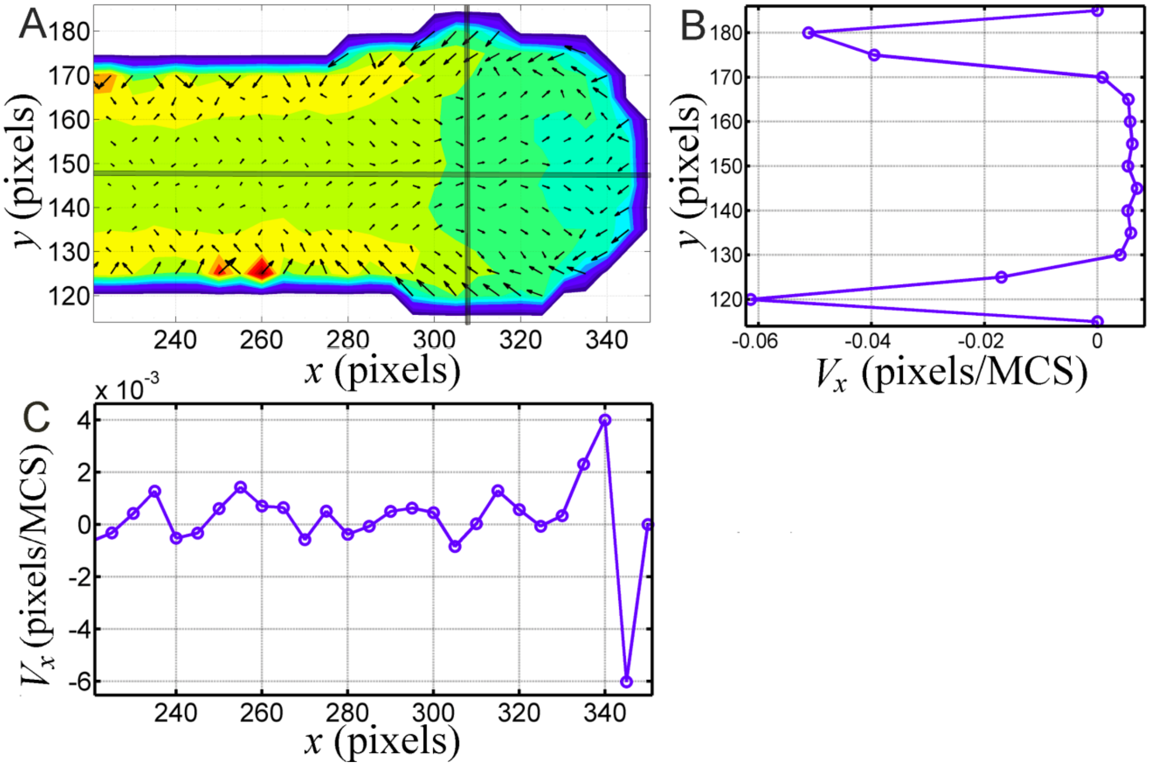

Figure I.6. Spatially binned time-averaged pressure gradients and cell velocity fields at the tip of a finger-like sprout in a simulation when the cord-thinning and cord-thickening instabilities have been reached dynamical equilibrium. A diffusion-length about 6 cell diameters produces a cord which is 10 cell diameters in width (A). (B) shows *x*-

component of the velocity vs. *y* at about *x* = 310 (vertical black line) and (C) shows *x*-component of the velocity vs. *x* at about *y* = 150 (horizontal black line). At dynamical equilibrium the out-flow cancels the in-flows, maintaining a fixed cord-width. For simulations parameters, see section I.3.

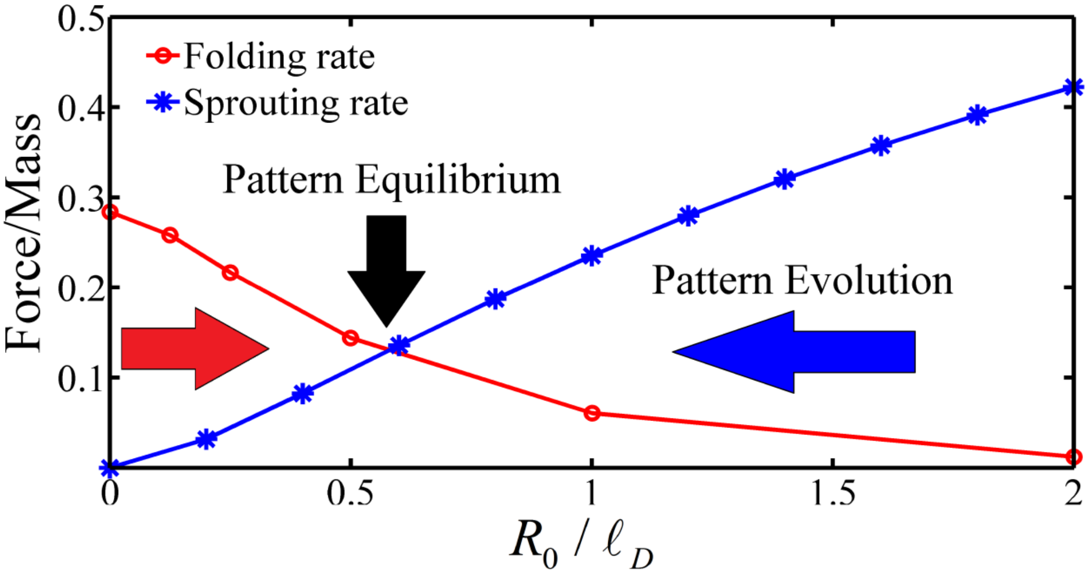

Figure I.7. Folding and sprouting rates as a function of R_0 / ℓ_D. Blue line: $\vec{F}_{\text{total}}$ (at the tip of a sprout) vs. R_0 / ℓ_D for a fixed wavenumber $k = 2$ and a perturbation amplitude $\delta / R_0 = 0.1$. Red line: Angular component of the total force, $2 \times \hat{\boldsymbol{\varphi}}.\vec{F}_{\text{total}}$ vs. R_0 / ℓ_D for fixed angle ($\varphi = 60°$). Folding instability (red arrow) and sprouting instability (blue arrow) balance for $R_0 / \ell_D \cong 0.6$ (black arrow).

I.2.4 *Scaling Behavior of Patterning Instabilities*

The previous section showed that the ratio of cord-width to the diffusion length evolves to a constant value, $2R_0 / \ell_D \cong 1.2$, independent of the initial cluster size and the cell size (as long the cell diameter is smaller than cord-width). This section derives a general scaling property of the chemoattractant diffusion equation (1.6) and uses a renormalization-group-like argument to explain this length-scale invariance.

Figure I.8 represent a cell or a cluster of cells by a domain Γ in $\mathbb{R}^2$. Rescaling both Γ and diffusion length by a scalar factor β (Figure I.8), rescales the chemotactic force acting on the boundary (3) by a factor of β^2 (Table I-1). However, the chemotaxis force per unit area remains the same after scaling (Table I-1). This scaling relationship explains why sprouting and folding rates, which are calculated using forces normalized by the surface area depend only a function of R_0 / ℓ_D.

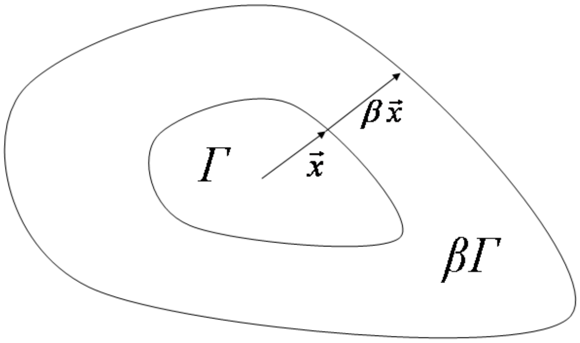

Figure I.8. Scaling of a 2D domain Γ uniformly and isotropically by a constant scaling factor β to produce the scaled domain $\beta\Gamma$.

Quantity	**Unscaled**	**Scaled**
Area of the 2D domain Γ	A	$\beta^2 A$
Diffusion length	ℓ_D	$\beta\ell_D$
Chemoattractant concentration field	$C_{\text{unscaled}}(\vec{x})$	$\beta^2 C_{\text{unscaled}}\left(\frac{\vec{x}}{\beta}\right)$
Gradient of concentration	$\vec{\nabla}C_{\text{unscaled}}(\vec{x})$	$\beta\vec{\nabla}C_{\text{unscaled}}\left(\frac{\vec{x}}{\beta}\right)$

Chemotaxis force per unit area $\frac{1}{A}\oint_{\text{cell boundary}} \vec{\nabla} C ds$	$\frac{1}{A}\oint_{\text{unscaled boundary}} \vec{\nabla} C(\vec{x}) ds$	$\frac{1}{\beta^2 A}\oint_{\text{scaled boundary}} \beta \vec{\nabla} C\left(\frac{\vec{x}}{\beta}\right)(\beta ds) =$ $\frac{1}{A}\oint_{\text{unscaled boundary}} \vec{\nabla} C(\vec{x}) ds$

Table I-1. Scaling relationships related to the chemotaxis force

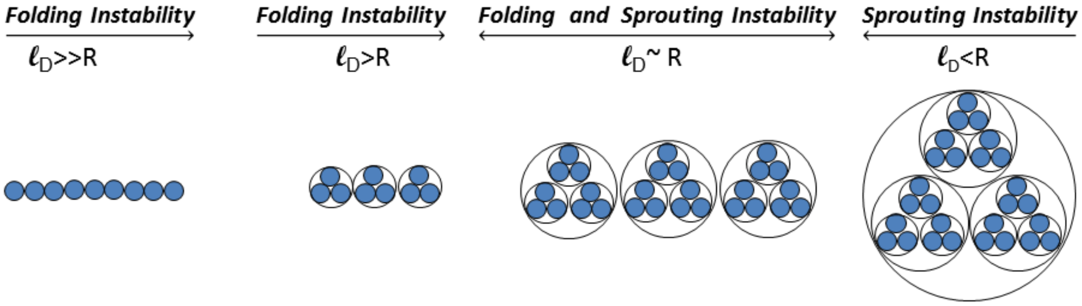

Figure I.9. Folding instability and sprouting instability dynamically balance at a certain cord-width for a given ℓ_D. The arrows show the dominant instability depending on R/ℓ_D ratio. Cells at larger scales (outlined circular domains) are composed of smaller cells (solid circular domains). Left to right: Folding instability dominates when the radius of cells in a thin cord is much smaller than diffusion length ($\ell_D \gg R$), reorganizing cells into an effectively thicker cord. Cells in the thicker cords grouped (outlined by circles), forming an effectively larger radius. Right to left: Sprouting instability dominates when the cluster radius is much larger than ℓ_D, forming thinner cords. The initial large cluster is decomposed into groups of cells (outlined by circles) that effectively have a smaller radius. This grouping and decomposition iterates until the folding instability and the sprouting instability reach a dynamical equilibrium.

Figure I.9 is a schematic illustration of how the two instability mechanisms, working simultaneously at different scales, self-organize cells into cords that reach a constant R_0/ℓ_D. Folding instability dominates when the width of a cord (a chain of cells) is much smaller than the diffusion length (Figure I.7: $\ell_D \gg R$ and Figure I.6: red arrow), reorganizing cells into an effectively thicker cord. We can group the cells composing the thicker cord and imagine that the new cord is a chain of cells with an effectively larger radius (Figure I.9, $\ell_D > R$) and use Figure I.7 to estimate the rates. If this resulting radius is still smaller than ℓ_D, folding instability thickens the cord again. Note that my regrouping schema allows to iteratively apply my analysis to estimate the rates for an effectively scaled/renormalized R. A similar argument holds when an initial cell cluster decomposes into smaller clusters repeatedly until $2R \cong 1.2\,\ell_D$ reached.

I.2.5 *Discussion*

Because tissues are composed of discrete cells, continuum models which neglect cell-scale interactions may predict qualitatively wrong results. Exploring the consequences of continuum assumptions and possible resulting artifacts is important but difficult. Ignoring cell-scale interactions in vascular patterning produced a continuum model that forms fractal-like patterns composed of infinitely thin cords rather than the fixed-width capillary-like networks of the multi-cell model and experiments.

Robustness is a key characteristic of biological pattern formation, especially during development. Capturing biological robustness in mathematical models is often difficult. A combination of physical laws of transport and a simple set of cell behaviors comprises an unstable dynamical system that robustly self-organize cells into capillary-like patterns. In the next two chapters, I study vascular patterning in the presence of external growth signals (paracrine), external chemotactic gradients in vascular tumor growth and in close contact with epithelium in choroidal neovascularization.

This chapter neglected cell proliferation. My analysis predicts that proliferation of ECs in a capillary-like network will result in formation of new sprouts. Proliferating cells in cord at equilibrium make the cord locally thicker than its equilibrium width, increasing the sprouting rate and forming a new sprout. Since cell motility limits the rate of formation and elongation, cell proliferation faster than a certain rate forms irregular networks, *e.g.* in tumor-induced angiogenesis where excess growth factors result in highly irregular poorly functioning vascular networks.

The analysis in this chapter extends to 3D angiogenesis. In 3D, sprouting instability modes have independent wavelengths in the azimuthal and polar spherical direction, allowing both finger-like sprouts and quasi-2D sheet-like sprouts. The additional degrees of freedom in 3D complicate analysis of folding instabilities. Calculation of effective folding rates in 3D requires enumeration of the possible folding scenarios for a 4-cell configuration and calculation of the contribution of each mode to the effective folding rate. Despite these differences, the forces that cause the instabilities scale identically in 3D and 2D. In 3D the chemotaxis force per unit volume/mass acting on a closed domain in 3D is:

$$\begin{aligned}&\frac{1}{\beta^3 V}\oint_{\text{scaled boundary}} \beta\vec{\nabla}C\left(\frac{\vec{x}}{\beta}\right)\left(\beta^2\, ds\right) = \\ &\frac{1}{V}\oint_{\text{unscaled boundary}} \vec{\nabla}C\left(\vec{x}\right)ds, \qquad (1.22)\end{aligned}$$

where V is the volume of an unscaled closed domain in 3D and ds is 2D surface element, and β is an arbitrary scaling factor. Figure I.10 shows a simulation of angiogenesis in 3D. The simulation starts with a spherical cluster of about 1000 ECs in Figure I.10A. During the first 6 hours, small finger-like and quasi-2D sheet-like sprouts form (Figure

I.10B) which grow into larger sprouts after about 24 simulated hours (Figure I.10C). A capillary-like network entirely composed of tubular/elongated cords forms after about two simulated weeks. The cord-widths after two weeks are about two cell diameter.

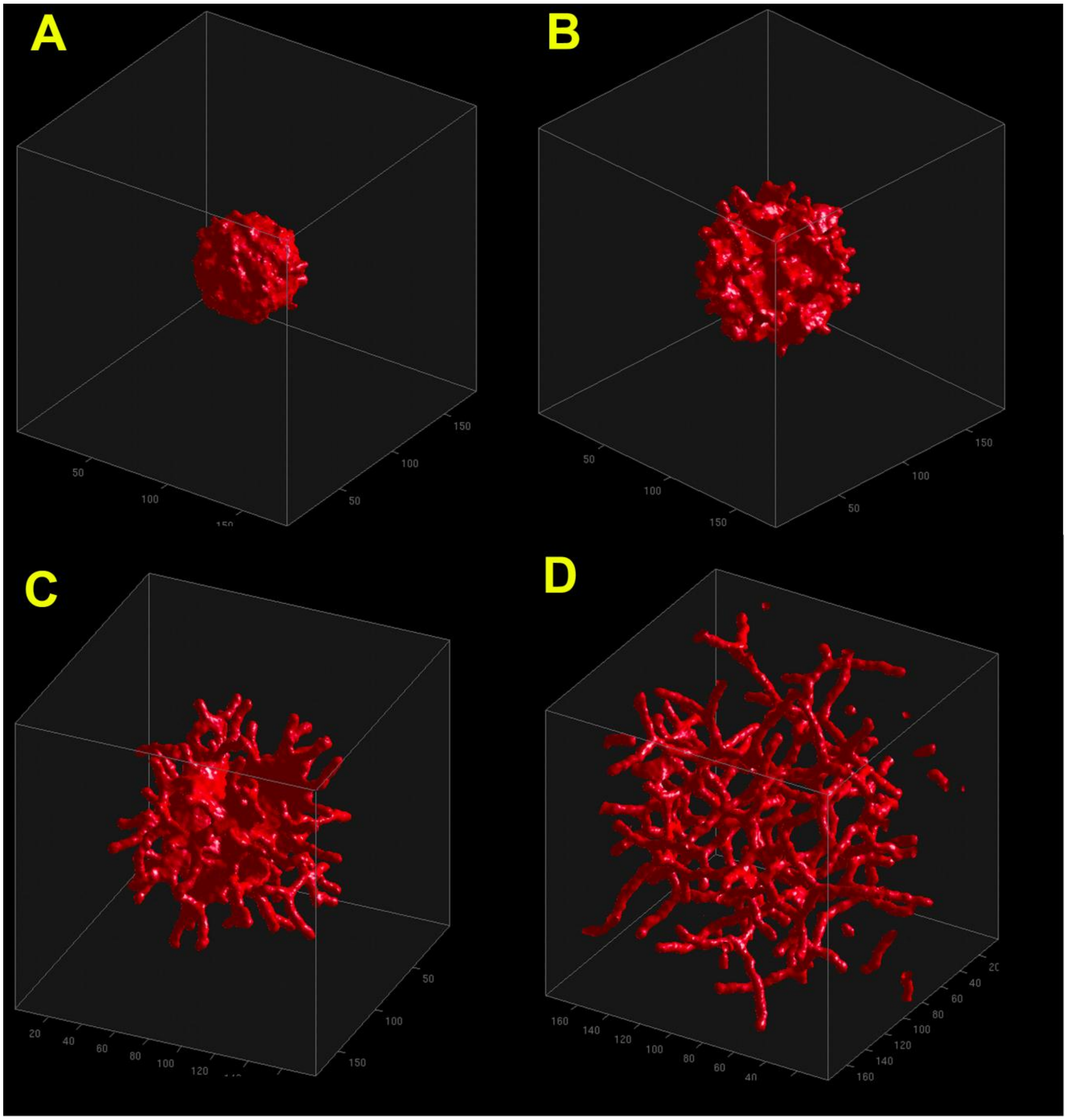

Figure I.10. 3D Multi-cell Angiogenesis. (A) Simulation initial condition is a cluster of about 1000 ECs. (B) At 6 hours, small finger-like and quasi-2D sheet-like sprouts begin to form. (C) At 24 hours; larger sprouts form. (D) At 2 weeks capillary-like network composed of tubular/elongated cords has formed. Individual cell boundaries are not rendered. The diffusion length is 3 times smaller than in the 2D simulation in Figure I.1

and contact energies are $J(c,c) = 10$ between the ECs, and $J(c,M) = 8$ between the ECs and the ECM (see also Video S1-2 and Appendix A).

I.3 Methods

I.3.1 *The Glazier–Graner–Hogeweg (GGH) Model*

The GGH represents biological cells as patches of identical lattice indices $\sigma\left(\vec{i}\right)$ on a 2D or 3D square or triangular lattice, where each index uniquely identifies, or labels a single biological cell. Each cell has an associated cell type, τ. Connections between neighboring lattice sites of unlike index $\sigma\left(\vec{i}\right) = \sigma\left(\vec{j}\right)$ represent adhesion between apposing cell membranes, where the *bond energy* is $J\left(\sigma\left(\vec{i}\right),\sigma\left(\vec{j}\right)\right)$, assuming that the types and numbers of adhesive cell-surface proteins determine J. In these simulations, a penalty increasing with the cell's deviation from a designated target volume $A_{\text{target}}(\sigma)$ imposes a *volume constraint* on the simulated cells. I define the pattern's *effective energy* (see also equation 1.2):

$$\begin{aligned} \mathcal{H}_{\text{GGH}} &= \sum_{\vec{i},\vec{j}\,\text{neighbors}} J\left(\tau\left(\sigma(\vec{i})\right),\tau\left(\sigma(\vec{j})\right)\right)\left(1-\delta\left(\sigma(\vec{i}),\sigma(\vec{j})\right)\right)+\sum_{\sigma}\lambda\,\left(A(\sigma)-A_{\text{target}}(\sigma)\right)^{2}, \\ \Delta\mathcal{H}_{\text{total}} &= \Delta\mathcal{H}_{\text{chemotaxis}}+\Delta\mathcal{H}_{\text{GGH}} \end{aligned} \tag{1.23}$$

where $\vec{i}$ and $\vec{j}$ are neighboring lattice sites (up to fourth-order neighbors), $A(\sigma)$ is the current area of cell σ, $A_{\text{target}}(\sigma)$ is its target area, λ represents a cell's resistance to compression, and the Kronecker delta is $\delta\left(x, y\right) = \{1, x = y;\ 0, x \neq y\}$. Each lattice site represents an area of 3 µm × 3 µm.

Since I assume that the ECs do not divide or grow during patterning, I set $A_{\text{target}}(\sigma) = 25$ lattice sites, corresponding to a cell diameter of about 15 µm, and $\lambda = 15$ for all cells. The ECs reside in a very thin layer of extracellular fluid, which is a generalized cell without a volume constraint and with $\sigma = 0$. I assume that the ECs and fluid sit on top of a rigid ECM through which the chemoattractant diffuses, but I do not represent this ECM in the GGH lattice. I also assume that the presence of the fluid does not disturb the chemoattractant distribution in the ECM. Unless I specify otherwise, I use a bond energy $J(c,c) = 10$ between the ECs, and $J(c,M) = 5$ between the ECs and the ECM. For these settings, the ECs do not adhere actively without chemotaxis.

To mimic cytoskeletally-driven pseudopod extensions and retractions, I randomly choose a source lattice site $\vec{i}$, and attempt to copy its index $\sigma(\vec{i})$ into a randomly-chosen neighboring lattice site $\vec{j}$. For better isotropy I select the source site from the twenty, first- to fourth-nearest neighbors [41]. A *Monte Carlo Step* (*MCS*) consists of *N copy attempts*, with *N* the number of sites in the lattice. I set the experimental time per MCS to 30 s; for this setting the simulated ECs move with nearly their experimental velocities [21]. I calculate how much the total effective energy would change if I performed the copy, and accept the attempt with probability:

$$P\left(\Delta\mathcal{H}_{\text{total}}\right)=\left\{e^{\frac{-\Delta\mathcal{H}_{\text{total}}}{T}},\Delta\mathcal{H}_{\text{total}}\geq 0;1,\Delta\mathcal{H}_{\text{total}}<0\right\} \tag{1.24}$$

where T defines the *intrinsic cell motility*. I use $T = 10$ for all simulations presented in this chapter.

I.4 A Novel Protocol for Rapid in Vitro Angiogenesis with Lumen Formation

To verify the predicted scaling law, I ran *in vitro* experiments and tried to alter the diffusive properties of growth factors like the short-diffusion isoforms of vascular endothelial growth factor-A. While severe disruption in angiogenesis and often endothelial cell death in my experiments prevented me from verifying the predicted scaling law *in vitro,* I did develop novel *in vitro* tissue engineering devices for assaying angiogenesis and for *in vitro* construction of viable capillaries. In this section, I briefly discuss characteristics of these new *in vitro* methods.

I.4.1 *Introduction*

In vitro angiogenesis assays play a crucial role in identifying factors involved in vascular development. Such assays are used in drug development as moderate-throughput screens for angiogenesis promoters and inhibitors related to wound healing, AMD, diabetes and cancer among other diseases (for comprehensive reviews of *in vitro* and *in vivo* assays, see [42-45]). *In vitro* angiogenesis is also increasingly important in tissue engineering in the construction of vascular replacements for human implantation [46,47].

Current 3D *in vitro* angiogenesis protocols are complex, slow and costly. 2D protocols produce poorly lumenized capillary networks. I present a novel *in vitro* angiogenesis protocol that produces capillary networks in quasi-*in vivo* conditions to produce a robust and implantable capillary network.

I.4.2 *State of the Art*

Current *in vitro* angiogenesis assays are either 2D or 3D. 2D assays are either *rapid* [48-52] or *long-term* [14,53-56]. In rapid 2D assays, the endothelial cells are seeded sub-confluently on top of a thick layer of a basement membrane gel which is made of a mixture of collagen, fibrin, or Matrigel [14,50,52]. Depending on the components and mechanical properties of the gel, endothelial cells align to form a capillary-like pattern within 1 to 3 days. Among rapid assays, the Matrigel assay is the most widely used, especially to characterize anti/pro-angiogenic factors. Long-term 2D assays generally refer to the culture of endothelial cells in normal culture medium in the absence ECM gel substrate [14]. As the endothelial cells divide, they form a confluent mono layer, after which some differentiate to spontaneously form capillary-like structures on top of a confluent layer of undifferentiated endothelial cells. Long-term assays require 2 to 8 weeks of cell culture, making them unsuitable for high-throughput experiments.

3D assays allow endothelial cells to invade a prefabricated 3D gel. Aortic rings in gelified matrices [57], endothelial cells seeded inside a gel or sandwiched between two layers of gel [58] and microcarrier beads coated with endothelial cells [59] are widely-used three-dimensional *in vitro* assays.

I.4.3 *Problems with Current Capillary Fabrication Protocols*

In current 2D Matrigel assays [60] (Figure I.11), cells plated on a thick layer (about 0.5 mm) of Matrigel experience unrealistically high levels of growth factors. A high concentration of growth factors in Matrigel is unnecessary and results in artifacts and over-stimulation as discussed in [45,61,62]. Even angiogenesis assays using Growth-Factor-Reduced Matrigel (GFR Matrigel), which on average contains half the levels of growth factors and cytokines of normal Matrigel, exposes endothelial cells to 15 to 30 times more growth factors than in my protocol, which also produces more realistic capillaries. The cost of the standard Matrigel assay also limits its applicability in high-throughput experiments.

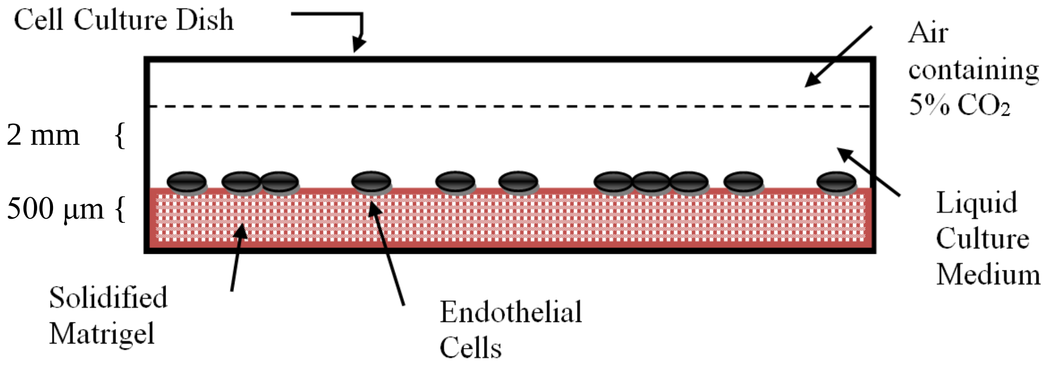

Figure I.11. Standard 2D Matrigel capillary fabrication. Matrigel solidifies at room temperature. Endothelial cells are plated on top of a 300-500 µm layer of solidified Matrigel, covered by about 2 mm of liquid culture medium and cultured at 37 °C. A quasi-2D capillary-like network forms on top of the solidified Matrigel over a period of about 18 hours.

I.4.4 *Fluid-State Protocols*

I use Matrigel from BD Biosciences and single-donor human umbilical-cord endothelial cells (*HUVECs*), endothelial growth medium and the DetachKit from

Promocell. I culture and harvest HUVECs according to the PromoCell protocols. I loaded Calcein AM (Invitrogen, C3100MP) according to the Invitrogen protocols (10 µM for 5 minutes) to fluorescently label HUVECs and determine cell viability.

I.4.5 *Protocol 1*

I dilute 1X Matrigel 30 to 60 times with 4 °C culture medium (from PromoCell) to produce a homogeneous mixture, and plate the diluted Matrigel into non-treated polystyrene petri dishes (3 ml of the mixture is enough for a 35mm dish). I incubate the dishes for 30 to 60 minutes in 5% CO_2 at 37 °C in a cell-culture incubator. I transfer the culture dishes containing cultured HUVECs and the 35mm dishes of diluted Matrigel from the incubator to a cell-culture hood at the same time to minimize heat shock. After harvesting the cultured HUVECs, I add them to the dishes containing diluted Matrigel at 150 to 200 cells/mm^2, then incubate them in 5% CO_2 at 37 °C. To distribute the plated HUVECs uniformly, I gently swirl the dishes alternately clockwise and counterclockwise. Every 48 hours I exchange the culture medium with fresh prewarmed culture media containing diluted Matrigel, prepared as above.

I.4.6 *Protocol 2*

I have also obtained reliable results when I mix the suspended cells and Matrigel immediately before cell plating (keeping the dilution ratio of Matrigel between 1:30 and 1:60). This shortcut eliminates the need to incubate the dishes for 30 to 60 minutes and makes the protocol appropriate for high-throughput experiments.

Although I used HUVECs in my experiments, my protocols should produce equally good results with other sources of endothelial cells, especially from nonhuman sources and vascular and embryonic stem cells.

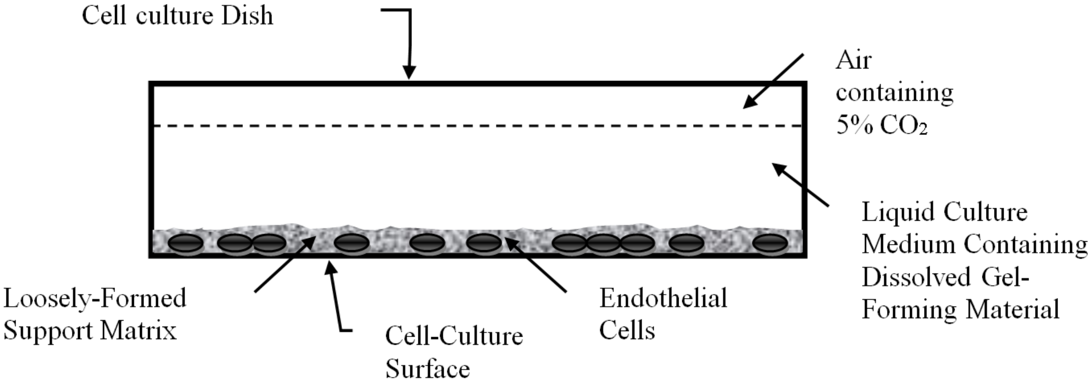

Figure I.12. Components of the capillary fabrication device. Support-generating medium which contains a dissolved gel-forming material forms a gel of support matrix of about 10 to 30 μm in thickness. Cells are covered by about 2 mm of support-generating medium. Lumenized capillary networks form inside the support matrix.

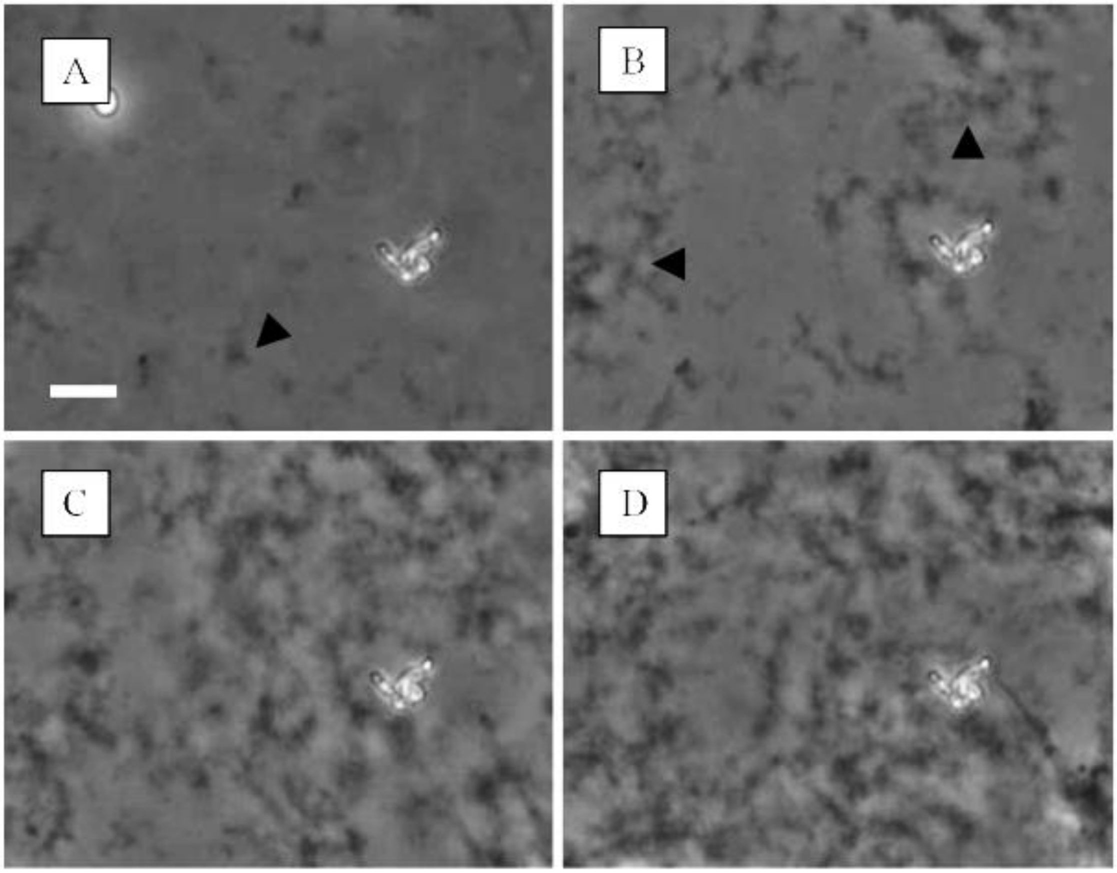

Figure I.13. Formation of support matrix. After covering the cell-culture surface with a dissolved gel-forming material (like Matrigel), a loosely-connected support matrix forms. Phase-contrast images of the support medium at 30 minutes (A), 3 hours (B), 6 hours (C) and 12 hours (D) after plating. Black arrow-heads in (A) and (B) points to clusters of support matrix. (C) Support matrix covers the entire surface after about 6 hours and does not change significantly thereafter. The lighter gray background is the hydrophobic cell-culture surface and the darker texture the support matrix. Bar, 20 µm.

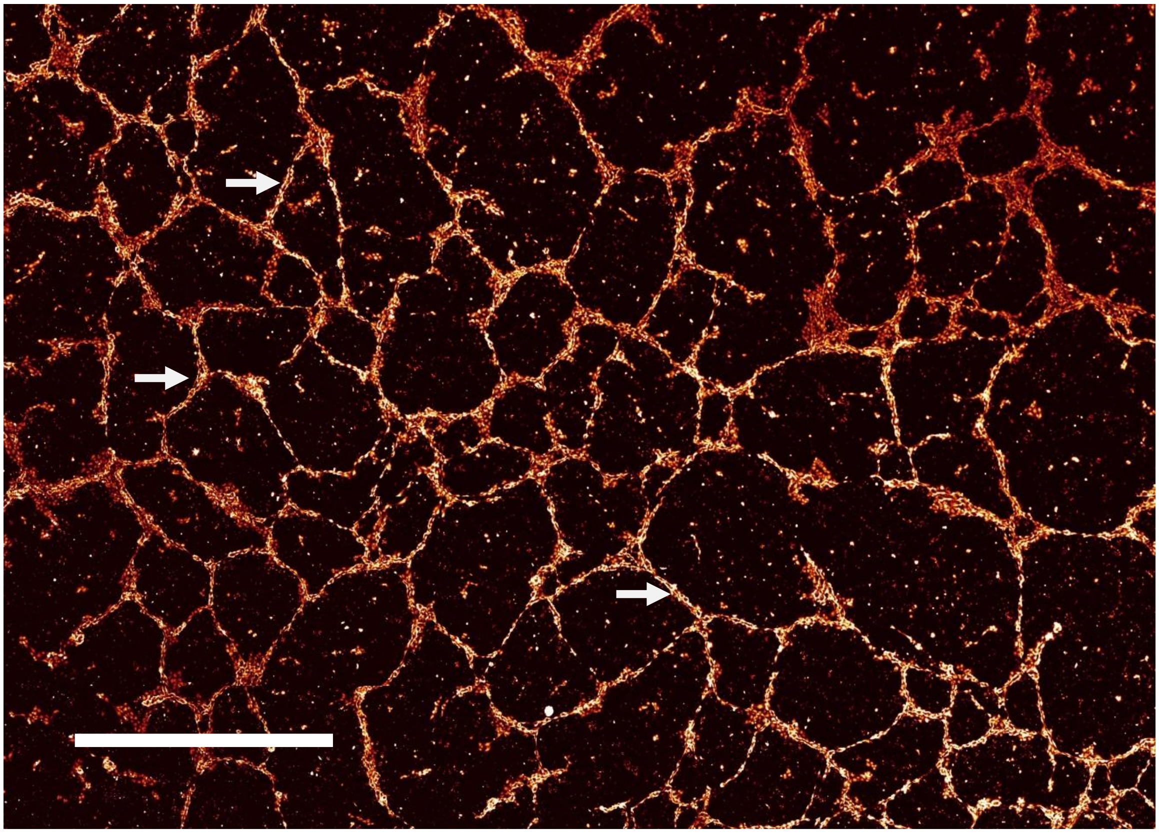

Figure I.14. Cultured HUVECs after 7 days of culture. Calcein AM was loaded for fluorescent imaging at 10 µM for 5 minutes. The lumenized capillaries have a length of 100 to 1500 µm. White arrows show segments of a viable lumenized capillary network. Bar, 2000 µm.

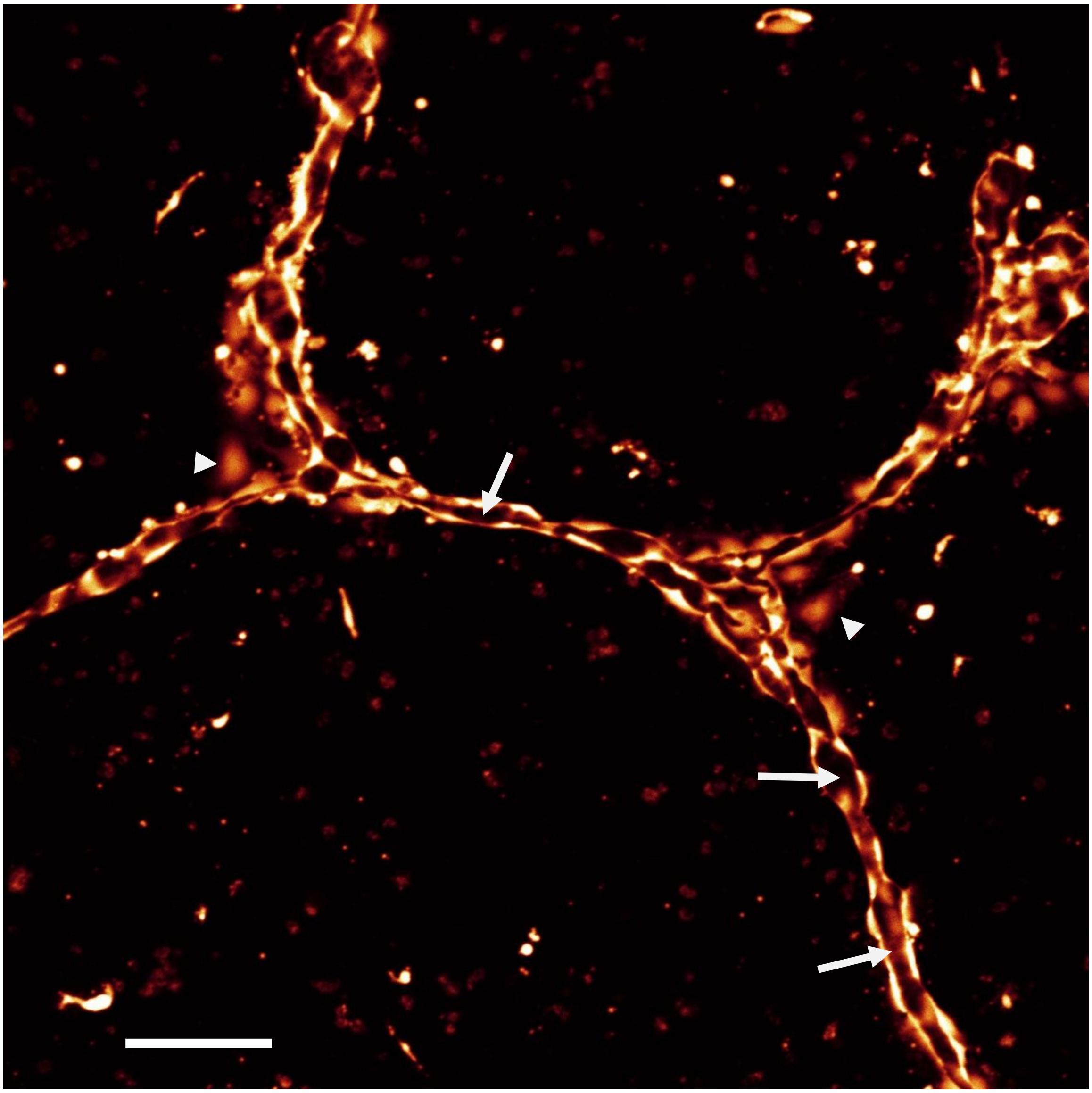

Figure I.15. Viable lumenized HUVECs capillary networks formed, after 36 hours of culture according to Protocol 1. White arrows show the lumen. The lumenized capillaries have a diameter of 5 to 25 µm. Arrow heads show endothelial cells which have not integrated into the lumenized capillary network. Bar, 50 µm.

Unlike the standard Matrigel protocol, I use non-treated polystyrene dishes which I loosely coat with Matrigel (Figure I.13), I do not solidify the Matrigel to produce a thick layer of basement membrane gel and I use much less of the very expensive Matrigel. After covering the cell-culture surface with a dissolved gel-forming material (like Matrigel), a loosely-connected support matrix forms (Figure I.13). Support matrix covers the entire surface after about 6 hours and does not change significantly thereafter. Cell-culture-treated dishes coated (according to my protocol) with Matrigel do not produce a capillary-like pattern, but increase proliferation of seeded endothelial cells compared to non-coated dishes and result in a confluent layer of undifferentiated endothelial cells. Cells cultured in non-treated polystyrene dishes without coating anoikis/apoptosis after a few hours. The combination of a loose Matrigel coating and non-treated polystyrene results in binding of specific integrin receptors in the endothelial cells which initiate transcription of anti-apoptotic genes, differentiation and tubulogenesis [63].

I.4.7 *Results*

The fluid-state protocol produces capillaries which improve in a number of ways on the standard 2D Matrigel assay [50,60]. Unlike the standard Matrigel assay, which produces a capillary-like structure composed of unnaturally elongated endothelial cells, the morphology of endothelial cells incorporated in the capillary cords and resulting lumens in the fluid-state protocol are very similar to those in capillaries formed *in vivo*, *e.g.*, in zebrafish embryo and chick allantois (Figure I.14 and Figure I.15). As Vailhé *et al.* have discussed [42], the standard Matrigel assay is unable to recapitulate normal cell motility or proliferation since endothelial cells plated on top of a thick layer of Matrigel show no or little proliferation and motility [15,50]. In my protocol, as observed in vivo, endothelial cells incorporated in capillary cords are not motile and show reduced proliferation because of strong junctional complexes; the rest of the cells proliferate and are motile (See supplemental Videos). Thus my protocol is less sensitive to the seeded cell density than the standard Matrigel assay [42,52], allowing formation of capillary networks from limited numbers of stem cells or from an autograft; the resulting capillary network would have lower chance of rejection in tissue repair and engineering applications. Thus, fluid-state protocol could be a used to assay cell proliferation, motility and tubulogenesis *in vitro*.

As in long term *in vitro* assays, the lumen capillary network remains viable at least a week after tubulogenesis (Figure I.14) (in most rapid assays the capillary-like networks degrade and disappear after tubulogenesis), which would be useful for studying the effects of pro/anti-angiogenic factors on both established lumenized capillary networks and the initial stages of tubulogenesis. Since I use hydrophobic non-treated polystyrene dishes, the adhesion of the Matrigel coating to the substrate is weak allowing detachment of the capillaries along with the underlying basement membrane for later use, *e.g.*, for implantation *in vivo* or tissue-engineering applications.

I.4.8 *Current State of Development*

After extensively optimizing my protocols and validating the quality of the vascular networks they produce, I am developing defined-matrix refinements to make the capillaries and the cell-remodeled matrix more suitable for human implantation. I am also studying the structural/mechanical and molecular differences, especially the missing components, which may distinguish my Matrigel coating from solidified Matrigel.

Since commercial polystyrene dishes have a thickness of about 1 mm, which impedes high-resolution imaging using inverted microscopes. In collaboration with Dr. Dragos Amarie, I am developing protocols to produce lumenized capillary networks on glass to improve imaging.

I.4.9 *Possible Therapeutic Applications*

Mancuso *et al.* [64] showed that regrowth of capillaries and pericyte recruitment occurs as ECs invade the empty sleeves of basement membrane left behind by destroyed capillaries. Since I can detach a developed capillary network (Figure I.16) with minimal damage, I am studying the possibility of washing the network to destroy the endothelial cells while retaining the basement membrane, then implanting the cell-remodeled basement membrane in a chick-embryo model to enhance growth/regrowth of vasculature. This organically-manufactured basement membrane could be especially useful for medical tissue-repair applications with minimal transfer of external factors, reducing the risk of rejection after implantation.

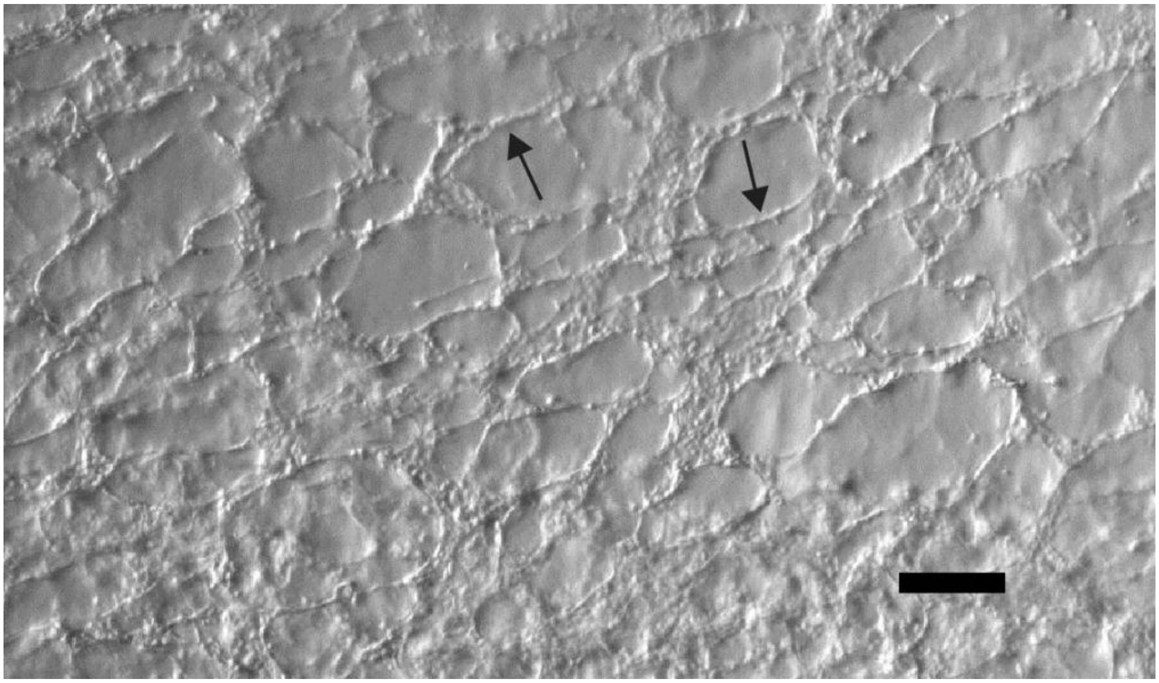

Figure I.16. Detached remodeled ECM made using the fluid-state protocol. Cultured HUVECs (according to Protocol 1) remodel initially uniformly distributed support matrix into a quasi-2D network. The manufactured ECM was detached from the bottom of a polystyrene dish by making the liquid culture media slightly acidic (pH ~ 6.0-6.5). Arrows show remodeled (cable-like) support matrix. Scale bar ~ 250 µm.

I.4.10 *Significance to Computational Modeling*

Even in a uniformly heated cell-culture incubator, the turbulent fluid flows in culture medium are strong enough to prevent formation of any diffusible chemical gradient. These turbulent flows are easily visible in time-lapse phase-contrast images of vascular pattering in the fluid-state protocol. I believe cell-ECM interactions that remodel support matrix (loosely deposited matrix, see Figure I.13) into a cable-like structures (Figure I.16) are less affected by these flows and are key processes in formation of both capillary-like network *in vitro* and also primary capillary plexus *in vivo* during vasculogenesis. Therefore, my *in vitro* techniques provide easily accessible tools to explore these interactions experimentally to develop computational models.

Chapter II: Angiogenesis in Cancer

II.1 Abstract

I present a 3D multi-cell simulation of a generic simplification of vascular tumor growth which can be easily extended and adapted to describe more specific vascular tumor types and host tissues. Initially, tumor cells proliferate as they take up the oxygen which the pre-existing vasculature supplies. The tumor grows exponentially. When the oxygen level drops below a threshold, the tumor cells become hypoxic and start secreting pro-angiogenic factors. At this stage, the tumor reaches a maximum diameter characteristic of an avascular tumor spheroid. The endothelial cells in the pre-existing vasculature respond to the proangiogenic factors both by chemotaxing towards higher concentrations of pro-angiogenic factors and by forming new blood vessels via angiogenesis. The tumor-induced vasculature increases the growth rate of the resulting vascularized solid tumor compared to an avascular tumor, allowing the tumor to grow beyond the spheroid in these linear-growth phases. First, in the linear-spherical phase of growth, the tumor remains spherical while its volume increases. Second, in the linear-cylindrical phase of growth the tumor elongates into a cylinder. Finally, in the linear-sheet phase of growth, tumor growth accelerates as the tumor changes from cylindrical to paddle-shaped. Substantial periods during which the tumor grows slowly or not at all separate the exponential from the linear-spherical and the linear-spherical from the linear-cylindrical growth phases. In contrast to other simulations in which avascular tumors remain spherical, my simulated avascular tumors form cylinders following the blood

vessels, leading to a different distribution of hypoxic cells within the tumor. My simulations cover time periods which are long enough to produce a range of biologically reasonable complex morphologies, allowing us to study how tumor-induced angiogenesis affects the growth rate, size and morphology of simulated tumors.[1]

---

[1] Portions of this chapter were published in PLoS One, 2009.

II.2 Introduction

II.2.1 *Biology Background*

The development of a primary solid tumor starts from a single cell that proliferates in an inappropriate manner, dividing repeatedly to form a cluster of tumor cells. Nutrient and waste diffusion lengths limit the size of such avascular tumor spheroids to about 1 mm [65]. The central region of the spheroid becomes necrotic, with a surrounding layer of cells whose hypoxia triggers a cascade of hypoxia-inducible factor-1 (HIF-1) and vascular-endothelial-growth-factor (VEGF)-mediated signaling events that initiate tumor vascularization by promoting growth and extension (angiogenesis) of nearby blood vessels [Marti, 2005]. This general sequence occurs in many types of tumors. Vascularized tumors are able to grow to a much larger size than spheroids and are more likely to spread and metastasize using blood vessels as pathways for invasion [66].

Both fetal and adult angiogenesis is primarily a response to hypoxia [67-71]. In adults, angiogenesis plays key roles during tissue repair and remodeling, e.g. during wound healing and expansion of tissues during the female reproductive cycle.

The level of HIF-1α DNA-binding activity in the nucleus varies exponentially with oxygen tension over the physiological range in mammalian cells [72]. Cells exposed to hypoxic conditions accumulate activated HIF-1α in their nuclei in less than 2 minutes [73]. HIF-1α changes the expression levels of numerous hypoxia-dependent genes including those responsible for oxygen transport, vascular regulation, angiogenesis, glucose uptake, and glycolysis (reviewed in [74]). HIF activation also upregulates key angiogenesis regulatory signaling molecules including VEGF-A and its receptors VEGFR-1 and VEGFR-2 [69]. VEGF-A has diffusive, ECM-bound, and semi-ECM-bound isoforms which differ in weight and heparin-binding affinity [75]. Tumors secreting different VEGF-A isoforms induce the formation of morphologically different neo-vascular beds [76].

Endothelial cells form two distinct types which respond differently to VEGF-A. Non-dividing tip cells form filopodia and migrate towards sources of VEGF-A, while non-migrating stalk cells proliferate but do not form filopodia [77-79]. Two cell types are functionally necessary because if every endothelial cell were a tip cell, the vessels would disintegrate, while uniform division of stalk cells would fail to form vessels in the correct pattern [77,78].

Cell-adhesion plays a crucial role in the formation and stabilization of nascent blood vessels (see [80,81] for reviews). Formation of cell-cell adhesion junctions via cadherins like VE-cadherin inhibits the chemotaxis response of endothelial cells to VEGF-A at endothelial cell-endothelial cell boundaries (contact-inhibited chemotaxis) and increases the stability of those boundaries [82]. The growth rate of cultured endothelial cells decreases as the area of VE-cadherin junctions increases (contact inhibition of growth) [83].

Normal new blood vessels and tumor-induced blood vessels differ greatly in morphology and function. Normal new vessels recruit pericytes and vascular smooth-muscle cells to sites adjacent to the endothelial cells to stabilize the vessel [84]. Tumor-induced blood vessels often lack a hierarchical arrangement and have irregular diameters, high tortuosity, random branching, and defective endothelial barrier function [85,86].

II.2.2 *Computational Background*

Because of the range of scales involved in cancer biology, cancer simulations employ a wide range of techniques depending on their biological focus. Standard partial-differential-equation (PDE) continuum models include scales down to the grid size used to solve the equations. Continuum multi-grid and adaptive-mesh techniques can cover scales from 10^2 μm to 10 cm. Hybrid models, which use cellular automata, agent-based or multi-cell techniques to represent individual cells and continuum PDEs to represent diffusion of molecules, can capture more detail than continuum models spanning scales from microns to millimeters (for comprehensive reviews of mathematical models of tumor-growth and angiogenesis see [87-91] and references therein).

Zheng et al. [92] have used an adaptive finite-element/level-set method to model solid tumor growth in combination with Anderson and Chaplain's hybrid model of angiogenesis [88]. Zheng's model treats tumor cells as a viscous fluid flowing through a porous medium obeying the Darcy-Stokes law. Zheng et al. have shown that both diffusional instability (competition of growth and surface tension) and co-option of the new anastomosed capillaries may be key glioma invasion mechanisms. Frieboes et al. [93] have used Zheng's level-set method in combination with Plank and Sleeman's hybrid continuum-discrete [94], lattice-free model of tumor angiogenesis to model the physiology and evolution of glioma neovasculature in 3D. Frieboes et al's model allowed them to correlate measurable tumor microenvironment parameters to cell phenotypes and potentially to tumor-scale growth and invasion. Cristini et al. [95] have also developed a continuum model of solid avascular tumors using a mixture model obeying Cahn-Hilliard-type equations. Cristini et al. found that taxis of tumor cells up gradients of nutrient produces fingering instabilities, especially when tumor cell proliferation is slow. The effects of blood flow on vascular remodeling and tumor growth have been extensively studied by Owen et al. [96], Alarcon et al., Bartha and Rieger [97], Welter et al. [98], McDougall et al. [99], Stephanou et al. [100,101], Pries et al. [102-104] and Macklin et al. [90]. Other vasculature and transport-related effects remain to be studied [105], for example how tumor cells interact with endothelial cells and enter and exit the blood stream (*intra/extravasation*) and spread to other organs (*metastasis*) via blood vessels. The simple model I present neglects the crucial effects of detailed transport due to blood flow and the effects of flow-induced vascular remodeling. I discuss some of the resulting artifacts and missing behaviors below.

Because the Glazier-Graner-Hogeweg model (*GGH*, also known as the Cellular Potts Model, *CPM*) [35,106] handles cell-cell and cell-ECM adhesion and cell motility more naturally than many other modeling methods, GGH simulations may provide additional insight into tumor growth and the complex roles of angiogenesis. Popławski et al. [107] developed a GGH simulation of avascular tumor based on Anderson’s model [108] to study the effects of adhesion and nutrient transport on the morphology of avascular tumors. Popławski et al. found that nutrient-deprived tumors are generally more invasive and that high tumor-ECM surface tension changes seaweed-like tumor-morphologies into dendritic morphologies. Rubenstein and Kaufman [109] have developed a GGH model of avascular tumors with explicit representation of two types of

ECM fibers to study the effect of ECM on growth of glioma spheroids in vitro. Rubenstein and Kaufman showed that invasion is maximized at intermediate collagen concentrations, as occurs experimentally.

In my simulations, the vascular structure produces inhomogeneities in oxygen tension on scales larger than those appearing in continuum simulations depending on inhomogeneities in Extracellular Matrix (*ECM*) and smaller than those due to tissue structure. These inhomogeneities may affect tumor growth rates and morphology and the somatic evolution of metastatic potential within tumors. Thus, simulating vascular structure at the cell level is crucial to developing biomedically-meaningful tumor simulations.

I simulate 3D solid tumor growth and angiogenesis using the multi-cell GGH model. My simulation omits many biological details, but provides a useful starting point for the construction of more realistic models. I focus on tumors where the vasculature remains peripheral to the growing tumor. My major simplifications include: 1) I neglect the distinction between veins and arteries, anastomosis, and the possible presence of pericytes and smooth muscle cells. 2) Since oxygen-depleted areas of a tissue coincide with nutrient-depleted and energy-depleted areas [110], I assume that oxygen serves as the single limiting substrate field. 3) Cells become hypoxic or necrotic by simple thresholding depending on the local concentration of oxygen. 4) I neglect the basal metabolic consumption of oxygen by tumor cells. 5) I assume that the oxygen concentration in the capillaries is constant along the blood vessels, neglecting vessel diameter, blood flow rate and vessel collapse due to external pressure. 6) I assume that oxygen diffuses uniformly in the host tissue and tumor. 7) I caricature the results of the hypoxic signaling pathways as constant-rate secretion by hypoxic cells of a single long-diffusion-length isoform of VEGF-A like VEGF-A_{121}. 8) Since I do not model blood flow explicitly, I neglect its biomedically important effects on vascular remodeling and the maturation of nascent blood vessels. 9) Rather than model tip-cell selection explicitly, I distribute a certain number of **inactive neovascular cells** (terms in **bold**, e.g. **neovascular**, refer to specific simulation classes), which behave identically to vascular cells until the concentration of VEGF-A exceeds an activation threshold. 10) I adopt the vascular-patterning hypothesis that activated vascular endothelial cells secrete and chemotax towards a short-diffusion-length chemoattractant (for a discussion of possible chemoattractant candidates see section I.1.2). 11) I employ a simplified model of tight junctions between endothelial cells in the preexisting vasculature. 12) I do not represent the ECM and the cells in the surrounding normal tissue explicitly and neglect mechanisms related to ECM and normal tissue remodeling, like secretion of ECM proteins by tumor cells, secretion of ECM-degrading enzymes (*matrix metalloproteinases*), and lactic acid accumulation.

II.3 Results

I ran otherwise identical simulations with and without angiogenesis to study how tumor-induced vasculature affects tumor growth and morphology. Figure II.1 shows a time-series of a growing tumor without angiogenesis. The tumor grows exponentially for the first 10 days (Figure II.2A and Figure II.3A, region 1 red); growth then slows and the tumor reaches a diameter of about 200 μm (Figure II.1B). **Hypoxic** domains form on day 8 (Figure II.3C) and **necrosis** begins 12 hours later. The tumor grows slowly and remains almost spherical until day 25 (Figure II.3A, region 2 red). At this stage, **normal** tumor cells form a layer of maximum thickness 75 µm near blood vessels and no **normal** cells persists far from the vasculature. The oxygen inhomogeneity produces tumor protrusions towards the adjacent blood vessels. Eventually the growing tumor pushes and stretches the vessels it contacts, finally rupturing them on day 31 (see Video S2-1 and Figure II.1C). At this stage, the tumor is large enough to span the gaps between vessels and thus to access new vessels. This strategy allows the tumor to grow at a moderate (Figure II.3A, region 3 red) rate throughout the 75 day simulation even without angiogenesis and produce a cylindrical tumor with a diameter of about 200 µm following the path of nearby blood vessels with **normal** cells only present near blood vessels. This avascular tumor growth is reminiscent of the first and second stages of growth of gliomas [111] although glioma cells usually form a peripheral cluster encompassing the blood vessel. (The growth and morphology of the tumor after day 31 is an artifact of the simplified oxygen transport in my model, see section II.4).

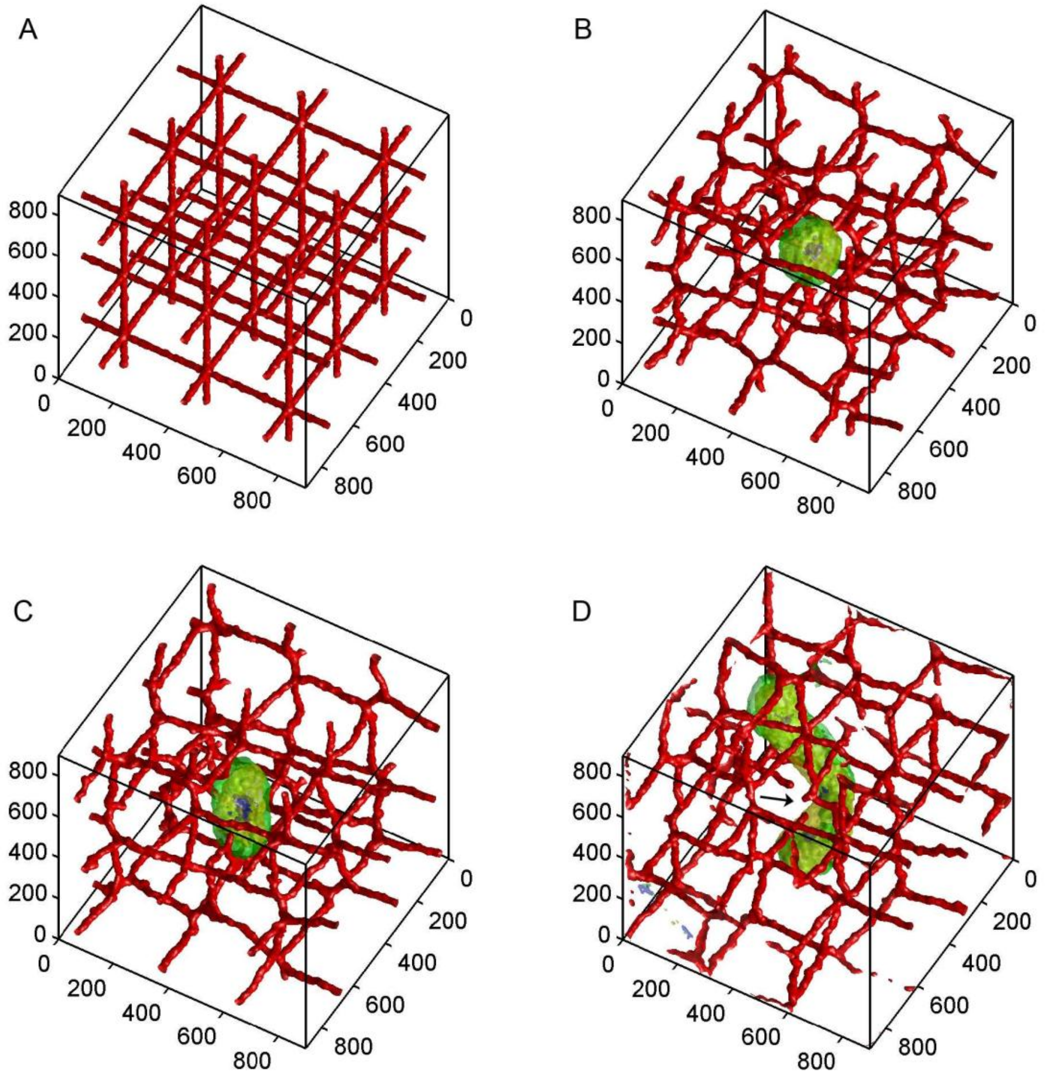

Figure II.1. Time-series of simulated tumor growth without angiogenesis. A) Day 0: Pre-existing vasculature and the initial normal tumor cell at: x=425 µm, y=425 µm, z=425 µm. B) Day 15: The tumor grows into a sphere with a maximum diameter of about 200 µm and remains at this size from day 10 to day 25. C) Day 30: The tumor grows into a cylinder with a diameter of about 200 µm and a length of about 300 µm. The vasculature is about to rupture. D) Day 75: The black arrow shows the location of the ruptured vessels. Cell types: Green: normal; yellow: hypoxic; blue: necrotic; red: vascular; purple: neovascular. Axes are labeled in µm.

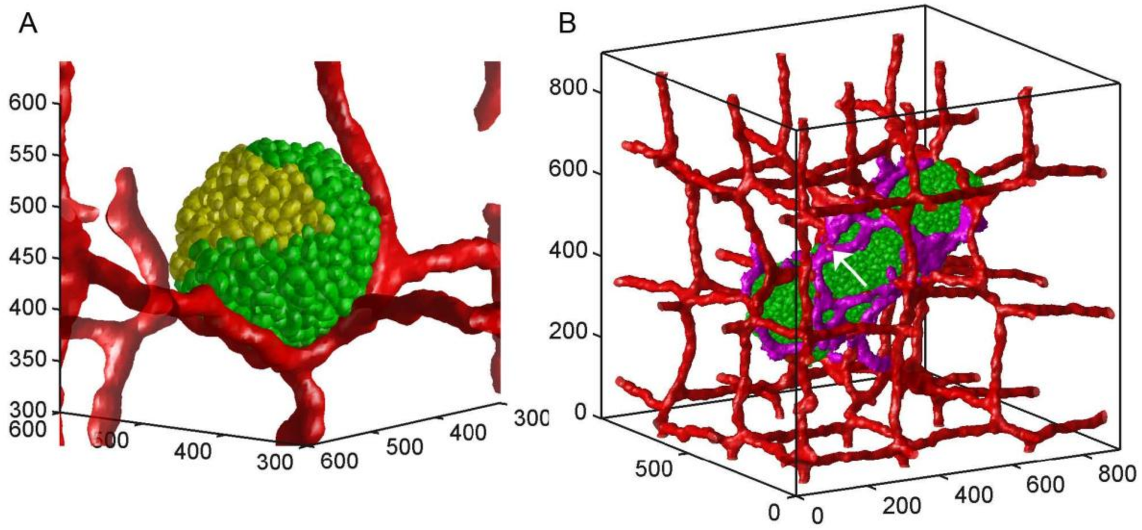

Figure II.2. Single-cell rendering of tumor cells. The green cells are normal tumor cells and the yellow cells are hypoxic cells. The preexisting vasculature is rendered in red. A) Day 10: a spherical tumor without angiogenesis with normal tumor cells only present near blood vessels. B) Day 60: A cylindrical tumor with angiogenesis, diameter ~ 300 µm and length ~ 800 µm. The purple cells are active neovascular cells which are not rendered individually. The white arrow indicates a vascular cell incorporated into a neovascular branch. Axes are labeled in µm.

In simulations with angiogenesis, tumor growth resembles that without angiogenesis for the first 15 days. Figure II.4 shows the time evolution of the number of living tumor cells in representative examples of both types of simulations. Growth is initially exponential (Figure II.3A, region 1 black). On day 8, **hypoxic** domains form and start secreting VEGF-A (Figure II.3C). VEGF-A reaches and activates the nearest inactive **neovascular** cells a few hours later. Activated **neovascular** cells then proliferate and chemotax up the VEGF-A gradient. The elastic attachment of the initial **neovascular** cells and contact inhibition of growth slow the cell-cycle time of **active neovascular** cells in the preexisting vasculature to ~ 4 days (Figure II.3C). Daughter **neovascular** cells which lack elastic links and can have less contact with neighbors have cell cycles of

~ 1-2 days. The tumor does not grow significantly from day 10 to day 14 when the first angiogenic sprouts appear (Figure II.3A, region 2 black). **Neovascular** cells form a connected peritumor network about 12 days after activation. Figure II.3A shows that the induced peri-tumor vasculature results in a phase of linear tumor growth which I call the *linear-spherical phase* (Figure II.3A, region 3 black). During this phase, the tumor grows linearly in volume, remaining spherical until it reaches a diameter of about 300µm on day 18. Growth then slows drastically from day 18 to 25 (Figure II.3A, region 4 black). After day 25 the larger tumor is more sensitive to inhomogeneities in cell proliferation, initiating a second phase of linear growth as tumor changes from spherical to cylindrical (the *linear-cylindrical phase*, Figure II.3A, region 5 black). This change in shape can be interpreted as the growth of the mode with the longest unstable wavelength which allows the tumor to grow indefinitely as long as the peri-tumor vasculature covers the entire tumor. By day 60, the cylindrical tumor has a bigger diameter than that in the simulation without angiogenesis, with **normal** cells distributed symmetrically about its axis. Positive feedback between **hypoxic** cells and **neovascular** cells results in extensive growth of **neovascular** cells. **Neovascular** cells self-organized into quasi-2D vascular sheets instead of 1D vascular branches at **neovascular** densities higher than a critical density. These thicker branches initiate a third phase of *linear-sheet* growth on day 60 (Figure II.3A, region 6) as the cylindrical tumor (Figure II.2B) grows into a paddle-like structure (Figure II.4D).

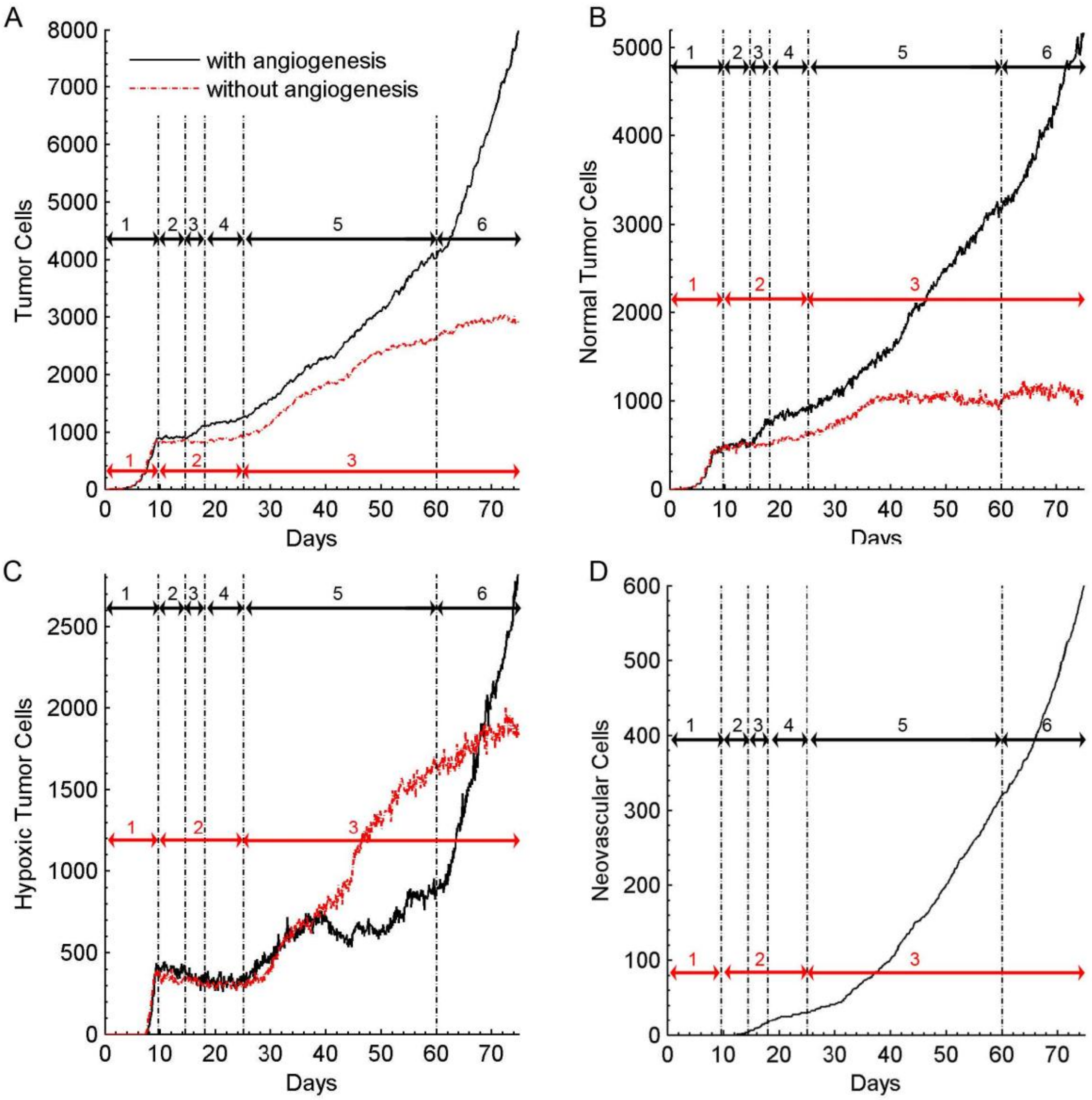

Figure II.3. Growth curves for simulated tumors with (black) and without (red) angiogenesis. Black arrows: (1) the exponential growth phase of the spherical tumor; (2) no growth; (3) the linear-spherical phase; (4) slow growth; (5) the linear-cylindrical phase; (6) the linear-sheet phase. Red Arrows: (1) the exponential growth phase of the spherical tumor; (2) slow growth; (3) cylindrical growth phase. A) The number of live tumor cells (normal and hypoxic) during 75 days of simulated tumor growth with and without angiogenesis. B) Development of the number of normal tumor cells vs. time. C) The number of hypoxic tumor cells vs. time. D) The number of neovascular cells in the simulation with angiogenesis vs. time.

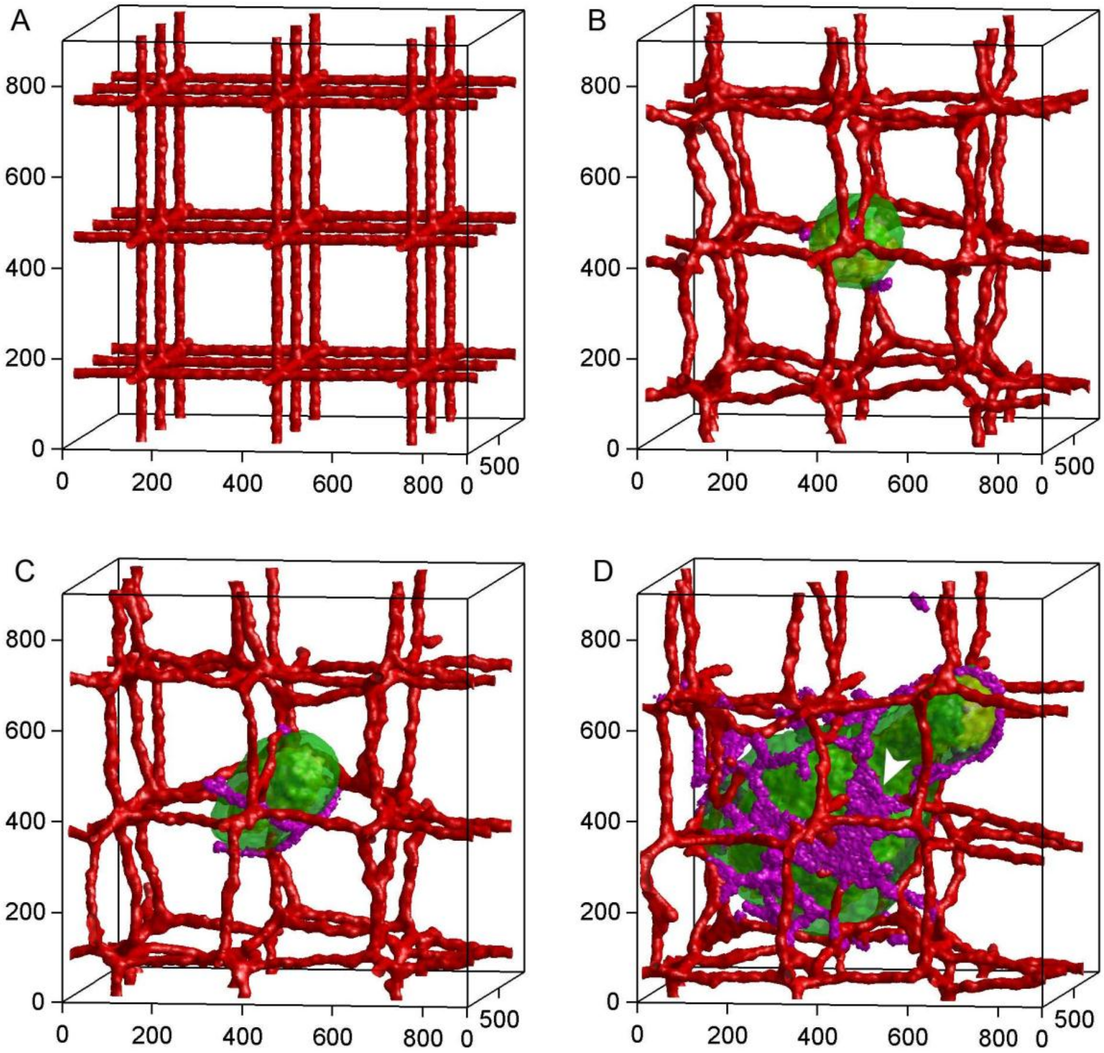

Figure II.4. Time-series of tumor growth with angiogenesis. A) Day 0: The pre-existing vasculature and the initial normal tumor cell. B) Day 15: The tumor grows into a sphere with a maximum diameter of about 300 µm. The purple cells are active neovascular cells. C) Day 30: The tumor grows into a cylinder with a length of about 350 µm and a diameter of about 300 µm. The vasculature is about to rupture. D) Day 75: The developed vascularized tumor. The white arrow-head shows neovascular cells organized into 2D sheets. Cell types: Green: normal; yellow: hypoxic; blue: necrotic; red: vascular; purple: neovascular. Axes are labeled in µm.

II.4 Discussion

In general, tumors in my simulation are smaller than those studied by Macklin et al. [90]. Macklin et al. found that avascular tumors remained spherical during 45 days of simulated growth, independent of the possible production or degradation of ECM. In my simulations, the avascular tumors become more cylindrical after day 25 and grow along (parallel to) the nearest blood vessel. The models are sufficiently different that I cannot yet identify the cause of this discrepancy. Both models produce similar growth during the first 25 days and the hypoxic core forms about the same time in both models (compare Figure II.3A-C, region 2 and 3 red to Figure 3 and 11 from [90]). In both my simualtions with angiogenesis and Macklin et al.'s (vascular growth simulation with the effect of solid pressure-induced neovascular responce and enhanced ECM degredation from [90]) the new vasculature remains outside the tumor, which becomes elongated and paddle-shaped. Vascular glioma tumors in Zheng et al.'s model [92], like avascular tumors in my model, show co-option behavior although gliomas in their model breaks up into fragments and encompasses newly formed blood vessels. In my model, reducing tumor cell-cell adhesion and increasing tumor cell-ECM adhesion could recapitulate observed blood-vessel co-option.

My simulations assume that angiogenic sprouts can partially support oxygen transport even before anastomosis. This assumption affects tumor growth between days 15 and 20 when most vascular sprouts have not formed closed loops. Requiring anastomosis for oxygen transport would both delay the onset of the vascular phase of tumor growth and make that growth more rapid once it starts. Later in the simulation, most neovascular cells form closed loops, so my simplification should have less effect.

Another artifact of my model of oxygen transport is that the tumor in the simulation without angiogenesis grows to a size comparable to the one in the simulation with angiogenesis, albeit more slowly. In the simulation without angiogenesis, inhomogeneity in tumor-cell proliferation exerts a force on the preexisting vasculature which can stretch and even rupture vascular cords (Figure II.1D, Video S2-1). Since I do not consider blood flow, such vascular damage does not change $P_{\text{blood}}^{\text{vascular}}$ (oxygen transport). If I calculated blood flow, the tumor would stop growing on day 31, then shrink slightly due to lack of oxygen. Vascular ruptures also happen in the simulation with angiogenesis (Figure II.2B), but neovascular cells usually form new vessels to fill the gaps.

In reality, oxygen supply depends on blood vessel characteristics like diameter and length. Because the production of O_2 in my simulations is proportional to the number of voxels in blood vessels, more **EC**s supply more oxygen, regardless of their organization. For example, formation of thick vascular cords and 2D vascular sheets in the simulation with angiogenesis (Figure II.1D, Video S2-1) on day 60 initiates a phase of fast linear growth which is an artifact of my simplified oxygen transport. Including the effects of vascular-network connectivity and depletion of oxygen along the direction of blood flow would produce more realistic tumor growth and morphology.

In my simulations, the preexisting vasculature with an average vascular branch length of about 300 μm supplies oxygen initially. Vascular networks with shorter average vascular branch lengths (keeping the average partial pressure of oxygen the same) would produce larger solid tumors both with and without angiogenesis. Since a tumor can grow to a maximum diameter of 200 μm without angiogenesis, average vascular branch lengths shorter than 200 μm will produce infinitely long cylindrical solid tumors.

The random motility of **normal** and **hypoxic** cells within the tumor also affects growth, reducing the inhomogeneities in cell proliferation which change spherical tumors into cylinders. Higher cell motilities paradoxically arrest tumor growth at diameters of 200 µm (no angiogenesis) and 300 µm (with angiogenesis) (data not shown). In contrast, lower cell motilities enhance formation of fingers and nodules which increase the invasiveness of the solid tumor. In reality, motility also depends on the adhesiveness of cells to each other and to the ECM, so this effect may not be clinically relevant.

I also assume that the vasculature remains peripheral to the tumor. Formation of blood vessels inside the tumor enhances oxygen transport and allows arbitrarily large tumors and faster, though not necessarily more invasive, growth.

Tumor growth in real tissues leads to increasing hydrostatic and solid pressures, inducing tumor-cell quiescence and necrosis and also causing blood vessels to collapse. Because **ECM** in my simulation is not confined by physical boundaries and does not have a volume constraint, the pressure in my tumor does not change due to tumor growth. Explicitly modeling the cells and ECM in the peri-tumor region would result in a more realistic pressure.

My simplified tumor induces angiogenesis through VEGF signaling, but neglects other tumor-induced changes in the surrounding vasculature, including apoptosis of endothelial cells because of reduced pericyte coverage and lowered pH. Combining these vascular remodeling mechanisms with blood-flow calculations would give further insight into the effects of angiogenesis on vascular tumor growth.

Although my high-resolution simulation represents a fairly small tissue volume, my results can scale to treat larger tissue volumes at lower spatial resolution. Such scaling tradeoffs may be useful for simulating tumors like prostate cancer, which involve multiyear progressions and centimeter-scale tissues.

A real solid tumor with a volume of about 1 cm^3 typically has 10^8 cells. My current version of CompuCell3D (see section II.5.2) can simulate 75 days of growth of a tumor containing 10^4 cells in 7 days on a single-core processor. To simulate more realistic tumors without needing to treat cluster of cells as single generalized cells, CC3D developers are investigating parallel computation techniques. Chen et al. [112] have developed a Message Passing Interface Standard (*MPI*) parallel implementation of the GGH which permits simulations with more than 10^7 cells. More recent versions of CompuCell3D (version 3.5.0 and later) take advantage of multi-core processors with shared memory and graphics processing units. The new version of CompuCell3D is able to simulate more than 10^7 cells in 7 days.

My next extension of these simulations will include blood flow to improve my description of substrate transport and also include shear effects on vascular remodeling.

II.5 Methods

II.5.1 *The Glazier-Graner-Hogeweg Model*

My simulation uses the Glazier-Graner-Hogeweg model (*GGH*, also known as the Cellular Potts Model, *CPM*), a multi-cell, lattice-based, stochastic model which describes biological cells and their interactions in terms of **Effective Energies** and constraints. For a detailed discussion of a basic GGH model see section III.13.

My model contains three tumor-cell types: **normal**, **hypoxic** and **necrotic** (I use the designation tumor cell to refer to both **normal** and **hypoxic** cells). **Normal** tumor cells become **hypoxic** when the oxygen partial pressure (pO_2) is less than 5 mmHg [86,110,113] and become **necrotic** when pO_2 drops below 1 mmHg. Normal and hypoxic cells take up oxygen (see below) and proliferate at a rate which depends on the oxygen partial pressure according to a Michaelis-Menten form. To model **tumor cell** proliferation, I increase the cell's target volume (V_t) according to:

$$\frac{dV_\mathrm{t}(\mathbf{tumor})}{dt} = \frac{G_m pO_2(\vec{i})}{O_0 + pO_2(\vec{i})}, \tag{2.1}$$

where $pO_2(\vec{i})$ is the pO_2 at the center-of-mass of the cell. I discuss the *maximum growth rate,* G_m, in the next section. When a cell's volume reaches its *doubling volume*, I split the cell along the x-y plane. The two daughter cells receive equal target volumes of half of the target volume of the mother cell at mitosis. **Necrotic** cells lose volume at a constant rate:

$$\frac{dV_\mathrm{t}(\mathbf{necrotic})}{dt} = -k_n. \tag{2.2}$$

I remove zero-volume cells. **Hypoxic** cells secrete the **field** $V(x)$, which models the pro-angiogenic factor VEGF-A. **Hypoxic** cells stop secreting VEGF-A and become **normal** if pO_2 is above 5 mmHg and become **necrotic** if pO_2 drops below 1 mmHg. **Hypoxic** cells secrete $V(x)$ at a constant normalized rate $\alpha_\mathrm{V} = 1$ per MCS at each voxel in their volume. $V(x)$ diffuses with diffusion constant D_V and decays at a rate ϵ_V, so $V(x)$ evolves according to:

$$\frac{\partial V}{\partial t} = -\epsilon_V V + \delta(\tau(\sigma(\vec{x})), \mathbf{hypoxic})\alpha_V + D_V \nabla^2 V, \tag{2.3}$$

where $\delta(\tau(\sigma(\vec{x})), \mathbf{hypoxic}) = 1$ at voxels belong to **hypoxic** cells and = 0 elsewhere. Since cell motility is large, cells diffuse and rearrange fast enough to prevent artifacts due to their fixed cleavage plane [114].

My model also contains two basic endothelial cell (**EC**) types: **vascular** and **neovascular**. I further distinguish two types of **neovascular** cells, **inactive neovascular** and **active neovascular**. **Vascular** cells build the preexisting mature vasculature. To represent tight junctions between endothelial cells in mature capillaries which maintain the integrity of blood vessels, linear springs connect the centers-of-mass of vascular **cells**. The springs obey the elastic constraint, $E_{\text{elastic}} = \lambda_{\text{elastic}}(l - l_{\text{t}})^2$, where l_{t} is the equilibrium length of the connection and l is the distance between the two neighbors. To model vascular rupture I set $\lambda_{\text{elastic}} = 0$ between the two neighbors when l between the two neighbors is greater than $l_{\max}$. **Inactive neovascular** cells behave exactly like vascular cells. However, above a threshold value V_0 of $V(\vec{i})$ **inactive neovascular** cells switch irreversibly into **active neovascular cells**. **Active neovascular** cells can proliferate and chemotax up gradients of VEGF-A. To account for the contact-inhibited growth of **neovascular** cells, when the common surface area with other vascular, **inactive neovascular** and **active neovascular cells** is less than a threshold, I increase the target volume of the active **neovascular cells** according to the Michaelis-Menten relation:

$$\frac{dV_{\mathrm{t}}(\mathbf{neovacular})}{dt} = \frac{G_v V(\vec{i}\,)}{nV_0 + V(\vec{i}\,)}, \tag{2.4}$$

where $V(\vec{i}\,)$ is the concentration of VEGF-A at the center-of-mass of the cell and n is a scaling constant describing the proportionality of the activation concentration to the concentration at which the growth rate is half its maximum. **Active neovascular** cells divide along the *x-y* plane when their volume reaches a specified *doubling volume*. After mitosis, both daughter cells are **active neovascular** and inherit half of their mother's target volume. **Active neovascular** cells at the tip of a sprout share two features with real tip-cells: 1) Compared to stalk cells, they have more free boundary which can respond to gradients of VEGF-A, dragging the rest of the sprout up the gradients. 2) Dragging reduces the contact area between **active neovascular** cells, promoting neovascular growth. Unlike real tip-cells, **active neovascular** cells at the tip of a sprout proliferate. Thus sprouts grow faster in steeper gradients of VEGF-A as long as the concentration of VEGF-A is well below the saturation concentration. I add a saturated Savill-Hogeweg -type chemotaxis term with contact inhibition to the basic ΔH_{GGH} of the Effective Energy to represent the net effect of preferential formation of pseudopods in response to the gradient of the chemoattractant **field** near the **active neovascular** cell's boundary:

$$\begin{aligned}
&\Delta\mathcal{H}_{\mathrm{chemotaxis}} = \big(\mu(\sigma_{\mathrm{target}}) - \mu(\sigma_{\mathrm{source}})\big)\Big(\frac{V(\vec{i}_{\mathrm{target}})}{sV_0 + V(\vec{i}_{\mathrm{target}})} - \frac{V(\vec{i}_{\mathrm{source}})}{sV_0 + V(\vec{i}_{\mathrm{source}})}\Big),\\
&\Delta\mathcal{H}_{\mathrm{chemotaxis}} = 0 \text{ at } \mathbf{EC} - \mathbf{EC} \text{ boundaries},\\
&\Delta\mathcal{H}_{\mathrm{total}} = \Delta\mathcal{H}_{\mathrm{chemotaxis}} + \Delta\mathcal{H}_{\mathrm{GGH}},
\end{aligned} \tag{2.5}$$

where μ is the degree of chemotactic response of the cell and s is a positive number which scales the VEGF-A concentration **field** relative to the **neovascular** activation threshold. μ(**ECM**) = 0.

Growth and chemotaxis of **active neovascular** cells up gradients of VEGF-A produce a dispersed growing population of **neovascular** cells rather than a connected capillary network [1]. To self-organize **vascular** and **neovascular** cells into a capillary-like structure I extended to 3D Merks' 2D model of angiogenesis in which endothelial cells self-organize into capillary-like networks in response to **autocrine** chemotaxis to a very short-diffusing chemoattractant [1]. I denote this chemoattractant **field** by $C(x)$. **Vascular** and **neovascular** cells secrete it at a constant rate α_{C} at all their voxels, the chemoattractant degrades at a constant rate ϵ_C in the **ECM**, and diffuses at a constant rate D_{C} everywhere:

$$\frac{\partial C}{\partial t} = \alpha_C\ \delta(\tau(\sigma(\vec{x})),\mathrm{EC}) - \epsilon_C\ C\ (1-\delta(\tau(\sigma(\vec{x})),\mathrm{EC})) + D_C \nabla^2 C, \tag{2.6}$$

where $\delta(\tau(\sigma(\vec{x})),\mathrm{EC}) = 1$ inside **vascular** and **neovascular** cells and = 0 elsewhere. Both **vascular** and **neovascular** cells in my model chemotax up gradients of $C(x)$. I include a linear version of (27) [1] to model contact-inhibited chemotaxis:

$$\begin{aligned} &\Delta\mathcal{H}_{\text{chemotaxis}} = \big(\mu(\sigma_{\text{target}}) - \mu(\sigma_{\text{source}})\big)\big(V(\vec{i}_{\text{target}}) - V(\vec{i}_{\text{source}})\big), \\ &\Delta\mathcal{H}_{\text{chemotaxis}} = 0 \text{ at } \mathbf{EC}-\mathbf{EC} \text{ boundaries}, \\ &\Delta\mathcal{H}_{\text{total}} = \Delta\mathcal{H}_{\text{chemotaxis}} + \Delta\mathcal{H}_{\text{GGH}}. \end{aligned} \tag{2.7}$$

Autocrine chemotaxis produces a capillary-like structure, while the elastic constraint between **vascular** cells makes the preexisting vasculature more stable and less flexible.

Vasculature transports oxygen to the host tissue and the tumor. I represent the oxygen partial pressure, pO_2, by a **field** $P(x)$. Since I initialize my simulations with a fully anastomosed preexisting vasculature and since not all **neovascular** cells form in closed loops, I assume that the oxygen partial pressure in the preexisting capillaries, $P_{\text{blood}}^{\text{vascular}}$, is higher than $P_{\text{blood}}^{\text{neovascular}}$ in the tumor-induced vasculature (see [115,116], for more accurate blood-flow calculations). I assume that the oxygen **field** concentration neighboring a vessel changes proportionally to pO_2 according to a solubility coefficient, $O_2 = K_0 P(x)$. Available O_2 diffuses at a constant rate D_{O} in the surrounding tissue and is consumed by **tumor** cells. Since oxygen consumption of human cells is almost constant until pO_2 drops below 0.5-1 mmHg and the consumption rate is constant below this pressure, I use a piecewise-linear approximation of Michaelis-Menten kinetics to model oxygen consumption. **Tumor** cells take up oxygen at a rate proportional to $P(x)$ with a maximum rate of $O_{\text{max}}^{\text{tumor}}$. The cells near the vasculature consume oxygen at their maximum rate, but cells far from the vasculature have growth limited by the available oxygen and take up oxygen at a rate $\epsilon_O^{\text{tumor}} P$. To represent oxygen consumption by host cells in the normal tissue, which I do not model explicitly, I assume an oxygen consumption rate of $\epsilon_{\text{O}}^{\text{tissue}} P$ saturating at a maximum rate of $O_{\text{max}}^{\text{tissue}}$ in the **ECM**. I include oxygen consumption by **EC** cells in the adjusted oxygen partial pressure. Thus oxygen evolves according to:

$$\begin{aligned}\frac{\partial P(x)}{\partial t} &= -\min\{\epsilon_{\mathrm{O}}^{\mathrm{tissue}}\ P(x), O_{\max}^{\mathrm{tissue}}\}\ \delta(\tau(\sigma(x)),\mathrm{ECM}) \\ &\quad -\min\{\epsilon_{\mathrm{O}}^{\mathrm{tumor}}\ P(x), O_{\max}^{\mathrm{tumor}}\}\ \delta(\tau(\sigma(x)),\mathrm{tumor}) + K_O D_O \nabla^2 P(x), \\ P(x) &= P_{\mathrm{blood}}^{\mathrm{vascular}}\delta(\tau(\sigma(x)),\mathrm{vascular}) + P_{\mathrm{blood}}^{\mathrm{neovascular}}\delta(\tau(\sigma(x)),\mathrm{neovascular}),\end{aligned} \tag{2.8}$$

where $\delta(\tau(\sigma(\vec{x})),\mathrm{vascular}) = 1$ and $\delta(\tau(\sigma(\vec{x})),\mathrm{neovascular}) = 1$ inside **vascular** and **neovascular** cells and $\delta(\tau(\sigma(\vec{x})),\mathrm{tumor}) = 1$ while $\delta(\mathrm{necrotic},\mathrm{tumor}) = 0$ and $\delta(\tau(\sigma(\vec{x})),\mathrm{tumor}) = 0$ elsewhere. $\epsilon_{\mathrm{O}}^{\mathrm{tumor}}$ is the oxygen consumption rate for both **normal** and **hypoxic** cells. I have summarized the properties of the **fields** in Table II-1 and cell types and their behaviors in Table II-2.

II.5.2 *Implementation Parameters and Initial Conditions*

My simulations use the open-source CompuCell3D simulation environment (http://www.compucell3d.org/) [117]. I ran my simulation on a 180 ×180 ×180 lattice with periodic boundary conditions. One voxel is equivalent to 125 µm. The cell lattice represents a tissue with a volume of 0.9 × 0.9 × 0.9 mm^3. My average simulated tumor cell has a volume of about 27 voxels or 3375 µm. I stored the cell-lattice configuration every 3 simulated hours and rendered each snapshot using the MATLAB volume-visualization functions (CompuCell3D version 3.5.0 has extensive post-rendering capabilities). Since rendering individual cells is computationally expensive, in Figure II.1 and Figure II.4 and Supplemental Videos (Video S2-1 and S2-2) I have only rendered boundaries between cells which differ in type. For demonstration purposes, I have rendered the boundaries of individual **tumor** cells in the simulation with angiogenesis on day 60 (Figure II.2B) and in the simulation without angiogenesis on day 10 (Figure II.2A).

Experimentally, tumor cells from lines such as U-87 human glioma [118-121] can move at a rate of about 0.35 µm/min. For typical parameter settings in my simulations tumor cells move at about 0.1 pixels/MCS. Equating the experimental and simulated mean cell speeds implies 1000 MCS ~ 24 h.

I start my simulation with a single **normal** tumor cell near the center of the cell lattice and a preexisting network of blood vessels (see Figure II.1). I assume that $P_{blood}^{vascular} = 90$ mmHg in preexisting vasculature and $P_{\mathrm{blood}}^{\mathrm{neovascular}} = 50$ mmHg in the tumor-induced vasculature. I set the diffusion constant of oxygen in my simulations to 10^3 µm^2/s, about half its diffusion constant in water. Since **hypoxic** cells in my simulations become necrotic if $P(\vec{i})$ drops below 1 mmHg, I set both $\epsilon_{\mathrm{O}}^{\mathrm{tissue}}$ and $\epsilon_{\mathrm{O}}^{\mathrm{tumor}}$ to 1. I $O_{\max}^{\mathrm{tissue}}$ so the average $P(\vec{i})$ of the tissue reaches an asymptotic value of 20 mmHg. I assume that the density of cells in the tumor is about 10 times the density of the cells distributed in the **ECM** (which I do not represent explicitly). I assume that both **hypoxic** and **normal** tumor cells in my model consume oxygen at a rate up to 3 times that of the cells in the surrounding tissue, thus $O_{\max}^{\mathrm{tumor}} = 3 \times 10 \times O_{\max}^{\mathrm{tissue}}$. Higher oxygen consumption results in shorter oxygen penetration lengths and smaller solid tumors. I set $O_0 = 10$ mmHg and choose G_m so that the cell cycle of **tumor** cells at $P(\vec{i}) = 25$ is 24 h. For these parameters my simulations produce solid tumors with maximum diameters of 200 µm.

Experimentally, the VEGF-A diffusion constant is about 10 µm^2/s in typical tissues and its decay rate is about 0.65 h^{-1} [Serini et al., 2003]. I set the activation VEGF-A concentration $V_0 = 0.5$, $s = 1$, and pick G_v do that a **neovascular** cell that does not contact any **vascular** or **neovacular** cells has a minimum cell-cycle time of 24 h. Due to contact-inhibition of growth, **neovascular** cells incorporated in a tumor-induced vessel grow at a negligible rate.

I assume that integrins are down-regulated in **tumor** cells and that cell-cell adhesion via cadherins keeps the tumor solid, i.e. that the surface tension at the **tumor-ECM** interface is positive, *J*(***tumor***, ***tumor***) < *2J*(***tumor***, ***ECM***) (for definitions of surface tensions see [35,122]). I set a positive surface tension between **EC** (**vascular** and **neovascular**) and **tumor** cells (*J*(**tumor**,**ECM**)+ *J*(**EC**,**ECM**) <*J*(**tumor**,**EC**)) which keeps the vasculature peripheral to the tumor. For the specific values of *J* and the other parameters, see the Appendix B for *XML* and *python* code.

Fields	Definition	Role/Properties
$P(x)$	partial pressure of oxygen	-regulates **tumor** cell growth -induces **normal** ↔ **hypoxic** transition -induces **hypoxic** → **necrotic** transition
$V(x)$	long-diffusing proangiogenic factor	-hypoxic signaling -induces **inactive neovascular** → **active neovascular** transition -regulates **neovascular** growth -chemoattractant for **vascular** and **neovascular** cells
$C(x)$	short-diffusing chemoattractant	-self-organizes **vascular** and **neovascular** cells into capillary networks

		-chemoattractant for **vascular** and **neovascular** cells

Table II-1. Diffusive molecules in the vascular tumor-growth simulation. All molecules diffuse everywhere uniformly and isotropically. Boundary conditions of the lattice are periodic.

Cells	Behaviors
Tumor cells	
Normal	-proliferate -consume oxygen -change to hypoxic -change to necrotic
Hypoxic	-proliferate -consume oxygen field -change to normal -change to necrotic -secrete long-diffusing proangiogenic field $V(x)$
Necrotic	-shrink -disappear
Endothelial cells	
Vascular	-consume oxygen field -supply oxygen field at partial pressure $P_{\text{blood}}^{\text{vascular}}$ -secrete short-diffusing chemoattractant field $C(x)$ -chemotax up gradients of field $C(x)$ -elastically connect to neighboring vascular and inactive neovascular cells -lose elastic connections, when $l > l_{max}$

Inactive neovascular	-consume oxygen field -supply oxygen field at partial pressure $P_{\text{blood}}^{\text{vascular}}$ -secrete short-diffusing chemoattractant field $C(x)$ -chemotax up gradients of field $C(x)$ -elastically connect to neighboring vascular and inactive neovascular cells -lose elastic connections, when $l > l_{max}$ -change to active neovascular
Active neovascular	-consume oxygen field -supply oxygen field at partial pressure $P_{\text{blood}}^{\text{neovascular}}$ -secrete short-diffusing chemoattractant field $C(x)$ -chemotax up gradients of field $C(x)$ -chemotax up gradients of field $V(x)$ -proliferate

Table II-2. Cell types in the simulations and their behaviors.

Chapter III: Mechanisms of Choroidal Neovascularization

III.1 Abstract

Choroidal neovascularization (CNV) of the macular area of the retina is the major cause of severe vision loss in adults. In CNV, after choriocapillaries initially penetrate Bruch's membrane (BrM), invading vessels may regress or expand (CNV initiation). Next, during Early and Late CNV, the expanding vasculature usually spreads in one of three distinct patterns: in a layer between BrM and the retinal pigment epithelium (sub-RPE or Type 1 CNV), in a layer between the RPE and the photoreceptors (sub-retinal or Type 2 CNV) or in both loci simultaneously (combined pattern or Type 3 CNV). While most studies hypothesize that CNV primarily results from growth-factor effects or holes in BrM, my three-dimensional simulations of multi-cell model of the normal and pathological maculae recapitulate the three growth patterns, under the hypothesis that CNV results from combinations of impairment of: 1) RPE-RPE epithelial junctional adhesion, 2) Adhesion of the RPE basement membrane complex to BrM (RPE-BrM adhesion), and 3) Adhesion of the RPE to the photoreceptor outer segments (RPE-POS adhesion). My key findings are that when an endothelial tip cell penetrates BrM: 1) RPE with normal epithelial junctions, basal attachment to BrM and apical attachment to POS resists CNV. 2) Small holes in BrM do not, by themselves, initiate CNV. 3) RPE with normal epithelial junctions and normal apical RPE-POS adhesion, but weak adhesion to BrM

(e.g. due to lipid accumulation in BrM) results in Early sub-RPE CNV. 4) Normal adhesion of RBaM to BrM, but reduced apical RPE-POS or epithelial RPE-RPE adhesion (e.g. due to inflammation) results in Early sub-retinal CNV. 5) Simultaneous reduction in RPE-RPE epithelial binding and RPE-BrM adhesion results in either sub-RPE or sub-retinal CNV which often progresses to combined pattern CNV. These findings suggest that defects in adhesion dominate CNV initiation and progression.[1]

---

[1] Portions of this chapter were published in PLoS Comp. Bio., 2012.

III.2 Introduction

III.2.1 *Organization*

I first review the key components of the retina and the processes commonly hypothesized to underlie CNV. I then discuss my main hypotheses for CNV mechanisms and why I believe adhesion may play an important role in both initiation and progression of CNV. I then use a multi-cell computer simulation of a mechanistic computational model of the choriocapillaris, BrM and photoreceptors to investigate the effects of adhesion variations on CNV initiation and progression. Finally, I focus on how adhesion in the BrM-RPE-POS complex changes due to aging and inflammation both in human retina and in animal models of CNV and discuss the biomedical implications of my results.

III.2.2 *Modeling Terminology*

Because terminology in biological modeling and simulation is often inconsistent, I would like to define certain key modeling concepts and their designations. I distinguish types of models by their *level*, *i.e.*, their degree of abstraction, and by the *length scales* which they primarily treat. At each abstraction level and length scale, any model requires at least the following: *objects* (the physical components to be described), *properties* (the intrinsic properties of the objects, like volume, location, shape, …), *processes* (how objects affect each other. Biologists often call processes mechanisms, behaviors or interactions), *dynamics* (how objects and processes change in time) and *initial conditions* (the initial identity, configuration and state of all objects and processes) (Figure III.1).

In the context of experimental biology, the term *biological model* often refers to an *in vitro* or *in vivo* cell or animal experiment that exhibits a biological phenomenon. However, in my computational-biology context, a *biological model* is a qualitative (possibly complex) description of a set of hypothesized objects, processes and relationships, dynamics and initial conditions, developed to explain a biological phenomenon. Biologists employ such biological models when they form mental images which they construct by integrating results from many different types of experiment. A *mathematical model* is a formalized, **quantifiable** representation of a biological model, which embodies explicitly the rules governing the biological behavior in a quantitative form (often as sets of equations); a *computational model* is an implementation of a mathematical model in the form of algorithms, which use particular methods and sets of possibly method-dependent parameters, initial conditions and boundary conditions; a *simulation* is an *instance* of a computational model expressed as computer-executable code with specific parameter values (I often employ families of simulations to evaluate a model's response to changes in boundary conditions or initial conditions); and a *visualization* is a set of images presenting a selection of the data a simulation produces. In practice, when developing a model, I begin at the most abstract level, by building a biological model, then gradually add details to develop less abstract models. At each level of abstraction, I must explicitly state the simplifications and assumptions that I have made in addition to those already introduced. Finally, I compare my visualization results to experimental data and refine or correct my biological model and the corresponding models at each level as needed.

When I refer to a *model* without further qualification, I refer to an ensemble of corresponding biological, mathematical and computational models and their corresponding simulations and visualizations, *i.e.*, a particular set of hypotheses and their descriptions at all levels of abstraction.

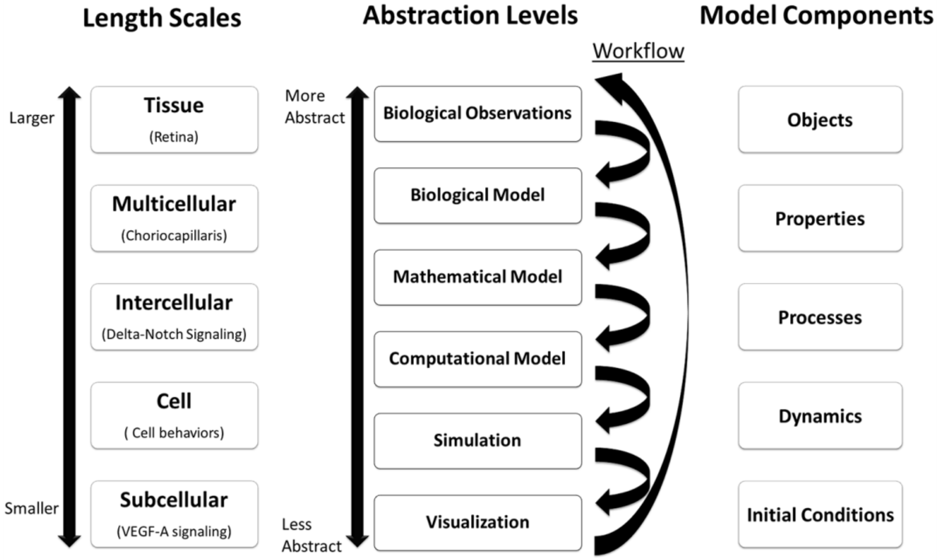

Figure III.1. Models and their components. Left: A Multi-scale model includes processes and objects at multiple spatial length scales (with an illustrative example for each scale). Middle: Any model can be formulated at different levels of abstraction, from a verbal or schematic biological model to an algorithmic computation model which can be implemented as simulation code and visualized in a particular way. Model development begins at the most abstract level, by building a biological model, then gradually adding detail to develop less abstract models. Model development and validation involve continuous cycling from more abstract to less abstract levels, followed by comparison of visualization data with biological observations and model refinement. Right: To be complete and useful, all models at all spatial scales and levels of abstraction must include a basic set of model components: specifically what is modeled (objects), the capabilities of these objects, which include their behaviors and interactions (processes), how these objects and processes change in time (dynamics) and the situation modeled (initial conditions).

III.2.3 *Age-Related Macular Degeneration and Pathological Choroidal Neovascularization*

Growth of new blood vessels by sprouting from preexisting capillaries or major blood vessels is known as *angiogenesis*. *Sprouting angiogenesis* occurs in response to chemical and mechanical stimuli and to hypoxia in both adult and embryonic tissues. Sprouting angiogenesis requires activation of normally quiescent endothelial cells in pre-existing blood vessels, breakdown of existing basement membranes, migration of activated cells led by one or more endothelial *tip cells* or immune cells (which can also function as tip cells) in response to environmental and cell-contact cues and proliferation of a subset of activated endothelial cells (*stalk cells*) with possible recruitment of support cells (pericytes and smooth muscle cells) during blood-vessel maturation [2].

In pathological angiogenesis, *e.g.* in vascular tumors, vessels do not mature, resulting in leaky capillary vasculature which causes severe edema, inefficient blood transport and reduced oxygenation. Maturation failure can result in a pathological feedback loop, where worsening hypoxia leads to higher levels of proangiogenic factors, including vascular endothelial growth factor A (*VEGF-A*) and platelet-derived growth factor (*PDGF*), and the greater excess of proangiogenic factors produces even more inefficient capillaries, worsening the hypoxia.

The hallmark of *wet* or *exudative* age-related macular degeneration (*AMD*), which is the leading cause of irreversible blindness in North America, Europe, and Australia [123], is lesioning choroidal neovascularization (*CNV*), the invasion of the retina by new blood vessels growing from the choriocapillaris (*CC*). In humans, CNV frequency increases with age, independent of other risk factors or specific insults, though numerous risk factors and insults can greatly increase its probability of occurrence in an individual. CNV in all patients shares the same basic neoangiogenic steps. I distinguish the following three temporal phases: *Initiation*, when endothelial cells first cross Bruch's membrane (*BrM*); *Early CNV*, when endothelial cells spread and form capillaries in a defined locus, and *Late CNV*, when additional loci may become involved, often leading to retinal pigment epithelium (*RPE*) detachment and degeneration, CNV regression/involution and photoreceptor death.

The diverse CNV scenarios are categorized based on histological [124] and clinical observations [125]. Neovascular vessels originating from the choroid can grow in the plane between the RPE and BrM (*sub-RPE*, *occult* or *Type 1 CNV*), between the retina and the RPE (*sub-retinal*, *classic* or *Type 2 CNV*) or in both locations (*combined* or *Type 3 CNV*). Type 3 CNV can also form as a late stage of Early Type 1 or Early Type 2 CNV. In wet AMD, severe visual loss results from subretinal hemorrhage from the leaky CNV, which leads to the eventual formation of a disciform scar. While CNV is generally a disease of the elderly, with onset occurring after 70 years, progression after onset may be rapid. According to the Macular Photocoagulation Study Group [126], about 40% of patients with untreated Type 1 CNV loose significant visual acuity within 12 months. 23% of these patients develop Type 3 CNV within 3 months and an additional 23% develop Type 3 CNV within 12 months. Current therapeutic strategies depend on the CNV locus (subfoveal, juxtafoveal or extrafoveal) and include photodynamic therapy, laser photocoagulation and most-commonly, anti-angiogenic drugs (Lucentis, Macugen or Avastin) [127]. Long-term prognoses are poor; only 20% of patients with Type 1 CNV have stabilized or improved vision 36 months after initial diagnosis and treatment [126].

Developing more effective targeted intervention strategies will depend on understanding CNV mechanisms. However, because of the structural complexity of the normal and diseased retina and the numerous homeostatic and developmental mechanisms operating concurrently, experiments have yet to identify clearly the mechanisms responsible for either CNV initiation or progression. As a novel approach to developing such understanding, this study applies quantitative models and computer simulations to test hypotheses for the mechanisms leading to CNV initiation and controlling early and late Type 1, 2 and 3 CNV.

III.3 Biological Components and Processes in CNV

CNV involves the interaction of two fundamental structures, the retina with its supporting structures and the choriocapillaris. I briefly review the functional and structural properties of their components in the context of CNV.

III.3.1 *Retina, RPE, Bruch's Membrane and CC*

The retina consists of two concentric regions, the *inner retina* and the *outer retina* proper (Figure III.2). Beneath the outer retina proper lies the retinal pigment epithelium (*RPE*), a monolayer of pigmented epithelial cells situated between the photoreceptors and the choroid. The RPE plays numerous roles in maintenance of the retina. Beneath the RPE, *Bruch's membrane* (*BrM*), a strong, multi-layered, 2-to-4-μm-thick porous membrane structurally stabilizes the RPE (Figure III.2). The very dense choriocapillaris (or choroid) lies behind the outer retina, separated from it by BrM and the RPE.

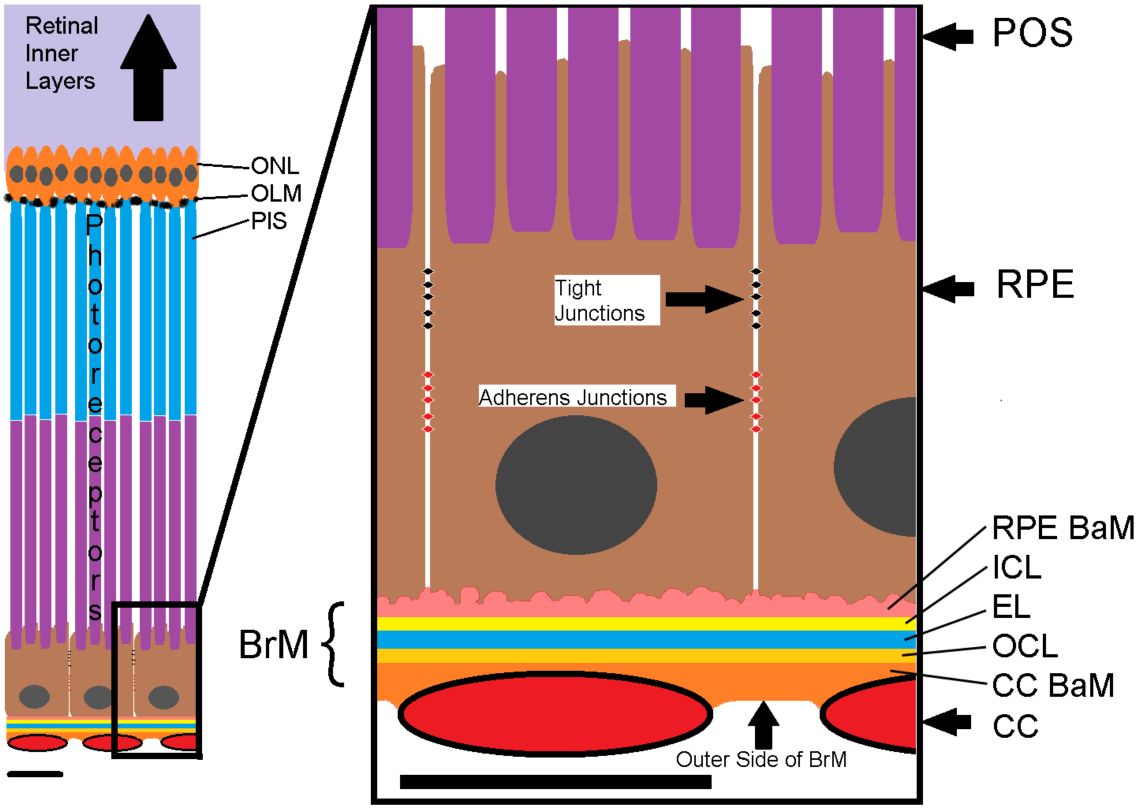

Figure III.2. Retinal Structure, the Retinal Pigment Epithelium, Bruch's Membrane and the Choriocapillaris. *Left large-scale*: Structure of the outer retinal layers, the RPE and the CC. *Right*: Detail of the CC-BrM-RPE-POS complex. *CC*: choriocapillaris, *BrM*: Bruch's membrane, *RPE*: Retinal pigment epithelium, *CC BaM*: Basement membrane of the CC, *OCL*: Outer collagenous layer, *EL*: Elastin layer, *ICL*: Inner collagenous layer, RPE BaM: Basement membrane of the RPE (I abbreviate RPE BaM as *RBaM*), *POS*: Photoreceptor outer segment, *PIS*: Photoreceptor inner segment, *ONL*: Outer nuclear layer. Light purple shading indicates the location of the inner retina. Scale bars ~ 10 µm.

The inner retina, adjacent to the vitreous humor, includes the inner retinal vasculature and layers of neural cells. The outer retina, adjacent to the RPE, includes the rod and cone photoreceptors. Each rod or cone cell has three regions along its axis in the direction perpendicular to the retinal layers: the *cell body*, the *photoreceptor outer segment* (*POS*), which contains the light-absorbing outer-segment disks, and the *photoreceptor inner segment* (*PIS*) (Figure III.2). The ensemble of POSs forms a well-defined layer in the retinal plane. Similarly, the ensemble of photoreceptor cell bodies forms the outer nuclear layer (*ONL*) separated from the PIS layer (the ensemble of PISs) by a membrane called the *outer* (or *external*) *limiting membrane* (*OLM*). The OLM supports and orients the cells which cross it and impedes the extracellular diffusion of large molecules [128].

The properties of the retinal layers vary depending on the in-layer distance from the *fovea*. The outer retina is thinner in the *periphery* far from the fovea and thicker in the fovea, where the density of photoreceptors is higher and vision is most acute. CNV is most damaging when it occurs in the subfoveal area. In the central fovea, the inner retina is thinnest and lacks inner-retinal vasculature [129,130].

The thickness, porosity, elasticity and composition of BrM all change due to aging [131] (see [132], for a comprehensive review). Extracellular material (mostly waste byproducts from phagocytosis) accumulates between the RPE and BrM forming *basal deposits*. Basal deposits located between the RPE plasma membrane and its basement membrane (*RBaM*) are called *basal laminar deposits* (*BlamD*). Basal deposits external to the RBaM in the *inner collagenous layer* or *inner collagenous zone* are called *basal linear deposits* (*BlinD*). Deposits that appear clinically as yellowish-white spots in the retina are called *drusen*. *Hard drusen* are mechanically stiff nodular deposits with defined edges and do not strongly correlate with CNV [133]. *Soft drusen* are mechanically softer, have less defined sloping edges and correlate strongly with CNV.

CNV is usually limited to the sub-RPE space (*i.e.* between the RPE and BrM) and sub-retinal space (*i.e.* between the RPE and photoreceptors), though anastomosis of CNV capillaries with the inner-retinal vasculature occasionally occurs [134].

III.3.2 *Oxygen Transport and Metabolism in the Retina*

Two capillary beds supply oxygen and nutrients to most regions of the retina and remove waste products, the inner-retinal capillaries and the choriocapillaris (*CC*). The CC supplies more than 90 percent of the oxygen to the photoreceptors in dark-adapted conditions and almost 100 percent in light-adapted conditions [135]. The inner retinal capillaries supply oxygen to the inner layers of the retina, maintaining the oxygen partial pressure (PO_2) almost constant in both light and dark-adapted conditions [135,136]. The normal oxygen concentration at the OLM varies slightly, depending on the in-layer distance from the fovea.

The PIS is packed with mitochondria, so photoreceptors have the highest oxygen consumption rates of any cells in the human body. The metabolic activity and oxygen concentration of the photoreceptors depend on the intensity of light they receive. In dark-adapted conditions, photoreceptors consume oxygen at about twice their light-adapted rates.

III.3.3 *Adhesion Properties of the RPE, POS and PIS*

The lipid bilayer forming the cell membrane is flimsy and cannot, by itself, transmit large forces from cell to cell or from cell to *extracellular matrix* (*ECM*).

Anchoring junctions solve this problem by forming strong membrane-spanning structures that tether inside the cell to the tension-bearing filaments of the cytoskeleton.

RPE cells are apicobasally polarized. On the lateral surfaces of RPE cells, two *bands of epithelial adhesion junctions* connect to neighboring RPE cells (). On the apical-most lateral surfaces of RPE cells, a band of *tight junctions* (*TJ*s) (z*onula occludens, ZO, Mesh*) seal adjacent RPE cells together, forming the outer blood-retina (*oBRB*) barrier and restricting transport of material (*e.g.* albumin) into and out of the retina [137-139]. On the lateral surfaces of RPE cells, basal to the TJs, *adherens junctions* (*AJ*s) form another junctional band that goes all the way around each cell and mechanically connects the cytoskeleton of each RPE cell to the neighboring RPE cells, giving structural integrity to the RPE. RPE cells form AJs predominantly via N-cadherins [140,141] (RPE cells also produce a small amount of E-cadherin, the most common adhesion molecule in the AJs of most other epithelial tissues). In addition to these junctional bands, *desmosome plaques* (*DP*s) and *gap junctions* distributed on the lateral surfaces of the RPE cells connect neighboring RPE cells. Desmosomes are crucial for tissue integrity, resist calcium-depletion in developed tissue and help to resist shearing forces. When I refer to e*pithelial junctions* without further qualification, I refer to the ensemble of junctional structures that participate in RPE-RPE adhesion, including TJs, AJs and DPs. The basal surfaces of RPE cells adhere to the very thin *basal laminae* of the RBaMs so strongly that the basal laminae behave like extensions of the cells' plasma membranes [142]. *Intergrins* mediate RPE-basal lamina adhesion. The RBaMs attach to the inner collagenous layer of BrM via microfibrils passing through both the elastic layer of BrM and the RBaMs [142,143]. When I refer to the *RPE-BrM complex*, I refer to the RPE-

RBaM-BrM ensemble. Soft drusen reduce the adhesion between the RBaMs and the inner collagenous zone (Figure III.2) of BrM and correlate with localized detachment of the RPE from BrM [133,144-146]. Age-related modifications of BrM, especially soft drusen, also inhibit reattachment of transplanted RPE cells to BrM [147,148].

Photoreceptors pass spent photo-sensitive disks to the apical processes of RPE cells. This apical contact attaches photoreceptors to the RPE [149-151] more weakly than would RPE-RPE epithelial adhesion or attachment of RBaMs to BrM, so detachment of photoreceptors from the RPE (*retinal detachment*) due to impact is more likely than *RPE tears* (which break RPE-RPE epithelial junctions) or *RPE detachment* (which breaks RBaM-BrM attachment). Disruptions of RPE-POS contact affect not only the integrity of the oBRB, they also induce pathological cell growth and division in the RPE [152-154], disrupting the RPE epithelial structure and preventing successful therapeutic retinal reattachment (see Table III-1).

Photoreceptors have limited or no motility and are held together in constant positions by multiple ECM components in the outer retina and OLM, ensuring consistent positional mapping of the visual field to the photoreceptors and the corresponding neurons in the visual cortex (*somatotopic mapping*). This somatotopic consistency is crucial to the development and maintenance of high-resolution visual perception.

III.3.4 *Angiogenic and Antiangiogenic factors*

Since laterally adjacent RPE cells form tight junctions, factors secreted by the photoreceptors on the apical side of the RPE do not pass through an intact RPE epithelial sheet to affect the choriocapillaris or CNV capillaries. The RPE secretes two VEGF-A isoforms from its basolateral surfaces to maintain the CC. VEGF-A_{120} diffuses freely and does not bind to heparin-sulfate. More than 75% of RPE-derived VEGF is the VEGF-A_{165} isoform [155] which has a weak affinity for heparin-sulfate, allowing it to diffuse across BrM while remaining resident long enough to bind to the VEGF receptors of the CC (otherwise the constant fluid flow from the vitreous humor to the CC and the high rate of CC blood flow would elute the VEGF before it bound to the EC's VEGF receptors). Mutant mice producing only VEGF-A_{188}, which binds strongly to extracellular matrix and therefore has a short diffusion length, develop a normal CC but suffer CC atrophy and RPE and BrM abnormalities, leading to RPE loss and dramatic choroidal remodeling beginning at 7 months [156], suggesting that RPE-derived free-diffusing VEGF-A isoforms are necessary to maintain the choriocapillaris. These VEGF isoforms may also help support other retinal cell types. When I refer to VEGF-A without qualifications, I mean VEGF-A_{165}, which appears to play the dominant role in CNV. In addition to RPE-derived VEGF-A, ECs, in general, produce multiple isoforms of VEGF-A, among which short-diffusing isoforms can serve as autocrine chemoattractants, playing a key role in capillary patterning (for a detailed discussion of capillary patterning mechanisms, see [1,157]). In many cases, ECs can only sense ECM-bound isoforms of VEGF-A when they are released from the ECM by matrix-degrading enzymes.

Since the retina is the most metabolically active tissue in the body, the density of capillaries in the CC is unusually high. The CC has small inter-capillary distances (~ 20 μm) compare to typical inter-capillary distances (~ 100 μm to 200 μm). To maintain this dense population of ECs in the CC, RPE-derived VEGF secretion must be substantial.

The denser population of ECs consuming RPE-derived VEGF globally balances the higher secretion rate of RPE-derived VEGF. However, because of inhomogeneities in the CC-BrM-RPE complex, RPE-derived VEGF does not diffuse uniformly, producing relatively high local concentrations of RPE-derived VEGF, sufficient to maintain a substantial population of activated ECs in the CC even in the healthy retina.

RPE cells also produce the antiangiogenic *pigment-epithelium-derived factor* (*PEDF*). At homeostasis, proangiogenic and antiangiogenic factors balance. In the aged human retina, PEDF has a spatial distribution similar to that of VEGF-A [158].

Numerous other diffusible pro and antiangiogenic factors [159,160] may help modulate capillary behavior, but I do not consider them in this study (see section III.3.6, below). While angiogenesis requires proangiogenic factors to dominate antiangiogenic factors, normal angiogenesis requires the factors to remain in rough balance. In pathological situations, when the levels of proangiogenic factors are too large relative to antiangiogenic factors, the resulting vessels do not mature and remain leaky and insufficient at oxygen and nutrient transport.

III.3.5 *Angiogenesis and BrM Degradation*

High levels of VEGF-A activate normally quiescent endothelial cells in blood vessels. Via a Delta/Notch contact-inhibition selection mechanism, small populations of these activated ECs become *tip cells* which lead angiogenic *sprouts* up gradients of VEGF-A [161,162]. A morphologically distinct population of activated ECs called *stalk* cells form the body of these angiogenic sprouts. While tip and stalk cells are distinct at any instant, they can dynamically exchange identities [163]. Macrophages and other immune cells can substitute for tip cells in their pathfinding role. Tip cells have very low rates of proliferation, while stalk cells proliferate at moderate rates.

Excess proteolytic activity of macrophages and activated endothelial cells can cause focal thinning of BrM [164-168]. Tip cells and immune cells express a number of matrix degrading enzymes which locally break down ECM and BrM, while BrM is continuously reformed by poorly understood means. RPE cells also secrete numerous inactive MMPs and tissue inhibitor of mellapoteinases (*TIMP*s) that inhibit activated MMPs [169-173]; *E.g.*, tip cells and macrophages express transmembrane type-1 MMP (*MT1-MMP*) which activates MMP-2, which plays a key role in tip-cell and macrophage migration and breakdown of basement membrane in tumor invasion [174-178]. A similar mechanism is plausible for tip-cell and immune-cell breakdown of BrM.

III.3.6 *Inflammation*

Inflammation and immune cells play major roles in CNV. Macrophages in normal retina remove debris accumulated in BrM [179], helping to maintain normal retinal structure and function. However, chronic or excessive acute inflammation can promote CNV initiation and impair the integrity of the RPE, promoting CNV progression. Irregularities in regulation of the complement cascade and overactivity of immune cells may perturb RPE cells, causing them to form more basal deposits (both soft and hard drusen), which in turn induce a stronger immune response which can initiate angiogenesis [180,181]. *Angiopoietin-2*, a key proangiogenic inflammatory factor, activates quiescent ECs with a response modulated by local VEGF concentrations and increases ECs' directional motility. *Angiopoietin-1*, on the other hand, inhibits activation of ECs and helps newly-formed vessels mature [182]. Pro-inflammatory cytokines, *e.g.*, tumor necrosis factor alpha (*TNF-α*) and *interleukin-1β* and *-8*, result in extensive breakdown of both the oBRB and inner blood-retinal barrier (*iBRB*) which separates inner-retinal capillaries from the outer retina [139,183-186].

Inflammation may affect early and late-stage CNV by weakening RPE-RPE and RPE-POS adhesion. Inflammation also impairs the juxtacrine Delta/Notch inhibitory signaling which couples adjacent ECs and normally promotes ECs quiescence and inhibits tip-cell selection, increasing EC activation [187].

III.4 Current Hypotheses for CNV Initiation and Progression

Multiple hypotheses compete to explain CNV initiation, growth and patterning (for comprehensive reviews, see [188,189]). These hypotheses form two major groups depending on their primary mechanism of action: 1) VEGF overexpression, and 2) irregularities in BrM (including focal defects and basal deposits). Inflammation affects both mechanisms because it promotes formation of irregularities in BrM and participates in angiogenesis. To better understand CNV, I consider its risk factors and correlated pathological conditions and briefly discuss their relationship to the steps of angiogenesis.

Excessive expression of VEGF, mainly in response to injuries and hypoxia, without balancing expression of angiogenesis inhibitors is a major stimulator of neoangiogenesis in most tissues. Excess VEGF has been considered a primary cause of

CNV [158] because anti-VEGF drugs can significantly inhibit CNV progression. This hypothesis seems reasonable, because activation, proteolytic activity and survival of ECs depend on VEGF concentrations, and directional migration of tip cells depends on gradients of VEGF, which in turn depend on the composition of the ECM and the proteolytic activity of ECs [162] (in many cases VEGF-A is bound to the ECM and is only sensed by ECs when released by proteolytic enzymes). In animal models, excess secretion of VEGF by the RPE due to subretinal injections of reactive oxygen species (*ROS*) [190] or adenovirus [191] can induce CNV. However, other studies in transgenic mice show that increased expression of VEGF-A and/or angiopoietin-2 in RPE is **not sufficient** to initiate CNV and that overexpression of VEGF can only initiate CNV when combined with subretinal injections [192] which disturb the integrity of the RPE, probably by triggering inflammation, reducing RPE-POS contact adhesion and inducing RPE growth [152-154]. Also in transgenic mice [193], overexpression of VEGF-A_{164} in the RPE causes extensive intrachoroidal neovascularization, but does not lead to sub-RPE or sub-retinal CNV, again suggesting that an intact Bruch's membrane/RPE barrier prevents choroidal neovascularization from penetrating into the subretinal space. Immunohistochemical analyses of human subjects with a history of chorioretinal disease show that compared to age-matched control subjects (mean age about 80 years) their PEDF levels are significantly lower than their VEGF levels in RPE cells, the RPE basal lamina, BrM and the choroidal stroma [158,194]. This imbalance shows that disturbed angiogenic and antiangiogenic factor levels correlate with late-stage chorioretinal disease, but the relative expression levels of these factors would need to be measured experimentally **before** CNV initiation to establish whether the imbalance is a cause or a result of CNV. However, secreted proteome profiling in human RPE cell cultures derived from donors with AMD shows a 2- to 3-fold increase in their levels of PEDF compared to age-matched healthy donors [195]. Thus, while the experimental evidence shows a clear increase in proangiogenic factors, this increase may be compensated by an increase in antiangiogenic factors. Whether an imbalance develops is thus not definitively established. Another serious objection to the VEGF-hypothesis is that it fails to explain the distinct loci and progression of CNV. VEGF levels are high throughout the retina and cannot provide spatial cues to lead to the localization of CNV to either the RPE-BrM boundary (Type 1) or the RPE-POS boundary (Type 2). Indeed, no experiment has established the presence of VEGF gradients within the BrM-RPE-POS complex.

Both age-related changes of the retina and pathological conditions can increase VEGF expression. Life-long accumulation of lipids in BrM and their gradual oxidation (producing reactive oxygen species and recruiting immune cells) correlate with increased production of VEGF by the RPE and greater likelihood of developing CNV [196]. Hypoxia also temporarily increases the secretion of VEGF in cultured RPE cells by up to 3-fold over 48 hours, followed by a return to baseline [197,198]. Inflammatory cells also secrete VEGF and other proangiogenic and antiangionegic factors (see section III.3.6 above).

Irregularities of BrM include focal breaks and thinning in BrM, abnormal production of ECM by the RPE, and formation of soft drusen. All of these BrM defects correlate with CNV [146,199]. However, the common hypotheses that BrM presents a physical barrier to the invasion and/or growth of choriocapillaries into the retina and that small gaps in BrM may be responsible for initiation of CNV, contradict several experimental and clinical observations: 1) BrM is never an impenetrable barrier to immune and tip cells and has not been shown to physically block the invasion of activated ECs into the sub-RPE space. BrM is only 2-4 µm thick, with pores up to 0.5 µm diameter [200]. The BrM elastin layer in the macula of healthy young adults (age $<$ 62) can have gaps of up 2 µm [201]. 2) Activated endothelial cells, which are always present in the normal choriocapillaris, probe their micro-environment by sending out processes (like filopodia) as thin as 0.1 µm and as long as 200 µm even in dense embryonic and adult tissues. Such filopodial processes can easily cross BrM through its pores. Leukocytes can cross BrM rapidly under both normal and inflammatory conditions [202] (taking at most a few hours to cross the BrM-RPE barrier and only a few minutes to cross the endothelium in an *in vitro* flow model [203]). ECs digest and penetrate an intact BrM in less than a week when RPE is severely damaged due to phototoxicity in a rat model [164]. 3) The rate of CNV in persons younger than 50 years old is negligible (except in cases of excess inflammatory response in the eyes). 4) The CNV initiation probability when BrM is mechanically disrupted in animal models is about 10% [204]. These observations suggest that focal defects and thinning of BrM do not significantly reduce the already minimal efficacy of the physical barrier function of healthy BrM. Instead, other mechanisms may explain the correlation of focal defects in BrM with CNV, *e.g.*, breaks in BrM due to calcification may disrupt both the RBaMs and the basement membranes of CC cells, disrupting the epithelial junctional structure of the RPE [146] and activating CC endothelial cells. This simultaneous activation of ECs and disruption of the RPE may explain the correlation of focal defects in BrM with CNV.

However, while BrM does not form a mechanical barrier to persistent EC penetration of the retina, BrM and the RPE attached to it clearly do form an effective barrier to choroidal penetration, even in the presence of small holes in BrM. The nature of this barrier is not clear. Haptotaxis may play a role. ECs exhibit strong haptotactic preference for their own basement membrane. The basement membrane of the RPE (RBaM) differs in structure and components from the CC basement membrane (CC BaM) (reviewed in [132]). ECs preferentially adhere to their own basal lamina and new blood vessels follow the pattern of any pre-existing EC-manufactured basal lamina after capillary atrophy [205]. Thus, in the absence of factors that induce directed migration of ECs (chemotaxis or haptotaxis), I hypothesize that activated ECs of the choriocapillaris prefer to stay on the outer side of BrM, which has a high level of CC BaM, and not to invade sub-RPE space, which almost entirely lacks CC BaM.

Since neither overexpression of VEGF nor reduction in BrM's barrier function can explain CNV initiation, multiple types, loci and progression [146], other mechanisms are likely involved.

III.5 Adhesion Failure and CNV

While not usually considered crucial to CNV, a great deal of experimental evidence suggests that failures of adhesion are essential for the development of CNV. The strict spatial separation of the CC from the normal retina and the distinct loci of Type 1 and Type 2 CNV suggest that the physical structure and properties of the BrM-RPE-POS complex may determine both CNV initiation and progression. Experimental evidence suggests that reduced RBaM-BrM adhesion may enable CNV to invade the sub-RPE space. The differences in properties and effects of hard and soft drusen support this hypothesis. Soft drusen are strong risk factors for CNV and are often associated with detachment of the RPE from BrM, suggesting that they substantially reduce RBaM-BrM adhesion [133,147,148]. However, hard drusen, which contain hyalinised material and attach firmly to the inner collagenous layer of BrM (based on EM images) do not greatly increase the likelihood of CNV [133,199]. Softening of hard drusen, which reduces their adhesion to RBaM, correlates with CNV [144,145]. Similarly, the ability of inflammation to induce CNV suggests that impaired lateral adhesion between cells in the RPE promotes Type 2 CNV. Pathological conditions that compromise the integrity of the oBRB by weakening junctional epithelial adhesion in the RPE cause a wide range of neovascular diseases in the retina [137,139,206-208]. Recent studies show that subretinal drusenoids, which are drusen-like deposits that accumulate between the RPE and photoreceptors, perturb RPE-POS adhesion and correlate with CNV [209-211]. Finally, the detachment of the POS from the RPE (retinal detachment) reduces the integrity of the oBRB and significantly increases the risk of CNV in animal models of CNV, suggesting that impaired RPE-POS adhesion also promotes CNV.

Since the relative importance, roles and interactions among the different types of adhesion impairment during CNV initiation and progression are unclear, this body of experimental evidence motivated us to study the role of adhesion failures in the BrM-RPE-POS complex in CNV.

III.5.1 *The Need for Models and Simulation*

While a detailed experimental analysis of adhesion effects in CNV is desirable, it is currently impractical. No animal model exhibits the full range of AMD-related CNV pathologies [212], while *in vitro* experiments do not reproduce the complex layering and porosity of BrM, the interlocking of the RPE and POS, the accumulation of lipids in the BrM layers or the formation of soft drusen. Independent quantitative control of biological mechanisms is experimentally difficult, especially *in vivo*. I therefore chose to develop computational models which allow us to titrate the effects of specific mechanisms without confounding crosstalk or quantitative uncertainties and to study the synergistic or antagonistic effects of multiple mechanisms acting simultaneously or sequentially. Computational models also allow us to explore many more combinations of bio-mechanistic hypotheses and parameter choices than I could in experiments. My computational models include key retinal components, cell-cell, cell-ECM and ECM-ECM adhesion mechanisms and major angiogenesis-related processes, like BrM breakdown by proteases, hypoxic signaling upregulating VEGF production and VEGF and oxygen transport. My computational model of the retina allows us to investigate the significance of these hypothesized mechanisms in both CNV initiation and progression. In this chapter, I focus on the significance of adhesion failures in the BrM-RPE-POS complex to CNV early and late progression, deferring a detailed comparative study of the roles of VEGF overexpression and BrM defects to future publications.

	Context		Adhesion			Effects		
	Condition	Subject	RPE - RPE	RBaM -BrM	RPE-POS	RPE Viability	CNV Loci	Simulation Results
1	Normal Aging (No Drusen)	Human	+	+	+	+	--	No initiation even in presence of small holes in **BrM** (Table III-13)
2	Hard Drusen [133,146]	Human	-	-	+	-	-	See section III.4
3	Soft Drusen [133,144-146]	Human	-/+	--/-	-/+	-/+	Sub-RPE	**S11**, **T12**, **P13** **CNV** (Tables III-14, 17-19)
4	Sub-retinal Drusenoid (reticular pseudodrusen) [210,211,213]	Human	--/-	--/-/+	--/-	-/+	Sub-Retinal and/or Sub-RPE	**T12, S22, P23** **CNV** (Tables III-18, 20-21)
5	BrM Calcification [146,199]	Human	-/+	-/+	+	-/+	*	*
6	Active Inflammation [214]	Young Human	--	+	--/-/+	-/+	Sub-Retinal	**S22 CNV** (Table III-20)
7	Retinal Detachment [139,152]	Cat	--/-	+	--	+	*	**S22 CNV** (Table III-20)

8	High Fat Diet + Aging + Blue Light [167]	Mouse	-/+	--/-	+	+/-	Early Sub-RPE	**ET1 CNV** (Table III-14)
9	Chemotoxicity [215]	Rabbit	--	-/+	--	--	Sub-Retinal	**P23 CNV** (Table III-21)
10	Sub-Retinal Injection [216-219]	Rat, Rabbit	--	-/+	--	-/+	Sub-Retinal	**S22**, **P23 CNV** (Tables III-20, 21)
11	Sub-retinal Injection and VEGF Overexpression [192]	Rat	--	-/+	--	-/+	Sub-Retinal	**S22**, **P23 CNV** (Tables III-20, 21)

Table III-1. Pathological Conditions and Injuries, Their Effects on Adhesion and Their Correlations with CNV. Columns: Condition: type of condition, injury or perturbation in clinical or experimental observations. Subject: human or animal. Adhesion: strength of adhesion (+ = normal, - = moderately impaired, -- = severely impaired). Effects: RPE viability (+ = most RPE cells remain viable, - = some RPE cells die, -- = most RPE cells die), CNV loci (-- = no or low probability of initiation and progression, sub-RPE = Type 1, sub-retinal = Type 2, combined pattern = Type 3, * = no data presented/available). Simulation results (boldface words = model objects. CNV Type definitions: see Table III-3 and Table III-4. * = no data presented/available. See sections III.7 and III.10 for details of simulation results).

III.6 A Quantitative Model of the Retina-RPE-CC Complex

To allow unbiased study of CNV mechanisms, my model of the retina-RPE-CC includes objects and processes capable of recapitulating all the major CNV hypotheses (VEGF overexpression, BrM defects, adhesion failures and inflammation). I translate my quantitative model into a computational model in section III.13. To avoid confusion, I use normal fonts for biological objects and **boldface** to represent objects and times in the quantitative model, *e.g.* **RPE** denotes the model's representation of biological RPE and one **year** denotes one simulated biological year. I also use **boldface** to distinguish the specific simulation interactions of **junctional adhesion**, **labile adhesion** and **plastic coupling** in my model from their biological correlates, but I do not use a separate font to distinguish other modeled and biological processes.

III.6.1 *Anatomical Components of the Model*

Since CNV is usually limited to the outer retina, I model the choriocapillaris, BrM, RPE and parts of the outer retina in detail, and represent the inner retina implicitly through appropriate boundary conditions at the *outer limiting membrane*. My model does not explicitly represent the OLM which defines the innermost (towards the inner retina) **boundary** of the modeled outer retina. The properties of the retinal layers depend on the in-layer distance from the fovea. I could represent these typical anatomical/thickness variations of the biological retina in my model by changing a limited number of geometrical and metabolic parameters, though I do not do so in this chapter. My model explicitly represents **BrM**, but neglects its layered structure and assumes that the inner and outer basal laminae and basement membrane of **BrM** provide equivalent adhesion substrates. Modeled **BrM** is composed of small blocks of non-diffusible solid material (frozen generalized **cells**). I assume that **cells** cannot cross intact **BrM**. So my modeled **BrM** blocks **cell** migration (See section III.11.7 for more details). My model does not explicitly represent basal deposits, which play a major role in CNV initiation and progression, but includes them implicitly via their effects on the adhesion properties of the RPE-BrM complex. Since CNV originates from the outgrowth of capillaries in the choriocapillaris, my model represents the capillary network of the **choriocapillaris** (***CC***) and the **endothelial cells** (***EC*s**) explicitly. Modeled **CNV** capillaries are composed of **stalk cells** (see section III.6.5, below). My model represents extracellular fluid in the tissue by a generalized **cell**, **medium** that fills spaces unoccupied by **cells** or **BrM**.

III.6.2 *Oxygen Transport and Metabolism in the Model Retina*

The **choriocapillaris** secretes diffusing **oxygen** at a constant rate and PO_2 at the OLM **boundary** is constant. Numerous experimental and theoretical studies of oxygen tension profiles in the retina show that the oxygen consumption rate of the RPE is negligible compared to that of the PIS [220]. My model assumes that **RPE** oxygen uptake is negligible [220,221]. My model neglects the effects of blood flow entirely and assumes that PO_2 is independent of position along a capillary, or whether a capillary is a sprout or has anastomosed with other vessels. My model neglects the effects of blood flow entirely and assumes that PO_2 is independent of position along a capillary, or whether a capillary is a sprout or has anastomosed with other vessels. The effects of blood flow on vascular remodeling and tumor growth have been extensively studied by Owen *et al.* [96], Szczerba and Székely [222], Perfahl *et al.* [223], Alarcon *et al.*, Bartha and Rieger [97], Welter *et al.* [98,224], McDougall *et al.* [99], Stephanou *et al.* [100,101], Pries *et al.* [102-104,225] and Macklin *et al.* [90]. My flow-related simplifying assumptions generally have the effects of increasing oxygen availability, reducing the rate and extent of neovascularization. I have performed simulations (data not shown) in which PO_2 at **choriocapillaris** is set to half of its normal level, representing continuous systemic hypoxia. These simulations show that lower PO_2 at the **choriocapillaris** has little effect on the generic behavior of my model.

III.6.3 *Adhesion Properties of EC, RPE, POS and PIS cells*

My model has two types of **cell-cell** and **cell-BrM** adhesion: 1) ***labile adhesion*** and 2) ***junctional adhesion***. Modeled **labile adhesion** represents cell-cell or cell-ECM surface adhesion in the absence of strong junctional structures (*e.g.* RPE-POS adhesion). **Junctional adhesion** combines **labile** adhesion at **cell** boundaries with **plastic coupling** (*e.g.* between neighboring **cells** or between **BrM** and **cells**). The **plastic coupling** simulates cytoskeletally-coupled junctional structures as breakable springs (see section III.13.3) that mechanically connect neighboring **cells** and also connects **cells** to **BrM**. **Junctional adhesion** represents biological epithelial/endothelial junctional adhesion or cell-ECM focal adhesion. My representation of adhesion gives us the flexibility to represent both mesenchymal cells and cells organized in an epithelium. When **plastic coupling** between neighboring or ECM-adhering **cells** is strong relative to other effects including **labile adhesion**, **cells** are less likely to break their **plastic couplings** and change their neighbors, as is typical in epithelial-junction-coupled cells in an epithelium (*e.g.* a layer of differentiated epithelial cells *in vitro* at 100% confluency). However, when **plastic coupling** is weak or absent, **cells** can relatively easily migrate or change their neighbors, as is typical of mesenchymal cells or epithelial cells *in vitro* well below 100% confluency. In my model, I use this flexibility to vary the strengths of **labile**

adhesion and **plastic coupling** independently to represent the differing adhesion properties of cells in healthy and pathological tissues.

My model represents the in-plane epithelial junctions between healthy RPE cells by **junctional adhesion** with both strong **labile adhesion** and strong **plastic coupling** between **RPE cells** (Figure III.3). Since RPE cells adhere strongly to their basement membranes, I treat the RBaM as a part of each **RPE cell** and assume that attachment of RPE cells to BrM depends on the adhesion of the RBaM (not of basal lamina) to BrM. During RPE detachment, cleavage occurs between the RBaM and BrM. Since I do not model the RBaM, I represent this RPE-RBaM-BrM adhesion as a single **junctional adhesion** between **RPE** and **BrM cells** (**RPE-BrM junctional adhesion**) (Figure III.3). Since no known junctional structures couple RPE to the POS, I represent RPE-POS adhesion by relatively weak **RPE-POS labile adhesion** between **RPE cells** and **POS cells**. **RPE-POS labile adhesion** is weak relative to the strength of **labile adhesion** in **RPE-RPE junctional adhesion**. Neighboring **PIS** and **POS cell segments** adhere via **junctional adhesion** (Figure III.3), limiting traverse **photoreceptor** displacement under normal conditions.

In an endothelium, ECs mainly adhere to other ECs via *vascular endothelial cadherin* (*VE-Cadherins*) and tight junctions. When forming the **CC**, modeled **ECs** adhere via **junctional adhesion** to neighboring **ECs** and **BrM** (Figure III.3). **Stalk cells** (representing activated ECs) adhere to all other **ECs** via **junctional adhesion** with **labile adhesion** at the same strength as **ECs** in the **CC**, but have relatively weak **plastic coupling** to **ECs** and **BrM** (Figure III.3). I assume **ECs** adhere to the **RPE** and to photoreceptor segments (**PIS** and **POS** generalized **cells**) weakly via **labile adhesion** representing nonspecific biological surface adhesion (Figure III.3).

Adherent cells suspended in liquid assume a spherical shape, meaning that non-specific cell-liquid adhesion is weak. I represent this weak cell-liquid adhesion by weak **labile adhesion** between **cells** and **medium**. Thus **cells** prefer to adhere to other **cells** or **BrM** rather than to be surrounded by **medium**.

I do not model explicitly the differences in adhesion between the apical, lateral, and basal surfaces of biological RPE cells and photoreceptors. In my model **labile adhesion** strengths depend only on the types of **cells** or **membranes** in contact, not on the apical, basal or lateral identity of the contacting regions. However, effective cell polarization in the model develops from the specific geometry and contacts which occur in the normal and diseased retina, so at most times, **cells** emergently exhibit correctly polarized adhesivity, even though I do not impose it. I also neglect temporal adhesion changes observed clinically or experimentally during CNV progression, assuming temporally constant adhesivity of **RPE**, **POS**, **PIS cells** in my individual simulations.

Since I can vary independently the strength of the **labile adhesion** and **plastic coupling** which contribute to junctional adhesion, I refer to the labile components of **RPE-RPE** or **RPE-BrM junctional adhesion** as **RPE-RPE** or **RPE-BrM labile adhesion** and to the **plastic coupling** components of **RPE-RPE** or **RPE-BrM junctional adhesion** as **RPE-RPE** or **RPE-BrM plastic coupling**.

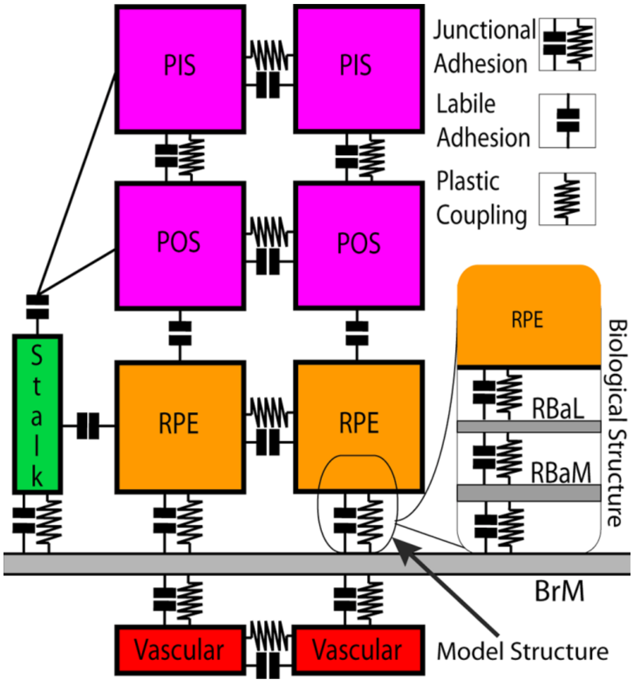

Figure III.3. Adhesive Interaction Processes in the Model Retina. My model includes two types of cell-cell and cell-BrM adhesion: 1) *labile adhesion* and 2) *junctional adhesion*. Modeled labile adhesion represents cell-cell or cell-ECM labile adhesion in the absence of strong junctional structures (*e.g.*, RPE-POS adhesion). Junctional adhesion combines labile adhesion at cell boundaries with plastic coupling (*e.g.*, between neighboring cells or between BrM and cells). Plastic coupling simulates cytoskeletally-coupled junctional structures as breakable springs that mechanically connect neighboring cells and also connect cells to BrM. Junctional adhesion represents biological epithelial or endothelial junctional adhesion or cell-ECM focal adhesion. In the model, a single junctional adhesion between RPE cells and BrM represents the complex biological adhesion between RPE cells and their basal laminae (RBaL), adhesion between the basal laminae and their basement membrane (RBaM) and adhesion between RBaM and BrM (inset). Modeled adhesion processes are: EC-EC and EC-BrM junctional adhesion; EC-RPE, EC-POS and EC-PIS labile adhesion; RPE-RPE and RPE-BrM junctional adhesion; RPE-PIS and RPE-POS labile adhesion; PIS-PIS, PIS-POS and POS-POS junctional adhesion. Key: BrM: Bruch's membrane, RPE: retinal pigment epithelium, RBaM: basement membrane of the RPE, RBaL: basal lamina of the RPE, POS: photoreceptor outer segment, PIS: photoreceptor inner segment.

III.6.4 *Angiogenic and Antiangiogenic Factors*

To aggregate the effects of RPE-derived diffusible growth factors on the **choriocapillaris** and **CNV** capillaries I include a diffusible growth-factor **field, RPE-**

derived VEGF-A which represents the aggregate proangiogenic effect of all biological long-diffusing proangiogenic and antiangiogenic factors. All types of **ECs** in my model take up **RPE-derived VEGF-A** uniformly at a constant rate. I omit growth factors and cytokines from other sources. Since I assume that PEDF affects CNV only as an anti-angiogenic factor and that it diffuses at the same rate as RPE-derived VEGF, I can combined the effects of the two RPE-derived VEGF isoforms (120 and 165) and PEDF on CNV growth and regression into an effective cell response to **RPE-derived VEGF-A**. While numerous other diffusible proangiogenic and antiangiogenic factors [159,160] may play a modulatory role in capillary behavior (see section III.3.6), we lack detailed experimental data on their spatial and temporal distribution and function. All modeled **ECs** (including **CC** and activated **ECs**, see below) secrete a **short-diffusing VEGF-A**. The **short-diffusing VEGF-A** is not a survival factor for **ECs** and I ignore its uptake by **ECs**. Both **short-diffusing VEGF-A** and **RPE-derived VEGF-A** decay at constant rates and diffuse uniformly everywhere in my modeled **retina**. However, the two **VEGF-A** *diffusion lengths* differ significantly. Typically, **RPE-derived VEGF-A** diffuses ~ 5 times farther than **short-diffusing VEGF-A**. Assuming the decay rates for both **RPE-derived VEGF-A** and **short-diffusing VEGF-A** are the same, a five-fold difference in diffusion length translates into a twenty-five fold larger diffusion constant for **RPE-derived VEGF-A** compared to **short-diffusing VEGF-A** (Table III-8)

III.6.5 *Angiogenesis and BrM Degradation*

Computer simulations can help us analyze the role of multiple mechanisms during angiogenesis both in pathological conditions like tumor-induced angiogenesis [115,157,226,227] and in healthy tissues like muscle [228]. Here, I use a multi-cell 3D angiogenesis model which I have previously described [157] to simulate **CNV** growth and patterning. My model includes two types of activated **ECs**: **tip cell** and **stalk cell types**. The **tip cell type** is a transient **cell type** that lasts one day, then differentiates into the **stalk cell type**. **Cells** of **stalk cell type** remain **stalk cells**. Both **stalk** and **tip cells** chemotax up gradients of both **RPE-derived VEGF-A** and **short-diffusing VEGF-A** at any **cell** boundaries which are not in contact with other **ECs**, *i.e.* they exhibit contact-inhibited chemotaxis. Thus, a **stalk cell** at the tip of an angiogenic sprout, which has less contact area with other **ECs**, chemotaxes more strongly than other **stalk cells** in response to **VEGF-A** gradients. Thus **stalk cells** can function as biological endothelial tip cells, leading other **stalk cells** in the trunk of an angiogenic sprout, as seen in experiments. **Stalk cells** self-organize into capillary-like network patterns [1].

Since experiments suggest that both ECs and macrophages can function as tip cells in CNV, I can interpret a **tip cell** either as an EC tip cell or as an immune cell that invades BrM. Modeled **tip cells** secrete a single **MMP field**. My model is agnostic about the type of MMP, though experiments seem to favor MMP-2 which is activated on contact with tip cells or macrophages expressing MT1-MMP. My model's **MMP field** represents a very short-diffusing molecule that degrades **BrM**. If I assume that other types of MMP remain bound to the EC, it does not greatly affect my simulations, data not shown. When a **tip cell** comes into contact with **BrM**, the **MMP** it secretes degrades

BrM locally and forms a roughly one cell-diameter hole in **BrM**, which allows **cells** to cross **BrM** in both directions. I neglect the slow reconstruction of BrM by RPE cells.

III.6.6 *Inflammation*

I represent the adhesion-reducing effects of inflammation due to inflammatory factors and immune cells implicitly by weakening **RPE-RPE**, **RPE-POS** (due to acute inflammation) and **RPE-BrM adhesion** (due to chronic irregularities in complement cascade). I neglect the role of inflammation on juxtacrine Delta/Notch coupling between ECs.

III.6.7 *Cell Proliferation and Death*

Typically, adherent cells like RPEs need to adhere to other cells (of the same or different types) or to an appropriate substrate to remain viable. Otherwise they die. Modeled **RPE cells** require **RPE-RPE** and **RPE-BrM** contact to remain viable. In the absence of such contact, **RPE cells** die. **RPE cells** do not proliferate or grow. Both **CC** and **ECs** require a low concentration of **RPE-derived VEGF** to remain viable, and die below a threshold level of **RPE-derived VEGF-A**. **Stalk cells** grow at a rate depending on the local concentration of **RPE-derived VEGF-A** unless their growth is inhibited by **stalk-EC** contact (contact-inhibited growth, see section III.13.6 for details).

III.6.8 *Simplifying Assumptions of My Model*

1. *In vivo* cell and ECM adhesion properties vary across a retina. I neglect these inhomogeneities to simplify interpretation of my results and because my simulations only cover patches of 120×120 μm^2, a scale over which adhesion and attachment properties are fairly uniform *in vivo*. I can partially reconstruct the properties of CNV over larger retinal regions by combining smaller patches with appropriate adhesion properties.
2. Under normal conditions, RPE cells do not proliferate *in vivo*, though they can proliferate under pathological conditions. **RPE cells** do not proliferate in my model.
3. All **RPE cells** have the same volume.
4. Photoreceptors degenerate in advanced AMD. Modeled photoreceptors (**POS** and **PIS**) do not die.
5. Pathological conditions often gradually weaken both the epithelial adhesion and attachment of RPE cells to BrM as CNV progresses. I do not include these adhesion changes.
6. Since I represent neither the basal lamina of RPE cells nor the RBaM explicitly**,** I represent the combined biological adhesion of the RPE to its basement membrane and of the basement membrane to BrM by **junctional adhesion** between **RPE cells** and **BrM**.
7. Cell-cell and cell-ECM adhesion depends on the time after contact, since it requires the accumulation of transmembrane and cytoplasmic molecules at the contact surface. My model assumes that **adhesion** is patent (functional) immediately on contact.

8. RPE cells are polarized. In my model **RPE cells** are not intrinsically polarized but do effectively polarize when organized in epithelia.
9. I select and activate a single **tip cell** manually, so that the location of the initial **tip** cell is the same in all simulation replicas.
10. **Tip cells** degrade **BrM** only during the first 24 **hours**. Since **tip cell** properties are quite generic, a **tip cell** could also represent a cell of another type, *e.g.*, a macrophages or an endothelial cell penetrating into the retina.
11. **Tip cells** differentiate into **stalk cells** after 24 **hours**, independent of environmental factors. **Stalk cells** at the leading edge of a sprout retain the stalk-guiding ability of tip cells.
12. *In vivo*, only a small population of endothelial cells have colony-forming potential. In my model all **stalk cells** have infinite proliferative potential.
13. I simplify the complex multi-layered structure of BrM into a passive one-layered **BrM**.
14. CNV is usually contained in a fibrovascular tissue. I do not model ECM synthesis and remodeling (except BrM breakdown) and ignore the fibrous components of other types of ECM.
15. I combine all vascular growth factors into two freely-diffusing **VEGF fields**, one fast diffusing and one slow diffusing, and neglect cell-membrane-bound and ECM-bound VEGF.
16. I assume that all **RPE-cell** surfaces uniformly secrete **RPE-derived VEGF-A** at a uniform rate depending on the level of **Oxygen partial pressure**.

17. **RPE** cells secrete **RPE-derived VEGF-A** at a higher rate when the **Oxygen partial pressure** drops below 49 mmHg (see section III.14.5 for details).
18. I ignore passive and pumped fluid flow from the vitreous humor to the CC and its effects on VEGF and oxygen transport.
19. I represent inflammation only through its effects on adhesion and epithelial integrity.
20. I neglect inflammatory cells and their contribution to angiogenesis.
21. I ignore fluid accumulation, *e.g.* due to inflammation.
22. I model continuous light-adapted conditions rather than alternation between light-adapted and dark-adapted conditions.
23. I do not model blood flow or the effects of vessel diameter and length. I simplify oxygen transport by assuming a constant rate of **Oxygen** secretion throughout an **EC**'s volume.

III.7 Results

In this section, I discuss how adhesion in the **BrM-RPE-POS** complex forms an effective physical barrier to CNV and how adhesion failures increase the risk of CNV initiation. I then relate the different modes of adhesion failure to the resulting **CNV** loci (CNV types), **CNV** progression and translocation (changes of CNV locus). I also discuss the **CNV** dynamics for individual adhesion scenarios and individual simulations representative of those adhesion scenarios.

All simulations begin with either no **tip cell** or one **tip cell**. In my simulations, the **tip cell** degrades **BrM** via **MMP** secretion, forming a hole in **BrM** which allows it to cross **BrM** into the **retina**. The **tip cell** does not divide, but 24 **hours** after the start of the simulation, it differentiates into a **stalk cell**. All other **stalk cells** descend from this **stalk cell**. **Stalk cells** at the tip of angiogenic sprouts behave like biological tip cells. This tip-cell-like behavior allows **stalk cells** to migrate away from existing **stalk-cell** clusters, releasing their contact-inhibition. They then grow and divide when they reach a preset doubling-volume. **CNV** refers to the ensemble of **stalk cells** in a simulation. I define the time of **CNV onset** (the ***CNV** initiation time*) to be the time at which the total number of **stalk cells** exceeds three. For implementation parameter values and additional simulation details see section III.14.

I simulated 108 different adhesion *scenarios* (sets of adhesion parameters) (ID: 1 to 108) assigning one of three levels: *normal*: 3, *moderately impaired*: 2 and *severely impaired* (*weak*): 1 (listed in Table III-11 and Table III-12) to each of the five key adhesion parameters: 1) the **RPE-RPE labile adhesion** strength (*RRl*), 2) the **RPE-RPE plastic coupling** strength (*RRp*), 3) the **RPE-BrM labile adhesion** strength (*RBl*), 4) the **RPE-BrM plastic coupling** strength (*RBp*), and 5) the **RPE-POS labile adhesion** strength (*ROl*). For each adhesion scenario I simulated my **retina** both in the absence and presence of a **tip cell** for one simulated **year**. In the presence of a **tip cell**, **CNV** may initiate (see section 3.7, below). I ran 10 simulation replicas for each adhesion scenario in which I included a **tip cell** (1080 simulations), and 3 simulation replicas for each adhesion scenario in the absence of a **tip cell** (324 simulations). Although not all the adhesion scenarios are physiologically likely (for example, Table III-19: adhesion scenario ID: 90), a comprehensive exploration of the adhesion-parameter space clarifies the role of each corresponding mechanism in **CNV** initiation and progression.

The results of my simulations are 3D time-varying **structures** and **fields**. Quantitative comparison and classification of patterns and changes in patterns in 3D are often challenging. I have developed a morphometric quantification and classification algorithm (see section III.14.6 for more details) that is able to classify CNV patterns, *i.e.* CNV types, and their time-dependent (CNV-type) changes, *i.e.* CNV progression. My algorithm calculates a *morphometric weight* (*MW*, see section III.14.6 for more details) based on the total contact area between **stalk cells** and **BrM**, and between **stalk cells** and the **POS**. A *MW* close to 1 indicates that most **stalk cells** are confined between the **RPE** and **BrM** (**sub-RPE**) in **Type 1 CNV**. A *MW* close to 0 indicates that most **stalk cells** are confined between the **RPE** and **POS** (**sub-retinal**) in **Type 2 CNV**. A *MW* close to 0.5 usually indicates **Type 3 CNV** (see section III.14.6 for additional conditions when *MW* ~ 0.5). My computational classification is compatible with current static histological classifications and can be applied to images of appropriately labeled histological sections and 3D microscopy images of the retina.

I use multiple-regression analysis to relate the **CNV** initiation probability, types, progression and dynamics to the typical adhesion scenarios which cause them. When statistical inference is ambiguous ($R^2 < 0.7$), I look at individual simulation time series in detail.

III.7.1 *Necessary and Sufficient Conditions for CNV Initiation*

CNV initiation in my simulations requires: 1) a **tip cell**, and 2) adhesion failures. A **tip cell** is not sufficient to initiate **CNV** if all adhesions are normal. Even when a **tip cell** makes a hole in **BrM**, crosses **BrM** and differentiates into a **stalk cell CNV** does not initiate if all adhesions are normal (Table III-13, adhesion scenario ID:1).

The strong adhesion of **RPE cells** to neighboring **RPE cells**, **POSs** and **BrM** means that the **BrM-RPE-POS** ensemble behaves as a mechanically stable *complex*. This complex effectively obstructs CNV by limiting the proliferation and invasion of **stalk cells** into the **sub-RPE** and **sub-retinal** spaces. I discuss, in greater detail below, how different modes of adhesion failure in the **complex** allow **stalk cells** to proliferate and invade. Chemotaxis greatly affects how **stalk cells** invade the **sub-RPE** and **sub-retinal** spaces. **Stalk cells** chemotax up gradients of both **short-diffusing** and **RPE-derived VEGF-A**. **RPE-derived VEGF-A** is especially important because its concentration is maximal in the **RPE**, encouraging **stalk cells** to migrate from the **CC** into the **sub-RPE** and **sub-retinal** spaces. Adhesion between components of the **BrM-RPE-POS** complex opposes such invasion, inhibiting **CNV** initiation. My simulations show that finite-strength adhesive interactions among the components of the **BrM-RPE-POS** complex can prevent invasion by **stalk cells** if the adhesion forces are greater than the forces which **stalk cells** exert on the **RPE-RPE** and **RPE-BrM** boundaries due to chemotaxis. Because of the complicated interactions among components during angiogenesis, the existence of such adhesion thresholds is not obvious *a priori*. My simulations therefore allow us to refine my understanding of these thresholds to show that EC-EC adhesion is also important in vivo. Self-organization of **ECs** into a capillary network pattern requires: 1) Strong chemotaxis forces that balance **EC-EC** adhesion (**ECs** form clusters rather than networks when chemotaxis to both **short-diffusing** and **RPE-derived VEGF-A** is weak), 2) the **EC-EC** adhesion strength must be comparable to the adhesion strengths in the **BrM-RPE-POS** complex. Thus the strength of adhesion among **RPE-RPE**, **RPE-BrM** and **RPE-POS** required to resist chemotaxing **ECs** also depends on **EC-EC** adhesivity.

I performed multiple-regression analysis (see section III.14.7 for details) against five adhesion parameters (*RRl, RRp, RBl, RBp, ROl*) to relate specific adhesion failures to the probability of **CNV** initiation. The five adhesion parameters and their (multi)linear combinations account for 88% of the observed variance in the **CNV** initiation probability (adjusted $R^2 = 0.83$). To visualize the five-dimensional (*5D*) regression relations, I reduce 5D to 3D by assuming that $RRp = RRl$ and $RBp = RBl$. I call this reduction *symmetric* since it assumes that impairing **RPE-RPE labile adhesion** also impairs **RPE-RPE plastic coupling**. *E.g.*, I would expect changes in cytoskeletal architecture due to inflammation to affect both adhesion mechanisms together. I consider *asymmetric reductions* in adhesion later in this section. Figure III.4 shows a 3D volumetric visualization the of the **CNV** initiation probability (P_{init}) in the symmetrically reduced parameter space ($RRp = RRl$ and $RBp = RBl$). Regression predicts a minimum **CNV** initiation probability of 0.08 for normal adhesion, while **CNV** did not initiate in any of my simulation replicas for normal adhesion. Thus the simulated **CNV** initiation probability for normal adhesion is effectively 0, as observed clinically, while the regression-inferred 0.08 initiation probability is an artifact of the linear inference, an example of the greater predictive power of mechanistic simulations compared to pure statistical inference.

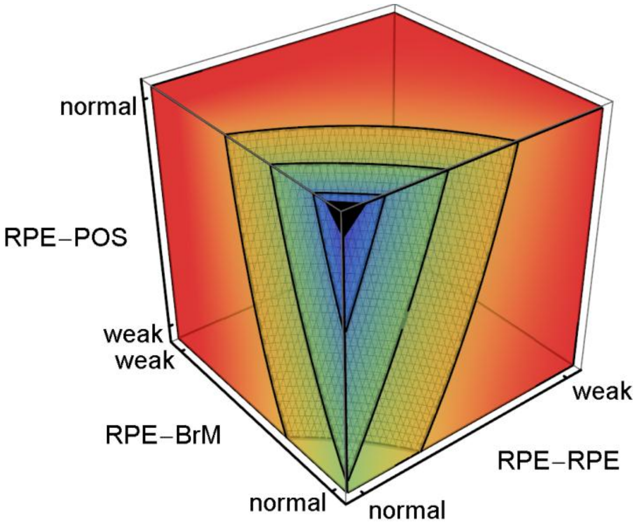

Figure III.4. **CNV** Initiation Probability Dependence on Key Adhesion Mechanisms. 3D plot of the regression-inferred **CNV** initiation probability (P_{init}) vs. three key adhesion strengths using ten simulation replicas for each adhesion scenario in the 3D parameter space obtained by setting *RRp* = *RRl* and *RBp* = *RBl*. Red corresponds to $P_{\text{init}} = 1$ and purple to $P_{\text{init}} = 0$. The black region at the top-front corner indicates the locus of normal adhesion. The three isosurfaces of **CNV** initiation probability correspond to $P_{\text{init}} = 0.25$ (front), 0.5 (middle) and 0.75 (back). The five adhesion parameters and their (multi)linear combinations account for 88% of the observed variance in **CNV** initiation probability (adjusted $R^2 = 0.83$). Regression predicts a minimum **CNV** initiation probability of 0.08 for normal adhesion, much higher than observed in either our simulations or experiments. For normal **RPE-POS labile adhesion**, moderate impairment of either **RPE-RPE** (*RRp* = *RRl*) or **RPE-BrM** (*RBp* = *RBl*) **junctional adhesion** increases the **CNV** initiation probability to ~ 50%. Severe impairment of **RPE-POS** increases the **CNV** initiation probability to ~ 50% even when both **RPE-RPE** and **RPE-BrM** are normal.

Figure III.4 shows that when **RPE-POS labile adhesion** is normal, even moderate impairment of either **RPE-RPE** (*RRp* = *RRl*) or **RPE-BrM** (*RBp* = *RBl*) **junctional adhesion** increases the **CNV** initiation probability to ~ 50%. When both **RPE-RPE** and **RPE-BrM junctional adhesion** are normal (*RRp* = *RRl* = *RBp* = *RBl* = 3) and **RPE-POS labile adhesion** is severely impaired (*ROl* = 1) **CNV** initiation probability is also ~ 50%. Thus, for severe impairments of any one of the three adhesion failure mechanisms can each independently induce **CNV**, as predicted both by my regression model and my mechanistic interpretation. Adhesion failures in the **BrM-RPE-POS** complex show strong combinatorial effects. When either **RPE-RPE** or **RPE-BrM junctional adhesion** is moderately impaired and **RPE-POS labile adhesion** is severely impaired, **CNV** initiation probability increases to 100%. Table III-7 shows that asymmetrical impairment of either **RPE-RPE** or **RPE-BrM plastic coupling** alone, without impairment of the corresponding **labile adhesion** barely increases the probability of **CNV** initiation. Thus, the **plastic coupling** strengths have only a minor effect on the ability of the **BrM-RPE-POS** complex to oppose **CNV**.

III.8 Early and Late CNV and CNV Progression

To classify **CNV** progression during a simulated **year**, I determine the ***early*** and ***late*** loci of **stalk cells**, using the mean (weighted by the number of **stalk cells**) *MW*s during the first and last three **months** of each simulation whether or not **CNV** initiates (I can calculate the *MW* even if CNV fails to spread and thus in the absence of initiation). The mean *MW* measures the ability of the **BrM-RPE-POS** complex to confine **stalk cells** to specific regions. A $MW \geq 0.75$ during a given time interval indicates that most **stalk cells** lie between **BrM** and the **RPE** (in the **sub-RPE** space) and that they do not contact the **POS**. I therefore assign the time interval to **Type 1 CNV**. A $MW \leq 0.25$ during a given time interval indicates that most **stalk cells** lie between the **RPE** and the **POS** (in **sub-retinal** space) and do not contact **BrM**. I therefore assign the time interval to **Type 2 CNV**. $0.25 < MW < 0.75$ usually indicates that **stalk cells** occur in both the **sub-RPE** and **sub-retinal** spaces (since few **sub-RPE stalk cells** touch the **POS** and few **sub-retinal**

stalk cells touch **BrM**). I therefore assign the time interval to **Type 3 CNV**. In a few exceptional cases (Table III-22) with $0.25 < MW < 0.75$, most **stalk cells** lie between neighboring **RPE cells** rather than in either the **sub-RPE** or **sub-retinal** spaces (discussed section III.9.6, below). The type of **CNV** during the early window which I call the **early CNV type** (the first three months of a simulation) is especially revealing, because all simulations start from the same initial condition. The **early CNV type** shows the efficacy of the **BrM-RPE-POS** complex in blocking **stalk cell** invasion of the **sub-RPE** and **sub-retinal** spaces. Since tissue structure and cell function can change significantly in the **BrM-RPE-POS** complex during a simulated **year**, changes in **CNV type** between the **early** and **late** windows can result from either structural or barrier-function changes in the **BrM-RPE-POS** complex. For example, the adhesion failures which typically lead to **Early Type 3 CNV** differ from those which typically leading to **Late Type 3 CNV**.

Because my simulations are stochastic, different replicas of the same adhesion scenario can lead to different combinations of **early** and **late types** of **CNV**. Such variation is common clinically and indicates that a simple population average of *MW*s over simulation replicas may reveal neither the **types**, progression dynamics nor degree of heterogeneity of outcomes. To retain this dynamic and population information, I classify **CNV** dynamics (progression) in each simulation separately based on its **early** and **late CNV type**, for a total of 9 CNV dynamics scenarios (Table III-4). I use the term *progression* when a simulation replica initially develops either **Early Type 1 CNV** or **Early Type 2 CNV** and then develops **Late Type 3 CNV** and *translocation* when a replica initially develops either **Early Type 1 CNV** or **Early Type 3 CNV**, then **Late**

Type 2 CNV or initially develops either **Early Type 2 CNV** or **Early Type 3 CNV**, then **Late Type 1 CNV**. Three translocation scenarios **sub-retinal** to **sub-RPE CNV** (**T21 CNV**), **Type 3** to **sub-RPE CNV** (**T31 CNV**) and **Type 3** to **sub-retinal CNV** (**T32 CNV**) did not occur in my simulations.

Morphometric Weights (MWs)	CNV Type
$MW \geq 0.75$	**Type 1**
$MW \leq 0.25$	**Type 2**
$0.25 < MW < 0.75$	**Type 3**

Table III-2. Classification of **CNV** type based on Morphometric Weight. I define the type of **CNV** based on the mean morphometric weight during a three **month** window. A $MW \geq 0.75$ throughout the window indicates that most **stalk cells** lie between **BrM** and the **RPE** (in the **sub-RPE** space) and do not contact the **POS**. We therefore assign the time window to **Type 1**. A $MW \leq 0.25$ throughout the window indicates that most **stalk cells** lie between **RPE** and the **POS** (in **sub-retinal** space) and do not contact **BrM**. I therefore assign the time window to **Type 2 CNV**. $0.25 < MW < 0.75$ usually indicates that **stalk cells** occur in both the **sub-RPE** and **sub-retinal** spaces. In a few exceptional cases (Table III-22) with $0.25 < MW < 0.75$, most **stalk cells** lie between neighboring **RPE cells** rather than in either the **sub-RPE** or **sub-retinal** spaces (discussed section III.9.6).

CNV Classification	Relevant Adhesion Scenarios
Early Type 1 (ET1)	Table III-14
Late Type 1 (LT1)	-

Early Type 2 (ET2)	Table III-15
Late Type 2 (LT2)	-
Early Type 3 (ET3)	Table III-16
Late Type 3 (LT3)	-

Table III-3. (Temporal) Nomenclature for CNV. To classify **CNV** progression dynamics during a simulated **year**, I determine the ***early*** and ***late*** loci of **stalk cells** using the mean *MW*s during the first and last three **months** of each simulation (I can make this calculation whether or not **CNV** initiates).

Dynamics Classification	CNV Dynamics	Relevant Adhesion Scenarios
Stable Type 1 (***S11***)	**Early Type 1 → Late Type 1**	Table III-17
Sub-RPE to Sub-Retinal Translocation (***T12***)	**Early Type 1 → Late Type 2**	Table III-18
Sub-RPE to Sub-Retinal Progression (***P13***)	**Early Type 1 → Late Type 3**	Table III-19
Sub-Retinal to Sub-RPE Translocation (***T21***)	**Early Type 2 → Late Type 1**	Not Observed
Stable Type 2 (***S22***)	**Early Type 2 → Late Type 2**	Table III-20
Sub-Retinal to Sub-RPE Progression (***P23***)	**Early Type 2 → Late Type 3**	Table III-21
Type 3 to Sub-RPE Translocation (***T31***)	**Early Type 3 → Late Type 1**	Not Observed
Type 3 to Sub-Retinal	**Early Type 3 → Late Type 2**	Not Observed

Translocation (***T32***)		
Stable Type 3 (***S33***)	**Early Type 3 → Late Type 3**	Table III-22

Table III-4. Nomenclature for **CNV** Dynamics. I classify **CNV** progression dynamics in each simulation based on its **early** and **late CNV types**, allowing for nine **CNV**-dynamics scenarios. I use the term *progression* when a simulation replica initially develops either **Early Type 1 CNV** or **Early Type 2 CNV** and then develops **Late Type 3 CNV** and *translocation* when a replica initially develops either **Early Type 1 CNV** or **Early Type 3 CNV**, then **Late Type 2 CNV** or initially develops either **Early Type 2 CNV** or **Early Type 3 CNV**, then **Late Type 1 CNV**. Three translocation scenarios, **T21**, **T31** and **T32**, did not occur in our simulations.

III.8.1 *Early Type 1 (ET1) CNV*

Stalk cells remain confined to the **sub-RPE** space in two main classes of adhesion scenarios: 1) When **RPE-BrM labile adhesion** is moderately to severely impaired, **RPE-BrM plastic coupling** satisfies $RBl + RBp \leq 4$, and both **RPE-RPE** and **RPE-POS labile adhesion** are normal ($RRl = 3$ and $ROl = 3$). 2) When both **RPE-RPE** and **RPE-BrM labile adhesion** are severely impaired ($RRl = 1$ and $RBl = 1$), **RPE-BrM plastic coupling** is moderately to severely impaired ($RBp \leq 2$), and both **RPE-RPE plastic coupling** and **RPE-POS labile adhesion** are normal ($RRp = 3$, $ROl = 3$) (Table III-14, adhesion scenario ID: 83 and 84). In both classes of adhesion scenarios, **CNV** initiation leads to **Early Type 1 CNV** (**ET1**). Table III-14 shows the *MW* and **CNV** initiation probabilities for the adhesion scenarios most prone to **ET1 CNV** ($MW > 0.9$).

Multiple-regression analysis of the five adhesivities accounted for 93% of the observed variance in the average *MW* for all 108 adhesion scenarios (adjusted $R^2 = 0.89$). Figure III.5 shows the **stalk cell** locus regression-inferred from the average *MW* as a function of the adhesion parameters obtained by setting *RRp* = *RRl* and *RBp* = *RBl*. Since Figure III.5 shows the **stalk cell** locus even when **CNV** fails to initiate, a region *prone* to **ET1 CNV**, develops **ET1 CNV** only if **CNV** initiates. Severe impairment of **RPE-POS labile adhesion** greatly reduces the *MW*, so **ET1 CNV** can only occur when **RPE-POS labile adhesion** is near normal. Scenarios with severe impairment of **RPE-BrM junctional adhesion** (*RBp* = *RBl* = 1), and normal **RPE-POS labile adhesion** are prone to **ET1 CNV** over a wide range of **RPE-RPE junctional adhesion** impairment (*MW* > 0.95 for *RRp* = *RRl* > 1.5). The red region with *MW* > 0.9 has P_{init} > 0.8 (Figure III.5).

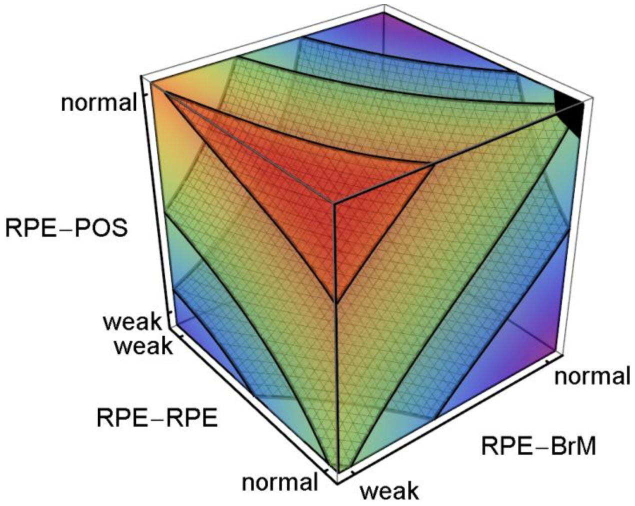

Figure III.5. **Sub-RPE CNV** Dependence on Adhesion. 3D plot of the regression-inferred average *MW* using 10 simulation replicas for each adhesion scenario in the 3D parameter space obtained by setting *RRp* = *RRl* and *RBp* = *RBl*. The average *MW* shows the **stalk cell** locus even when **CNV** fails to initiate, so a region *prone* to **ET1 CNV** develops **ET1 CNV** only if **CNV** initiates. Red corresponds to *MW* = 1 and purple corresponds to *MW* = 0. The black region at the top-left corner indicates the locus of normal adhesion. *MW* = 1.0 for **RPE-RPE junctional adhesion** normal, **RPE-BrM junctional adhesion** severely impaired (weak) and **RPE-POS labile adhesion** normal. The three isosurfaces correspond to *MW* = 0.25 (back), 0.5 (middle) and 0.90 (front). The five adhesion parameters and their (multi)linear combinations account for 93% of the observed variance in average *MW* for all 108 adhesion scenarios (adjusted R^2 = 0.89). Severe impairment of **RPE-POS labile adhesion** greatly reduces the *MW*, so **ET1 CNV** can only occur when **RPE-POS labile adhesion** is near normal. Scenarios with severe impairment of **RPE-BrM junctional adhesion** ($RBp = RBl = 1$), and normal **RPE-POS labile adhesion** are prone to **ET1 CNV** for a wide range of **RPE-RPE junctional adhesion** impairment ($MW > 0.95$ for $RRp = RRl > 1.5$). The red region with $MW > 0.9$ has $P_{\text{init}} > 0.8$. To show the structure of the isosurfaces, we have rotated the axes relative to Figure III.4.

.

III.8.2 *Early Type 2 (ET2) CNV*

Stalk cells initially invade the **sub-retinal** space (**Early Type 2 CNV**) in three main classes of adhesion scenarios: 1) When **RPE-RPE labile adhesion** is normal ($RRl = 3$), **RPE-BrM labile adhesion** is normal or moderately impaired ($RBl \geq 2$), and **RPE-POS labile adhesion** is severely impaired ($ROl = 1$). 2) When **RPE-RPE labile adhesion** is severely impaired ($RRl = 1$) and **RPE-BrM labile adhesion** is either normal or moderately impaired ($RBl \geq 2$). 3) When **RPE-RPE**, **RPE-BrM** and **RPE-POS labile adhesion** are severely impaired ($RRl = RBl = ROl = 1$), and the combination of **RPE-RPE** and **RPE-BrM plastic coupling** satisfies $RBp + RRp > 3$. Unless all **labile adhesions** are severely impaired, impairment of either **RPE-RPE** or **RPE-BrM plastic coupling** has little effect on the average *MW*, though it does increase the **CNV** initiation probability. For example, adhesion scenarios ID: 22 and 24, which differ only in their **RPE-BrM plastic coupling**, exhibit the same mean *MW*; however, $P_{\text{init}} = 0.8$ for normal **RPE-BrM plastic coupling** (ID: 22) and $P_{\text{init}} = 1$ for severely impaired **RPE-BrM plastic coupling** (ID: 24).

Figure III.6 shows (1 - *MW*), which measures the degree of *confinement* of **stalk cells** to the **sub-retinal** space, based on the regression-inferred average *MW* (see, section III.8.1, above) as a function of the five adhesion parameters, reduced to 3D by setting

RRp = *RRl* and *RBp* = *RBl*. The red region with (1 - *MW*) > 0.9, can be divided into three sub-regions: 1) When **RPE-RPE junctional adhesion** is normal, **RPE-BrM junctional adhesion** is moderately impaired, and **RPE-POS labile adhesion** is severely impaired (weak). 2) When **RPE-RPE junctional adhesion** is severely impaired (weak) and **RPE-BrM junctional adhesion** is normal, independent of **RPE-POS labile adhesion**. 3) When **RPE-RPE junctional adhesion** is severely impaired (weak), **RPE-BrM junctional adhesion** is moderately to severely impaired, and **RPE-POS labile adhesion** is severely impaired. Figure III.6 does not include all the adhesion scenarios in Table III-15 leading to **Early Type 2 CNV**.

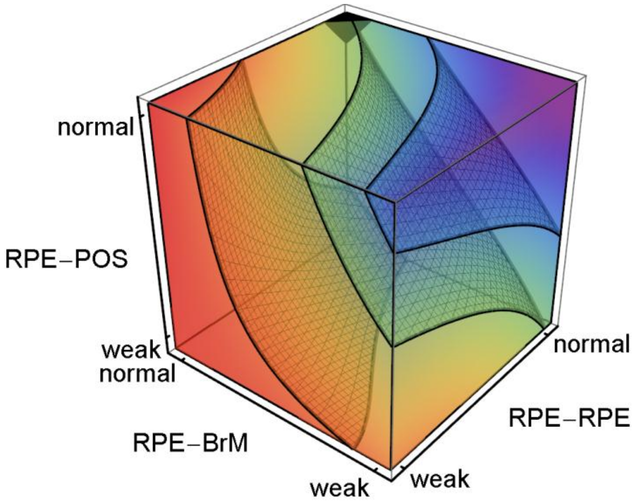

Figure III.6. **Sub-Retinal CNV** Dependence on Adhesion. 3D plot of the regression-inferred average (1 - *MW*) using 10 simulation replicas for each adhesion scenario in the 3D parameter space obtained by setting *RRp* = *RRl* and *RBp* = *RBl*. The average (1 - *MW*) shows the **stalk cell** locus even when **CNV** fails to initiate, so a region *prone* to **ET2 CNV**, develops **ET2 CNV** only if **CNV** initiates. Red corresponds to (1 - *MW*) = 1 and purple corresponds to (1 - *MW*) = 0. The black region at the top-back corner indicates the locus of normal adhesion. The three isosurfaces correspond to (1 - *MW*) = 0.25 (right), 0.5 (middle) and 0.90 (left). The five adhesion parameters and their (multi)linear combinations account for 93% of the observed variance in average *MW* for all 108 adhesion scenarios (R^2 = 0.89). The red region with (1 - *MW*) > 0.9, can be divided into three sub-regions: 1) When **RPE-RPE junctional adhesion** is normal, **RPE-BrM junctional adhesion** is moderately impaired, and **RPE-POS labile adhesion** is severely impaired (weak). 2) When **RPE-RPE junctional adhesion** is severely impaired (weak) and **RPE-BrM junctional adhesion** is normal, independent of **RPE-POS labile**

adhesion. 3) When **RPE-RPE** adhesion is weak, **RPE-BrM** adhesion is moderately to severely impaired, and **RPE-POS** adhesion is severely impaired. The red region does not include all adhesion scenarios in Table III-15 leading to **Early Type 2 CNV**. To show the structure of the isosurfaces, I have rotated the axes relative to Figure III.4.

III.8.3 *Early Type 3 (ET3) CNV*

In **Early Type 3** (**ET3**) **CNV**, **Stalk cells** initially grow both between the **RPE** and **BrM** and between the **RPE** and the **POS**. Most adhesion scenarios have severely impaired **RPE-RPE labile adhesion** (*RRl* = 1), normal **RPE-POS labile adhesion** (*ROl* = 3) and either severely or moderately impaired **RPE-BrM labile adhesion** ($RBl \leq 2$) (Table III-16). In these adhesion scenarios, **RPE-RPE** and **RPE-BrM plastic coupling** have little effect on mean *MW* and **CNV** initiation probability. For example, adhesion scenarios ID: 82 (*RRp* = 3), 85 (*RRp = 2*) and 88 (*RRp* = 1) have similar mean *MW* and **CNV** initiation probability, despite differing in their **RPE-RPE plastic coupling** strengths (*RRp*).

III.9 CNV Progression Dynamics

III.9.1 *Stable Type 1 CNV (S11): Early Type 1 → Late Type 1 CNV*

In most adhesion scenarios that develop **Early Type 1 CNV** with *MW* > 90% the **CNV** remains in the **sub-RPE** space during one simulated **year** (**Late Type 1 CNV**, *MW* > 75%). *I.e.* they exhibit **Stable T1 CNV** (**S11 CNV**). **S11 CNV** occurs primarily when **RPE-BrM labile adhesion** is moderately to severely impaired ($RBl \leq 2$), **RPE-BrM plastic coupling** satisfies $RBl + RBp \leq 4$, and **RPE-RPE** and **RPE-POS labile adhesion** are both normal (*RRl* = 3 and *ROl* = 3). This class of scenarios corresponds to the first sub-class of adhesion scenarios prone to **ET1** (Table III-14). Adhesion scenarios prone to **ET1 CNV** with severely impaired **RPE-RPE labile adhesion** (*RRl* = 1) (Table III-14, ID: 83 and 84; both *MW* > 0.9) or with severely impaired **RPE-BrM labile adhesion** (*RBl* = 1) and **plastic coupling** (*RRp* = 1) (Table III-14, ID: 75, 78, 81, 84; all *MW* > 0.9) do not remain stable, exhibiting **RPE** detachment and degeneration followed by **CNV** involution.

Multiple-regression analysis of the five adhesion parameters accounted for 76% of the observed variance in the probability of occurrence of **S11 CNV** in all 108 adhesion scenarios (adjusted $R^2 = 0.67$). Figure III.7 shows the regression-inferred probability of occurrence of **S11 CNV** as a function of the five adhesion parameters, obtained by setting *RRp* = *RRl* and *RBp* = 3. Severe impairment of either **RPE-POS labile adhesion** or **RPE-RPE labile adhesion** greatly reduces the *MW*, so **S11 CNV** can only occur when both adhesion strengths are near normal (Figure III.7). The maximal regression-inferred probability of **S11 CNV** is 0.93 when **RPE-RPE junctional adhesion** is normal (*RRp* = *RRl* = 3), **RPE-BrM labile adhesion** is severely impaired (*RBl* = 1), **RPE-BrM plastic coupling** is normal (*RBp* = 3), and **RPE-POS labile adhesion** is normal (*ROl* = 3) (Figure III.7). Severe impairment of both **RPE-BrM labile adhesion** and **plastic coupling** (*RBl* = *RBp* = 1) causes the **RPE** to detach from **BrM**, leading to either **T12 CNV** translocation or **T13 CNV** progression and causing **RPE** degeneration followed by **CNV** involution. The probability of **S11 CNV** for two of the adhesion scenarios in Table III-17, ID: 3 and 41, is significantly larger than regression analysis predicts.

Generally, **CNV** *growth speed* differs from replica to replica in adhesion scenarios prone to **S11 CNV** (compare to **S22 CNV** dynamics, below). Figure III.8 shows typical **S11 CNV** dynamics for 10 simulation replicas of a single adhesion scenario (*RRl* = 3, *RRp* = 3, *RBl* = 2, *RBp* = 2, *ROl* = 3) (Table III-17, adhesion scenario ID: 38). I visualize snapshots of **S11 CNV** dynamics in one replica in Figure III.9 and Video S3-1. 9 of the ten simulation replicas initiate **CNV**, then develop **ET1 CNV** (Figure III.9A, black arrows) and **S11 CNV** during one simulated **year** (Figure III.8B and Figure III.9D). Only 3 simulation replicas formed fully developed capillary networks composed of about 45 **stalk cells** (~ 3000 **cells**/mm^2) (Figure III.8B and Figure III.9D). In general when **stalk cells** form large aggregates the concentration of **RPE-derived VEGF-A** at the center of the aggregate is less than the threshold below which **stalk cells** die. A few **stalk cells** in 5 of the simulation replicas die during one simulated **year** (Figure III.8A). While s**talk cells** do contact the **POS** during the **early** window, **Type 2 CNV** does not develop (Figure III.8C). The **RPE** remains viable and its total contact area with **BrM** decreases as **stalk cells** proliferate (Figure III.8D-E). The **POS** never contacts **BrM**, indicating that the **RPE** does not develop any holes (Figure III.8F and Figure III.9A-D).

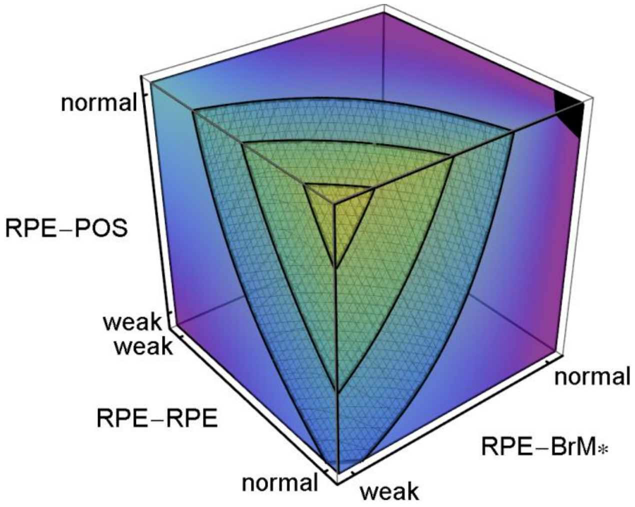

Figure III.7. **Stable Type 1 CNV** Dependence on Adhesion. 3D plot of the regression-inferred probability of occurrence of **Stable Type 1 CNV** (**S11 CNV** probability) using 10 simulation replicas for each adhesion scenario in the *asymmetrically* reduced parameter space obtained by setting *RRp* = *RRl* and *RBp* = 3 (indicated by the **RPE-BrM*** axis label). Red corresponds to a **S11 CNV** probability of 1 and purple corresponds to a **S11 CNV** probability of 0. The black region at the top-left corner indicates the locus of normal adhesion. The maximal regression-inferred probability of **S11 CNV** is 0.93 when **RPE-RPE junctional adhesion** is normal (*RRp* = *RRl*), **RPE-BrM labile adhesion** is severely impaired (*RBl* = 1), **RPE-BrM plastic coupling** is normal (*RBp* = 3), and **RPE-POS labile adhesion** is normal. The three isosurfaces correspond to **S11 CNV** probabilities of 0.25 (back), 0.5 (middle) and 0.8 (front). The five parameters and their (multi)linear combinations account for 76% of the observed variance in the probability of occurrence of **S11 CNV** (R^2 = 0.67). Severe impairment of **RPE-POS labile adhesion** and **RPE-RPE junctional adhesion** greatly reduces *MW*, so **S11 CNV** can only occur when both adhesion strengths are near normal. To show the structure of the isosurfaces, I have rotated the axes relative to Figure III.4.

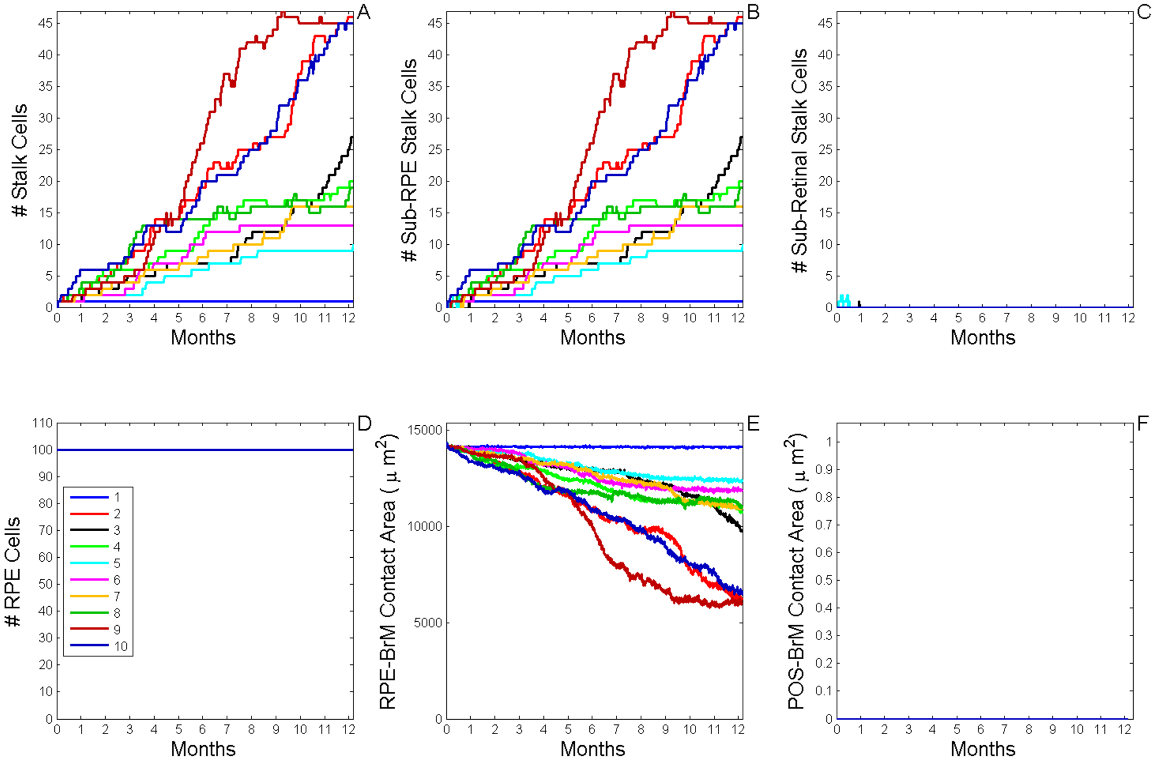

Figure III.8. Dynamics of **Stable Type 1 CNV** (**S11 CNV**). A) Total number of **stalk cells** vs. **time**. B) Total number of **stalk cells** confined in the **sub-RPE** space vs. **time**. C) Total number of **stalk cells** in contact with the **POS** (**stalk cells** in the **sub-retinal** space) vs. **time**. D) Total number of **RPE cells** vs. **time**. E) Total contact area between **RPE cells** and **BrM** vs. **time**. F) Total contact area between **POS cells** and **BrM** vs. **time**. The different colors represent the dynamics of 10 simulation replicas of the adhesion scenario (*RRl* = 3, *RRp* = 3, *RBl* = 2, *RBp* = 2, *ROl* = 3) (Table III-17, adhesion scenario ID: 38). (A, B) **CNV** initiates in 9 out of 10 simulation replicas. All develop **Early Type 1 CNV**. **CNV** remains confined in the **sub-RPE** space during one simulated **year** (**Stable Type 1 CNV**). A Fully developed **sub-RPE** capillary network contains about 45 **stalk cells** (~ 3000 **cells**/mm^2). In 5 simulation replicas a few **stalk cells** die during the simulated **year** due to lack of **RPE-derived VEGF-A**. (C) **Stalk cells** have minimal contact with the **POS**. (D, E) The **RPE** remains viable and its total contact area with **BrM** decreases as **stalk cells** proliferate. (F) The **POS** never contacts **BrM**, indicating that the **RPE** does not develop any holes.

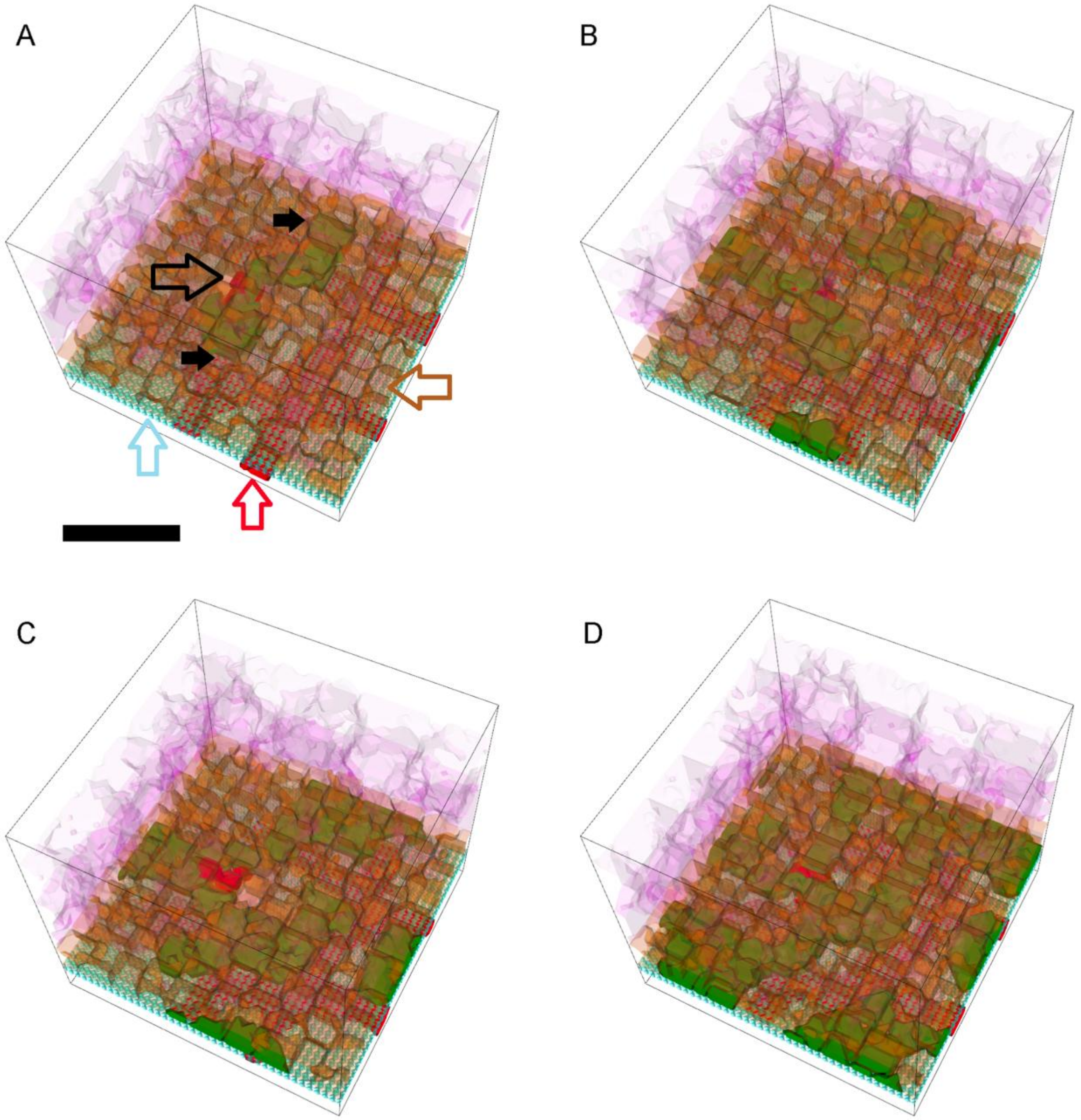

Figure III.9. Snapshots of a Simulation Replica with **Stable Type 1 CNV**. 3D visualization of a simulation replica exhibiting **Stable Type 1 CNV** over one simulated **year** (adhesion scenario ID: 38, simulation ID: 902) (*RRl* = 3, *RRp* = 3, *RBl* = 2, *RBp* = 2, *ROl* = 3). Snapshots of the simulation at **months** 3 (A), 6 (B), 9 (C) and 12 (D). (A) **Stalk cells** (black arrows) invade the **sub-RPE** space through a hole (black outline arrow) in **BrM** (light blue outline arrow) that the **tip cell** opens during the first 24 **hours**. Brown outline arrow shows the **RPE cells**. Red outline arrow shows the **CC** (B, C) **Stalk cells** proliferate until they fill the **sub-RPE** space in **month** 9, after which proliferation slows down (D) The 45 **stalk cells** form a connected capillary network in the **sub-RPE** space. **Cell type** colors: 1) **POS** and **PIS**: light purple, 2) **RPE**: brown, 3) **Stalk cells**: green, 4) **Vascular cells** (**CC**): red, 5) **BrM**: light blue. Scale bar ~ 50 µm. We have rendered the boundaries of individual cells as semi-transparent membranes. **POS**, **PIS** and **RPE** cells are more transparent to show the underlying structures. See also Video S3-1.

III.9.2 *Sub-RPE to Sub-Retinal CNV Translocation (T12 Translocation): Early Type 1 → Late Type 2 CNV*

Sub-RPE to **sub-Retinal** translocation occurs when **stalk cells** of **Early Type 1 CNV** ($MW \geq 0.75$) later translocate to the **sub-retinal** space to produce **Late Type 2 CNV** ($MW \leq 0.25$). **T12** translocation occurs primarily when **RPE-RPE labile adhesion** is normal ($RRl = 3$), both **RPE-BrM** and **RPE-POS labile adhesion** are severely impaired ($RBl = 1$ and $ROl = 1$), and the combination of **RPE-BrM** and **RPE-POS plastic coupling** satisfies $RRp + RBp \geq 4$, except for the case $RRp = RBp = 2$.

Adhesion scenarios in which some replicas exhibit **T12 CNV** can also have replicas which exhibit either **S22** or **S11** over one simulated **year**. Figure III.10 shows **CNV** dynamics for 10 simulation replicas of the adhesion scenario ($RRl = 3$, $RRp = 3$, $RBl = 1$, $RBp = 1$, $ROl = 1$) (Table III-18, adhesion scenario ID: 93). I visualize snapshots of the **T12 CNV** dynamics in one replica in Figure III.11 and Video S3-2. **CNV** initiates in all replicas; 8 replicas develop **ET1 CNV** (Figure III.10A-B and Figure III.11A). 7 replicas exhibit **T12 CNV**. I show snapshots of the **T12 CNV** dynamics that occur in one of those replicas in Figure III.11. After 3 **months**, most replicas form a developed **sub-RPE** capillary network (black arrow, Figure III.11A) composed of ~ 20 to 40 **stalk cells** (~ 1500 to 3000 **cells**/mm^2). One replica exhibits **S11 CNV**. Two replicas form **S22 CNV** (Figure III.10C, black and dark red lines). The **RPE** remains viable in all replicas (Figure III.10D). The contact area between the **RPE** and **BrM** decreases as **ET1 CNV** or **S11**

CNV develops, and remains constant during **ET2 CNV** (Figure III.10E). **RPE** reattaches to **BrM** during **T12 CNV** (*e.g.* see the dark green line in Figure III.10E). The **POS** never contacts **BrM**, indicating that the **RPE** does not develop any tears or holes (Figure III.10F and Figure III.11D).

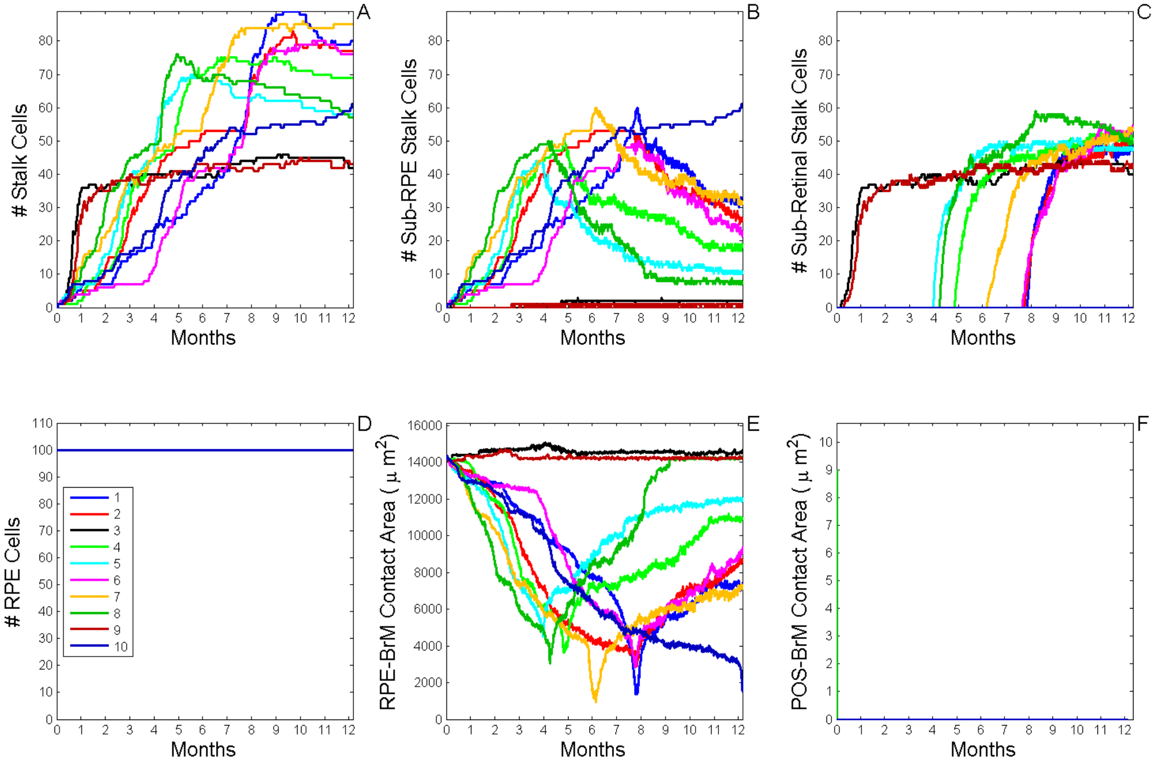

Figure III.10. Dynamics of **Sub-RPE to Sub-Retinal Translocation** (**T12 Translocation**). A) Total number of **stalk cells** vs. **time**. B) Total number of **stalk cells** confined in the **sub-RPE** space vs. **time**. C) Total number of **stalk cells** in contact with the **POS** (**stalk cells** in the **sub-retinal** space) vs. **time**. D) Total number of **RPE cells** vs. **time**. E) Total contact area between **RPE cells** and **BrM** vs. **time**. F) Total contact area between **POS cells** and **BrM** vs. **time**. The different colors represent the results of 10 simulation replicas of the adhesion scenario (*RRl* = 3, *RRp* = 3, *RBl* = 1, *RBp* = 1, *ROl* = 1) (Table III-18, adhesion scenario ID: 93). (A, B) **CNV** initiates in all replicas. By 3 **months**, most replicas form a developed **sub-RPE** capillary network composed of ~ 20 to 40 **stalk cells** (~ 1500 to 3000 **cells**/mm^2). 8 replicas develop **Early Type 1** (**ET1**) **CNV**. Only one replica shows **Stable Type 1** (**S11**) **CNV**. Some **stalk cells** in most replicas die due to lack of **RPE-derived VEGF-A**. (C) Two replicas show **Stable Type 2** (**S22**) **CNV** (**Early** (**ET2**) and **Late Type 2** (**LT2**) **CNV**, black and dark red lines). 7 replicas show **LT2 CNV**. (D) The **RPE** remains viable in all replicas. (E) The contact area between the **RPE** and **BrM** decreases as either **ET1 CNV** or **S11 CNV** develops, and remains constant during **ET2 CNV**. **RPE** reattaches to **BrM** during **T12 CNV**. (F) The **POS** contacts **BrM** once, but the contacts area and duration are both small, so the **RPE** does not develop any persistent or substantial holes.

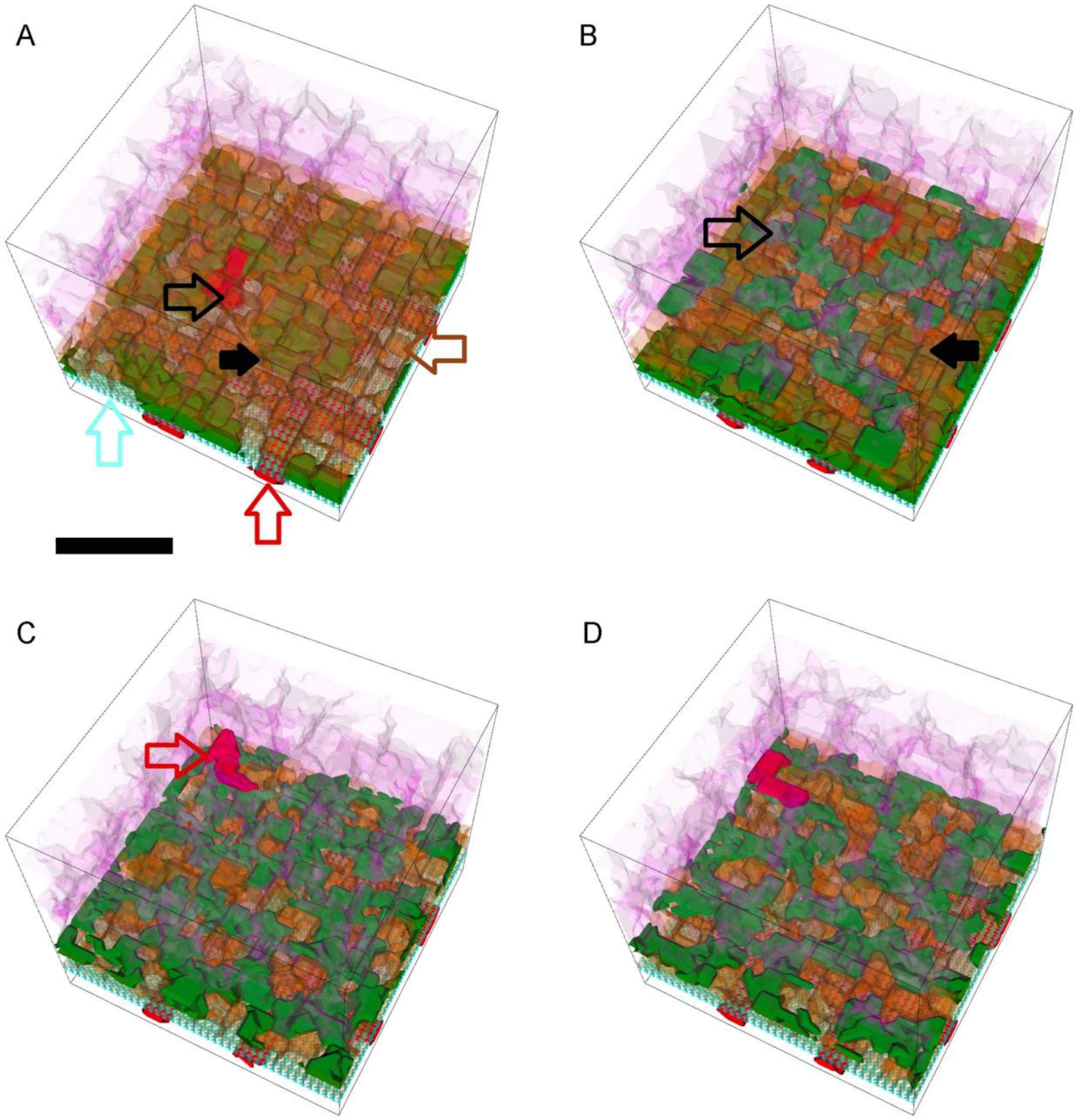

Figure III.11. Snapshots of a Simulation Replica Showing **Sub-RPE** to **Sub-Retinal Translocation** (**T12 Translocation**). 3D visualization of a simulation replica exhibiting **T12 CNV** translocation during one simulated **year** ($RRl = 3$, $RRp = 3$, $RBl = 1$, $RBp = 1$, $ROl = 1$) (adhesion scenario ID: 93, simulation ID: 849). Snapshots of the simulation at **months** 3 (A), 5 (B), 9 (C) and 12 (D). (A) **Stalk cells** (solid black arrow) invade the **sub-RPE** space through a hole in **BrM** (black outline arrow) and form a capillary network. All **stalk cells** remain in the **sub-RPE** space during the first 3 **months**. A few **vascular cells** fill the hole in **BrM** (black outline arrow) to connect **CNV** capillaries to the **CC** (red outline arrow). Brown outline arrow shows an **RPE cell**. (B) Half of the **stalk cells** (black outline arrow) have crossed the **RPE** and transmigrated into the **sub-retinal** space, forming a new capillary network in the **sub-retinal** space. The black arrow shows a **stalk cell** in the **sub-RPE** space. (C) Most **stalk cells** have transmigrated into the **sub-retinal** space and the **RPE** has completely reattached to **BrM** (Figure III.10E, dark green line). A few **vascular cells** of the **CC** have transmigrated into the **sub-retinal** space (red outline arrow) (D) The **sub-retinal** capillary network has fewer **stalk cells** than (C) since **stalk cells** that migrate into the retina far from the **RPE** die. **Cell type** colors: 1) **POS** and **PIS**: light purple, 2) **RPE**: brown, 3) **Stalk cells**: green (**stalk cells** in the **sub-retinal** space have lighter shading), 4) **Vascular cells** (**CC**): red, 5) **BrM**: light blue. Scale bar ~ 50 µm. We have rendered the boundaries of individual cells as semi-transparent membranes. **POS**, **PIS** and **RPE** cells are more transparent to show the underlying structures. See also Video S3-2.

III.9.3 *Sub-RPE CNV to Sub-Retinal CNV Progression (P13 Progression): Early Type 1 → Late Type 3 CNV*

In **sub-RPE CNV** to **sub-Retinal CNV** progression (**P13** progression), **stalk cells** initially grow between the **RPE** and **BrM** in **ET1 CNV** then invade the **sub-retinal** space to initiate **LT3**. **P13** progression primarily occurs when both **RPE-RPE** and **RPE-BrM labile adhesion** are severely impaired ($RRl = 1$ and $RBl = 1$), **RPE-BrM plastic coupling** strength is moderately to severely impaired ($RBp \leq 2$), and **RPE-POS labile adhesion** is normal ($ROl = 3$) (Table III-19). In adhesion scenarios leading to **T13 CNV**, because both **RPE-RPE** and **RPE-BrM labile adhesion** are severely impaired, the **BrM-RPE-POS** complex can block **stalk cells** neither from invading the **sub-RPE** space nor the **sub-retinal** space. However, **stalk cells** consistently invade the **sub-RPE** space first and then progress to the **sub-retinal** space (Figure III.12 and Figure III.13). **Stalk cells** invade the **sub-retinal** space first primarily because of three mechanisms: 1) The **junctional adhesion** by which **stalk cells** adhere to **BrM** is stronger than both **stalk-**

RPE and **stalk-POS labile adhesion**. 2) Normal **RPE-POS labile adhesion** (*ROl* = 3) opposes **stalk cell** invasion of the **sub-retinal** space. 3) The gradient of **RPE-derived VEGF-A** in the apicobasal direction changes its direction from into the retina to out of the retina at the mid-plane of the **RPE** (the concentration of **RPE-derived VEGF-A** is maximal at the mid-plane of the **RPE**). Thus stalk cells entering the **sub-retinal** space across the **RPE** must migrate from regions with higher concentrations of **RPE-derived VEGF-A** to regions with lower concentrations, a migration opposed by chemotaxis.

Generally, **CNV** dynamics is very similar across all replicas in adhesion scenarios prone to the **P13 CNV** and much less heterogeneous than for **T12 CNV**. Figure III.12 shows typical **P13 CNV** dynamics for 10 simulation replicas of the adhesion scenario (*RRl* = 1, *RRp* = 3, *RBl* = 1, *RBp* = 2, *ROl* = 3) (Table III-18, adhesion scenario ID: 83). I visualize snapshots of **P13 CNV** dynamics in one replica in Figure III.13 and Video S3-3. **CNV** initiates in all replicas and all develop **ET1 CNV** (Figure III.12A-B and Figure III.13A). Between **months** 1 and 2, **stalk cells** (black outline arrow, Figure III.13B) cross the **RPE** and invade the **sub-retinal** space once the number of **stalk cells** in the **sub-RPE** space reaches ~ 60 **cells** (Figure III.12B-C). **CNV** progression into the **sub-retinal** space finishes around **month** 5 (Figure III.12C and Figure III.13C-D). A few **stalk cells** in most replicas die due to lack of **RPE-derived VEGF-A**. The **RPE** remains viable in all replicas (Figure III.12D). The contact area between the **RPE** and **BrM** decreases as **ET1** develops, and remains constant afterwards during **LT3 CNV** (Figure III.12E). The **POSs** do contact **BrM** a few times, but the contact area and duration are very small (Figure III.12F), so the **RPE** does not develop any persistent or substantial holes (Figure III.13D).

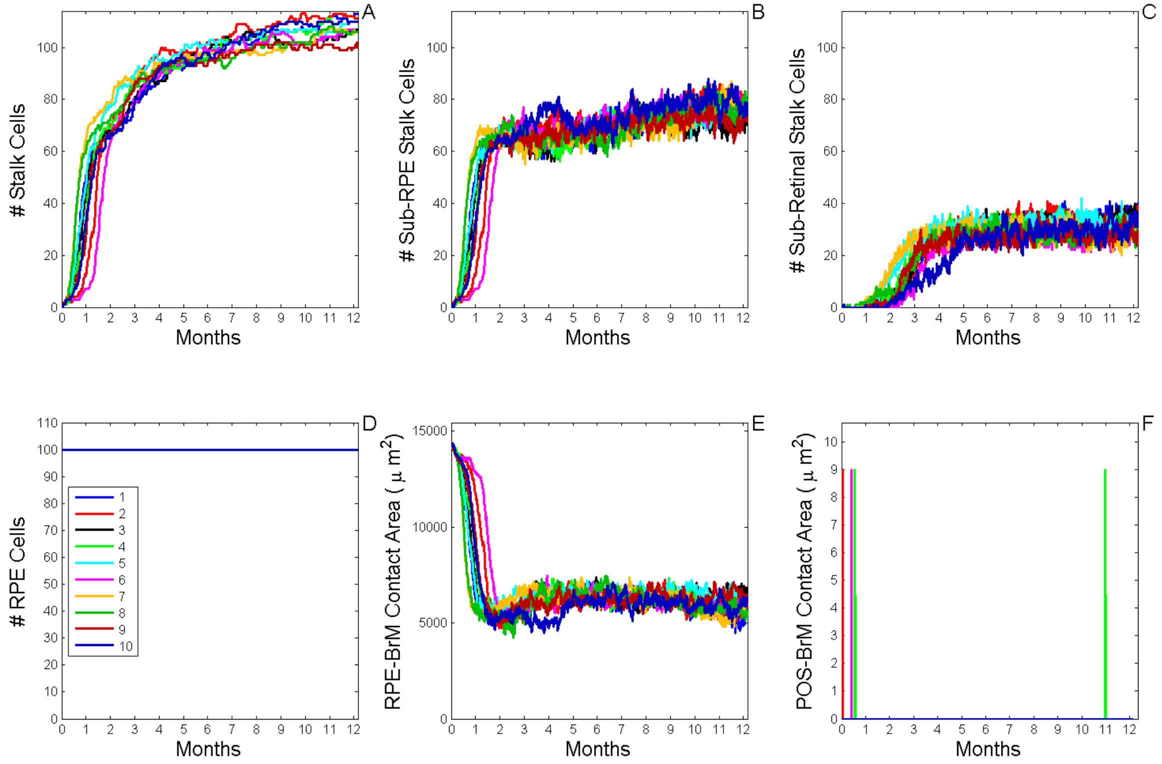

Figure III.12. Dynamics of **Sub-RPE CNV** to **Sub-Retinal CNV Progression** (**P13 Progression**). A) Total number of **stalk cells** vs. **time**. B) Total number of **stalk cells** confined in the **sub-RPE** space vs. **time**. C) Total number of **stalk cells** in contact with the **POS** (**stalk cells** in the **sub-retinal** space) vs. **time**. D) Total number of **RPE cells** vs. **time**. E) Total contact area between **RPE cells** and **BrM** vs. **time**. F) Total contact area between **POS cells** and **BrM** vs. **time**. The different colors represent the results of 10 simulation replica of the adhesion scenario (*RRl* = 1, *RRp* = 3, *RBl* = 1, *RBp* = 2, *ROl* = 3) (Table III-19, adhesion scenario ID: 83). **CNV** initiates in all replicas and all develop **ET1 CNV**. A few **stalk cells** in most replicas die due to lack of **RPE-derived VEGF-A**. (C) **Stalk cells** cross the **RPE** and invade the **sub-retinal** space once the number of **stalk cells** in the **sub-RPE** space reaches ~ 60 **cells**, which usually occurs within first two **months** after initiation. **CNV** progression to the **sub-retinal** space is complete around **month** 5. (D) The **RPE** remains viable in all replicas. (E) The contact area between the **RPE** and **BrM** decreases as **ET1 CNV** develops, and remains constant afterwards throughout **LT3 CNV**. (F) The **POS** contacts **BrM** a few times, but the contact area and duration are both small, so the **RPE** does not develop any persistent or substantial holes.

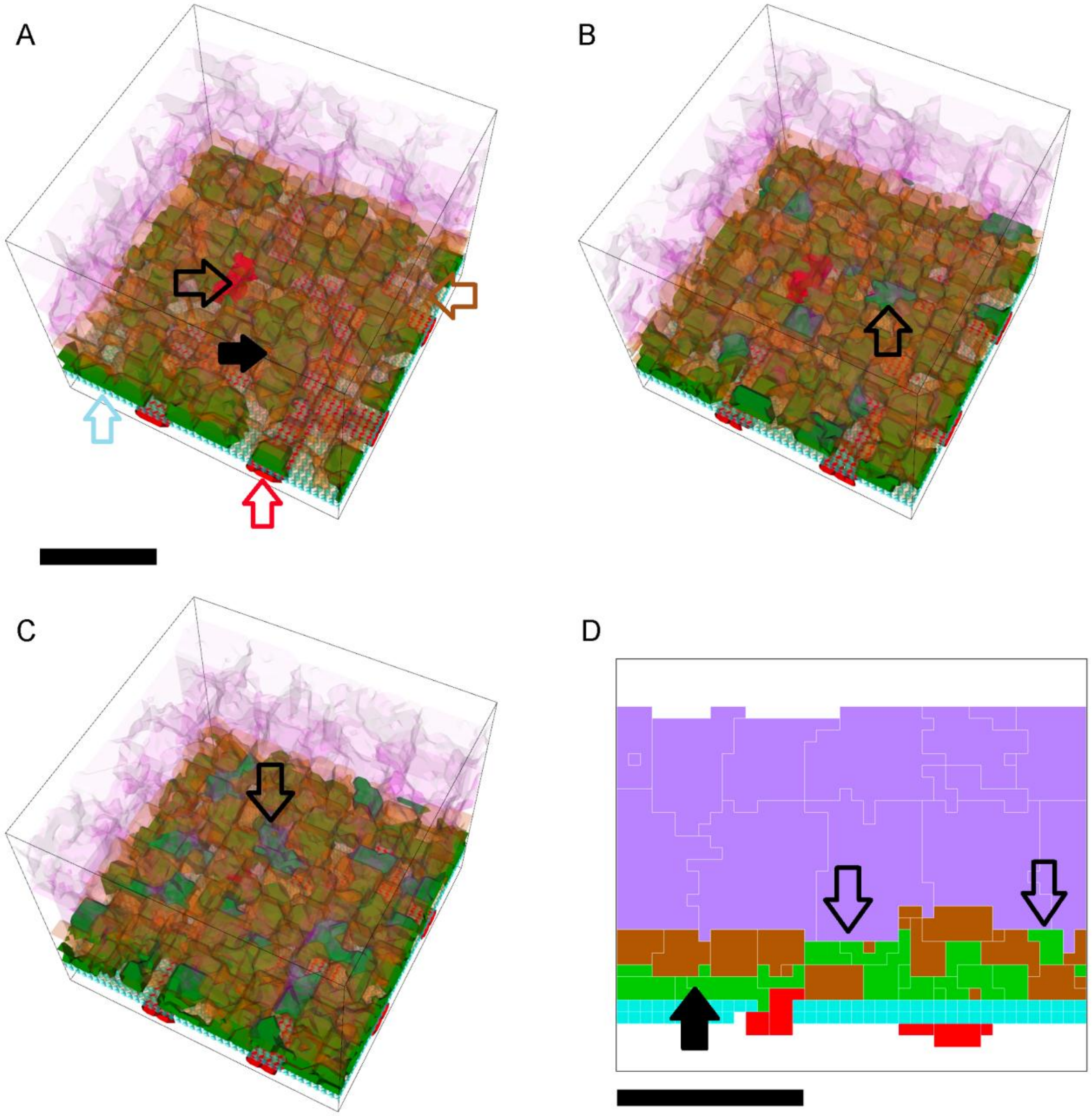

Figure III.13. Snapshots of a Simulation Replica Showing **Sub-RPE CNV to Sub-Retinal CNV Progression** (**P13 Progression**). 3D and 2D visualizations of a simulation replica exhibiting **P13 CNV** progression during one simulated **year** (*RRl* = 1, *RRp* = 3, *RBl* = 1, *RBp* = 2, *ROl* = 3) (Table III-19, adhesion scenario ID: 83, simulation ID: 515). Snapshots of the simulation at **months** 1 (A), 2 (B), 6 (C) and 12 (D). (A) **Stalk cells** (solid black arrow) invade the **sub-RPE** space through a hole in **BrM** (blue outline arrow) and form a capillary network. The **vascular cells** (black outline arrow) of the **CC** (red outline arrow) occupy the hole that the **tip cell** forms during the first 24 **hours** of the simulation, connecting the **CNV** capillaries to the **CC**. All **stalk cells** remain in the **sub-RPE** space during the first **month** of the simulation. (B) A few **stalk cells** (black outline arrow) cross the **RPE** into the **sub-retinal** space. (C) Additional **stalk cells** migrate into the **sub-retinal** space and form vascular cords (black outline arrow). (D) A 2D cross-section of the **retina** showing the hole in **BrM**. The **stalk cells** form a **sub-RPE** capillary network (black arrow) connected to a **sub-retinal** capillary network (black outline arrows). Two **vascular cells** connect the **CC** to the **CNV** capillaries through the hole in **BrM**. **Cell type** colors: 1) **POS** and **PIS**: light purple, 2) **RPE**: brown, 3) **Stalk cells**: green (**stalk cells** in the **sub-retinal** space have lighter shading), 4) **Vascular cells** (**CC**): red, 5) **BrM**: light blue. Scale bar ~ 50 µm. We have rendered the boundaries of individual cells as semi-transparent membranes. **POS**, **PIS** and **RPE** cells are more transparent to show the underlying structures. See also Video S3-3.

III.9.4 *Stable Type 2 CNV (S22): Early Type 2 CNV → Late Type 2 CNV*

In **Stable Type 2 CNV** (**S22 CNV**), **stalk cells** initially invade the **sub-retinal** space to develop **Early Type 2 CNV** and remain confined in the **sub-retinal** space in **Late Type 2 CNV**. The **ET2 CNV** classification is based on a $MW \leq 0.25$ (Table III-2) during the first three months. Most adhesion scenarios that develop **ET2 CNV** in which the MW remains less than 0.15 during the first three months also exhibit **S22 CNV**. Thus, the three main classes of adhesion scenarios that cause **ET2 CNV** predominantly lead to **S22 CNV**. Table III-15 (**ET2 CNV**) shows only adhesion scenarios with $MW < 0.05$ throughout the first three **months**, so some of the adhesion scenarios in Table III-20 exhibiting **S22 CNV** are not listed in Table III-15 (**ET2 CNV**).

Multiple-regression analysis of the five adhesivities for the probability of occurrence of **S22 CNV** accounted for 89% of the observed variance in the probability of occurrence of **S22 CNV** in all 108 adhesion scenarios (adjusted $R^2 = 0.84$). Figure III.14 shows the regression-inferred probability of occurrence of **S22 CNV** as a function of the five adhesion parameters, obtained by setting $RRp = RRl$ and $RBp = RBl$. The multiple-regression results show that moderate to severe impairment of **RPE-RPE junctional adhesion** ($RRp = RRl < 2$) and normal to moderately impaired **RPE-BrM junctional**

adhesion (*RBp* = *RBl* > 2) develop **S22 CNV**, independent of the strength of **RPE-POS** adhesion (0.9 isosurface, Figure III.14).

Generally, **CNV** dynamics is very similar across all replicas of the adhesion scenarios prone to **S22 CNV**. As for **P13 CNV**, the variability from replica to replica is smaller than for **S11 CNV**. Figure III.15 shows typical **S22 CNV** dynamics for 10 simulation replicas of the adhesion scenario (*RRl* = 1, *RRp* = 1, *RBl* = 3, *RBp* = 3, *ROl* = 3) (Table III-20, adhesion scenario ID: 16). I show snapshots of the **S22 CNV** dynamics in one replica in Figure III.16 and Video S3-4. **CNV** initiates in all replicas and all develop **ET2 CNV** (Figure III.15A-B and Figure III.16A-D). During first two **months** after initiation, **stalk cells** develop a capillary network in the **sub-retinal** space (Figure III.16B and Figure III.15C). **CNV** development in the **sub-retinal** space finishes around **month** 4 (Figure III.15C and Figure III.16C-D). A few **stalk cells** in most replicas die due to lack of **RPE-derived VEGF-A**. The **RPE** remains viable in all replicas (Figure III.15D). The contact area between the **RPE** and **BrM** remains constant throughout **S22 CNV** (Figure III.15E). The **POSs** do contact **BrM**, but the contact area and duration are small (Figure III.15F), so the **RPE** does not develop any substantial or persistent holes (Figure III.16D).

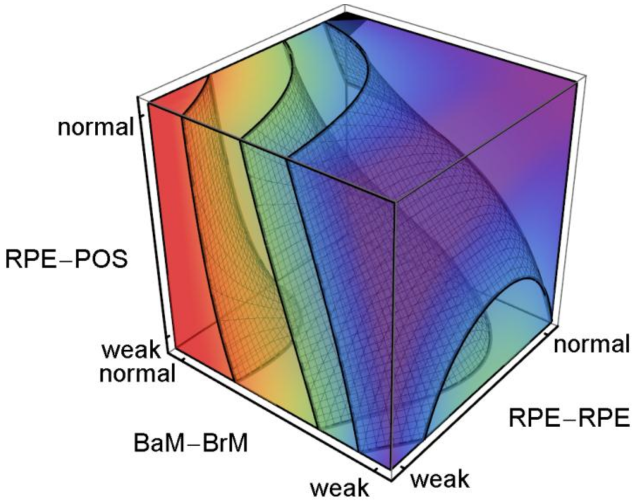

Figure III.14. **Stable Type 2 CNV** Dependence on Adhesion. 3D plot of the regression-inferred probability of occurrence of **Stable Type 2 CNV** (**S22 CNV** probability) using 10 simulation replicas for each adhesion scenario in the 3D parameter space obtained by setting *RRp* = *RRl* and *RBp* = *RBl*. Red corresponds to a **S22 CNV** probability of 1 and purple corresponds to a **S22 CNV** probability of 0. The black region at the top-back corner indicates the locus of normal adhesion. The three isosurfaces correspond to **S22 CNV** probabilities of 0.25 (right), 0.5 (middle) and 0.9 (left). The five parameters and their (multi)linear combinations account for 89% of the observed variance in the probability of occurrence of **S22 CNV** in all 108 adhesion scenarios (adjusted $R^2 = 0.84$). **S22 CNV** occurs primarily when **RPE-RPE junctional adhesion** is moderately to severely impaired, **RPE-BrM junctional adhesion** is normal or moderately impaired, independent of **RPE-POS labile** adhesion (red region with **S22 CNV** probability > 0.9). The red region does not include all adhesion scenarios in Table III-20 leading to **S22 CNV**. To show the structure of the isosurfaces, I have rotated the axes relative to Figure III.4.

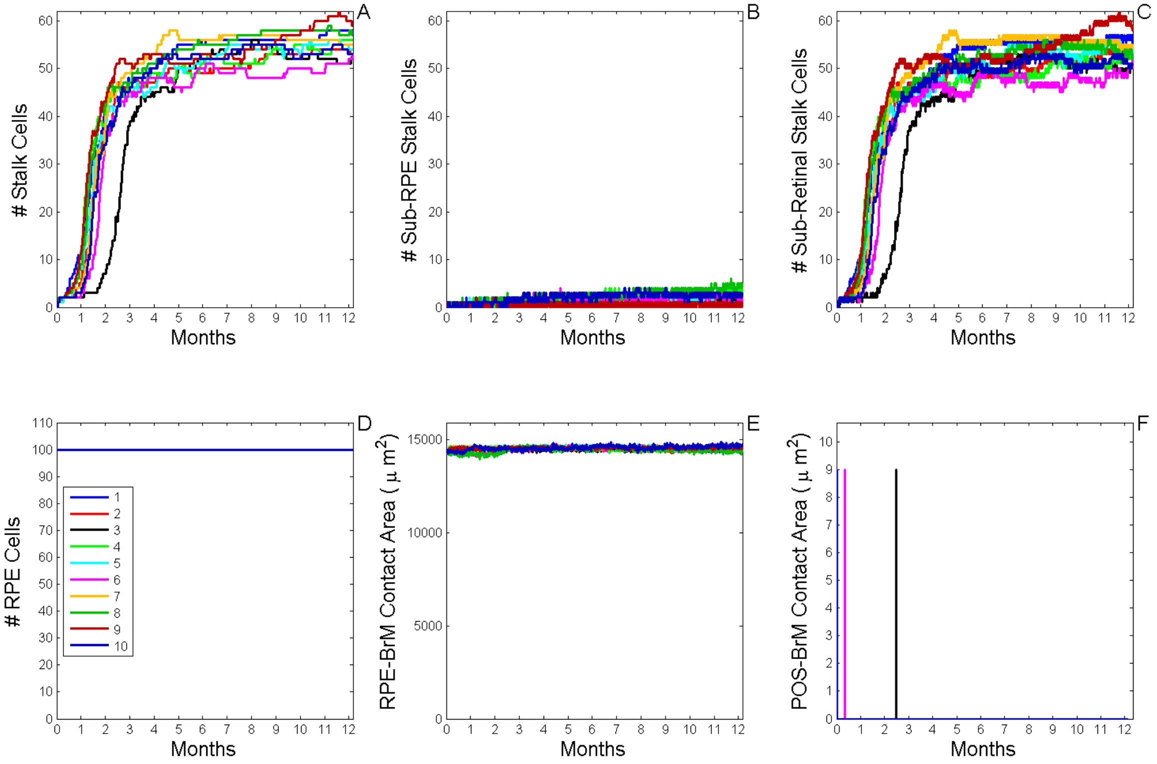

Figure III.15. Dynamics of **Stable Type 2 CNV** (**S22 CNV**). A) Total number of **stalk cells** vs. **time**. B) Total number of **stalk cells** confined in the **sub-RPE** space vs. **time**. C) Total number of **stalk cells** in contact with the **POS** (**stalk cells** in the **sub-retinal** space) vs. **time**. D) Total number of **RPE cells** vs. **time**. E) Total contact area between **RPE cells** and **BrM** vs. **time**. F) Total contact area between **POS cells** and **BrM** vs. **time**. The different colors represent the results of 10 simulation replicas of the adhesion scenario (*RRl* = 1, *RRp* = 1, *RBl* = 3, *RBp* = 3, *ROl* = 3) (Table III-20, adhesion scenario ID: 16). (A, C) **CNV** initiates in all replicas and all develop **ET2 CNV** during the first three **months** of the simulation. All replicas exhibit **S22 CNV**. A few **stalk cells** in most replicas die due to lack of **RPE-derived VEGF-A**. (C) Few or no **stalk cells** reach the **sub-RPE** space. (D) The **RPE** remains viable in all replicas. (E) The contact area between the **RPE** and **BrM** does not change as **S22** develops. (F) The **POS** contacts **BrM** a few times, but the contact area and duration are both small, so the **RPE** does not develop any persistent or substantial holes.

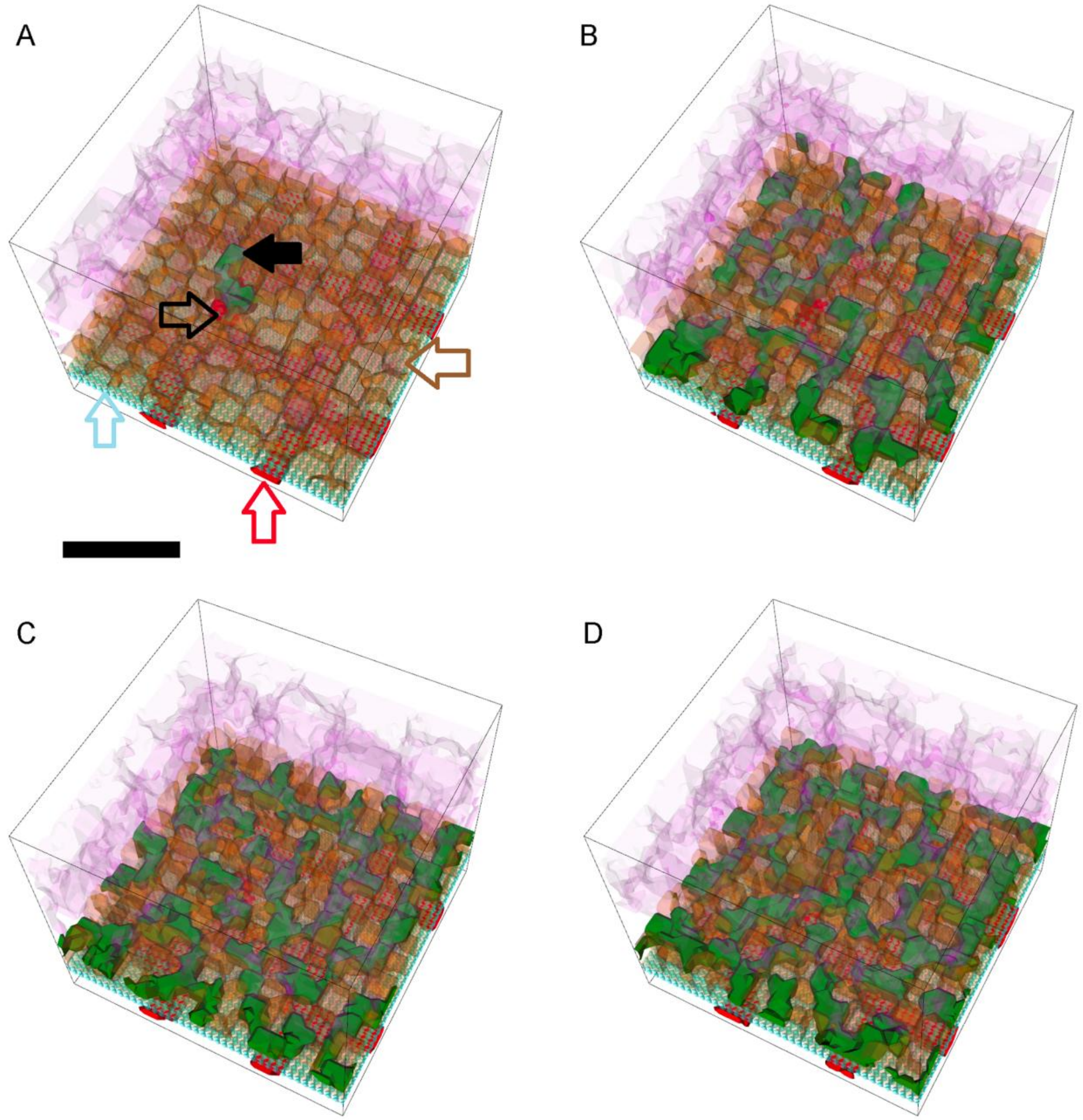

Figure III.16. Snapshots of a Simulation Replica showing **Stable Type CNV** (**S22 CNV**). 3D visualization of a simulation replica showing **S22 CNV** in one simulated **year** (*RRl* = 1, *RRp* = 1, *RBl* = 3, *RBp* = 3, *ROl* = 3) (adhesion scenario ID: 16, simulation ID: 556). Snapshots of the simulation at **months** 1 (A), 2 (B), 6 (C) and 12 (D). (A) **Stalk cells** (solid black arrow) invade the **sub-retinal** space through a hole in **BrM** (black outline arrow) and form a partially developed capillary network (B). **CNV** finishes **sub-retinal** invasion around **month** 5 and remains in the **sub-retinal** space throughout **LT2 CNV** (C-D). A few **vascular cells** (A, black outline arrow) fill the hole in **BrM** to connect the **CNV** capillaries to the **CC** (red outline arrow). Brown outline arrow shows an **RPE cell**. **Cell type** colors: 1) **POS** and **PIS**: light purple, 2) **RPE**: brown (**stalk cells** in the **sub-retinal** space have lighter shading), 3) **Stalk cells**: green, 4) **Vascular cells** (**CC**): red, 5) **BrM**: light blue. Scale bar ~ 50 µm. We have rendered the boundaries of individual cells as semi-transparent membranes. **POS**, **PIS** and **RPE** cells are more transparent to show the underlying structures. See also Video S3-4.

III.9.5 *Sub-Retinal to Sub-RPE Progression (P23 CNV Progression): Early Type 2 CNV → Late Type 3 CNV*

In **P23 CNV** progression, **stalk cells** initially invade the **sub-retinal** space to produce **Early Type 2 CNV**, then invade the **sub-RPE** space to progress to **Late Type 3 CNV**. **P23 CNV** primarily occurs when **RPE-RPE plastic coupling** is severely or moderately impaired ($RRp \leq 2$) and all other adhesions are severely impaired ($RRl = 1$, $RBl = 1$, $RBp = 1$, $ROl = 1$).

Generally, **CNV** dynamics is very similar across all replicas of the adhesion scenarios prone to **P23 CNV**. Variability from replica to replica is low and comparable to the variability observed in **P13 CNV** and **S22 CNV**. Figure III.17 shows typical **P23 CNV** dynamics for 10 simulation replicas of the adhesion scenario where all adhesions are severely impaired ($RRl = 1$, $RRp = 1$, $RBl = 1$, $RBp = 1$, $ROl = 1$) (adhesion scenario ID: 108). I visualize snapshots of the **P23 CNV** dynamics in one replica in Figure III.18 and Video S3-5. **CNV** initiates in all replicas and all replicas rapidly develop **ET2 CNV** (Figure III.17C). **Stalk cells** cross the **RPE** and invade the **sub-RPE** space (Figure III.17B and Figure III.18A2) once the number of **stalk cells** in the **sub-retinal** space reaches ~ 50 **cells** which occurs during the first **month** after initiation (Figure III.17C). **Stalk cells** gradually invade the **sub-RPE** space during the remainder of the simulated **year** (Figure III.17B and Figure III.18A2-D2). Unlike in previously discussed scenarios in which all **RPE cells** survive, **RPE cells** death increases with the number of **sub-RPE**

stalk cells (Figure III.17B). In two replicas 30 **cells** die (30% of the total of 100 **cells**) during the simulated **year** (Figure III.17D). The contact area between the **RPE** and **BrM** decreases as **P23 CNV** develops (Figure III.17E). In all replicas the **POS** contacts **BrM** persistently and extensively, as the **RPE** develops substantial holes (Figure III.17F and Figure III.18D1-2). Formation of a hole or tear in the **RPE** reduces its contact area with **BrM** (Figure III.17F).

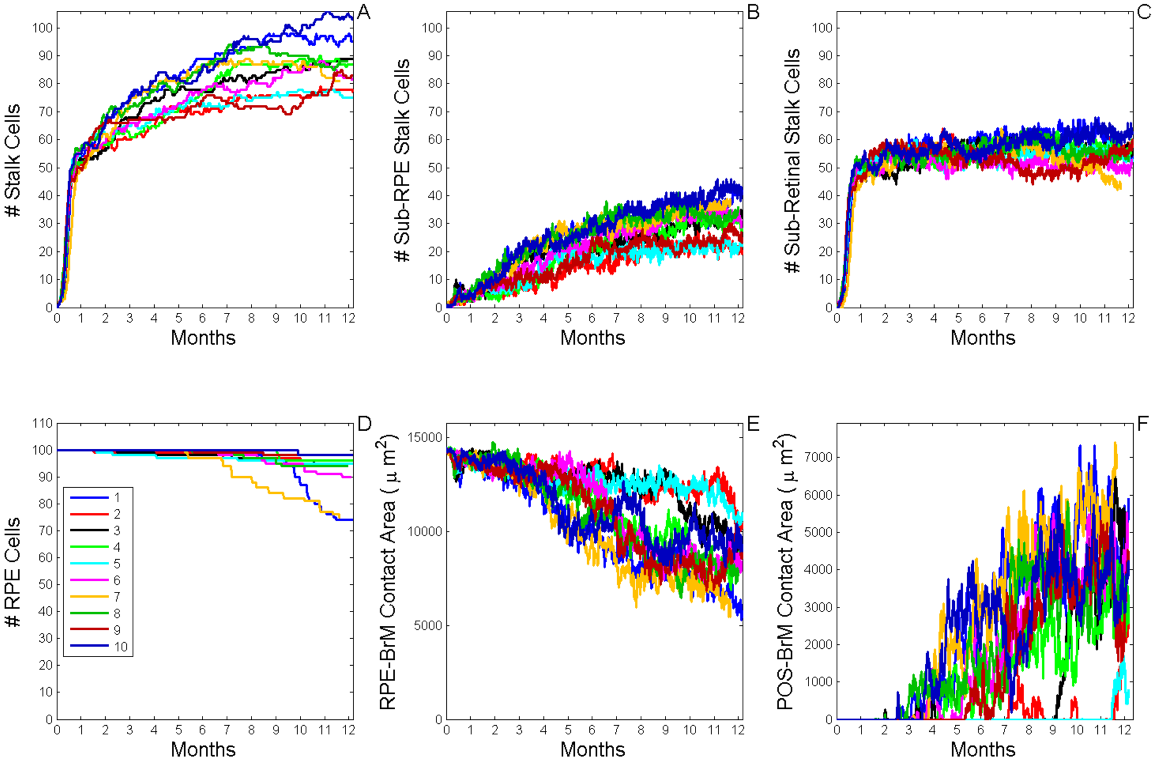

Figure III.17. Dynamics of **Sub-Retinal CNV** to **Sub-RPE CNV Progression** (**P23 CNV Progression**). A) Total number of **stalk cells** vs. **time**. B) Total number of **stalk cells** confined in the **sub-RPE** space vs. **time**. C) Total number of **stalk cells** in contact with the **POS** (**stalk cells** in the **sub-retinal** space) vs. **time**. D) Total number of **RPE cells** vs. **time**. E) Total contact area between **RPE cells** and **BrM** vs. **time**. F) Total contact area between **POS cells** and **BrM** vs. **time**. The different colors represent the results of 10 simulation replicas of the adhesion scenario (*RRl* = 1, *RRp* = 1, *RBl* = 1, *RBp* = 1, *ROl* = 1) (Table III-21, adhesion scenario ID: 108). **CNV** initiates in all replicas and all develop **ET2 CNV**. A few **stalk cells** in most replicas die due to lack of **RPE-derived VEGF-A**. (B) **Stalk cells** cross the **RPE** and invade the **sub-RPE** space once the number of **stalk cells** in the **sub-RPE** space reaches ~ 50 **cells**, which usually occurs during the first **month** after initiation. **Stalk cells** gradually invade the **sub-RPE** space during one simulated **year**. (D) Up to 30 **RPE cells** (30% of the total) die. The number of **RPE cell** deaths increases with the number of **sub-RPE stalk cells**. (E) The contact area between the **RPE** and **BrM** decreases as **P23 CNV** develops. (F) In all replicas the **POS** contacts **BrM** persistently and extensively, as the **RPE** develops substantial holes (see Figure III.18).

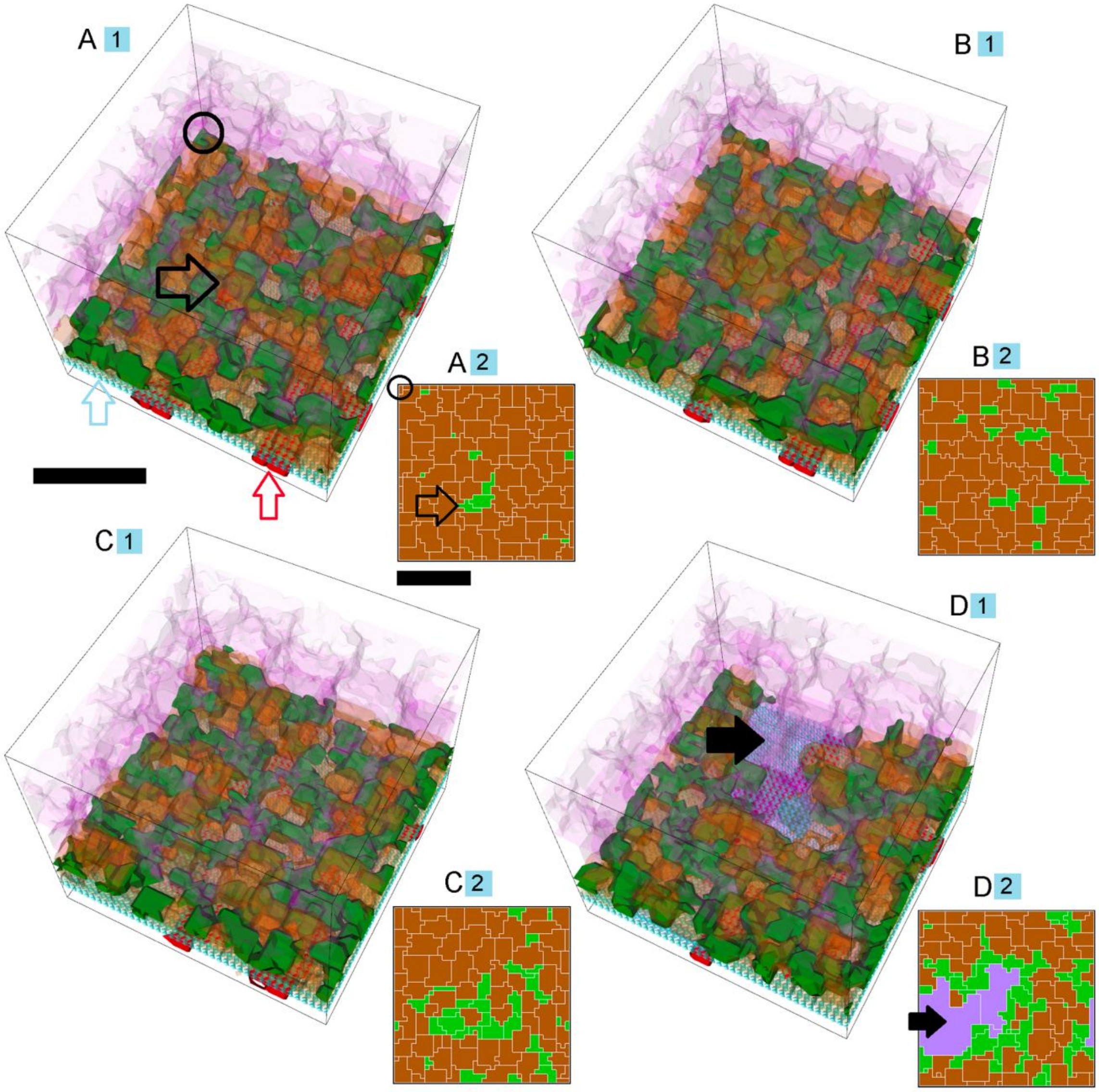

Figure III.18. Snapshots of a Simulation Replica Exhibiting **Sub-Retinal CNV** to **Sub-RPE CNV Progression** (**P23 CNV**). 3D and 2D visualization of a simulation replica forming **P23 CNV** in one simulated **year** (*RRl* = 1, *RRp* = 1, *RBl* = 1, *RBp* = 1, *ROl* = 1) (adhesion scenario ID: 108, simulation ID: 1080). Snapshots of the simulation at **months** 1 (A), 3 (B), 6 (C) and 12 (D). (A2-D2) Cross-sections of (A1-D1) parallel and adjacent to **BrM**, so **stalk cells** shown in (A2-D2) contact **BrM**. The black open circles (A1-2) at the top corner and outline back arrows (A1-2) at the location of the hole in **BrM** are guides to the eye to align A2 to A1. The alignment is consistent across all panels. (A) **Stalk cells** (solid black arrow) invade the **sub-retinal** space through the hole in **BrM** (A1-2, black outline arrows) that the **tip cell** form during the first 24 **hours** of the simulation and form a fully developed **sub-retinal** capillary network by **month** 1. (A2) Only a few **stalk cells**, mostly near the hole in **BrM**, invade the **sub-RPE** space during the first **month**. (B1, C1) The **sub-retinal** capillary network does not grow significantly. (B2, C2) Additional **stalk cells** invade the **sub-RPE** space. (D) More **stalk cells** invade the **sub-RPE** space, disrupting the **RPE** and causing a micro-tear (D1-2, black arrows). The **POS** contacts **BrM** at the location of the **RPE** tear. **Cell type** colors: 1) **POS** and **PIS**: light purple, 2) **RPE**: brown (**stalk cells** in the **sub-retinal** space have lighter shading), 3) **Stalk cells**: green (3D-visualized **stalk cells** in the **sub-retinal** space have lighter shading), 4) **Vascular cells** (**CC**): red, 5) **BrM**: light blue. Scale bars ~ 50 µm. We have rendered the boundaries of individual cells in A1-D1 as semi-transparent membranes. **POS**, **PIS** and **RPE** cells are rendered more transparent to show the underlying structures. See also Video S3-5.

III.9.6 *Stable Type 3 (S33 CNV): Early Type 3 CNV → Late Type 3 CNV*

In stable **Type 3 CNV**, **stalk cells** initially invade both the **sub-RPE** and **sub-retinal** space and remain in both loci for the entire simulated **year**. **Stalk cells** occasionally migrate in both directions between the **sub-retinal** space and the **sub-RPE** space. **S33 CNV** occurs primarily for two classes of adhesion scenarios: 1) When **RPE-RPE labile adhesion** is severely impaired (*RRl* = 1), **RPE-POS labile adhesion** is normal (*ROl* = 3), **RPE-BrM labile adhesion** is moderately impaired (*RBl* = 2) and **RPE-BrM plastic coupling** satisfies $RBl + RBp \leq 4$. 2) When **RPE-RPE labile adhesion** is severely impaired (*RRl* = 1), **RPE-POS labile adhesion** is normal (*ROl* = 3), **RPE-BrM labile adhesion** is severely impaired (*RBl* = 1) and **RPE-BrM plastic coupling** is normal (*RBp* = 3). **RPE-RPE plastic coupling** has no effect on the probability of **CNV** initiation or occurrence of **S33 CNV** in these scenarios. **RPE-BrM junctional adhesion** in adhesion scenarios causing **S33 CNV** is less impaired than in those which result in **P13 CNV**. The greater **RPE-BrM junctional adhesion** encourages **stalk cells** to invade both the **sub-retinal** space and the **sub-RPE** space simultaneously (in **P13 CNV** all **stalk cells** invade the **sub-retinal** space first).

Generally, **CNV** dynamics is very similar across all replicas of the adhesion scenarios prone to **S33 CNV**. Variability from replica to replica is comparable to the variability in **P13 CNV**, **S22 CNV** and **P23 CNV**. Figure III.19 shows the typical **S33 CNV** dynamics in 10 simulation replicas of the adhesion scenario (*RRl* = 1, *RRp* = 1, *RBl* = 2, *RBp* = 2, *ROl* = 3) (Table III-22, adhesion scenario ID: 53). I visualize snapshots of **S33 CNV** dynamics in one replica in Figure III.20 and Video S3-3. **CNV** initiates in all replicas and all develop **ET3 CNV**. During the first **month**, more stalk cells invade the **sub-RPE** space than invade the **sub-retinal** space (Figure III.19B-C and Figure III.20A1). Between **months** 1 and 2, about 30% of the **sub-RPE stalk cells** transmigrate into the **sub-retinal** space (dark blue line, Figure III.19B-C). After **month** 3, the number of **sub-RPE stalk cells** slowly increases, while the number of **sub-retinal stalk cells** remains constant. The contact area between the **RPE** and **BrM** rapidly decreases when **stalk cells** invade the **sub-RPE** space during the first **month** of the simulation, then rapidly increases as **sub-RPE stalk cells** transmigrate into the **sub-retinal** space between **months** 1 and 2. The contact area between the **RPE** and **BrM** slowly decreases during **months** 3 to 12. A few **RPE cell** die in most replicas, but **RPE cells** death is much less pervasive than in **P23 CNV**. In a few replicas the **POS** contacts **BrM** persistently, but the holes the **RPE** develops are significantly smaller than those occurring in **P23 CNV** (Figure III.17F and Figure III.18D1-2).

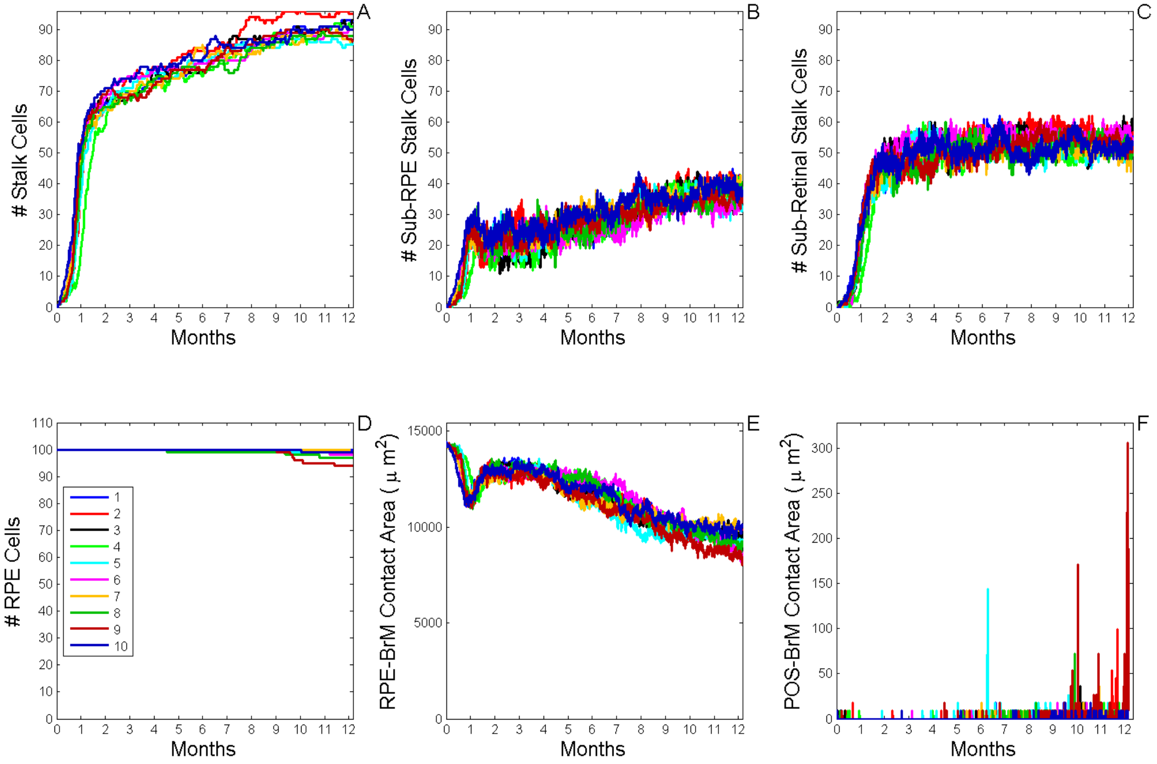

Figure III.19. Dynamics of **Stable Type 3 CNV** (**S33 CNV**)**.** A) Total number of **stalk cells** vs. **time**. B) Total number of **stalk cells** confined in the **sub-RPE** space vs. **time**. C) Total number of **stalk cells** in contact with the **POS** (**stalk cells** in the **sub-retinal** space) vs. **time**. D) Total number of **RPE cells** vs. **time**. E) Total contact area between **RPE cells** and **BrM** vs. **time**. F) Total contact area between **POS cells** and **BrM** vs. **time**. The different colors represent the results of 10 simulation replicas of the adhesion scenario (*RRl* = 1, *RRp* = 1, *RBl* = 2, *RBp* = 2, *ROl* = 3) (Table III-22, adhesion scenario ID: 53). (A, B, C) **CNV** initiates in all replicas and all replicas develop **ET3 CNV**. During the first **month** after initiation, stalk cells gradually invade both the **sub-RPE** space and the **sub-retinal** space, with more invading the **sub-RPE** space. Between **months** 1 and 2 about 30% of the **sub-RPE stalk cells** transmigrate into the **sub-retinal** space. After **month** 3, the number of **sub-RPE stalk cells** increases slowly, while the number of **sub-retinal stalk cells** remains constant. (E) During the first **month** of the simulation, the contact area between the **RPE** and **BrM** rapidly decreases as **stalk cells** invade the **sub-RPE** space. Between **months** 1 and 2, the contact area between the **RPE** and **BrM** rapidly increases as **sub-RPE stalk cells** transmigrate into the **sub-retinal** space. The contact area between the **RPE** and **BrM** slowly decreases after **month** 3 throughout the simulated **year**. (D) A few **RPE cells** die in most replicas. (F) In a few replicas the **POS** persistently contacts **BrM**, as the **RPE** develops small holes.

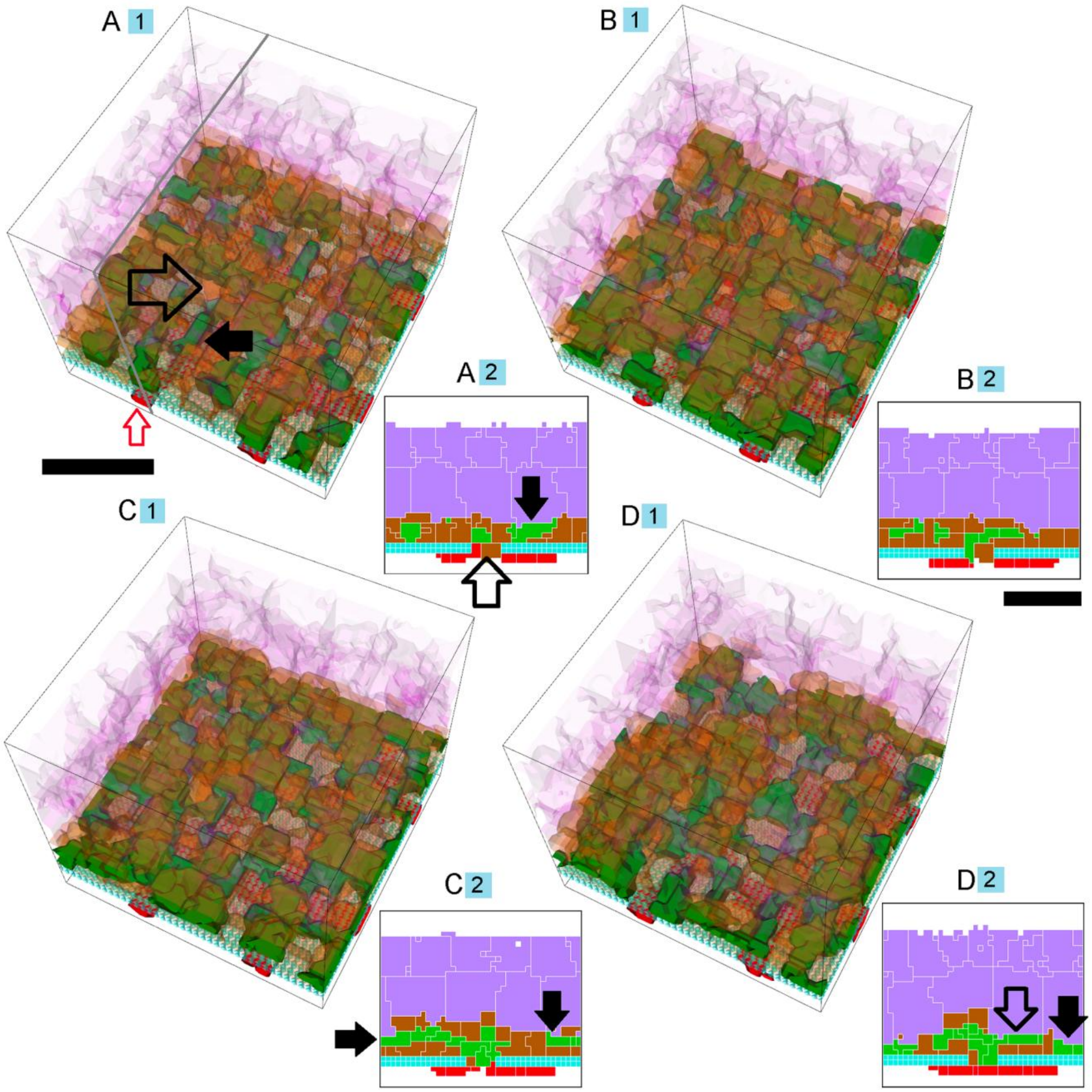

Figure III.20. Snapshots of a Simulation Replica Exhibiting **Stable Type 3 CNV** (**S33 CNV**). 3D and 2D visualization of a simulation replica developing **S33 CNV** in one simulated **year** (*RRl* = 1, *RRp* = 1, *RBl* = 2, *RBp* = 2, *ROl* = 3) (adhesion scenario ID: 53, simulation ID: 917). Snapshots of the simulation at **months** 1 (A), 2 (B), 6 (C) and 12 (D). (A2-D2) Cross-sections of (A1-D1). All cross-section planes in (A1-D1) panels defined by the two thick black lines in A1. (A) **Stalk cells** invade the **sub-RPE** space through a hole in **BrM** (A1-2, black outline arrows) that the **tip cell** forms during the first 24 **hours** of the simulation. These **stalk cells** then form a fully developed **sub-RPE** capillary network. (A2) Only a few **stalk cells** (black arrow, A1-2) reach the **sub-retinal** space during the first **month**. (B1, C1) The **sub-retinal** and **sub-RPE** capillary networks do not grow significantly. (C2) A capillary (black arrows), enveloped by a bilayer of **RPE cells**, connects the **sub-retinal** space to the **CC** via the hole in **BrM** (D) **Stalk cells** disrupt the **RPE**, forming small holes in the **RPE** (D2, black arrow). The **stalk cells** at the location of the hole in the **RPE** (D2, black arrow) contact both the **POSs** and **BrM**. The black outline arrow shows **sub-retinal stalk cells**. **Cell type** colors: 1) **POS** and **PIS**: light purple, 2) **RPE**: brown, 3) **Stalk cells**: green, 4) **Vascular cells** (**CC**): red, 5) **BrM**: light blue. Scale bar ~ 50 µm. We have rendered the boundaries of individual cells in A1-D1 as semi-transparent membranes. **POS**, **PIS** and **RPE** cells are rendered more transparent to show the underlying structures. See also Video S3-6.

		Typical Adhesion Scenario				
Early CNV	**Sub-classes**	*RRl*	*RRp*	*RBl*	*RBp*	*ROl*
Type 1	1	3	*	1,2	$RBl + RBp \leq 4$	3
	2	1	3	1	1,2	3
Type 2	1	3	*	2,3	*	1
	2	1	*	2,3	*	*
	3	1	$RBp + RRp > 3$	1	$RBp + RRp > 3$	1
Type 3	1	1	*	1,2	*	3

Table III-5. Adhesion Scenario Classification Based on Early **CNV** Type. Key: *RRl*: **RPE-RPE labile adhesion** strength, *RRp*: **RPE-RPE plastic coupling** strength, *RBl*: **RPE-BrM labile adhesion** strength, *RBp*: **RPE-BrM plastic coupling** strength, *ROl*: **RPE-POS labile adhesion** strength. Scaled adhesion strengths: 3: normal, 2: moderately impaired, 1: severely impaired (weak), *: all strength levels.

		Typical Adhesion Scenarios				
CNV Progression	**Sub-classes**	*RRl*	*RRp*	*RBl*	*RBp*	*ROl*

Dynamics						
S11	1	3	2, 3	1, 2	$3 \leq RBl + RBp \leq 4$	3
T12	1	3	$RRp + RBp \geq 4$ except $RRp = RBp = 2$	1	$RRp + RBp \geq 4$ except $RRp = RBp = 2$	1
P13	1	1	*	1	1, 2	3
S22	1	3	*	2, 3	*	1
	2	1	*	2, 3	*	*
	3	1	$RBp + RRp > 3$	1	$RBp + RRp > 3$	1
P23	1	1	1, 2	1	1	1
S33	1	1	*	2	$RBl + RBp \leq 4$	3
	2	1	*	1	3	3

Table III-6. Adhesion Scenario Classification Based on **CNV** Dynamics. To simplify, I list only the adhesion scenarios most prone to each type of **CNV** progression dynamics. Key: *RRl*: **RPE-RPE labile adhesion** strength, *RRp*: **RPE-RPE plastic coupling** strength, *RBl*: **RPE-BrM labile adhesion** strength, *RBp*: **RPE-BrM plastic coupling** strength, *ROl*: **RPE-POS labile adhesion** strength. Scaled adhesion strengths: 3: normal, 2: moderately impaired, 1: severely impaired (weak), *: all strength levels. See Table III-4, for nomenclature for **CNV** dynamics.

III.10 Discussion

My simulations show that variations in five key adhesion strengths suffice to explain many of the experimentally and clinically observed dependencies of CNV initiation on drusen, inflammation, retinal detachment and iatrogenic to reproduce the main observed types and progression dynamics of CNV associated with those defects.

Since pathological conditions can cause multiple adhesion failures in the BrM-RPE-POS complex, I simulated factorial combinations of graded impairments of the five adhesion types to explore the effects of biologically-coupled adhesion failures. In this section, I discuss the effects of both individual adhesion failures and their combinations on **CNV** initiation, **type** and **dynamics** and explain their clinical and experimental relevance.

Table III-1 aggregates a spectrum of clinical and experimental observations for a variety of conditions, with rough estimates of the degree of impairment of the three main inter-component adhesions present in the BrM-RPE-POS complex. Table III-1 also lists the most common types of CNV associated with each condition. In the section below, I compare clinical and experimental observations for these conditions to the results of my simulations for appropriate adhesion scenarios. Since I assume adhesion is constant over the duration of the simulation, to understand the effects of the gradual changes in adhesion which occur in patients as CNV develops, I must look successively at the results of multiple simulations for an appropriate series of adhesion impairments comparable at each time to those of the disease as it progresses.

III.11 Clinical and Experimental Types of CNV and their Relation to Simulations

III.11.1 *CNV Due to Soft Drusen in Older Humans*

As I discussed earlier (see section III.4), soft drusen significantly reduce the adhesion of the basement membrane of the RPE to BrM (RBaM-BrM adhesion). Sub-RPE CNV often starts by growing between these weakly adhered layers. Although soft drusen are seen clinically, the early stages of invasion of ECs into the sub-RPE space have little effect on visual acuity, so early EC invasions can remain unreported and unnoticed. In these patients, initial vision acuity prior to CNV initiation is not severely impaired compared to typical age-controlled visual acuity, suggesting that their photoreceptors remain healthy or at most moderately impaired compared to age-matched controls. Since the RPE plays multiple roles in maintaining both photoreceptors (*e.g.* through the phagocytosis of spent disks from the photo receptors) and the outer retina (*e.g.* through the transport of fluids), near-normal photoreceptors can only persist in the presence of near-normal RPE cells. Near-normal vision also requires that the POS remain attached to the RPE without accumulation of sub-retinal fluid or retinal detachment, indicating that RPE-POS adhesion must remain near-normal. Based on these observations, I hypothesize that in patients with soft drusen, both RPE-RPE and RPE-POS adhesion are near-normal, but BaM-BrM adhesion is impaired with the level of impairment differing patient-to-patient. This spectrum of adhesion impairments in the BrM-RPE-POS complex is comparable to the first sub-class of adhesions scenarios which are prone to **Early Type 1 CNV** (Table III-5). Within this sub-class, variation in the degree of adhesion impairment of **RPE-RPE** plastic coupling, **RPE-BrM** labile adhesion and **RPE-BrM** plastic coupling affects many aspects of **CNV** in simulations, including the **CNV** initiation probability, **CNV** onset time and **CNV** dynamics. Additionally, some adhesion scenarios in this class show significant variability among simulation replicas with identical adhesivities.

Patients with multiple large soft drusen or *confluent drusen* (*soft indistinct drusen*) have a higher chance of developing CNV [229], suggesting that CNV initiation probability depends on total area of drusen and their shape. In standard clinical usage, drusen with a diameter < 63 μm are called *small drusen* and those with a diameter > 125 μm are called *large drusen*. Confluent drusen or soft indistinct drusen form when multiple soft drusen touch and merge. Confluent drusen strongly correlate with CNV and serous RPE detachment due to fluid accumulation between BrM and the RPE, indicating severe impairment of RBrM-BrM adhesion due to the larger area of impaired RBrM-BrM adhesion and high lipid levels in the drusen affected regions. These experimental observations suggest that the probability of CNV initiation increases with both the degree and total area of RBrM-BrM adhesion impairment. In my simulations, the total area of impaired adhesion is the same in all replicas, so it does not affect the **CNV** initiation probability. However, the **CNV** initiation probability increases with the degree of impairment of **RPE-BrM junctional adhesion** in those adhesion scenarios exhibiting **ET1 CNV** (Table III-5, **ET1 CNV** first sub-class), supporting my experimentally-based hypothesis.

The locus of **stalk cells** in all simulation replicas of the first sub-class of **ET1 CNV** agrees with that in clinical and sub-clinical (sub-clinical CNV appears in histology but not clinically) sub-RPE CNV, the typical early CNV type in these patients. It also agrees with the appearance of drusen-like deposits and the initial stages of EC invasion into BrM observed in a fat-fed aged-mouse model (16 months old) exposed to non-phototoxic levels of blue light [167]. However, CNV did not progress in this mouse model [167].

While experimental and clinical results are incomplete, as I discussed above, they do suggest that patients with stable sub-RPE CNV do not suffer high rates of severe RPE detachment, indicating that their RBaM-BrM adhesion is not severely impaired. Among simulations with **ET1 CNV**, those in which **RPE-BrM junctional adhesion** is not too severely impaired (Table III-6, RBl =1 or 2 and $3 \leq RBl + RBp \leq 4$), exhibit **Stable Type 1 CNV**, agreeing with my interpretation of this clinical observation.

Since I hypothesize that more severe impairment of RBaM-BrM adhesion facilitates CNV spreading and progression, I expect higher variability of outcomes in patients with moderately impaired adhesion than in patients with severely impaired adhesion. In older patients, CNV progression timing and the size and growth rate of the CNV-affected area vary significantly patient-to-patient [126,230-232]. About one third of untreated sub-RPE CNV cases in older patients remain stable for extended periods of time (~ 30% remain stable 3 years after diagnosis). A slightly larger population of apparently similar patients progress to more damaging sub-retinal CNV in a short period of time (~ 40% develop sub-retinal CNV within the 12 months after diagnosis). According to a different study [230], sub-RPE CNV lesion size doubles in 12 months in ~ 30% of patients and quadruples in ~ 40% of patients and remained stable in the remainder. Such patient-to-patient variability corresponds closely to the variability I observe in **stalk cell** proliferation, **CNV** area growth and onset time in my corresponding simulations. As in clinical observations, simulations of adhesion scenarios with moderately impaired **RPE-BrM junctional adhesion** (Table III-6, RBl =1 or 2 and $3 \leq RBl + RBp \leq 4$,) have greater variability in stalk cell proliferation, CNV growth rate and

CNV onset time than simulations with severely impaired **RPE-BrM junctional adhesion** (Table III-5, *RRl* = 3, *RRp* = 3, *RBl* = 1, *RBp* = 1, *ROl* = 3). For example, in the 10 simulation replicas of an adhesion scenario with moderately impaired **RPE-BrM junctional adhesion** and all other adhesion normal (Table III-6, *RRl* = 3, *RRp* = 3, *RBl* = 2, *RBp* = 2, *ROl* = 3) (Figure III.8) nine out of ten replicas initiate **CNV**, but the total number of stalk cells after one simulated **year** shows a four-fold variation (from a minimum of 10 **stalk cells** to a maximum of 45 **stalk cells**) and the **CNV** onset time varies from a minimum of two **weeks** to a maximum of 4 **months** (after formation of the initial hole in **BrM**). For less impaired adhesion, when the **plastic** component of **RPE-BrM junctional adhesion** is severely impaired but the **labile** component is normal (Table III-13, *RRl* = 3, *RRp* = 3, *RBl* = 3, *RBp* = 1, *ROl* = 3), **CNV** initiates in only 30% of simulations, the initiation onset time is around 10 **months** (after formation of the initial hole in **BrM**) and the total number of **stalk cells** remains less than 6 in all replicas during the simulated **year**.

Overall, the **stalk cell** growth and proliferation rate among simulations that develop **ET1 CNV**, is slowest in those simulations exhibiting **S11 CNV** and fastest in those simulations exhibiting **P13 CNV**. The **stalk cell** division rate (the frequency of **stalk cell** division within the tissue) in **S11 CNV** ranges from one or two cell divisions per **year** to one cell division every 48 **hours**. The **stalk cell** division rate in **P13 CNV** is less variable, about one cell division every ~ 12 **hours** during **ET1 CNV** (Figure III.12A, the first **month** in most replicas). The long initiation delays and slow sub-RPE CNV development observed in some of my simulation replicas correspond to the slow sub-RPE CNV development and long-term CNV stability observed in a small population of patients (< 30% as mentioned in [232]). Fast-progressing **ET1 CNV** in some of these simulations agrees with the clinically-observed rapid increase in sub-RPE CNV size in a different set of otherwise similar patients. Based on the observed variability in **CNV** onset time and growth rate in my simulations and its dependence on the degree of adhesion impairment, I believe that the observed clinical patient-to-patient variability may result from both intrinsic stochasticity in certain adhesion regimes and from small patient-to-patient differences in the degree and type of adhesion impairments in the patient's BrM-RPE-POS complex.

In older patients, sub-RPE CNV may later also invade the sub-retinal space (sub-RPE CNV to CNV sub-retinal progression is a common CNV progression scenario). The factors involved in this transition are not well understood. Gradual degradation of the RPE due to sub-RPE hemorrhaging, formation of sub-RPE fibrosis and inflammation triggered by initial sub-RPE CNV are associated with this transition. The death of RPE cells during this degradation indicates that RPE-RPE adhesion is impaired. The rapid vision loss associated with the transition from sub-RPE CNV to sub-retinal CNV, indicates impaired RPE-POS adhesion, though, clinically, I do not know whether RPE-POS adhesion impairment is a cause or result of the transition. Thus these conditions imply impairment of **RPE-RPE junctional adhesion** and/or **RPE-POS labile adhesion** in addition to preexisting impairment of **RPE-BrM junctional adhesion** (due to lipid accumulation). Three classes of adhesion scenarios are relevant: 1) When both **RPE-POS labile adhesion** and **RPE-BrM junctional adhesion** are impaired, 2) when both **RPE-RPE** and **RPE-BrM junctional adhesion** are impaired, and 3) when **RPE-RPE junctional adhesion**, **RPE-POS labile adhesion**, **RPE-BrM junctional adhesion** are impaired. These three classes include all the sub-classes of adhesion scenarios leading to **T12 CNV**, **P13 CNV**, **S22 CNV**, **S23 CNV** and **S33 CNV**. These three classes never lead to **S11 CNV** (for definitions of the sub-classes of adhesion scenarios see Table III-6), suggesting that impairment of RPE-RPE and/or RPE-POS adhesion in addition to preexisting impairment of RBaM-BrM in patients is the primary mechanism leading to the sub-RPE CNV to sub-retinal CNV transition.

Clinically, adhesion strengths may change as CNV progresses. However my simulations show that P13 CNV progression can occur in patients even for time-independent adhesion. I can thus use my simulations to develop a prognosis for patients with sub-RPE CNV and in whom RPE-RPE and/or RPE-POS adhesion are impaired in addition to preexisting impairment of RBaM-BrM. Simulations that exhibit **ET1 CNV** and later invade the sub-retinal space in **P13 CNV** (Table III-6, $RRl = 1$, independent of RRp, $RBl = 1$, $RBp = 1$ or 2, $ROl = 3$) correspond to the most common clinically observed progression of AMD-induced CNV, which begins as sub-RPE CNV and later progresses to involve the sub-retinal space. Simulations with **T12 CNV** (Table III-6, $RRl = 3$, $RBl = 1$, $ROl = 1$, $RRp + RBp \geq 4$ except $RRp = RBp = 2$) do not appear to correspond to any standard clinical CNV progression dynamics, perhaps, because the transient nature of the sub-RPE to sub-retinal translocation makes its clinical detection difficult; I hypothesize that T12 CNV may be occurring but is not being diagnosed. Clinically, depending on the time of observation, T12 CNV could be diagnosed as sub-RPE CNV, Type 3 or sub-retinal CNV. Only frequent prospective eye examinations and long-term follow up can determine whether my prediction of clinical sub-RPE to sub-retinal translocations is correct.

Clinically, ET2 and ET3 CNV are not common in drusen-induced CNV in patients. However, the adhesion scenarios that exhibit **ET2** and **ET3** in my simulations might correspond to secondary CNV which develops later to a primary site of CNV in patients with pre-existing ET1 CNV. To explore the relevance of these scenarios, I could conduct simulations beginning with pre-existing **ET1 CNV** instead of a single **tip cell** in the **CC**. For example, I would expect the pre-existing **ET1 CNV** to translocate to the **sub-retinal** space when simulated in adhesion scenarios that exhibit primary **S22 CNV**. Such CNV dynamics would look like **T12 CNV** (discussed above). Clinically, this result implies that if I were to increase RBaM-BrM adhesion therapeutically (*e.g.* by extraction of lipids from BrM or by removing/reducing fluids between RBaM and BrM) in the presence of pre-existing sub-RPE CNV, stalk cells could translocate to the sub-retinal space in a transition to sub-retinal CNV. Since sub-retinal CNV is much more damaging to vision than sub-RPE CNV, this translocation would be a serious iatrogenic side effect. I can make similar analogies for the significance of simulated **S23 CNV** and **S33 CNV**.

Vascular RPE detachment caused by growth of CNV under the RPE is a common complication of sub-RPE CNV in AMD. I observe a corresponding pathology when **RPE-BrM junctional adhesion** is severely impaired (Table III-5, **Early Type 1** sub-class 1, $RBl = RBp = 1$). In this case, **Early Type 1 CNV** results in later **RPE** detachment, leading to either **T12 CNV** translocation or **P13 CNV** progression in conjunction with the formation of holes in the RPE (I will discuss late-stage CNV complications in detail in future papers).

III.11.2 *Inflammation-Induced CNV*

Sub-retinal CNV without prior diagnosed sub-RPE CNV occurs, but is not as common in older patients as drusen-induced CNV [233]. It also occurs in young patients in conjunction with acute inflammatory conditions, particularly in cases of serpiginous choroidopathy, multifocal choroiditis and panuveitis [214]. The mechanisms leading to this type of CNV are not well understood and I lack clinical insight into how specific risk factors affect the probability of CNV initiation. Younger patients usually lack both drusen [214] and significant dispersed build up of lipids in BrM. As I discussed earlier active inflammation reduces RPE-RPE epithelial adhesion. Alteration of RPE-RPE epithelial adhesion combined with edema due to active inflammation may also reduce RPE-POS adhesion. I do not know whether inflammation always impairs RPE-RPE and RPE-POS adhesion at the same time, or to the same degree. Since CNV initiation occurs promptly during acute inflammation, I do not expect acute inflammation to decrease RBaM-BrM adhesion significantly. Thus, in young patients inflammation both RPE-RPE epithelial adhesion and RPE-POS adhesion are impaired, but not RBaM-BrM adhesion. This adhesion impairment corresponds to impairments of **RPE-RPE junctional adhesion** and **RPE-POS labile adhesion**, while **RPE-BrM junctional adhesion** is near-normal (Table III-5, **Early Type 2 CNV** sub-class 1 and 2). Simulations of these adhesion scenarios consistently exhibit **Early Type 2 CNV** (**ET2 CNV**), in which **stalk cells** initially invade the **sub-retinal** space without prior invasion of the **sub-RPE** space, in agreement with clinically-observed sub-retinal CNV in these patients.

In my simulations, when **RPE-RPE labile adhesion** is severely impaired and all other adhesions are normal (*RRl* = 1, *RRp* = *RBl* = *RBp* = *ROl* = 3) (Table III-20, adhesion parameter set ID: 10) **CNV** always initiates, followed by **Early Type 2 CNV** (**ET2 CNV**). When **RPE-POS labile adhesion** is severely impaired and all other adhesions are normal (*RRl* = *RRp* = *RBl* = *RBp* = 3, *ROl* = 1) (Table III-20, adhesion parameter set ID: 19), the **CNV** initiation probability is 50% and initiation always leads to **ET2 CNV**. When both **RPE-RPE junctional adhesion** and **RPE-POS labile adhesion** are impaired **CNV**, always initiates and leads to **ET2 CNV** (see also Figure III.6, for more information on how **sub-retinal CNV** depends on adhesion). My results make two predictions that can be tested against clinical and experimental observations: 1) Disruption of RPE-RPE epithelial junctions, due to inflammation, by itself should lead to sub-retinal CNV in patients with a relatively intact retina, independent of any defects in RPE-POS adhesion 2) Disruption of RPE-POS contact, by itself, should increase the probability of developing sub-retinal CNV.

My understanding of CNV dynamics in young patients is incomplete. Neither sub-retinal CNV to sub-RPE CNV progression (P23 CNV) nor sub-retinal CNV to sub-RPE CNV translocation (T21 CNV) has been observed clinically or histologically (since CNV is not fatal, histological data for young patients with CNV is rare). I currently do not know whether this absence of observation is due to major retinal damage due to sub-retinal CNV, which precludes the later transition (and is not included in my model), or whether Late Type 1 CNV is simply overlooked clinically because sub-retinal CNV causes much more severe vision loss. My simulations make three predictions relevant to inflammation-induced CNV in young patients: 1) If **RPE-BrM adhesion junctional** is near normal (*RBl* = 2 or 3, independent of *RBp*) any combination of severely impaired **RPE-RPE junctional adhesion** (*RBl* = 1, independent of *RBp*) and **RPE-POS labile adhesion** (*ROl* = 1) will exhibit **Stable Type 2 CNV**. 2) When all adhesions are severely impaired (*RRl* = *RBl* = *RBp* = *ROl* = 1, *RRp* = 1 or 2), **Sub-retinal CNV** to **sub-RPE CNV** progression (**P23 CNV**) will occur. 3) **Sub-retinal CNV** to **sub-RPE CNV** translocation (**T21 CNV**) is unlikely. These predictions mean that once CNV invades the sub-retinal space, it will not leave this space, so CNV lesions will expand primarily in the sub-retinal space as long as RBaM-BrM is not severely impaired.

Chemotoxicity (10% solution of naphthalene force-fed by gavage for 5 weeks) in a rabbit model [215] causes degradation of photoreceptors and proliferation of RPE leading to sub-retinal CNV. In this rabbit model, the RPE cells proliferating phagocytose damaged photoreceptors during the first three weeks. Sub-retinal CNV follows about 3 months after the beginning of treatment. Because RPE cells with normal epithelial adhesion do not proliferate, I hypothesize that chemotoxicity in this animal model reduces RPE-RPE epithelial adhesion, allowing RPE cells to proliferate. Since the photoreceptors are damaged, I infer that RPE-POS adhesion is severely disrupted. BrM remains intact for the first 3 weeks of treatment. Initial signs of BrM invasion by RPE cells and ECs appear about 3 months after the beginning of treatment. Due to newly synthesized extracellular matrix at the location of the CNV, the RPE basement membrane and BrM become irregular after 6 months, with bundles of extracellular microfilaments connecting RPE basement membrane to BrM. These modifications of the RPE basement membrane and BrM, suggest that RBaM-BrM adhesion is initially normal and gradually decreases to moderately impaired over a period of six months. These adhesion impairments resemble adhesion impairments in younger patients with inflammation. For these adhesion scenarios (Table III-5, **Early Type 2 CNV** sub-class 1 and 2) my simulations always predict early **sub-retinal CNV**, in agreement with experiments.

III.11.3 *Iatrogenic CNV*

Iatrogenic sub-retinal CNV may develop after laser photocoagulation treatment of diabetic macular edema, central serous retinopathy, proliferative diabetic retinopathy, choroidal vascular and neoplastic lesions, vascular occlusive disease and degenerative retinal-pigment-epithelium disorders (reviewed in [234]). Some believed that the primary mechanism for such iatrogenic induction of sub-retinal CNV to be the creation of breaks in Bruch's membrane, with inflammatory cells, angiogenic factors and choroidal ischemia contributing to the development of CNV in some cases [234]. However, I believe that RPE phototoxicity due to excess (focal) laser exposure is more likely primary cause. Phototoxicity stresses RPE cells which can decrease RPE-RPE epithelial adhesion and RPE-POS adhesion and also promote excess expression of VEGF-A by RPE cells. This condition of pathologies is similar to those caused by inflammation, so I would expect these classes of iatrogenic CNV to resemble inflammation-induced CNV, as is indeed observed.

III.11.4 *Sub-Retinal Drusenoids*

Sub-retinal drusenoid deposits have components similar to that of soft drusen but are located in the subretinal space between the RPE and POS [235]. In more advanced stages, drusenoids form small mounds which can contact the PIS. The mechanisms of formation of sub-retinal drusenoids are not well understood. Some have hypothesized that the RPE loses its polarization, impairing the normal apico-basal transport of waste products. However, unlike normal drusen, sub-retinal drusenoids do not contact serum which leaks from the normal CC and do not contain unesterified cholesterol [209], so any loss of RPE polarization must not significantly impair the integrity of TJs between RPE cells (otherwise they come into contact with serum leaking from the CC through the RPE layer and accumulate unesterified cholesterol). Location of sub-retinal drusenoids does not correlate with sub-RPE deposits [235]. Sub-retinal drusenoid deposits occur in older patients with AMD and correlate strongly with both CNV and geographic atrophy [210,211,213]. In 100 patients, average age ~ 72 years old, with sub-retinal drusenoid and any type of AMD, 66% had CNV or develop CNV within 3 years [211]. In another study [213] of 100 patients newly diagnosed CNV, average age ~ 72 years old, 24% had sub-retinal drusenoids, 32% classic CNV, 41% occult CNV or 11% exhibited vascularized pigment epithelial detachment, 13% retinal angiomatous proliferation with or without PED and 3% hemorrhagic or fibrovascular scarring.

These observations suggest that sub-retinal drusenoids mainly impair the RPE-POS adhesion, while loss of RPE polarization impairs RPE-RPE epithelial adhesion. In my simulations these adhesion impairments would correspond to severely impaired **RPE-POS labile adhesion**, normal to severely impaired **RPE-BrM junctional adhesion**, and moderately to severely impaired **RPE-RPE junctional adhesion**, which can lead to three distinct types of CNV dynamics: 1) **T12 CNV** (Table III-6, $RRl = 3$, $RBl = 1$, $ROl = 1$, $RRp + RBp \geq 4$ except $RRp = RBp = 2$) , 2) **S22 CNV** (all three sub-classes of **S22 CNV**, Table III-6), 3) **P23 CNV** (Table III-6, $RRl = RBl = ROl = RBp = 1$, $RRp = 1$ or 2). My simulations of patients with sub-retinal drusenoids predict that: 1) the CNV initiation probability is 50% when RPE-POS adhesion is severely impaired and both RPE-RPE epithelial adhesion and RBaM-BrM are near normal 2) the early type of CNV will be either Type 1 or Type 2, never Type 3, 2) Early Type 1 CNV will always progress to the sub-retinal space. Development of **ET1 CNV** and **ET2 CNV** agrees with observed occult and classical CNV [213]. As I previously discussed **T12 CNV** and **P23 CNV** do not correspond to classical clinically observed types of CNV progression. I look forward to additional clinical and histological data on patients with sub-retinal drusenoid to allow a more extensive comparison with my simulations.

III.11.5 *CNV due to Sub-retinal Injections in Animal Models*

Subretinal injections in most animal models (Table III-1) lead to sub-retinal CNV adjacent to the site of injection within weeks, but not to sub-RPE CNV [216-218]. CNV initiation probability depends on the type and amount of material injected (Matrigel, polystyrene beads suspended in liquid, vitreous humor, …) (see [212], for a detailed review). Secondary sub-RPE CNV may follow sub-retinal CNV in some animal models, *e.g.*, in a rabbit model [219], a sub-retinal injection of a cocktail containing endotoxins and growth-factors, incorporated in heparin-sepharose leads rapidly to primary sub-retinal CNV and secondary sub-RPE CNV forms farther from site of injection between 2 weeks and 8 months later [219]. The mechanisms leading to this secondary sub-RPE CNV are not well understood. Ni et al. [219] believed that the major factors were changes in RPE cell function due to diffusion of soluble mediators originating from the area of primary CNV, *e.g.* from atrophied primary RPE cells or newly-formed activated secondary RPE cells or changes in function of endothelial cells, photoreceptors and Müller cells in regions peripheral to the primary CNV, *e.g.*, increased expression of FGF-1, FGF-2, TGF-alpha and VEGF.

Subretinal injections can cause acute physical retinal detachment, instantaneously destroying RPE-POS contact at the site of injection. However, RPE active pumping and passive flow gradually remove the excess sub-retinal fluid, allowing the retina to reattach within a few days. Sub-retinal injection also almost always induces significant inflammation, which gradually reduces RPE-RPE epithelial adhesion over a period lasting a few days to a few weeks. Such condition of transient detachment and followed by long-lasting inflammation induces RPE migration [216] and proliferation [219] (*RPE activation*). Because RPE cells neither proliferate nor migrate when they are in epithelium and RPE-RPE epithelial adhesion remain normal, the combination of RPE migration and proliferation suggest that RPE-RPE epithelial adhesion may decrease significantly over a period of a few days to a few weeks. Inflammation can also cause the death of photoreceptors [215], suggesting prolonged disruption of RPE-POS contact. Sub-retinal injections can also directly cause focal rupture in all layers of BrM, suggesting that RBaM-BrM adhesion is initially (near) normal at least far from the location of the rupture.

Based on these experimental observations, sub-retinal injections appear mainly to impair RPE-RPE and RPE-POS adhesion comparable to the adhesion scenarios prone to **Early Type 2 CNV** (Table III-5, **Early Type 2 CNV** sub-class 1 and 2) and in inflammation-induced CNV in younger patients. Thus my simulations both agree with the cause, initiation and progression of sub-retinal CNV in these animal models.

My simulations predict that for secondary sub-RPE CNV to develop near a pre-existing sub-retinal CNV RPE-BrM (RBaM-BrM) adhesion must be severely impaired, to develop, independent of the degree of impairment of other types of adhesion in the BrM-RPE-POS complex. To validate my prediction, experiments would need to examine in detail the interface between BrM and the RPE basement membrane in retinal regions far from site of injection and before any initiation of sub-RPE CNV.

In these animal models, sub-retinal injection often causes rapid (less than a month) CNV initiation. I can infer that injection impairs RPE-RPE adhesion because of observed inflammation and RPE proliferation and RPE-POS adhesion because of photoreceptor degradation [215,216,219]. In agreement with these experiments, my simulations show that severe impairment of **RPE-RPE labile adhesion**, when all other adhesions are normal (*RRl* = 1, *RRp* = *RBl* = *RBp* = *ROl* = 3) (Table III-20, adhesion parameter set ID: 10), increases the probability of **CNV** initiation within a **month** to 100%. In my simulations prolonged impairment of **RPE-POS labile adhesion** when all other adhesions are normal (*RRl* = *RRp* = *RBl* = *RBp* = 3, *ROl* = 1) (Table III-20, adhesion parameter set ID: 19) increases initiation probability to 50%, higher than observed for experimental RPE-POS detachment. This discrepancy may result from the long (up to six **month**) onset time for **CNV** in this adhesion scenario. Six months is much longer than the CNV initiation time due RPE-RPE adhesion impairment and the typical time for retinal reattachment and is too long to see in most experiments. Experiments exploring the effects of RPE-POS adhesion impairment on CNV would need to disrupt

RPE-POS adhesion for several months without inducing severe inflammation, *e.g.* by sub-retinal injection of neutral polystyrene microbeads (coated with anti-inflammation compounds).

III.11.6 *The nature of The BrM-RPE-POS complex barrier to CNV (activated ECs)*

As I discussed earlier (see section III.6.4), activated endothelial cells are present in the normal choriocapillaris, so the frequency of ECs crossing BrM is significant even in the normal eye. Clinically, the probability of CNV initiation before age 50 in a normal retina is negligible. My adhesion-based hypotheses for CNV initiation and progression may resolve this discrepancy. In simulations when all adhesions are normal (referenced to a normal human eyes aged less than 50 years old) activated **ECs** and small holes in **BrM** never initiate CNV, suggesting that strong adhesion among BrM-RPE-POS components is the crucial mechanism preventing activated **ECs** from invading the **sub-RPE** and **sub-retinal** space once they have crossed BrM.

III.11.7 *Comments*

My current simulations study worst-case scenarios. My simulated initiation probabilities are higher than observed in the experiments due to two simplifying assumptions of my model: 1) I assumed that all **stalk cells** can divide indefinitely. Limiting the number of **stalk-cell** divisions (due to senescence), would lower the probability of CNV initiations. In *in vitro* experiments, less than 2% of endothelial cells have high proliferation potential [236,237], so angiogenic sprouts may fail to grow, or even regress, if the ECs forming the sprouts have low proliferation potential. 2) I assumed that **stalk cells** adhere equally to both sides of **BrM**. BrM and CC basement membrane are histologically distinct, modeled **BrM** includes cells' basement membranes. In experiments, ECs haptotax to the basement membrane of the CC on the outer side of BrM (Figure III.2). In my model, strong chemotaxis to **RPE-derived VEGF-A** promotes **stalk cells** invasion of the **sub-retinal** and **sub-RPE** spaces. Increasing the adhesion between **stalk cells** and the **CC**-side of **BrM** would reduce the **CNV** initiation probability, since **stalk cells** would prefer to remain on the **CC**-side of **BrM**, where contact with the preexisting vasculature would inhibit their growth.

In experiments, ocular hypoxia caused by systemic hypoxia usually promotes retinal angiogenesis, but has no observed effect on the RPE and does not induce choroidal angiogenesis (reviewed in [139]). I do not know what levels of PO_2 can trigger hypoxic signaling by RPE cells. Based on experimentally-measured parameters, my simulations show that the PO_2 at the RPE decrease from ~ 65 mmHg to ~ 49 mmHg when the PO_2 at the CC decreases from 80 mmHg to 60 mmHg during systemic hypoxia in the anatomically normal retina (under light-adapted condition). If I assume that biological RPE cells are hypoxic during systemic hypoxia, then the PO_2 below which RPE cells become hypoxic is 49 mmHg. However, PO_2 ~ 50 mmHg is significantly higher than both PO_2 ~ 20 mmHg, the typical PO_2 in the inner retina and PO_2 ~ 1 mmHg, the PO_2 at which mitochondria work at their maximum metabolic rate. In my simulations, **RPE cells** become hypoxic ($PO_2 < 49$ mmHg) only after **RPE** detachment, a CNV-associated complication which I will discuss in a future paper. Thus neither the threshold for RPE hypoxia nor RPE hypoxic signaling affect the results I present in this chapter.

In transgenic mice with inducible expression of VEGF in their RPE cells, induction of excess VEGF only induces CNV if combined with sub-retinal injections which disrupt the RPE [192]. In my simulations, when **RPE** overexpresses **RPE-derived VEGF-A** at twice the normal level, the probability of CNV initiation increases (data not shown), but the **Early CNV** types and **CNV** dynamics do not change. Thus, my simulations show that VEGF overexpression can increase the CNV initiation probability, but does not determine either the early or late CNV loci.

I have previously discussed the role of active inflammation in altering adhesion in the BrM-RPE-POS complex; I now consider how local cytokines and growth factors that can increase the chemotactic activity of endothelial cells could affect CNV initiation and progression. My current simulation did not explore the role of these inflammation-associated factors on the chemotactic activity of ECs directly, however, based on my simulations using different VEGF-A levels, I expect that increased chemotactic activity of **stalk cells** will increase the **CNV initiation** probability, as in my simulations in which **RPE** expresses **RPE-derived VEGF-A** at twice the normal level. I also expect that if the inflammation-associated factors are short-diffusing and thus form local gradients, they can promote sub-RPE CNV if their source is localized in the sub-RPE space or promote sub-retinal CNV if their source is localized in the sub-retinal space. If the inflammation-associated factors are long-diffusing, I expect that the resulting global increase in chemotactic activity of **stalk cells** would not affect either early or late CNV loci, only the probability of initiation and the rate of progression.

In most pathological conditions, POS degradation and disruption of RPE-POS adhesion usually precede impairment of both RPE-RPE epithelial adhesion and RBrM-BrM adhesion, thus my adhesion scenarios with impaired **RPE-RPE** and **RPE-BrM junctional adhesion** and normal **RPE-POS labile adhesion** are physiologically unlikely. However, if I were able to induce these scenarios in an experiment, I would expect direct initiation of Stable Type 3 since, in my simulations, I always obtain **Stable Type 3 CNV**; *i.e.* stalk cells invade both the **sub-RPE** and **sub-retinal** spaces during first three months after initiation and remain in both loci throughout the simulated **year**.

I modeled the complex phenomena of epithelial adhesion between RPE cells, *i.e.* the ensemble of AJs, TJs, desmosome plaques and gap junctions, as **junctional adhesion**, a combination of **labile adhesion** at **cell** boundaries and **plastic coupling** between neighboring **RPE** cells. I explored adhesion impairments combinatorially with either one (*asymmetric*) or both (*symmetric*) components of the modeled **junctional adhesion** moderately or severely impaired. I can represent adhesion in aged or damaged RPE cells using symmetrical adhesion impairment, since all cellular processes are impaired in such cells. I can represent adhesion strength in young, but disturbed RPE cells, *e.g.* after sub-retinal injection in animals, using asymmetrical adhesion impairment. I are agnostic as to which junctional components asymmetric adhesion impairment affects. Indeed, multiple mechanisms could contribute to asymmetric impairment: 1) Microenvironmental conditions may differentially affect the strength of epithelial-junction components (AJs, TJs, …). For example, calcium-depletion greatly reduces the strength of AJs, but not of desmosome. I represent this class of adhesion impairment by moderately impaired or severely impaired **labile adhesion** and normal or moderately impaired **plastic coupling**, requiring that **labile adhesion** be more severely impaired than **plastic coupling**. 2) Different epithelial-junction components may assemble and disassemble at different rates. For example, when cultured epithelial cells reach confluency, N-cadherin accumulates at RPE-RPE contacts, after which N-cadherin organizes into AJ bands when as the cells form an epithelium. TJs and other junctional structures from later. In some diseases, young RPE cells express N-cadherin, but do not form other junctional components, so a normal RPE (epithelium) fails to form. I represent such condition by near-normal **labile adhesion** and impaired **plastic coupling** between **RPE** cells.

Simulations of adhesion scenarios exhibiting **P13** or **S22 CNV** appear to reach their final number of **stalk cells** and spatial **stalk cell** distribution (loci) within one simulation **year**. However, the total number of **stalk cells** in my simulation replicas exhibiting **S11 CNV** sometimes remain less than the maximal number of 45 cells (3000 **cells**/mm^2) throughout the simulated **year**. I expect that if I were to run these simulations for longer periods, most simulation replicas would develop fully-grown **sub-RPE** capillaries containing about 45 **cells**, which would fill the **sub-RPE** space at a normal **CNV** capillary density. For adhesion scenarios in which some replicas exhibit slow transitions or late onsets (*e.g.* **T12 CNV**, Figure III.10B, replica # 6, purple line) the simulation duration of a **year** may not always be sufficient to exhibit the long-time behavior in every case. An initiation time greater than one simulated **year** may also explain why adhesion scenarios that predominantly exhibit **T12 CNV** also show **Stable Type 1 CNV** for some simulations replicas (Figure III.10B, replica # 10, dark blue line). Endothelial cells use long thin filopodial processes (from 5 µm to 100 µm in length) to explore their microenvironment, increasing their ability to find defects in the BrM-RPE-

POS complex and regions with higher VEGF concentrations. The adhesive interaction of modeled **stalk cells** have a range of the sum of the **membrane fluctuation range** of 6 µm (2 **pixels**) and the **adhesion interaction range** of 6 µm (2 **pixels**) (see, section III.13). The range of chemotaxis interactions is the maximum **membrane fluctuation range** of 6 µm (2 **pixels**). Thus the simulated interaction ranges are smaller than the experimental ranges. However, their difference may be less significant than it first appears, because in my simulations the average thickness of the **RPE** layer is 12 µm, so a **stalk cell** next to **RPE** still can explore the **sub-retinal** space via both adhesion and chemotaxis, as in experiments.

III.12 Future Directions and Suggestions

My current model does not include several mechanisms which may also be important to CNV. In future refinements, I will include multiple types of basal deposits and fibrosis (synthesis of new ECM) explicitly to clarify their role in the initiation and progression of CNV. I particularly are interested in how differences in the size and structure of soft and hard drusen affect the initiation and progression of CNV and the frequency of occurrence of RPE detachment and RPE tear formation after therapeutic intervention to treat CNV.

Many hypothesized mechanisms for CNV initiation and progression involve irregularities in transport. I plan more realistic models including capillary maturation, blood flow and retinal-CC fluid flow to study how oxygen, nutrient and waste transport promote or inhibit CNV.

Since cell adhesion is essential to multicellularity and is important in embryonic development, homeostatic maintenance of adult tissues and diseases like cancer, its importance in CNV is, perhaps, not surprising, given CNV's many parallels with tumor-induced angiogenesis. However, *the role of adhesion in CNV has not been widely appreciated*, so neither the relationship between known CNV risk factors and specific adhesion failures, nor the actual adhesivities in the retina and RPE have been quantified experimentally. Quantitative measurements of these adhesion properties and their regulation in the normal and pathological retina would allow more clinically relevant models. Such experiments would greatly reduce uncertainty in my model definition, improve my understanding of CNV initiation and progression. Since measuring adhesivities directly may be difficult, especially in humans, my model also allows us to quantify adhesion failures by looking at how they affect CNV initiation and progression and matching those computational outcomes with experimental observations, then correlating the simulated adhesion changes with experimental risk factors.

Beyond retinal CNV, my results on CNV initiation and epithelial breakdown apply to any tissue in which a basement membrane separates a capillary network from a nearby epithelium, *e.g.* lung and gut. I expect that the relationships between specific classes of adhesion failures and the loci and dynamics of CNV which I observe in my simulations should carry over to the neovascularization-dependent pathologies of those tissues.

Ultimately, a database of verified simulations for different adhesion scenarios might allow systematic CNV prediction based on clinically-measurable properties of the eye, especially if the adhesion properties can be inferred noninvasively, *e.g.* by measuring optically, changes in CC or RPE morphology or autofluorescence due to lipid accumulation. In the absence of direct measurements of adhesivity, my simulations allow us to infer adhesion defects from pathologies. For example, if a patient with a functional retina exhibits micro-detachments of the RPE (due to lipid accumulation or small soft drusen), the relationship between the number and degree of detachments and the underlying classes of adhesion failures predicts the probability of CNV initiation and the distribution of CNV onset times, making clinically-useful suggestions for frequency of follow-up examinations and possible prophylactic interventions. To aid diagnosis and treatment I can also develop statistical analyses of the most significant scenarios capable of producing the observed pattern of disruption in each patient (including the probability of initiation, the time of onset of progression and progression speed,…). Follow-up observations could then narrow the range of admitted hypothetical scenarios to improve the accuracy of the prognosis. More accurate diagnoses may improve both administration of drugs and disease management.

One crucial aspect of a model-based approach to CNV diagnosis, prognosis and treatment is that both the simulation database and the statistical predictors could be continuously refined using feedback from both clinical and histopathological sources, so they would improve with use, providing a platform to integrate clinical and histopathological data for even more accurate diagnosis and prognosis.

III.13 Methods

III.13.1 *The Glazier-Graner-Hogeweg Method*

My simulations use the Glazier-Graner-Hogeweg model (*GGH*, also known as the Cellular Potts Model, *CPM*), a multi-cell, lattice-based, stochastic methodology which describes biological cells and their interactions in terms of *Effective Energies* and constraints [35]. GGH applications include models of vascular tumors [157], avascular tumor growth [114], biofilms [238], chick limb growth [239], somitogenesis [240], blood flow and thrombus development [241] and angiogenesis [1,22,226,242].

Each simulated generalized **cell** consists of a domain of *lattice sites*, or *voxels*, at locations $\vec{i}$, sharing the same *cell index,* σ, in a *cell-lattice*. Each **cell** has an associated *cell type*, τ. Any material object, including biological cells, subcompartment of biological cells, ECM or fluid medium can be represented by one or more generalized **cells**. My simulations employ several types of generalized **cell** which represent entire biological cells, two which represent clusters of compartments of biological cells (**PIS** and **POS**), one which represents the extracellular fluid medium (**medium**) and one which represents small amounts of BrM (**BrM**). The *Effective Energy* governs changes in the **cell-lattice** configuration. I describe the concentration of secreted morphogens and oxygen within the cells, medium and ECM macroscopically by concentration **fields** discretized at the resolution of the **cell-lattice**. **Fields** evolve according to partial-differential equations (*PDEs*) describing their diffusion, secretion, absorption and decay.

III.13.2 *Motility, Labile adhesion, Volume and Surface Area*

The basic GGH *Effective Energy* describes **cells** that have constrained volumes and surface areas interacting via **labile differential adhesion**:

$$H = \sum_{\substack{\vec{i},\vec{j} \\ \text{neighbors}}} J\left(\sigma\left(\vec{i}\right),\sigma\left(\vec{j}\right)\right)\left(1-\delta\left(\sigma\left(\vec{i}\right),\sigma\left(\vec{j}\right)\right)\right)+$$
$$\sum_{\substack{\sigma \\ \text{cells}}}\left[\lambda_{\text{vol}}\left(\sigma\right)\left(v\left(\sigma\right)-V_{\text{t}}\left(\sigma\right)\right)^2+\lambda_{\text{surf}}\left(\sigma\right)\left(s\left(\sigma\right)-S_{\text{t}}\left(\sigma\right)\right)^2\right], \tag{3.1}$$

where $v\left(\sigma\right)$ is the total number of lattice sites in **cell** σ, which is constrained to be close to the target volume $V_{\text{t}}\left(\sigma\right)$ (*i.e.*, deviation of $v\left(\sigma\right)$ from $V_{\text{t}}\left(\sigma\right)$ increases the *Effective Energy*), and $\lambda_{\text{vol}}\left(\tau\left(\sigma\right)\right)$ is the inverse compressibility of **cell**s of type τ. Similarly, $\lambda_{\text{surf}}\left(\tau\left(\sigma\right)\right)\left(s\left(\sigma\right)-S_{\text{t}}\left(\sigma\right)\right)^2$ constrains the surface area of **cell** σ, $s\left(\sigma\right)$ to be close to the target surface area $S_t(\sigma)$. $J\left(\tau\left(\sigma\left(\vec{i}\right)\right),\tau\left(\sigma\left(\vec{j}\right)\right)\right)$ is the contact energy per unit area between **cells** $\sigma\left(\vec{i}\right)$ and $\sigma\left(\vec{j}\right)$. Higher (more positive) contact energies between **cells** result in greater repulsion between the **cells** and lower (more negative) contact energies between **cells** result in greater adhesion between the **cells**. $2\lambda_{\text{vol}}\left(\tau\left(\sigma\right)\right)\left(V_{\text{t}}\left(\sigma\right)-v\left(\sigma\right)\right)$ is the internal pressure in **cell** σ.

To simulate the cytoskeletally-driven reorganization of **cells** and tissues, I model **cell** protrusions and retractions using a *modified Metropolis dynamics*. For each attempt of a **cell** to *displace* a neighbor, I select at random a **cell** boundary (*source voxel*) and a neighboring *target voxel* and calculate the change in the Effective Energy ΔH_{GGH}, if the source **cell** displaced the target **cell** at that voxel. If ΔH_{GGH} is negative, *i.e.*, the change is energetically favorable, I make it. If ΔH_{GGH} is positive, I accept the change with probability $e^{-\Delta H_{GGH}/T}$, where T describes the amplitude of cytoskeletal fluctuations in the **cells**. In my CNV simulations, all **cells** of a certain type have the same intrinsic motility $T\left(\tau\left(\sigma\right)\right)$. On a lattice with N sites, N displacement attempts represent my basic unit of time, one *Monte Carlo Step* (*MCS*). One MCS corresponds to 216 seconds (see *Simulation Parameters and Initial Configuration*).

I define a special, generalized **cell** representing the extracellular medium (**medium**). The total volume and surface area of **medium** are not constrained. **Medium** voxels can be both source voxels, *e.g.* during retraction of the trailing-edge of a **cell**, and target voxels, *e.g.* during formation of lamellipodia. Since **medium** does not have cytoskeletal fluctuations, I use the amplitude of cytoskeletal fluctuations of the non-**medium** target or source **cell** to determine the acceptance of a displacement involving **medium**.

I define a special, generalized **cell** representing a small volume of BrM (**BrM**). **BrM** generalized **cells** occupy one voxel and their total volume and surface area are constrained. I set both λ_{vol} and λ_{surf} for **BrM** very large and T for **BrM** to zero, so the ensemble of **BrM cells** behaves like a solid non-diffusing material. Biological BrM is modeled by a set of **BrM cells**/voxels arranged on a pair of flat quasi-two-dimensional layers, each one voxel thick.

III.13.3 *Plastic Coupling*

In the GGH model, **plastic coupling** simulates cytoskeletally-coupled junctional structures (*e.g.* TJs, AJs and desmosomes) as breakable linear springs that mechanically connect the centers-of-mass of neighboring **cells** and or of **cells** to adjacent regions of **BrM**:

$$H_{\text{plastic}} = \sum_{\text{links}} \lambda_{\text{plastic}}\left(\tau(\sigma),\tau(\rho)\right)\left(\ell(\sigma,\rho)-\ell_{\text{target}}(\sigma,\rho)\right)^2, \tag{3.2}$$

where $\ell(\sigma,\rho)$ is the distance between the centers-of-mass of the neighboring generalized **cells** σ and ρ, $\ell_{\text{target}}(\sigma,\rho)$ is a target length defining the unstretched distance between the objects and $\lambda_{\text{plastic}}\left(\tau(\sigma),\tau(\rho)\right)$ is the spring constant of the links that depends on the type of generalized **cells** σ and ρ (Table III-12). I calculate $\Delta H_{\text{plastic}}$ for each displacement attempt and add it to the change in the Effective Energy ΔH_{GGH}. For small displacements, equivalent to small stress, H_{plastic} constrains $\ell(\sigma,\rho)$ to be close to $\ell_{\text{target}}(\sigma,\rho)$. However, a link breaks whenever its $\ell(\sigma,\rho)$ reaches twice its target equilibrium (unstretched) length, so a material composed of generalized **cells** coupled by such links is *quasi-plastic* or *plastic*. The total number of such links for each **cell** is limited to a certain number depending on type of **cells** σ and ρ. For example, an **RPE** cells can form up to 6 links with its neighboring **RPE cells** and up to 6 links with **BrM**. When a link breaks both generalized **cells** to which it connected can form a new link with their neighbors with a probability, depending on an *activation energy* that I add to ΔH_{GGH}. Large negative activation energies increase the probability of formation new links. The target equilibrium lengths of new links are prespecified. I increase the target equilibrium length between **stalk cells** and other **ECs** as **stalk cells** grow (see *Growth, Proliferation and Death*).

III.13.4 *Fields*

I represent **RPE-derived VEGF-A** as a **field** $V_{\text{L}}\left(\vec{x}\right)$ with units of molecules per µm^3, which diffuses with diffusion coefficient $D_{\text{VEGF}}^{\text{RPE}}$ everywhere and decays at a rate γ_{VEGF}. **RPE cells** secrete **RPE-derived VEGF-A** into $V_{\text{L}}\left(\vec{x}\right)$ uniformly at all their voxels at a constant basal rate $SV_{\text{basal}}^{\text{RPE}}$ (molecules per voxel per 216 seconds) during normoxia. During hypoxia (for a definition, see the *Simulation Parameters and Configuration* section below) individual **RPE cells** secrete **RPE-derived VEGF-A** into the **RPE-derived VEGF-A field** at a higher rate, $SV_{\text{max}}^{\text{RPE}}$ (molecules per voxel per 216 seconds). I assign hypoxic **RPE cells**, to the **HRPE cell type**. **Vascular cells** in my model take up **RPE-derived VEGF-A** from the concentration **field** uniformly at a constant rate QV_{EC} (molecules per voxel per 216 seconds). Both **stalk cells** and the **tip cell** take up twice as much **RPE-derived VEGF-A** per voxel per unit time as **vascular cells**. So $V_{\text{L}}\left(\vec{x}\right)$ evolves according to:

$$\frac{\partial V_{\mathrm{L}}\left(\vec{x}\right)}{\partial t} = D_{\mathrm{VEGF}}^{\mathrm{RPE}} \nabla^2 V_{\mathrm{L}}\left(\vec{x}\right) - \gamma_{\mathrm{VEGF}}\, V_{\mathrm{L}}\left(\vec{x}\right) + S\left(\vec{x}\right) - Q\left(\vec{x}\right),$$
$$S\left(\vec{x}\right) = SV_{\mathrm{basal}}^{\mathrm{RPE}}\, \delta\left(\tau\left(\sigma\left(\vec{x}\right)\right), \mathbf{RPE}\right) + SV_{\mathrm{max}}^{\mathrm{RPE}}\, \delta\left(\tau\left(\sigma\left(\vec{x}\right)\right), \mathbf{HRPE}\right),$$
$$Q\left(\vec{x}\right) = QV_{\mathrm{EC}}\left(\delta\left(\tau\left(\sigma\left(\vec{x}\right)\right), \mathbf{CC}\right) + 2\,\delta\left(\tau\left(\sigma\left(\vec{x}\right)\right), \mathbf{CNV}\right)\right), \tag{3.3}$$

where $\delta\left(\tau\left(\sigma\left(\vec{x}\right)\right), \mathbf{RPE}\right) = 1$ inside **RPE cells** and 0 elsewhere, $\delta\left(\tau\left(\sigma\left(\vec{x}\right)\right), \mathbf{HRPE}\right) = 1$ inside **HRPE cells** and 0 elsewhere, $\delta\left(\tau\left(\sigma\left(\vec{x}\right)\right), \mathbf{CC}\right) = 1$ inside **vascular cells** and 0 elsewhere and $\delta\left(\tau\left(\sigma\left(\vec{x}\right)\right), \mathbf{CNV}\right) = 1$ inside **stalk cells** and the **tip cell** and 0 elsewhere.

I represent **short-diffusing VEGF-A** as a **field** $V_{\mathrm{S}}\left(\vec{x}\right)$ with units of molecule per μm^3, which diffuses at a constant rate $D_{\mathrm{VEGF}}^{\mathrm{EC}}$ everywhere and degrades at a constant rate γ_{VEGF} in the **medium**. **ECs** (**tip**, **stalk** and **vascular cells**) secrete **short-diffusing VEGF-A** into $V_{\mathrm{S}}\left(\vec{x}\right)$ uniformly at all their voxels at a constant rate SV^{EC}, so $V_{\mathrm{S}}\left(\vec{x}\right)$ evolves according to:

$$\frac{\partial V_{\mathrm{S}}\left(\vec{x}\right)}{\partial t} = D_{\mathrm{VEGF}}^{\mathrm{EC}} \nabla^2 V_{\mathrm{S}}\left(\vec{x}\right) - \gamma_{\mathrm{VEGF}}\, V_{\mathrm{S}}\left(\vec{x}\right) + SV^{\mathrm{EC}}\, \delta\left(\tau\left(\sigma\left(\vec{x}\right)\right), \mathrm{EC}\right), \tag{3.4}$$

where $\delta\left(\tau\left(\sigma\left(\vec{x}\right)\right), \mathbf{EC}\right) = 1$ inside **vascular**, **stalk cells** and the **tip cell** and 0 elsewhere.

I represent partial pressure of **Oxygen** by a **field** $PO\left(\vec{x}\right)$ with units of mmHg, which diffuses at a constant rate D_{ox} everywhere. **Vascular cells** secrete **Oxygen** into the **Oxygen field** uniformly at all their voxels at a rate SC_{ox} (O_2 (100 g **CC** tissue min)$^{-1}$)

that maintains $PO\left(\vec{x}\right)$ averaged over all voxels of the **CC** at 80 mmHg. **Stalk** cell of the **CNV**, secrete **Oxygen** uniformly at all their voxels at a rate NC_{ox} that maintains $PO\left(\vec{x}\right)$ averaged over all the voxels of **stalk cells** at 65 mmHg (for a detailed discussion see section III.14.5, below). **PIS cell-parts** take up **Oxygen** uniformly at a constant rate, QO_{PIS} with units of ml O_2 $(\text{min})^{-1}$ per 100g of **PIS** tissue. Since the rate of diffusion of oxygen is fast compare to all other processes in the model, its time-dependent concentration is close to its stationary profile, so I simulate its transport using a stationary diffusion equation:

$$\begin{aligned} &k\,D_{\text{ox}}\nabla^2 PO\left(\vec{x}\right)+SC_{\text{ox}}\,\delta\left(\tau\left(\sigma\left(\vec{x}\right)\right),\mathbf{CC}\right)+SN_{\text{ox}}\,\delta\left(\tau\left(\sigma\left(\vec{x}\right)\right),\mathbf{CNV}\right) \\ &-QO_{\text{PIS}}\,\delta\left(\tau\left(\sigma\left(\vec{x}\right)\right),\mathbf{PIS}\right)=0, \end{aligned} \tag{3.5}$$

where *k* is the solubility of oxygen per gram of retinal tissue and NC_{ox} and SC_{ox} are the amounts of oxygen secretion per unit time (ml O_2 $(100\text{ g tissue min})^{-1}$, 1 MCS = 3.6 minutes) locally from the **CC** and **stalk cells**, respectively (see Table III-8 for the parameters), $\delta\left(\tau\left(\sigma\left(\vec{x}\right)\right),\mathbf{CNV}\right)=1$ inside **stalk cells** and 0 elsewhere and $\delta\left(\tau\left(\sigma\left(\vec{x}\right)\right),\mathbf{CC}\right)=1$ inside the **CC** and 0 elsewhere.

I represent the **MMP** concentration as a **field** $M\left(\vec{x}\right)$ with units of molecule per μm^3, which diffuses at a constant rate D_{MMP} and degrades at a constant rate η_{MMP} everywhere. The **tip cell** secretes **MMP** into $M\left(\vec{x}\right)$ uniformly at all their voxels at a constant rate SM^{tip} (with units of molecules per voxel per 216 seconds), so $M\left(\vec{x}\right)$ evolves according to:

$$\frac{\partial M\left(\vec{x}\right)}{\partial t} = D_{\text{MMP}}\nabla^{2}M\left(\vec{x}\right) - \gamma_{\text{MMP}}M\left(\vec{x}\right) + SM^{\text{tip}}\delta\left(\tau\left(\sigma\left(\vec{x}\right)\right), \mathbf{tip}\right), \tag{3.6}$$

where $\delta\left(\tau\left(\sigma\left(\vec{x}\right)\right), \mathbf{tip}\right) = 1$ inside the **tip cell** and 0 elsewhere.

III.13.5 *Chemotaxis*

I include a chemotaxis term in the Effective Energy to model the VEGF-A response of ECs during angiogenesis. I add a saturated Savil-Hogeweg-type chemotaxis term with contact inhibition to the basic ΔH_{GGH} of the Effective Energy to represent the net effect of **ECs**' preferential formation of pseudopods in response to gradients of both **RPE-derived** and **short-diffusing VEGF-A** at **EC** boundaries with any generalized cell type except **ECs**:

$$\Delta H_{\text{chemotaxis}} = -\lambda_{\text{VS}}\left(V_{\text{S}}\left(\vec{i}_{\text{target}}\right) - V_{\text{S}}\left(\vec{i}_{\text{source}}\right)\right) - \lambda_{\text{VL}}\left(\frac{V_{\text{L}}\left(\vec{i}_{\text{target}}\right)}{V_{\text{L0}} + V_{\text{L}}\left(\vec{i}_{\text{target}}\right)} - \frac{V_{\text{L}}\left(\vec{i}_{\text{source}}\right)}{V_{\text{L0}} + V_{\text{L}}\left(\vec{i}_{\text{source}}\right)}\right), \tag{3.7}$$

where λ_{VS} and λ_{VL} are chemotaxis response coefficients and V_{L0} regulates saturation of the chemotaxis response to **RPE-derived VEGF-A**. Due to contact inhibition at **EC-EC** boundaries, $\Delta H_{\text{chemotaxis}} = 0$. Thus the total change in the Effective Energy is:

$$\Delta H_{\text{total}} = \Delta H_{\text{GGH}} + \Delta H_{\text{chemotaxis}}. \tag{3.8}$$

The effects of the saturation of the chemotaxis response to **short-diffusing VEGF** on capillary formation have been studied elsewhere [1].

III.13.6 *Growth, Proliferation and Death*

As described in [157], growth of **stalk cells** is inhibited when the common contact area between **stalk cells** and other **ECs** is greater than a threshold. This threshold contact area is fixed and does not change as the **stalk cells** grow. I describe **stalk cell** growth and proliferation by increasing the target volume of **stalk cells** according to:

$$\frac{dV_{\text{t}}(\sigma)}{dt} = \frac{G_{\text{S}} V_{\text{L}}\left(\vec{i}_{\text{CM}}(\sigma)\right)}{V_0 + V_{\text{L}}\left(\vec{i}_{\text{CM}}(\sigma)\right)}, \tag{3.9}$$

when growth is not inhibited. I divide the volume of a **stalk cell** equally between two daughter **stalk cells** when the volume reaches the doubling volume, 1728 µm^3. G_{S} in units of µm^3 min^{-1} is the *maximum growth rate,* V_0 is the concentration of **RPE-derived VEGF-A** at which the growth rate is half its maximum and $V_{\text{L}}\left(\vec{i}_{\text{CM}}(\sigma)\right)$ is the concentration of **RPE-derived VEGF-A** at the center-of-mass of the **stalk cell**. All voxels of a **stalk cell** (σ) take up diffusing **RPE-derived VEGF-A**. This uptake creates an intracellular gradient with a minimum concentration at the center of the **cell**. $V_{\text{L}}\left(\vec{i}_{\text{CM}}(\sigma)\right)$ is typically 10 times lower than the average $V_{\text{L}}\left(\vec{x}\right)$ at the boundary of the

cell. I pick G_S so that **stalk cells** not touching other **ECs** divide every 18 hours if $V_\mathrm{L}\left(\vec{i}_\mathrm{CM}(\sigma)\right)$ is 0.1 pM.

As **stalk cells** grow, the equilibrium lengths of their **plastic** links with other **EC**s also increase. Since the distance between **stalk cells** in contact with **BrM** does not change as they grow, I do not increase the equilibrium lengths of the **plastic links** between **stalk cells** and **BrM** generalized **cells**. Because **stalk cells** are long and thin, their typical length grows as v rather than $v^{1/2}$:

$$\ell_\mathrm{target}(\sigma,\rho)=\theta\times\left(v(\sigma)+v(\rho)\right),$$

(3.10)

where $v(\sigma)$ and $v(\rho)$ are the volumes of a **stalk cell** and an **EC**. θ is a constant that produces a $\ell_\mathrm{target}(\sigma,\rho)$ roughly equal to the prespecified initial $\ell_\mathrm{target}(\sigma,\rho)$ before **stalk-cell** growth. This growth in $\ell_\mathrm{target}(\sigma,\rho)$ prevents **junctional adhesions** from restricting **cell** growth.

If at any time an **RPE cell** loses all contact both with other **RPE cells** and **BrM**, it dies. I set both the target volume and target surface area of the dying cell to zero. When its actual volume reaches 0, I remove the **cell**. Similarly, **ECs** die when the level of **RPE-derived VEGF-A** at their center-of-mass at any time falls below a threshold level, V_L^T. In my simulations, V_L^T is 1000 times smaller than the level of **RPE-derived VEGF-A** at the center-of-mass of **vascular cells** of the **CC** in anatomically normal **CC-BrM-RPE-retina** (about 0.1 fM).

To model BrM degradation, I reduce the target volume of **BrM** voxels, $V_{\mathrm{t}}(\sigma)$, at a rate, G_B (the **BrM** *degradation rate*), proportional to concentration of the **MMP field** ($M(\vec{i})$) at that voxel:

$$\frac{dV_{\mathrm{t}}(\sigma)}{dt} = -G_B M(\vec{i}), \tag{3.11}$$

where G_B is a positive constant. I remove **BrM** voxels when their target volume ($V_{\mathrm{t}}(\sigma)$) becomes zero.

Object Types			**Processes**
Generalized Cells	**Endothelial Cells (EC)**	**Vascular Cells** (of the **CC**)	Adhere via **junctional adhesion** to **ECs** and **BrM** Adhere via **labile adhesion** to **RPE, PIS, POS** and **Medium** Take up **RPE-derived VEGF-A** Secrete **short-diffusing VEGF-A** Secrete **Oxygen** Die when **RPE-derived VEGF-A** is less than a threshold Have intrinsic random motility

			Chemotax up gradients of **short-diffusing VEGF-A** (Contact-inhibited)
		Stalk Cells (of the **CNV**)	All Processes of **Vascular Cells** and: Chemotax up gradients of **RPE-derived VEGF-A** (Contact-inhibited) Grow in response to **RPE-derived VEGF-A** (Contact-inhibited)
		Tip Cells	All Processes of **Vascular Cells** except secretion of **Oxygen**: Chemotax up gradients of **RPE-derived VEGF-A** (Contact-inhibited) Secrete **MMP**
		RPE Cells	Adhere via **junctional adhesion** to **RPE cells** and **BrM** Adhere via **labile adhesion** to **ECs, PIS, POS** and **Medium** Secrete **RPE-derived VEGF-A** **Die** in absence of contact with **RPE** and **BrM** Have intrinsic random motility
	r Compartmen	**POS Cell-parts**	Adhere via **junctional adhesion** to **POS** and **PIS cells** Adhere via **labile adhesion** to **ECs, RPE, BrM**

			and **Medium** Have intrinsic random motility
		PIS Cell-parts	All Processes of **POS Cell-parts** and: **Consume Oxygen**
	Extracellular Materials	**BrM**	Non-diffusing solid material (implemented as non-motile generalized **cells**) Adheres via **labile** and/or **junctional adhesion** (see **EC**, **RPE**, **PIS**, **POS**) Degraded by **MMP**
		Medium	Adheres via **labile adhesion** to **cells** and **BrM** Fills space unoccupied by **cells** or **BrM**
Fields		**Oxygen**	Diffuses
		RPE-derived VEGF-A	Diffuses Decays
		Short-diffusing VEGF-A	Diffuses Decays
		MMP	Diffuses Decays Degrades **BrM**

Table III-7. Model Objects and Processes.

III.14 Simulation Parameters and Initial Configuration

The ratios of the parameter values in the Effective Energy in my simulations determine the relative amplitudes of different **cell** behaviors. *E.g.*, the strength of chemotaxis to **RPE-derived VEGF-A** relative to **RPE-RPE** and **RPE-BrM junctional adhesion** and **RPE-POS labile adhesion** determines the **CNV type** and dynamics. I chose to keep the chemotaxis strength of **ECs** constant and change the five adhesion strength parameters: 1) the **RPE-RPE labile adhesion** strength (*RRl*), 2) the **RPE-RPE plastic coupling** strength (*RRp*), 3) the **RPE-BrM labile adhesion** strength (*RBl*), 4) the **RPE-BrM plastic coupling** strength (*RBp*), 5) the **RPE-POS labile adhesion** strength (*ROl*).

Since many parameters in my GGH model have not yet been measured experimentally, I must fit them to match measurable aspects of **cell** behavior in my simulations to those observed in experiments. *E.g.*, the intrinsic cell motility ($T\left(\tau\left(\sigma\right)\right)$) is not easy to measure experimentally, but the diffusion constant of cells in aggregates can be measured in both simulation and experiment and corresponds to a unique intrinsic motility ($T\left(\tau\left(\sigma\right)\right)$) in a simulation. Similarly, I can determine the effective form and strength of the chemotaxis response in my simulations from experimental dose-response curves for cell migration in response to concentration gradients of a chemoattractant.

III.14.1 *Implementation*

All my simulations use the open-source CompuCell3D simulation environment (http://www.compucell3d.org/) [117]. I ran my simulations on a computer cluster

(Quarry, Indiana University) using CompuCell3D v3.4.2. A typical simulation replica takes about 30 hours on a single core of a 2.0 GHz quad-core Intel Xeon 5335 processor. I stored the **cell** and **field**-lattice configurations every 6 simulated **hours** and rendered each snapshot using the integrated post-processing rendering provided by CompuCell3D.

III.14.2 *Geometrical Parameters*

The retina has a quasi-two-dimensional geometry. I take the smaller dimension, which extends from the choroid to the inner layers of the retina as the *z*-axis and choose the *x* and *y* axes so the retinal layers lie parallel to the *xy*-plane. Since a normal retina has a fairly uniform structure in the direction of its extended dimensions, I assume that that the **cell** and **field** lattices are periodic in the *x* and *y* directions, but not in the *z* direction. RPE cells form an epithelium that is ~ 11 µm thick in the macula [199]. The diameter of RPE cells in the macula is typically ~ 15 µm [243]. Assuming a hexagonal shape for RPE cells, their total volume is ~ 1600 µm^3. Since ECs in capillaries have irregular shapes, measuring EC volume is difficult experimentally. I use cubic voxels with a volume of 27 µm^3 (a side of 3 µm). At this spatial resolution, **RPE cells** are large enough so discretization artifacts are tolerable. Simulated **RPE cells** and **ECs** have volumes of about 1728 µm^3 and 864 µm^3 respectively. Individual photoreceptors are about 2 µm in diameter and about 65 µm in length. I coarse-grain 2 of their 3 main compartments as **cell-parts**; **POS cell-part** have a volume of 32 × 32 × 32 µm^3 and **PIS cell-part** having a volume of 24 × 24 × 24 µm^3. Each **cell-part** represents a cluster of many photoreceptors. BrM thickness typically ranges from 2 µm in young adults to 4 µm in older adults. I build

BrM out of two layer of small blocks, each of which of which has a volume of 27 µm^3, so the entire **BrM** has a volume of 120 × 120 × 6 µm^3. The total simulated volume is 120 × 120 × 78 µm^3. I assume that generalized **cells** have nearly the density of water.

I initialize my simulations with a simplified configuration representing a normal retina, where the **RPE** contacts and adheres to the **POS cell-parts** apically, adheres to neighboring **RPE cells** laterally and adheres to **BrM** basally (Figure III.1). The **CC** forms a rectangular quasi-two-dimensional mesh that adheres to the outer side of **BrM**.

III.14.3 *Temporal Parameters and Cell Motility*

I relate the simulation's MCS time-scale to seconds by comparing **cell** migration speeds in simulations to typical cell migration speeds in experiments. Bauer *et al* [226] estimated migration speeds of about 6 µm/day for invading angiogenic sprouts during tumor-induce angiogenesis. Growing stable capillaries in simulations restricts the average migration speeds of **stalk cells** to less than 0.005 voxels per MCS computed over 100 MCS intervals since faster **stalk cell** migration speeds produces unstable vasculature. Equating 6 µm/day to the maximal **stalk cell** speed of 0.005 voxel/MCS for a voxel size ~ 3 µm fixes the time-scale to 400 MCS ~ 24 hours or 1 MCS ~ 216 seconds.

III.14.4 *Bruch's Membrane Degradation Parameters*

BrM is composed of multiple layers of different extracellular proteins. In general, different MMPs diffuse at different rates and degrade specific sets of extracellular proteins. I assume my **MMP** diffuse because membrane-bound MMPs activate diffusible extracellular MMPs. In my model, the **tip cell** degrades **BrM** by secreting a single type of **MMP**. Because **MMP** represents the degradation effects of multiple matrix degrading enzymes, the diffusion constant of the **MMP field**, D_{MMP} , and its degradation rate γ_{MMP} are not available experimentally. In my model, I set the diffusion length of **MMP**, $L_{\text{MMP}} = \sqrt{\frac{D_{\text{MMP}}}{\gamma_{\text{MMP}}}}$, and the **BrM** degradation rate, G_B, rate so the **tip cell** that secretes **MMP** degrades **BrM** locally and forms a roughly one cell-diameter hole in **BrM**. For a fixed G_B, a larger diffusion length of **MMP**, would produce a larger hole in **BrM**.

III.14.5 *Oxygen Transport Parameters*

Moving inward through the layers of the retina, the O_2 contribution of the choriocapillaries decreases and the contribution from the retinal capillaries increases [135,220,244]. Near the OLM both sources of oxygen contribute equally and the partial pressure of oxygen reaches its lowest level. Light-adapted photoreceptors consume less oxygen than dark-adapted photoreceptors. So dark-adaptation shifts the position of the O_2 minimum towards the ONL (Figure III.1). I neglect this shift, since it negligibly affects the **Oxygen** partial pressure at the location of the **RPE cells**. I impose no-flux boundary condition for $PO(\vec{x})$ at $z = 0$ and fix the **Oxygen** partial pressure at the **OLM** boundary to 18 mmHg (less than the average inner retinal oxygen partial pressure PO_2 ~ 20 mmHg) for both normoxia and hypoxia [220]. I fix PO_2 at the **choriocapillaris** to 80 mmHg [220].

Average experimentally-measured light-adapted and dark-adapted oxygen consumption rates are 2.6 and 5.2 ml O_2 (100 g tissue min)$^{-1}$ [221,245]. Since the PIS consumes nearly 100% of the oxygen and only occupies 20% of the retina by volume, the actual consumption rates of the PIS in light-adapted and dark-adapted conditions are about five times these average oxygen consumption rates: 13 and 26 ml O_2 (100 g tissue min)$^{-1}$ respectively (for a detailed discussion see [220]). I adopt the consumption rates estimated in [220], and model continuous light-adapted conditions rather than alternation between light-adapted and dark-adapted conditions.

In my simulations, I adjust the flux of **Oxygen** per unit volume (Table III-8) transferred locally from the **choriocapillaries** to the **retina** to achieve an average $PO\left(\vec{x}\right)$ of 80 mmHg ($PO_{\mathrm{N}}^{\mathrm{CC}}$, averaged over voxels belong to the **CC**) under normoxia. For the parameter values in Table III-8, the average **Oxygen** partial pressure at the center-of-mass of **RPE cells** under light-adapted conditions is 65 ± 3 mmHg. Direct measurement of oxygen partial pressure in the human retina is difficult experimentally; however, my predicted average **Oxygen** partial pressure at the center-of-mass of **RPE cells** is close to estimated oxygen partial pressures in humans, based on measured values in animals [135].

In my simulations, **stalk cells** forming **sub-RPE** or **sub-retinal** capillaries contribute little **Oxygen** to the **retina**. I adjust the flux of **Oxygen** per unit volume of **stalk cells** so the average PO_2 (averaged over all **stalk-cell** voxels) is the minimum of two PO_2 levels: 1) 65 mmHg, which is the average $PO\left(\vec{x}\right)$ at the **RPE** in normal retina,

2) the highest level of $PO(\vec{x})$ on **RPE** side of **BrM**. This oxygen transport scheme ensures that the average PO_2 in **stalk cells** is always less than $PO(\vec{x})$ in the **CC**.

Experimentally, I do not know what levels of PO_2 trigger hypoxic signaling by RPE cells. Animals breathing 10% oxygen, experience mild systemic hypoxia. If I assume that biological RPE cells are hypoxic during systemic hypoxia, I can use my model to calculate the resulting $PO(\vec{x})$ in the RPE. Based on experimentally measured parameters, my simulations of normal retina predict that $PO(\vec{x})$ at the RPE decreases from ~ 65 mmHg to ~ 49 mmHg as the PO_2 at the CC decreases from 80 mmHg to 60 mmHg during systemic hypoxia in an anatomically normal retina under light-adapted condition. I assume that for **Oxygen** partial pressures less than 49 mmHg, **RPE cells** become hypoxic and secrete **RPE-derived VEGF-A** at the maximum rate $SV_{\max}^{RPE}$.

III.14.6 *Quantification and Classification of Simulations*

From the total contact areas between **stalk cells** and **BrM**, and between **stalk cells** and the **POS** I define the *morphometric weight*:

$$MW = \frac{(\textbf{stalk - BrM}\text{ contact area})}{(\textbf{stalk - BrM}\text{ contact area}) + (\textbf{stalk - POS}\text{ contact area})}. \tag{3.12}$$

The **stalk-BrM** contact area of a fully-developed capillary network is about the same as the **stalk-POS** contact area of a corresponding volume of fully-developed sub-retinal CNV. So, a *MW* close to 1 indicates that most **stalk cells** are confined between the **RPE** and **BrM** (**sub-RPE**) in **Type 1 CNV**. A *MW* close to 0 usually indicates that most **stalk**

cells are confined between the **RPE** and **POS** (**sub-retinal**) in **Type 2 CNV**. A *MW* close to 0.5 indicates **Type 3 CNV**. For each snapshot of a simulation I use the *MW* to estimate the number of **sub-RPE** and **sub-retinal stalk cells**:

$$\begin{aligned}&\#\ \textbf{Sub-RPE stalk cells} = \text{total}\ \#\ \textbf{stalk cells} \times MW,\\&\#\ \textbf{Sub-retinal stalk cells} = \text{total}\ \#\ \textbf{stalk cells} \times \left(1 - MW\right),\end{aligned} \tag{3.13}$$

I can calculate *MW* even when **CNV** fails to initiate, so the *MW* allows us to determine the **CNV** loci, even when CNV initiation fails. To classify **CNV** progression during a simulated **year**, I determine the ***early*** and ***late*** loci of the **stalk cells**, using the weighted mean *MW*s during the first or last three **months** of each simulation:

$$\left\langle MW \right\rangle = \frac{\sum_{i=1}^{N} S_i MW_i}{\sum_{i=1}^{N} S_i}, \tag{3.14}$$

where *N* is the total number of snapshots recorded during the first or last three **months**, as appropriate, S_i is total number of stalk cells in *i*th snapshot and MW_i is the morphometric weight of the *i*th snapshot.

Stalk cells in simulations that exhibit **Stable Type 3 CNV** often simultaneously touch **BrM** basally, touch **RPE cells** laterally and touch the **POS** apically, so they are contained neither in the **sub-RPE** space nor in the **sub-retinal** space.

If the **RPE** detaches completely from **BrM**, the **stalk-BrM** contact area decreases to zero, so *MW* = 0, incorrectly suggesting that all **stalk cells** are in the **sub-retinal** space.

Thus in case of **RPE** detachment, I must invoke other measurements beyond the *MW* to characterize the **CNV**. I do not consider situations with **RPE** detachment in this chapter.

III.14.7 *Statistical Methods*

I used the JMP statistical analysis package [246] to perform multiple-regressions to relate **CNV** initiation probabilities, types and dynamics to the underlying adhesion scenarios.

Geometrical Parameters		
Name	**Description**	**Values**
L_{OS}	**POS** layer thickness	~ 30 µm (compare to [130])
L_{IS}	**PIS** layer thickness	~ 24 µm (compare to [130])
L_{OLM}	Location of OLM measured from **RPE** side of **BrM**	~ 67 µm (compare to [130])
L_{BrM}	**BrM** thickness	6 µm (compare to [199])
L_{RPE}	**RPE** thickness	12 µm (compare to [199])
Oxygen Transport Parameters		
Name	**Description**	**Values**
D_{ox}	Diffusion coefficient of oxygen in retinal tissue	2.0×10^{-5} cm^2 s^{-1} [247]

QO_{PIS}	Light-adapted (dark-adapted) **Oxygen** consumption per 100g of **PIS** tissue	13 (26) ml O_2 min^{-1} [220,221,245]
$PO_{\mathrm{N}}^{\mathrm{CC}}$	**Oxygen** partial pressure in **choriocapillaries** under normoxia	80 mmHg [221,245]
$PO_{\mathrm{H}}^{\mathrm{CC}}$	**Oxygen** partial pressure in **choriocapillaries** under systemic hypoxia	60 mmHg (extrapolated from rat [248])
PO^{OLM}	**Oxygen** partial pressure at **OLM** under normoxia and hypoxia	18 mmHg [220]
$PO_{\mathrm{N}}^{\mathrm{RPE}}$	Average oxygen partial pressure in the **RPE** under normoxia	65 mmHg during light-adaptation, 61 mmHg during dark-adaptation (see *Oxygen Transport Parameters*)
$PO_{\mathrm{H}}^{\mathrm{RPE}}$	Average oxygen partial pressure in the **RPE** under systemic hypoxia	49 mmHg during light-adaptation, 45 mmHg during dark-adaptation (see *Oxygen Transport Parameters*)
$SC_{\mathrm{ox}}^{\mathrm{N}}$	Oxygen flux from 100g of **choriocapillaris tissue** to the retina under normoxic condition	3.42 (CC3D) or 102 ml O_2 (100 g tissue $\mathrm{min})^{-1}$ during dark-adaptation 2.67 (CC3D) or 80 ml O_2 (100 g tissue $\mathrm{min})^{-1}$ during light-adaptation

$SC_{\text{ox}}^{\text{H}}$	Oxygen flux from 100g of **choriocapillaris tissue** to the retina under systemic hypoxia	2.81 (CC3D) or 84 ml O_2 (100 g tissue min)$^{-1}$ during dark-adaptation 2.05 (CC3D) or 61 ml O_2 (100 g tissue min)$^{-1}$ during light-adaptation
VEGF Transport Parameters		
Name	**Description**	**Values**
γ_{VEGF}	Decay rate of **RPE-derived VEGF-A** and **short-diffusing VEGF-A**	1 h^{-1} [249,250]
$L_{\text{VEGF}}^{\text{RPE}}$	Diffusion length of **RPE-derived VEGF-A** secreted by **RPE cells**	13.4 µm $\left(\sqrt{\frac{D_{\text{VEGF}}^{\text{RPE}}}{\gamma_{\text{VEGF}}}}\right)$
$D_{\text{VEGF}}^{\text{EC}}$	Diffusion coefficient of **short-diffusing VEGF-A** secreted by **ECs**	$0.25 \times 10^{-10}\ \text{cm}^2\ \text{s}^{-1}$
$L_{\text{VEGF}}^{\text{EC}}$	Diffusion length of **short-diffusing VEGF-A** secreted by **ECs**	3 µm $\left(\sqrt{\frac{D_{\text{VEGF}}^{\text{EC}}}{\gamma_{\text{VEGF}}}}\right)$
$SV_{\max}^{RPE}$	Secretion rate of **VEGF** by **HRPE cells**	~50 pg (cell h)$^{-1}$ (compare to [251]) (0.1 molecules (voxel MCS)$^{-1}$)
SV_{basal}^{RPE}	Basal secretion rate of **VEGF** by **RPE cells**	~25 pg (cell h)$^{-1}$ (compare to [251]) (0.05 molecules (voxel MCS)$^{-1}$)
SV^{EC}	Basal secretion rate of **short-diffusing VEGF** by **ECs**	~25 pg (cell h)$^{-1}$ (0.2 (voxel MCS)$^{-1}$)

QV_{EC}	Basal uptake rate of **RPE-derived VEGF-A** by **vascular cells**	~ 300 ligated molecules per EC × 2.8×10^{-4} (internalization rate) [252] ~ 0.084 molecule (cell sec)$^{-1}$ = 0.28 molecule (voxel MCS)$^{-1}$
MMP Transport and BrM Degradation Parameters		
Name	**Description**	**Values**
SM^{tip}	Secretion rate of **MMP** by the **tip** cell	0.148 molecule (cell sec)$^{-1}$ (1 molecule (voxel MCS)$^{-1}$)
L_{MMP}	Diffusion length of **MMP** secreted by the **tip** cell	0.2 µm $\left(\sqrt{\frac{D_{\mathrm{MMP}}}{\gamma_{\mathrm{MMP}}}}\right)$
G_B	**BrM** degradation rate	0.0094 µm^3 (sec molecule)$^{-1}$ (0.075 voxel (MCS molecule)$^{-1}$)

Table III-8. Geometrical and Transport Parameters

Fields		
Name	**Description**	**Units**
$PO\left(\vec{x}\right)$	**Oxygen** partial pressure at $\vec{x}$	mmHg
$V_{\mathrm{L}}\left(\vec{x}\right)$	**RPE-derived VEGF-A** at $\vec{x}$	molecule/voxel
$V_{\mathrm{S}}\left(\vec{x}\right)$	**Short-diffusing VEGF-A** secreted by **ECs** at $\vec{x}$	molecule/voxel

$M\left(\vec{x}\right)$	**MMP** secreted by **tip cells** at $\vec{x}$	molecule/voxel

Table III-9. Field Object Names.

Cell Types	**Stalk**	**BrM**	**RPE**	**POS**	**PIS**	**Medium**
Stalk	-20	-10	-10	-10	-10	3
BrM		-12	-38/-28/-18	0	0	-1
RPE			-40/-18	-16/-1	-16/-1	3
POS				-16	-16	3
PIS					-16	3
Medium						0

Table III-10. Labile Adhesion Parameters (Contact Energies). Negative contact energies represent adhesive interactions; positive contact energies represent repulsive interactions. More negative contact energies indicate stronger adhesive interactions. (/) separates the reference, moderately impaired and severely impaired levels of **labile adhesion**.

		Labile Adhesion Strength		
Cell-Type Pairs	Name	Normal: 3	Moderately Impaired: 2	Severely Impaired: 1
RPE-RPE	*RRl*	-40	-	-18
RPE-BrM	*RBl*	-38	-28	-18
RPE-POS	*ROl*	-16	-	-1
POS-POS	**-**	-16	-	-

PIS-PIS	**-**	-16	-	-

Table III-11. Labile Adhesion Strengths (Contact Energies). More negative contact energies indicate stronger adhesive interactions. (-) denotes **labile adhesion** strengths not used in my simulations.

		Plastic Coupling Strength		
Cell-Type Pairs	Name	Normal: 3	Impaired: 2	Severely Impaired: 1
RPE-RPE	*RRp*	300	60	30
RPE-BrM	*RBp*	300	60	30
POS-POS	-	30	-	-
PIS-PIS	-	30	-	-
PIS-POS	-	30	-	-
Vascular-Vascular	-	200	-	-
Stalk-Vascular	-	150	-	-
Tip-Vascular	-	50	-	-
Stalk-Stalk	-	50	-	-
Stalk-Tip	-	50	-	-
Vascular-BrM	-	200	-	-
Stalk-BrM	-	25	-	-
Tip-BrM	-	25	-	-

Table III-12. Plastic Coupling Strengths ($\lambda_{\text{plastic}}\left(\tau(\sigma),\tau(\rho)\right)$) Links Between Cell-Type Pairs. Larger plastic coupling strengths represent stiffer linear springs. (-) denotes values of $\lambda_{\text{plastic}}\left(\tau(\sigma),\tau(\rho)\right)$ not used in my simulations.

III.15 Supplemental Tables

For the supplemental tables in this section I used identical abbreviation and color coding: ID: adhesion scenario ID. *RRl*: **RPE-RPE labile adhesion** strength, *RRp*: **RPE-RPE plastic coupling** strength, *RBl*: **RPE-BrM labile adhesion** strength, *RBp*: **RPE-BrM plastic coupling** strength, *ROl*: **RPE-POS labile adhesion** strength. P_{init}: **CNV** initiation probability. <*MW*>: mean morphometric weight. Both <*MW*> and P_{init} are calculated from 10 simulation replicas for each adhesion scenario. Scaled adhesion strengths: 3: normal (green), 2: moderately impaired (yellow), 1: severely impaired (weak) (red).

ID	*RRl*	*RRp*	*RBl*	*RBp*	*ROl*	P_{init}
1	3	3	3	3	3	0.00
4	3	2	3	3	3	0.20
2	3	3	3	2	3	0.30
3	3	3	3	1	3	0.30
7	3	1	3	3	3	0.30

Table III-13. Adhesion Scenarios with Infrequent or No **CNV** Initiation. Adhesion scenarios that result in **CNV** initiation with probability less than or equal to 0.3 ($P_{\text{init}} \leq 0.3$).

ID	*RRl*	*RRp*	*RBl*	*RBp*	*ROl*	P_{init}	<*MW*>
3	3	3	3	1	3	0.30	1.00
38	3	3	2	2	3	0.90	1.00
39	3	3	2	1	3	1.00	1.00
73	3	3	1	3	3	1.00	1.00
74	3	3	1	2	3	1.00	1.00
75	3	3	1	1	3	1.00	1.00
41	3	2	2	2	3	1.00	0.99
76	3	2	1	3	3	1.00	1.00
77	3	2	1	2	3	1.00	1.00
78	3	2	1	1	3	1.00	1.00
79	3	1	1	3	3	1.00	1.00

80	3	1	1	2	3	1.00	1.00
81	3	1	1	1	3	1.00	1.00
83	1	3	1	2	3	1.00	0.90
84	1	3	1	1	3	1.00	0.93

Table III-14. Adhesion Scenarios Prone to **Early Type 1 CNV** ($MW > 0.9$) if **CNV** Initiates. A large *MW* indicates that almost no **stalk cells** cross the **RPE** and come into contact with the **POS**.

ID	*RRl*	*RRp*	*RBl*	*RBp*	*ROl*	P_{init}	<*MW*>
19	3	3	3	3	1	0.50	0.04
20	3	3	3	2	1	0.80	0.01
21	3	3	3	1	1	0.90	0.01
55	3	3	2	3	1	0.50	0.03
22	3	2	3	3	1	0.80	0.02
23	3	2	3	2	1	1.00	0.01
24	3	2	3	1	1	1.00	0.02
58	3	2	2	3	1	0.90	0.02
60	3	2	2	1	1	1.00	0.04
25	3	1	3	3	1	0.90	0.01
26	3	1	3	2	1	0.90	0.02
27	3	1	3	1	1	1.00	0.01
61	3	1	2	3	1	1.00	0.01
62	3	1	2	2	1	1.00	0.03
10	1	3	3	3	3	1.00	0.02
28	1	3	3	3	1	1.00	0.00
11	1	3	3	2	3	1.00	0.03
29	1	3	3	2	1	1.00	0.01
12	1	3	3	1	3	1.00	0.03
30	1	3	3	1	1	1.00	0.01
64	1	3	2	3	1	1.00	0.01
65	1	3	2	2	1	1.00	0.01
66	1	3	2	1	1	1.00	0.01
100	1	3	1	3	1	1.00	0.02
101	1	3	1	2	1	1.00	0.05
13	1	2	3	3	3	1.00	0.03
31	1	2	3	3	1	1.00	0.02
14	1	2	3	2	3	1.00	0.03
32	1	2	3	2	1	1.00	0.03
15	1	2	3	1	3	1.00	0.05
33	1	2	3	1	1	1.00	0.03
67	1	2	2	3	1	1.00	0.03
68	1	2	2	2	1	1.00	0.04

69	1	2	2	1	1	1.00	0.04
103	1	2	1	3	1	1.00	0.04
16	1	1	3	3	3	1.00	0.03
34	1	1	3	3	1	1.00	0.02
17	1	1	3	2	3	1.00	0.03
35	1	1	3	2	1	1.00	0.03
36	1	1	3	1	1	1.00	0.03
70	1	1	2	3	1	1.00	0.03
72	1	1	2	1	1	1.00	0.05
106	1	1	1	3	1	1.00	0.05

Table III-15. Adhesion Scenarios Prone to **Early Type 2 CNV** ($MW < 0.05$) if **CNV** Initiates. A small *MW* indicates that most **stalk cells** cross the **RPE** and come into contact with the **POS**.

ID	*RRl*	*RRp*	*RBl*	*RBp*	*ROl*	P_{init}	<*MW*>
47	1	3	2	2	3	1.00	0.39
48	1	3	2	1	3	1.00	0.49
82	1	3	1	3	3	1.00	0.44
51	1	2	2	1	3	1.00	0.43
85	1	2	1	3	3	1.00	0.44
54	1	1	2	1	3	1.00	0.40
88	1	1	1	3	3	1.00	0.45

Table III-16. Adhesion Scenarios Prone to **Early Type 3 CNV** ($0.35 < MW < 0.65$) if **CNV** initiates. $0.35 < MW < 0.65$ indicates that **stalk cells** come into contact with both **BrM** and the **POS**.

ID	*RRl*	*RRp*	*RBl*	*RBp*	*ROl*	P_{init}	**S11** Probability
3	3	3	3	1	3	0.30	1.00
41	3	2	2	2	3	1.00	1.00
80	3	1	1	2	3	1.00	0.90
79	3	1	1	3	3	1.00	0.90
77	3	2	1	2	3	1.00	0.90
76	3	2	1	3	3	1.00	0.90
74	3	3	1	2	3	1.00	0.90
73	3	3	1	3	3	1.00	0.90
39	3	3	2	1	3	1.00	0.90
38	3	3	2	2	3	0.90	0.90

Table III-17. Adhesion Scenarios Prone to **Stable Type 1 CNV** (**S11 CNV** Probability > 0.9). Adhesion scenarios that develop **Early Type 1 CNV** (**ET1 CNV**, $MW > 75\%$) in which **CNV** remains confined to the **sub-RPE** space (**Late Type 1 CNV**, $MW > 75\%$).

ID	*RRl*	*RRp*	*RBl*	*RBp*	*ROl*	P_{init}	**T12** Probability

91	3	3	1	3	1	0.90	0.50
92	3	3	1	2	1	1.00	0.40
93	3	3	1	1	1	1.00	0.70
94	3	2	1	3	1	1.00	0.30
97	3	1	1	3	1	1.00	0.30

Table III-18. Adhesion Scenarios Prone to Sub-RPE to Sub-Retinal Translocation (**T12** Translocation).

ID	*RRl*	*RRp*	*RBl*	*RBp*	*ROl*	P_{init}	**P13** Probability
83	1	3	1	2	3	1.00	1.00
86	1	2	1	2	3	1.00	1.00
90	1	1	1	1	3	1.00	1.00
89	1	1	1	2	3	1.00	1.00

Table III-19. Selected Adhesion Scenarios Prone to Sub-RPE to Sub-Retinal Progression (**P13** Progression) (**P13** Probability > 0.7).

ID	*RRl*	*RRp*	*RBl*	*RBp*	*ROl*	P_{init}	**S22** Probability
21	3	3	3	1	1	0.90	0.90
23	3	2	3	2	1	1.00	1.00
24	3	2	3	1	1	1.00	1.00
58	3	2	2	3	1	0.90	0.90
60	3	2	2	1	1	1.00	1.00
25	3	1	3	3	1	0.90	0.90
26	3	1	3	2	1	0.90	0.90
27	3	1	3	1	1	1.00	1.00
61	3	1	2	3	1	1.00	1.00
62	3	1	2	2	1	1.00	1.00
63	3	1	2	1	1	1.00	1.00
10	1	3	3	3	3	1.00	1.00
28	1	3	3	3	1	1.00	1.00
11	1	3	3	2	3	1.00	1.00
29	1	3	3	2	1	1.00	1.00
12	1	3	3	1	3	1.00	1.00
30	1	3	3	1	1	1.00	1.00
46	1	3	2	3	3	1.00	1.00
64	1	3	2	3	1	1.00	1.00
65	1	3	2	2	1	1.00	1.00
66	1	3	2	1	1	1.00	1.00
100	1	3	1	3	1	1.00	1.00
101	1	3	1	2	1	1.00	1.00
102	1	3	1	1	1	1.00	1.00
13	1	2	3	3	3	1.00	1.00

31	1	2	3	3	1	1.00	1.00
14	1	2	3	2	3	1.00	1.00
32	1	2	3	2	1	1.00	1.00
15	1	2	3	1	3	1.00	1.00
49	1	2	2	3	3	1.00	1.00
67	1	2	2	3	1	1.00	1.00
68	1	2	2	2	1	1.00	1.00
103	1	2	1	3	1	1.00	1.00
104	1	2	1	2	1	1.00	0.90
16	1	1	3	3	3	1.00	1.00
34	1	1	3	3	1	1.00	1.00
17	1	1	3	2	3	1.00	1.00
35	1	1	3	2	1	1.00	1.00
52	1	1	2	3	3	1.00	1.00
70	1	1	2	3	1	1.00	1.00
71	1	1	2	2	1	1.00	0.90
106	1	1	1	3	1	1.00	1.00

Table III-20. Adhesion Scenarios Prone to **Stable Type 2 CNV** (**S22**) (**S22** Probability > 0.9).

ID	*RRl*	*RRp*	*RBl*	*RBp*	*ROl*	P_{init}	**P23** Probability
105	1	2	1	1	1	1.00	0.60
108	1	1	1	1	1	1.00	1.00

Table III-21. Adhesion Scenarios Prone to Sub-Retinal **CNV** to Sub-RPE **CNV** Progression (**P23 CNV**) (**P23** Probability > 0.6).

ID	*RRl*	*RRp*	*RBl*	*RBp*	*ROl*	Initiation Probability	**S33** Probability
88	1	1	1	3	3	1.00	1.00
54	1	1	2	1	3	1.00	1.00
53	1	1	2	2	3	1.00	1.00
85	1	2	1	3	3	1.00	1.00
51	1	2	2	1	3	1.00	1.00
50	1	2	2	2	3	1.00	1.00
82	1	3	1	3	3	1.00	1.00
48	1	3	2	1	3	1.00	1.00
47	1	3	2	2	3	1.00	1.00

Table III-22. Adhesion Scenarios Prone to **Stable Type 3 CNV** (**S33 CNV**) (**S33** Probability > 0.9).

Chapter IV: Future Work

IV.1 Cancer Evolution

Cancers is not a single disease, but a complex spectrum of diseases which may be characterized by a series of hallmarks, including deregulated proliferation, replicative immortality and ability to induce angiogenesis. According to current *dogma*, those behaviors, and so the cancer, result primarily from accumulated mutations in the cancer cell's genetic material (*DNA*), which have not been repaired after a cell division. I believe a more general approach focusing on cell behaviors and the situations that drive selection for particular behavior combinations may provide new insights into cancer mechanisms and therapies. More specifically, I wish to investigate how a cell changes its microenvironment and how the microenvironment applies selection pressure for specific cancer cell behaviors. This feedback makes cancer evolution an emergent phenomenon that cannot be understood by looking at either cells or environment in isolation. Since heritable behavioral changes can result from both genetic changes and numerous types of epigenetic modifications, I will use the term *mutation* to refer to any heritable changes of cell behavior, whether due to genetic changes or epigenetic effects.

My collaboration with Dr. Gilberto Thomas applies my computational techniques to study how somatic evolution leads to tumor progression. In our current cancer evolution model, we study the evolution of cell behaviors due to both applied and emergent environmental variations. We specifically focus on evolutionary mechanisms leading to disruption of cell-cell adhesion, enabling cancer cells to invade surrounding tissue and metastasize. Our current model includes two populations of tumor cells: stem-like tumor cells (*SLTC*), with unlimited proliferative potential, and nonstem-like tumor cells (*NSLTC*) that are capable of dividing a limited number of times. In some of our simulations, key cell behaviors and properties (*traits*) like cell-cell and cell-ECM adhesion, cell motility, the maximum number of replications per cell, cell cycle rate, glucose consumption rate and strength of aerobic glycolysis are initially identical across both populations. Other simulations start with populations of cells differing in these behaviors. Tumor cells have two phases: a *quiescent* phase and a *proliferating* phase. A well-fed cell in the quiescent phase becomes a proliferating cell. Cell proliferation depends on the availability of nutrient (glucose) and a cell's probability of dying depends on it's accumulation of damage due to starvation and other environmental factors (loss of contact with other cells or ECM, accumulation of lactate, attack by host immune cells, drug treatment or partial surgical removal). When a SLTC divides it has a specific probability of producing either one SLTC and one NSLTC or two SLTCs. At division one NSLTC cell produces two NSLTCs. To simulate genetic and epigenetic mutations, after each cell division, all or a subset of cell behaviors can change over given ranges with certain probabilities.

Specific scenarios represent different *in vivo* or *in vitro* situations. For example, we used our model to explore how spatio-temporal nutrient heterogeneity (due to tumor-induced angiogenesis and blood-vessel collapse due to compression [111,253] generated by tumor cell proliferation) could cause the cells in the tumor to evolve and increase invasiveness by favoring reduced cell-cell adhesion. In these simulations, initially cohesive tumor cells grow in a 5mM background glucose concentration supplied by the

ECM. This background glucose concentration drops as the tumor grows. The tumor cells initially form a small solid tumor cluster consisting of both SLTCs and NSLTCs. To mimic the spatio-temporal nutrient heterogeneity produced by phases of angiogenesis and vascular collapse, a rotating sector of a ring surrounding the simulated tissue produces extra nutrient (redder region in Figure IV.1B). Cells close to regions with high glucose concentration (close to the location of the rotating nutrient source) proliferate faster. Cells in low-glucose regions accumulated damage due to starvation, making them likely to die. Our simulations use a range of glucose secretion rates and rotation periods for the time-varying source. In one series of simulations, we kept the secretion rate of glucose fixed and varied the rotation period from 36 minutes to 3.6 months (36 minutes, 6 hours, 6 days, 3.6 months). Each simulation ran for 3 simulated years. Even this highly simplified scenario has multiple time-scales that directly influence the rates of cell division and cell death and the rate and direction of tumor evolution (towards more cohesive or less cohesive cells). Our initial finding is that an intermediate glucose-source rotation period of 6 days promotes tumor aggressiveness more effectively than slower or fast glucose-source rotation. This optimal period is comparable to the typical time-scales of tumor-induced angiogenesis and regression of newly formed capillaries [253,254], suggesting that tumor-induced angiogenesis could indeed promote tumor invasiveness by it introducing spatio-temporal nutrient heterogeneity at length and time scales which favor cells with reduced cell-cell adhesion.

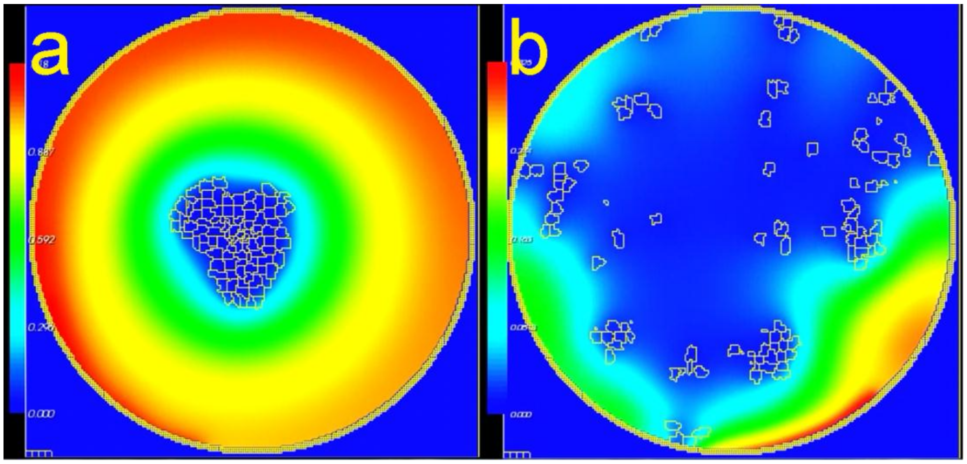

Figure IV.1. (A) A stem cell proliferates in response to a spatiotemporally varying nutrient field, forming a cluster of initially cohesive tumor cells (B) Tumor cells become invasive, spreading out and forming small nodules. Nutrient concentration field color code: Red: high nutrient concentration. Blue: low nutrient concentration.

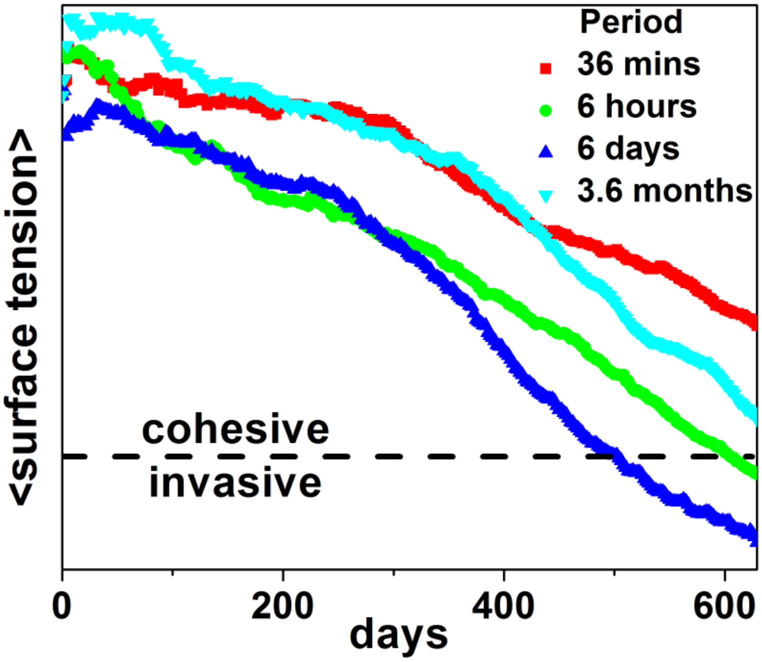

Figure IV.2. Evolution of cell-ECM surface tension. Average surface tension between tumor cells and ECM averaged over 10 simulation replicas for each rotation period. Cells with effective surface tensions below the dashed line actively separate from the tumor cluster and invade the ECM.

IV.2 Mechanisms of CNV Initiation and Progression

In Chapter III, I discussed how different modes of adhesion failure in the CC-BrM-RPE-POS complex lead to different CNV types. I have also used my multi-cell model of the retina to investigate the role of other key hypothesized CNV mechanisms. Specifically, I used my model to simulate the effects of VEGF-A overexpression in the RPE and the effects of defects in BrM on CNV initiation and progression. In this series of simulations, I induced systemic hypoxia by setting pO_2 at the choriocapillaris to 60 mmHg. In these simulations, RPE cells two-fold overexpress VEGF-A. My key finding is that VEGF-A overexpression increases the risk of initiating sub-retinal CNV, but does not promote sub-RPE CNV. In another set of simulations, I increased the diameter of the hole in BrM by increasing the rate at which MMPs degrade BrM, G_B. My key finding is that holes in BrM larger than about 40 μm, disrupt RPE integrity, leading to sub-retinal CNV, but not to sub-RPE CNV. These findings suggest that lipid accumulation in BrM is a dominant cause of the initiation of sub-RPE CNV and that both VEGF-A overexpression and defects in BrM facilitate CNV progression in AMD in which BrM-RPE adhesion is already reduced. I am preparing a manuscript based on these findings.

IV.3 Predicting the Effects of Toxins on Intersegmental Blood-Vessels in Zebrafish Embryo

Sprouting and patterning of intersegmental blood-vessel formation is a complex multistep process (Figure IV.3). Angiogenesis begins with sprouting of single endothelial cells which is controlled by subcellular signaling networks whose state is determined by cell-cell interactions and environmental cues at the tissue scale. Toxin exposure perturbs subcellular networks, cell behaviors, the microenvironment, cell-microenvironment interactions and cell-cell interactions. To integrate these interactions across multiple scales and build a predictive model of zebrafish angiogenesis for toxicology, we need a multicell-multiscale model.

Therefore, in collaboration with Drs. Sherry Clendenon (Indiana University) and Maria Bondesson and Catherine McCollum (University of Houston), I am building a refined 3D model of intersegmental blood-vessel (*ISV*) formation in zebrafish embryos to predict the effects of toxins on angiogenesis during development Our model starts with two bare bone/base models: 1) a GGH multicell model that describes cell and tissue objects and interactions spanning scales from a segment of developing tail to single cells, 2) subcellular models of the signaling and regulatory pathways in these cells. Initially, I developed and verified these base models separately, then integrated them and performed model verification against known biological perturbations.

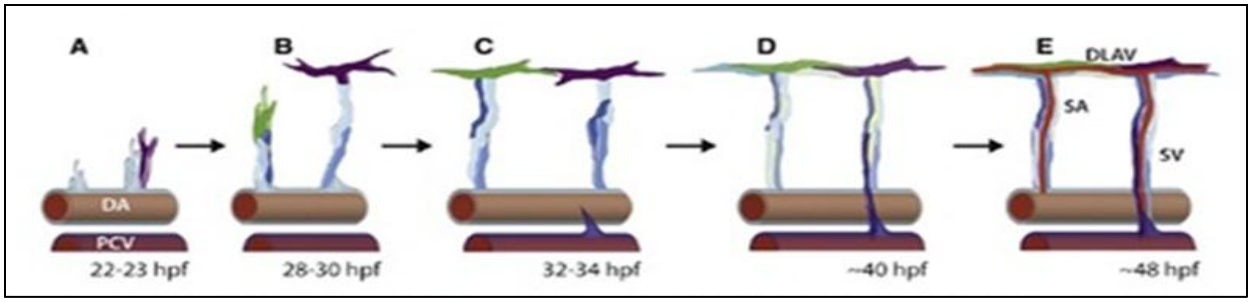

Figure IV.3. Sprouting and patterning of intersegmental blood-vessel. (A) ISVs sprout from the dorsal aorta (*DA*) and extend dorsally, traveling adjacent to the notochord through intersomitic extracellular matrix. After reaching the dorsal side of the notochord, ISVs continue extending between the neural tube and myotomes toward the dorsal surface of the neural tube, but do not remain within the confines of the intersomitic ECM. On reaching the dorsal surface of the neural tube, ISVs bifurcate and anastomose with their lateral neighbors to form the dorsal longitudinal anastomosing vessel (*DLAV*). Sprouts subsequently emerge from the posterior caudal vein (*PCV*) and anastomose with primary ISVs and the ISVs assume either a veinous or arterial identity (Figure from [255]).

The growth dynamics of ISVs are currently an untapped resource for determining the signatures of specific types of developmental toxicity. We have developed image quantification techniques to extract both *static* and *dynamic perturbation signatures*. We expect that changes in these signatures will differentiate control from toxin-exposed embryos and uniquely identify the toxin and level of exposure. Static signatures include the number, length and branching of filopodia in ISV cells (Figure IV.4). Dynamic signatures calculated from microscopic *in vivo* time-series include; the frequency of tip cell extension and retraction, the amplitude of ISV extension and retraction, the average directed migration speed, and the time delay between the sprouting of neighboring ISVs (in the anterior-posterior direction). We will use these quantitative signatures for model verification and validation.

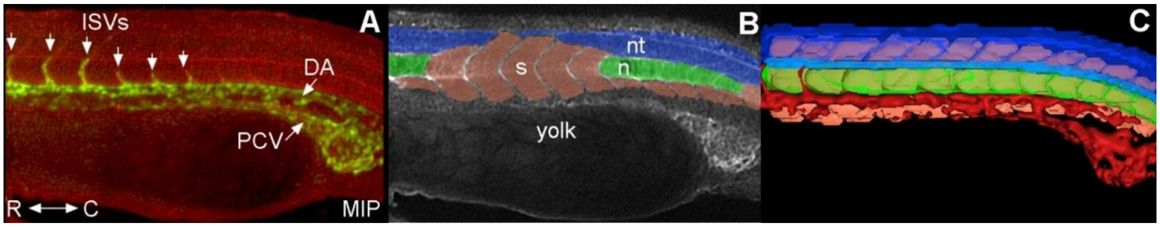

Figure IV.4. Three-dimensional datasets of optical sections were acquired, segmented and used to define initial conditions for the computational model of ISV growth. Vascular development is visible in one-day-old zebrafish expressing green fluorescent protein in their vascular endothelial cells (green). (A) The fish is counterstained with a fluorescent conjugate of lens-culinaris agglutinin to visualize the surrounding tissue morphology (red). (B) Single optical sections of the 3D image were segmented using TrakEM2 within the FIJI distribution of the ImageJ image processing package. Color overlays delineate neural tissue (blue), notochord (green) and somites (salmon). (C) The segmented neural tissue (blue), notochord (green) and somites (salmon) was combined with segmentation of vascular endothelial cells (red) and rendered as a 3D surface to serve as the initial condition for our model of blood vessel growth. ISVs, intersegmental vessels; R, rostral; C, caudal; DA, dorsal aorta; PVC, posterior caudal vein; s, somites; n, notochord; nt, neural tube. Images courtesy of Dr. Sherry Clendenon.

Based on our initial observations: 1) Both tip cells and stalk cells in the ISVs in zebrafish treated with physiologically relevant doses of arsenic have numerous, highly active filopodia (tip-cell like activity), 2) Some ISVs fail to migrate dorsoventrally through the intersegmental space and regress to the DA (Figure IV.5), 3) Cells with tip-cell activity have higher levels of VEGF receptor-2 (*VEGFR-2*) expression, 4) Cells with tip-cell activity also migrate more slowly through the intersegmental space (Figure IV.5). Arsenic treatment in chick downregulates Dll4 in atrioventricular explants and upregulates VE-cadherin [256]. Downregulation of Notch/Dll4 signaling increases filopodial activity in both tip and stalk cells, so all cells exhibit a tip cell phenotype [78].

Based on these experiments and simulations, we can understand the arsenic phenotype, as folloes: We believe that a key guidance cue for ECs during the early stages of ISV formation is a VEGF-A gradient that forms dynamically (in front of the tip cells) by release of ECM-bound VEGF-A due to MMP secretion by the tip cells. We hypothesize that the higher level of VEGFR-2 and MMP expression together in the ECs, initially create a steep VEGF-A gradient. Later, the slower than normal migration of tip-cell like cells (due to their higher levels of VE-cadherin and excessive filopodial activity), results in depletion of the limited amount of VEGF-A in the intersegmental ECM. This VEGF-A depletion, in turn, leads to regression of the angiogenic sprout before the sprout has migrated all the way through the intersegmental space to reach the midline. We will use our computational model to verify this hypothesis.

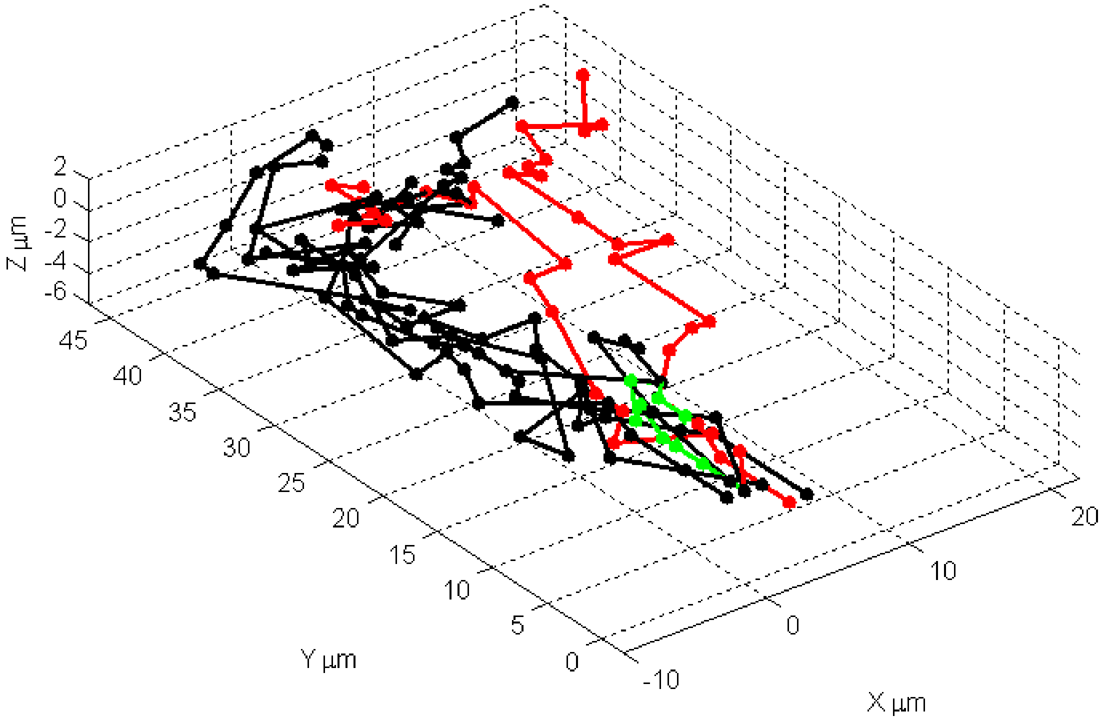

Figure IV.5. The effects of arsenic exposure on ISV trajectories during the first five hours after formation of a sprout. Black lines show the trajectories of five tip cells in three control embryos. Green lines trajectories of a tip cell that fails to form an ISV in an arsenic exposed embryo. Red lines show the trajectories of two tip cells in an arsenic-exposed embryo that form an ISV, but mislocalized. ISV trajectories in both control embryos and arsenic-treated embryos initially migrate along the intersegmental space. These ISVs in arsenic-treated embryos leave the intersegmental space about 1 hour after sprouting. I have used standard 3D elastic image registration techniques to correct for movement due to embryonic growth and tissue deformations.

Appendices

A: Vascular Patterning Simulation Codes

To run the simulation, load the XML file. This simulation is compatible with CC3D version 3.0 and later.

Vascular Patterning in 2D:

2DAngiogenesis.xml:

```
<CompuCell3D version="3.6.0">
   <Potts>
      <Dimensions x="300" y="300" z="1"/>
      <Steps>1000000</Steps>
      <Temperature>10</Temperature>
      <NeighborOrder>4</NeighborOrder>
      <Boundary_x>Periodic</Boundary_x>
      <Boundary_y>Periodic</Boundary_y>
   </Potts>
   <Plugin Name="CellType">
      <CellType TypeId="0" TypeName="Medium"/>
      <CellType TypeId="1" TypeName="V1"/>
   </Plugin>
   <Plugin Name="Contact">
      <Energy Type1="Medium" Type2="Medium">10</Energy>
      <Energy Type1="Medium" Type2="V1">5</Energy>
      <Energy Type1="V1" Type2="V1">10</Energy>
      <NeighborOrder>4</NeighborOrder>
   </Plugin>


   <Plugin Name="Volume">
      <VolumeEnergyParameters CellType="V1" LambdaVolume="13.0"
TargetVolume="25"/>
   </Plugin>


 <Plugin Name="ConnectivityGlobal">
     <Penalty Type="V1">1000</Penalty>
   </Plugin>

   <Plugin Name="Chemotaxis">
             <ChemicalField Source="FlexibleDiffusionSolverFE" Name="VEGF">
             <ChemotaxisByType Type="V1" Lambda="250"
ChemotactTowards="Medium"/>
             </ChemicalField>
    </Plugin>

    <Plugin Name="PDESolverCaller">
```

```
             <CallPDE PDESolverName="FlexibleDiffusionSolverFE"
ExtraTimesPerMC="3"/>
    </Plugin>

    <Steppable Type="FlexibleDiffusionSolverFE">

             <DiffusionField>
                   <DiffusionData>
                          <FieldName>VEGF</FieldName>
                          <DiffusionConstant>0.24</DiffusionConstant>
                          <DecayConstant>14e-3</DecayConstant>
                          <DoNotDecayIn>V1</DoNotDecayIn>
                   </DiffusionData>
                   <SecretionData>
                          <Secretion Type="V1" >10e-3</Secretion>
                   </SecretionData>
             </DiffusionField>
    </Steppable>

   <Steppable Type="UniformInitializer">
      <Region>
         <BoxMin x="10" y="10" z="0"/>
         <BoxMax x="160" y="160" z="1"/>
         <Gap>6</Gap>
         <Width>3</Width>
         <Types>V1</Types>
      </Region>
       <Region>
         <BoxMin x="165" y="165" z="0"/>
         <BoxMax x="215" y="215" z="1"/>
         <Gap>0</Gap>
         <Width>3</Width>
         <Types>V1</Types>
      </Region>
    </Steppable>
</CompuCell3D>
```

Vascular Patterning in 3D :

3DAngiogenesis.xml:

```
<CompuCell3D version="3.6.0">
   <Potts>
      <Dimensions x="50" y="50" z="50"/>
      <Steps>100000</Steps>
      <Temperature>10</Temperature>
      <NeighborOrder>3</NeighborOrder>
      <Boundary_x>Periodic</Boundary_x>
      <Boundary_y>Periodic</Boundary_y>
      <Boundary_z>Periodic</Boundary_z>
   </Potts>
   <Plugin Name="CellType">
      <CellType TypeId="0" TypeName="Medium"/>
      <CellType TypeId="1" TypeName="V1"/>
   </Plugin>
```

```
   <Plugin Name="Contact">
      <Energy Type1="Medium" Type2="Medium">10</Energy>
      <Energy Type1="Medium" Type2="V1">10</Energy>
      <Energy Type1="V1" Type2="V1">8</Energy>
      <NeighborOrder>2</NeighborOrder>
   </Plugin>
   <Plugin Name="Volume">
      <VolumeEnergyParameters      CellType="V1"      LambdaVolume="15.0"
TargetVolume="64"/>
   </Plugin>
   <Plugin Name="Surface">
   </Plugin>
     <Plugin Name="Chemotaxis">
            <ChemicalField            Source="FlexibleDiffusionSolverFE"
Name="Chemo1">
            <ChemotaxisByType          Type="VEGF"          Lambda="4000"
ChemotactTowards="Medium"/>
            </ChemicalField>
    </Plugin>

    <Plugin Name="PDESolverCaller">
            <CallPDE           PDESolverName="FlexibleDiffusionSolverFE"
ExtraTimesPerMC="2"/>
    </Plugin>

    <Steppable Type="FlexibleDiffusionSolverFE">

            <DiffusionField>
                  <DiffusionData>
                        <FieldName>VEGF</FieldName>
                        <DiffusionConstant>0.14</DiffusionConstant>
                        <DecayConstant>0.12</DecayConstant>
                        <DoNotDecayIn>V1</DoNotDecayIn>
                  </DiffusionData>
                  <SecretionData>
                        <Secretion Type="V1" >10e-3</Secretion>
                  </SecretionData>
            </DiffusionField>
    </Steppable>

   <Steppable Type="UniformInitializer">
      <Region>
         <BoxMin x="15" y="15" z="15"/>
         <BoxMax x="35" y="35" z="35"/>
         <Gap>0</Gap>
         <Width>4</Width>
         <Types>V1</Types>
      </Region>
    </Steppable>
</CompuCell3D>
```

B: 3D Vascular Tumor growth Simulation Code

The XML files and python scripts for CNV simulations are compatible with CC3D VER 3.3.1. To run the simulation copy all the following files into CC3D root folder (e.g. /home/user/Compucell3d/) and load the XML file:

1- XML_Template_TumorVasc3D_Movie_08052009_01_45_36.xml

2- angio_growth_08052009_01_45_36.py

3- angio_growth_plugins_08052009_01_45_36.py

4- angio_growth_steppables_08052009_01_45_36.py

5- TumorVasc3D_180x180x180_08052009_01_45_36.txt

XML_Template_TumorVasc3D_Movie_08052009_01_45_36.xml

```
<CompuCell3D>
<PythonScript>angio_growth_08052009_01_45_36.py</PythonScript>
   <Potts>
      <Dimensions x="180" y="180" z="180"/>

      <Steps>100000</Steps>
      <Flip2DimRatio>1</Flip2DimRatio>
      <Boundary_x>Periodic</Boundary_x>
      <Boundary_y>Periodic</Boundary_y>
      <Boundary_z>Periodic</Boundary_z>
      <CellMotility>
      <MotilityParameters CellType="InactiveNeovascular" Motility="0"/>
      <MotilityParameters CellType="Vascular" Motility="0"/>
      <MotilityParameters CellType="ActiveNeovascular" Motility="0"/>
      <MotilityParameters CellType="Vascular" Motility="0"/>
      <MotilityParameters CellType="Normal" Motility="100"/>
      <MotilityParameters CellType="Hypoxic" Motility="100"/>
      <MotilityParameters CellType="Necrotic" Motility="`100"/>
   </CellMotility>
      <NeighborOrder>3</NeighborOrder>
   </Potts>


   <Plugin Name="CellType">
      <CellType TypeName="Medium" TypeId="0"/>
      <CellType TypeName="Normal" TypeId="1"/>
      <CellType TypeName="Hypoxic" TypeId="2"/>
```

```
      <CellType TypeName="Necrotic" TypeId="3"/>

      <CellType TypeName="ActiveNeovascular" TypeId="4" />
      <CellType TypeName="Vascular" TypeId="5" />
      <CellType TypeName="InactiveNeovascular" TypeId="6" />

   </Plugin>

   <Plugin Name="NeighborTracker"/>

   <Plugin Name="Chemotaxis">
      <Algorithm>merks</Algorithm>
      <ChemicalField  Source="FlexibleDiffusionSolverFE"  Name="VEGF1">
         <ChemotaxisByType  Type="ActiveNeovascular"  Lambda="85"
ChemotactTowards="Medium,Normal,Hypoxic" />
      </ChemicalField>


      <ChemicalField  Source="FlexibleDiffusionSolverFE"  Name="VEGF1">
         <ChemotaxisByType  Type="Vascular"  Lambda="90"
ChemotactTowards="Medium,Normal,Hypoxic" />
      </ChemicalField>


      <ChemicalField  Source="FlexibleDiffusionSolverFE"  Name="VEGF1">
         <ChemotaxisByType  Type="InactiveNeovascular"  Lambda="90"
ChemotactTowards="Medium,Normal,Hypoxic" />
      </ChemicalField>
      <ChemicalField  Source="KernelDiffusionSolver"  Name="VEGF2">
         <ChemotaxisByType  Type="InactiveNeovascular"  Lambda="750"
SaturationCoef="1"/>
      </ChemicalField>
      <ChemicalField  Source="KernelDiffusionSolver"  Name="VEGF2">
         <ChemotaxisByType  Type="ActiveNeovascular"  Lambda="750"
SaturationCoef="1"/>
      </ChemicalField>
   </Plugin>

   <Plugin Name="CenterOfMass"/>

   <Plugin Name="PlayerSettings">

      <InitialProjection Projection="xy"/>
      <VisualControl ZoomFactor="4" ScreenshotFrequency="50"
ScreenUpdateFrequency="5"/>
      <TypesInvisibleIn3D Types=""/>
      <Settings SaveSettings="False"/>
   </Plugin>

<Plugin Name="Contact">
      <Energy Type1="Medium" Type2="Medium">0</Energy>
      <Energy Type1="Normal" Type2="Medium">8</Energy>
      <Energy Type1="Normal" Type2="Normal">6</Energy>

      <Energy Type1="Hypoxic" Type2="Medium">8</Energy>
```

```
      <Energy Type1="Hypoxic" Type2="Normal">6</Energy>
      <Energy Type1="Hypoxic" Type2="Hypoxic">6</Energy>

      <Energy Type1="Necrotic" Type2="Medium">0</Energy>
      <Energy Type1="Necrotic" Type2="Normal">0</Energy>
      <Energy Type1="Necrotic" Type2="Hypoxic">0</Energy>
      <Energy Type1="Necrotic" Type2="Necrotic">0</Energy>



      <Energy Type1="ActiveNeovascular" Type2="Medium">13</Energy>
      <Energy Type1="ActiveNeovascular" Type2="Normal">25</Energy>
      <Energy Type1="ActiveNeovascular" Type2="Hypoxic">25</Energy>
      <Energy Type1="ActiveNeovascular" Type2="Necrotic">25</Energy>
      <Energy Type1="ActiveNeovascular"
Type2="ActiveNeovascular">3</Energy>

      <Energy Type1="Vascular" Type2="Medium">13</Energy>
      <Energy Type1="Vascular" Type2="Normal">25</Energy>
      <Energy Type1="Vascular" Type2="Hypoxic">25</Energy>
      <Energy Type1="Vascular" Type2="Necrotic">25</Energy>
      <Energy Type1="Vascular" Type2="Vascular">3</Energy>
      <Energy Type1="Vascular" Type2="ActiveNeovascular">5</Energy>


      <Energy Type1="InactiveNeovascular" Type2="Medium">13</Energy>
      <Energy Type1="InactiveNeovascular" Type2="Normal">25</Energy>
      <Energy Type1="InactiveNeovascular" Type2="Hypoxic">25</Energy>
      <Energy Type1="InactiveNeovascular" Type2="Necrotic">25</Energy>
      <Energy Type1="InactiveNeovascular" Type2="Vascular">3</Energy>
      <Energy Type1="InactiveNeovascular"
Type2="InactiveNeovascular">3</Energy>
      <Energy Type1="InactiveNeovascular"
Type2="ActiveNeovascular">3</Energy>
      <NeighborOrder>5</NeighborOrder>

   </Plugin>

  <Plugin Name="VolumeLocalFlex"/>
   <Plugin Name="SurfaceLocalFlex"/>
   <Plugin Name="PDESolverCaller">
         <CallPDE PDESolverName="FlexibleDiffusionSolverFE"
ExtraTimesPerMC="1"/>
   </Plugin>

     <Plugin Name="PlasticityTracker">
    <IncludeType>InactiveNeovascular</IncludeType>
    <IncludeType>Vascular</IncludeType>

 </Plugin>

   <Plugin Name="PlasticityEnergy">
    <TargetLengthPlasticity>3</TargetLengthPlasticity>
    <LambdaPlasticity>400</LambdaPlasticity>
    <MaxPlasticityLength>20</MaxPlasticityLength>
```

```
 </Plugin>

   <Steppable Type="PIFDumper" Frequency="100">
      <PIFName>TumorVasc3D_180x180x180</PIFName>
   </Steppable>

  <Steppable Type="PIFInitializer">

<PIFName>TumorVasc3D_180x180x180_08052009_01_45_36.txt</PIFName>
  </Steppable>

   <Steppable Type="FlexibleDiffusionSolverFE">
      <!--Serialize Frequency="100"/-->

         <DiffusionField>
            <DiffusionData>

               <FieldName>VEGF1</FieldName>
               <!--ConcentrationFileNam e></ConcentrationFileName-->
               <DiffusionConstant>0.14</DiffusionConstant>
               <DecayConstant>65e-3</DecayConstant>
               <DeltaT>1</DeltaT>
               <DeltaX>1.0</DeltaX>
               <DoNotDecayIn>InactiveNeovascular</DoNotDecayIn>
               <DoNotDecayIn>ActiveNeovascular</DoNotDecayIn>
             <DoNotDecayIn>Vascular</DoNotDecayIn>
            </DiffusionData>

            <SecretionData>
               <Secretion Type="ActiveNeovascular">1</Secretion>
               <Secretion Type="InactiveNeovascular">1</Secretion>
               <Secretion Type="Vascular">1</Secretion>
            </SecretionData>
         </DiffusionField>
   </Steppable>


   <Steppable Type="KernelDiffusionSolver" >
    <Serialize Frequency="1000"/>
   <DiffusionField>
             <Kernel>35</Kernel>
               <CoarseGrainFactor>3</CoarseGrainFactor>
            <DiffusionData>

               <FieldName>Oxygen</FieldName>
               <!--
ConcentrationFileName>oxygen_180x180x180_20.txt</ConcentrationFileName-
->
               <DiffusionConstant>3440</DiffusionConstant>

               <DeltaT>1</DeltaT>
               <DeltaX>1.0</DeltaX>

            </DiffusionData>
            <SecretionData>
```

```
               <Uptake Type="Medium"  MaxUptake="0.8"
RelativeUptakeRate="0.99"/>
               <Uptake Type="Hypoxic"  MaxUptake="24"
RelativeUptakeRate="0.99"/>
               <Uptake Type="Normal"  MaxUptake="24"
RelativeUptakeRate="0.99"/>
               <Uptake Type="Necrotic"  MaxUptake="0.0001"
RelativeUptakeRate="0.99"/>


            <ConstantConcentration
Type="Vascular">90</ConstantConcentration>
             <ConstantConcentration
Type="ActiveNeovascular">50</ConstantConcentration>
               <!--ConstantConcentration
Type="Medium">8</ConstantConcentration-->


            </SecretionData>


         </DiffusionField>

        <DiffusionField>
              <Kernel>10</Kernel>
               <CoarseGrainFactor>3</CoarseGrainFactor>
            <DiffusionData>
               <FieldName>VEGF2</FieldName>
               <ConcentrationFileName></ConcentrationFileName>
               <DiffusionConstant>38</DiffusionConstant>
               <DecayConstant>0.01</DecayConstant>
               <DeltaT>1</DeltaT>
               <DeltaX>1.0</DeltaX>
            </DiffusionData>

            <SecretionData>
               <Secretion Type="Hypoxic">1</Secretion>
            </SecretionData>
         </DiffusionField>


 </Steppable>


</CompuCell3D>
```

angio_growth_08052009_01_45_36.py:

```
####
#### The simulation code is compatible with CompuCell3D ver 3.3.1
####
```

```
import sys
from os import environ
import string
sys.path.append(environ["PYTHON_MODULE_PATH"])

#

import CompuCellSetup

sim,simthread = CompuCellSetup.getCoreSimulationObjects()

#Create extra player fields here or add attributes

pyAttributeAdder,listAdder=CompuCellSetup.attachListToCells(sim)

CompuCellSetup.initializeSimulationObjects(sim,simthread)

#
##################
##########  PLUGINS
##################
#

import CompuCell

from angio_growth_plugins_08052009_01_45_36 import *

changeWatcherRegistry=CompuCellSetup.getChangeWatcherRegistry(sim)

stepperRegistry=CompuCellSetup.getStepperRegistry(sim)


mitPy=MitosisPyPlugin(sim,changeWatcherRegistry,stepperRegistry)

#### seting doubling volumes for normal, hypoxic, ActiveNeovascular,
InactiveNeovascular
doublingVolumeDict = {1:54,2:54,4:80,6:80}
mitPy.setCellDoublingVolume(doublingVolumeDict)

#
##################
##########  STEPPABLES
##################
#


from PySteppables import SteppableRegistry
steppableRegistry=SteppableRegistry()

from angio_growth_steppables_08052009_01_45_36 import *

#sim,frequency,areaThresh,nutrientThresh,necroticThresh
volumeParamSteppable=VolumeParamSteppable(sim,1,1,5,1)
steppableRegistry.registerSteppable(volumeParamSteppable)
```

```


#
##################
##########  COMPUCELL3D LOOPS
##################
#

CompuCellSetup.mainLoop(sim,simthread,steppableRegistry)
```

angio_growth_plugins_08052009_01_45_36.py:

```
####
#### The simulation code is compatible with CompuCell3D ver 3.3.1
####

from CompuCell import MitosisSimplePlugin
from PyPlugins import *
from PySteppables import CellList
from CompuCell import NeighborFinderParams
import time,sys

class MitosisPyPluginBase(StepperPy,Field3DChangeWatcherPy):
   def
__init__(self,_simulator,_changeWatcherRegistry,_stepperRegistry):


      Field3DChangeWatcherPy.__init__(self,_changeWatcherRegistry)
      self.simulator=_simulator
      self.mitosisPlugin=MitosisSimplePlugin()
      self.mitosisPlugin.setPotts(self.simulator.getPotts())
      self.mitosisPlugin.turnOn()
      self.mitosisPlugin.init(self.changeWatcher.sim)
      self.counter=0
      self.mitosisFlag=0
      self.doublingVolumeDict=0
      _changeWatcherRegistry.registerPyChangeWatcher(self)
      _stepperRegistry.registerPyStepper(self)




   def setPotts(self,potts):
      self.mitosisPlugin.setPotts(potts)

   def setDoublingVolume(self,_doublingVolume):
      self.doublingVolume=_doublingVolume;
      self.mitosisPlugin.setDoublingVolume(self.doublingVolume)

   def setCellDoublingVolume(self,_doublingVolumeDict):
      self.doublingVolumeDict=_doublingVolumeDict;
      for i in self.doublingVolumeDict.keys():
         print self.doublingVolumeDict[i]
```

```
   def field3DChange(self):
      cell = self.changeWatcher.newCell
      if cell and self.doublingVolumeDict.has_key(cell.type) and
cell.volume>self.doublingVolumeDict[cell.type]:
         print "Type: ", cell.type, " Doubling Volume: ",
self.doublingVolumeDict[cell.type], " Current Volume: ", cell.volume
         self.setDoublingVolume(self.doublingVolumeDict[cell.type])

self.mitosisPlugin.field3DChange(self.changeWatcher.changePoint,self.ch
angeWatcher.newCell,self.changeWatcher.newCell)
         self.mitosisFlag=1

   def step(self):
      if self.mitosisFlag:
         print "ABOUT TO DO MITOSIS"
         self.mitosisFlag=self.mitosisPlugin.doMitosis()
         self.childCell=self.mitosisPlugin.getChildCell()
         self.parentCell=self.mitosisPlugin.getParentCell()
         self.updateAttributes()
         self.mitosisFlag=0

   def updateAttributes(self):
      self.childCell.targetVolume=self.parentCell.targetVolume
      self.childCell.lambdaVolume=self.parentCell.lambdaVolume
      self.childCell.type=self.parentCell.type


class MitosisPyPlugin(MitosisPyPluginBase):
   def __init__(self , _simulator , _changeWatcherRegistry ,
_stepperRegistry):

MitosisPyPluginBase.__init__(self,_simulator,_changeWatcherRegistry,_st
epperRegistry)


   def updateAttributes(self):
## Mitosis of normal tumor and hypoxic cells
      if self.parentCell.type==1 or self.parentCell.type==2:
         self.childCell.type=1
       self.childCell.targetVolume=33
         self.childCell.lambdaVolume=10
         self.childCell.targetSurface=90
         self.childCell.lambdaSurface=2
         self.parentCell.targetVolume=33
         self.parentCell.lambdaVolume=10
         self.parentCell.targetSurface=90
         self.parentCell.lambdaSurface=2
## Mitosis of ActiveNeovascular and InactiveNeovascular cells
      if self.parentCell.type==6 or self.parentCell.type==4:
         self.childCell.type=4
       self.childCell.targetVolume=60
         self.childCell.lambdaVolume=13
         self.childCell.targetSurface=150
         self.childCell.lambdaSurface=3
```

```
         self.parentCell.targetVolume=60
         self.parentCell.lambdaVolume=13
         self.parentCell.targetSurface=150
         self.parentCell.lambdaSurface=3
```

angio_growth_steppables_08052009_01_45_36.py:

```
####
#### The simulation code is compatible with CompuCell3D ver 3.3.1
####
from PySteppables import *
import CompuCell
import sys
import time

class VolumeParamSteppable(SteppablePy):
   def
__init__(self,_simulator,_frequency=1,_areaThresh=0,_nutrientThresh=0,_
necroticThresh=0):
      SteppablePy.__init__(self,_frequency)
      self.simulator=_simulator
      self.inventory=self.simulator.getPotts().getCellInventory()
      self.cellList=CellList(self.inventory)
      self.nTrackerPlugin=CompuCell.getNeighborTrackerPlugin()
      self.areaThresh = _areaThresh
      self.nutrientThresh = _nutrientThresh
      self.necroticThresh = _necroticThresh
      self.fieldNameNeoVascular = 'VEGF2'
      self.fieldNameNormal = 'Oxygen'
      #self.output_file =
open("CellDiffusionData_08052009_01_45_36.txt",'w')

   def start(self):
      for cell in self.cellList:
         if cell.type==4 or cell.type==5 or cell.type==6:
          cell.targetVolume=60
            cell.lambdaVolume=13.0
          cell.targetSurface=150
            cell.lambdaSurface=3.0
         else:
          cell.targetVolume=33.0
            cell.lambdaVolume=10.0
          cell.targetSurface=90.0
            cell.lambdaSurface=2

   def step(self,mcs):

fieldNeoVasc=CompuCell.getConcentrationField(self.simulator,self.fieldN
ameNeoVascular)

fieldMalig=CompuCell.getConcentrationField(self.simulator,self.fieldNam
eNormal)
```

```
      #print mcs

      for cell in self.cellList:

         # Inactive neovascular differentiation
         if cell.type == 6:
            totalArea = 0
            pt=CompuCell.Point3D()
            pt.x=int(round(cell.xCM/max(float(cell.volume),0.001)))
            pt.y=int(round(cell.yCM/max(float(cell.volume),0.001)))
            pt.z=int(round(cell.zCM/max(float(cell.volume),0.001)))
            concentration=fieldNeoVasc.get(pt)
            if concentration>0.5:


cellNeighborList=CellNeighborListAuto(self.nTrackerPlugin,cell)
            for neighborSurfaceData in cellNeighborList:
              #Check to ensure cell neighbor is not medium
                if neighborSurfaceData.neighborAddress:
                 if neighborSurfaceData.neighborAddress.type == 5 or
neighborSurfaceData.neighborAddress.type == 6 or
neighborSurfaceData.neighborAddress.type == 7:

                  #sum up common surface area of cell with its
neighbors
                    totalArea+=neighborSurfaceData.commonSurfaceArea
                  #print "concentration: ", concentration,"
commonSurfaceArea:",neighborSurfaceData.commonSurfaceArea
            print cell.type,totalArea
            if totalArea < 70:
             #Growth rate equation
             #print cell.type,"##surface area",cell.surface,"##cell
volume:",cell.volume,"##cell target
volume:",cell.targetVolume,"##common surface area:",totalArea
             cell.targetVolume+=0.06*concentration/(0.5 +
concentration)
             cell.targetSurface+=0.15*concentration/(0.5 +
concentration)
               #print 0.02*concentration/(0.5 + concentration)+0.04

         ## Active neovascular growth
         if cell.type == 4:
            totalArea = 0
            pt=CompuCell.Point3D()

pt.x=int(round(cell.xCM/max(float(cell.volume),0.00000001)))

pt.y=int(round(cell.yCM/max(float(cell.volume),0.00000001)))

pt.z=int(round(cell.zCM/max(float(cell.volume),0.00000001)))
            concentration=fieldNeoVasc.get(pt)
            if concentration>0.5:


cellNeighborList=CellNeighborListAuto(self.nTrackerPlugin,cell)
```

```
            for neighborSurfaceData in cellNeighborList:
              #Check to ensure cell neighbor is not medium
                if neighborSurfaceData.neighborAddress:
                 if neighborSurfaceData.neighborAddress.type == 5 or
neighborSurfaceData.neighborAddress.type == 7 or
neighborSurfaceData.neighborAddress.type == 6:

                  #sum up common surface area of cell with its
neighbors
                    totalArea+=neighborSurfaceData.commonSurfaceArea
                  #print "concentration: ", concentration,"
commonSurfaceArea:",neighborSurfaceData.commonSurfaceArea
            #print cell.type,totalArea
            if totalArea < 50:
             #Growth rate equation
             #print cell.type,"##surface area",cell.surface,"##cell
volume:",cell.volume,"##cell target
volume:",cell.targetVolume,"##common surface area:",totalArea
             cell.targetVolume+=0.06*concentration/(0.5 +
concentration)
             cell.targetSurface+=0.15*concentration/(0.5 +
concentration)
               ##print 0.02*concentration/(0.5 + concentration)+0.04



         #Malignat and Hypoxic Cells growth
         if cell.type == 1 or cell.type == 2:
            #print cell.volume

            pt=CompuCell.Point3D()
            pt.x=int(round(cell.xCM/max(float(cell.volume),0.001)))
            pt.y=int(round(cell.yCM/max(float(cell.volume),0.001)))
            pt.z=int(round(cell.zCM/max(float(cell.volume),0.001)))
            #self.output_file.write("%f %f %f " %(cell.xCM/cell.volume,
cell.yCM/cell.volume,cell.zCM/cell.volume))

            concentration2=fieldMalig.get(pt)
            #switch to Hypoxic cell type
            if (concentration2 < self.nutrientThresh and mcs>100):
             cell.type=2

          #switch to Necrotic cell type
          if (concentration2 < self.necroticThresh and mcs>100):
               cell.type=3

            #set growth rate equation
            if (mcs>100):
             cell.targetVolume+=0.04*concentration2/(10+concentration2)

cell.targetSurface+=0.12*concentration2/(10+concentration2)

         #Hypoxic Cells
         if cell.type == 2:
            #print " #Hypoxic Volume: ", cell.volume
```

```
            pt=CompuCell.Point3D()
            pt.x=int(round(cell.xCM/max(float(cell.volume),0.001)))
            pt.y=int(round(cell.yCM/max(float(cell.volume),0.001)))
            pt.z=int(round(cell.zCM/max(float(cell.volume),0.001)))
            concentration3=fieldMalig.get(pt)
            #switch to Necrotic cell type
            if (concentration3 < self.necroticThresh and mcs>100):
               cell.type=3
          #switch to Normal cell type
          if (concentration3 > self.nutrientThresh):
               cell.type=1

         #Necrotic Cells
         if cell.type == 3:
            #set growth rate equation
            cell.targetVolume-=0.5
            cell.lambdaSurface=0
```

C: CNV Simulation Code

The XML files and python scripts for CNV simulations are compatible with CC3D VER 3.4.2. To get correct oxygen diffusion, adaptive secretion rates and boundary conditions, replace the “SteadyStateDiffusionSolver.cpp” from CC3D source code with the SteadyStateDiffusionSolver.cpp included in the supplemental files and compile CC3D VER 3.4.2. To run the simulation copy all the following files into CC3D root folder (e.g. /home/user/Compucell3d/) and load the XML file:

1- 902-JRB-28_JRR-40_JRP-16_LRB60_LRR300_r1.xml

2- angio_growth_19112010_11_16_47.py

3- angio_growth_plugins_19112010_11_16_47.py

4- angio_growth_steppables_19112010_11_16_47.py

5- 40x40-OuterRetina-BrM-CC.txt

902-JRB-28_JRR-40_JRP-16_LRB60_LRR300_r1.xml:

```
<CompuCell3D>
 <PythonScript>angio_growth_19112010_11_16_47.py</PythonScript>
   <Potts>
      <Dimensions x="40" y="40" z="35"/>
      <Steps>146000</Steps>
      <Flip2DimRatio>1</Flip2DimRatio>
      <Boundary_x>Periodic</Boundary_x>
      <Boundary_y>Periodic</Boundary_y>
      <Boundary_z>NoFlux</Boundary_z>
      <CellMotility>
         <MotilityParameters CellType="Tip" Motility="100"/>
         <MotilityParameters CellType="Stalk" Motility="100"/>
         <MotilityParameters CellType="Vascular" Motility="20"/>
         <MotilityParameters CellType="RPE" Motility="200"/>
         <MotilityParameters CellType="HRPE" Motility="200"/>
       <MotilityParameters CellType="POS" Motility="100"/>
       <MotilityParameters CellType="PIS" Motility="100"/>
         <MotilityParameters CellType="Drusen" Motility="20"/>
      </CellMotility>
      <RandomSeed>498377</RandomSeed>
      <NeighborOrder>4</NeighborOrder>
   </Potts>


   <Plugin Name="CellType">
      <CellType TypeId="0" TypeName="Medium"/>
      <CellType TypeId="1" TypeName="RPE"/>
      <CellType TypeId="2" TypeName="HRPE"/>
      <CellType TypeId="3" TypeName="BrM"/>
      <CellType TypeId="4" TypeName="Drusen"/>
      <CellType TypeId="5" TypeName="Tip"/>
      <CellType TypeId="6" TypeName="Stalk"/>
      <CellType TypeId="7" TypeName="Vascular"/>
      <CellType TypeId="8" TypeName="POS"/>
      <CellType TypeId="9" TypeName="PIS"/>
      <CellType TypeId="10" TypeName="NonStick" Freeze=""/>


   </Plugin>
   <Plugin Name="NeighborTracker"/>
   <Plugin Name="Chemotaxis">
      <Algorithm>merks</Algorithm>
      <ChemicalField Name="VEGF1" Source="FlexibleDiffusionSolverFE">
         <ChemotaxisByType
ChemotactTowards="Medium,RPE,HRPE,Drusen,BrM,POS,PIS,NonStick"
Lambda="12000.0" Type="Tip"/>
      </ChemicalField>
      <ChemicalField Name="VEGF1" Source="FlexibleDiffusionSolverFE">
         <ChemotaxisByType
ChemotactTowards="Medium,RPE,HRPE,Drusen,BrM,POS,PIS,NonStick"
Lambda="12000.0" Type="Stalk"/>
      </ChemicalField>
      <ChemicalField Name="VEGF1" Source="FlexibleDiffusionSolverFE">
```

```
         <ChemotaxisByType
ChemotactTowards="Medium,RPE,HRPE,Drusen,BrM,POS,PIS,NonStick"
Lambda="5000.0" Type="Vascular"/>
      </ChemicalField>
      <ChemicalField Name="VEGF2" Source="FlexibleDiffusionSolverFE">
         <ChemotaxisByType
ChemotactTowards="Medium,RPE,HRPE,Drusen,BrM,POS,PIS,NonStick"
Lambda="2500.0" SaturationCoef="0.09" Type="Tip"/>
      </ChemicalField>
      <ChemicalField Name="VEGF2" Source="FlexibleDiffusionSolverFE">
         <ChemotaxisByType
ChemotactTowards="Medium,RPE,HRPE,Drusen,BrM,POS,PIS,NonStick"
Lambda="2500.0" SaturationCoef="0.09" Type="Stalk"/>
      </ChemicalField>
   </Plugin>
   <Plugin Name="CenterOfMass"/>
   <Plugin Name="Contact">
      <Energy Type1="Medium" Type2="Medium">0</Energy>

      <Energy Type1="RPE" Type2="Medium">3</Energy>
      <Energy Type1="RPE" Type2="RPE">-40</Energy>

      <Energy Type1="HRPE" Type2="Medium">3</Energy>
      <Energy Type1="HRPE" Type2="RPE">-40</Energy>
      <Energy Type1="HRPE" Type2="HRPE">-40</Energy>

      <Energy Type1="BrM" Type2="Medium">-1</Energy>
      <Energy Type1="BrM" Type2="BrM">-12</Energy>
      <Energy Type1="BrM" Type2="RPE">-28</Energy>
      <Energy Type1="BrM" Type2="HRPE">-28</Energy>

      <Energy Type1="Drusen" Type2="Medium">0</Energy>
      <Energy Type1="Drusen" Type2="Drusen">0</Energy>
      <Energy Type1="Drusen" Type2="RPE">0</Energy>
      <Energy Type1="Drusen" Type2="HRPE">0</Energy>
      <Energy Type1="Drusen" Type2="BrM">0</Energy>

      <Energy Type1="Tip" Type2="Medium">3</Energy>
      <Energy Type1="Tip" Type2="Tip">-20</Energy>
      <Energy Type1="Tip" Type2="RPE">-10</Energy>
      <Energy Type1="Tip" Type2="HRPE">-10</Energy>
      <Energy Type1="Tip" Type2="BrM">-10</Energy>
      <Energy Type1="Tip" Type2="Drusen">-10</Energy>

      <Energy Type1="Stalk" Type2="Medium">3</Energy>
      <Energy Type1="Stalk" Type2="Stalk">-20</Energy>
      <Energy Type1="Stalk" Type2="Tip">-20</Energy>
      <Energy Type1="Stalk" Type2="RPE">-10</Energy>
      <Energy Type1="Stalk" Type2="HRPE">-10</Energy>
      <Energy Type1="Stalk" Type2="BrM">-10</Energy>
      <Energy Type1="Stalk" Type2="Drusen">-10</Energy>

      <Energy Type1="Vascular" Type2="Medium">3</Energy>
      <Energy Type1="Vascular" Type2="Vascular">-20</Energy>
      <Energy Type1="Vascular" Type2="Tip">-20</Energy>
```

```
      <Energy Type1="Vascular" Type2="Stalk">-20</Energy>
      <Energy Type1="Vascular" Type2="RPE">-10</Energy>
      <Energy Type1="Vascular" Type2="HRPE">-10</Energy>
      <Energy Type1="Vascular" Type2="BrM">-10</Energy>
      <Energy Type1="Vascular" Type2="Drusen">-10</Energy>

      <Energy Type1="POS" Type2="Medium">3</Energy>
      <Energy Type1="POS" Type2="POS">-16</Energy>
      <Energy Type1="POS" Type2="RPE">-16</Energy>
      <Energy Type1="POS" Type2="HRPE">-16</Energy>
      <Energy Type1="POS" Type2="BrM">0</Energy>
      <Energy Type1="POS" Type2="Drusen">0</Energy>
      <Energy Type1="POS" Type2="Tip">-5</Energy>
      <Energy Type1="POS" Type2="Stalk">-5</Energy>
      <Energy Type1="POS" Type2="Vascular">-5</Energy>

      <Energy Type1="PIS" Type2="Medium">3</Energy>
      <Energy Type1="PIS" Type2="PIS">-16</Energy>
      <Energy Type1="PIS" Type2="RPE">-16</Energy>
      <Energy Type1="PIS" Type2="HRPE">-16</Energy>
      <Energy Type1="PIS" Type2="BrM">0</Energy>
      <Energy Type1="PIS" Type2="Drusen">0</Energy>
      <Energy Type1="PIS" Type2="Tip">-5</Energy>
      <Energy Type1="PIS" Type2="Stalk">-5</Energy>
      <Energy Type1="PIS" Type2="Vascular">-5</Energy>
      <Energy Type1="PIS" Type2="POS">-15</Energy>


      <Energy Type1="NonStick" Type2="Medium">0</Energy>
      <Energy Type1="NonStick" Type2="NonStick">0</Energy>
      <Energy Type1="NonStick" Type2="RPE">25</Energy>
      <Energy Type1="NonStick" Type2="HRPE">25</Energy>
      <Energy Type1="NonStick" Type2="BrM">25</Energy>
      <Energy Type1="NonStick" Type2="Drusen">25</Energy>
      <Energy Type1="NonStick" Type2="Tip">25</Energy>
      <Energy Type1="NonStick" Type2="Stalk">25</Energy>
      <Energy Type1="NonStick" Type2="Vascular">25</Energy>
      <Energy Type1="NonStick" Type2="POS">25</Energy>
      <Energy Type1="NonStick" Type2="PIS">25</Energy>

      <NeighborOrder>4</NeighborOrder>
   </Plugin>
   <Plugin Name="VolumeLocalFlex"/>
   <Plugin Name="SurfaceLocalFlex"/>
   <Plugin Name="FocalPointPlasticity">
      <Parameters Type1="Vascular" Type2="BrM">
         <Lambda>200.0</Lambda>
         <ActivationEnergy>-100.0</ActivationEnergy>
         <TargetDistance>2.0</TargetDistance>
         <MaxDistance>4.0</MaxDistance>
         <MaxNumberOfJunctions>2</MaxNumberOfJunctions>
      </Parameters>
      <Parameters Type1="Vascular" Type2="Vascular">
         <Lambda>200.0</Lambda>
         <ActivationEnergy>-100.0</ActivationEnergy>
```

```
         <TargetDistance>4.0</TargetDistance>
         <MaxDistance>8.0</MaxDistance>
         <MaxNumberOfJunctions>3</MaxNumberOfJunctions>
      </Parameters>
      <Parameters Type1="RPE" Type2="RPE">
         <Lambda>300</Lambda>
         <ActivationEnergy>-100.0</ActivationEnergy>
         <TargetDistance>4.2</TargetDistance>
         <MaxDistance>8.0</MaxDistance>
         <MaxNumberOfJunctions>6</MaxNumberOfJunctions>
      </Parameters>
      <Parameters Type1="RPE" Type2="HRPE">
         <Lambda>300</Lambda>
         <ActivationEnergy>-100.0</ActivationEnergy>
         <TargetDistance>4.2</TargetDistance>
         <MaxDistance>8.0</MaxDistance>
         <MaxNumberOfJunctions>3</MaxNumberOfJunctions>
      </Parameters>
      <Parameters Type1="HRPE" Type2="HRPE">
         <Lambda>300</Lambda>
         <ActivationEnergy>-100.0</ActivationEnergy>
         <TargetDistance>4.2</TargetDistance>
         <MaxDistance>8.0</MaxDistance>
         <MaxNumberOfJunctions>6</MaxNumberOfJunctions>
      </Parameters>
      <Parameters Type1="RPE" Type2="BrM">
         <Lambda>60</Lambda>
         <ActivationEnergy>100.0</ActivationEnergy>
         <TargetDistance>3.5</TargetDistance>
         <MaxDistance>7.0</MaxDistance>
         <MaxNumberOfJunctions>6</MaxNumberOfJunctions>
      </Parameters>
      <Parameters Type1="HRPE" Type2="BrM">
         <Lambda>60</Lambda>
         <ActivationEnergy>100.0</ActivationEnergy>
         <TargetDistance>3.5</TargetDistance>
         <MaxDistance>7.0</MaxDistance>
         <MaxNumberOfJunctions>6</MaxNumberOfJunctions>
      </Parameters>
      <Parameters Type1="Vascular" Type2="Tip">
         <Lambda>50.0</Lambda>
         <ActivationEnergy>-5.0</ActivationEnergy>
         <TargetDistance>3.5</TargetDistance>
         <MaxDistance>7.0</MaxDistance>
         <MaxNumberOfJunctions>2</MaxNumberOfJunctions>
      </Parameters>

      <Parameters Type1="Stalk" Type2="Stalk">
         <Lambda>50.0</Lambda>
         <ActivationEnergy>400.0</ActivationEnergy>
         <TargetDistance>4.5</TargetDistance>
         <MaxDistance>9.0</MaxDistance>
         <MaxNumberOfJunctions>2</MaxNumberOfJunctions>
      </Parameters>
      <Parameters Type1="Stalk" Type2="Tip">
```

```
      <Lambda>50.0</Lambda>
      <ActivationEnergy>200.0</ActivationEnergy>
      <TargetDistance>4.5</TargetDistance>
      <MaxDistance>9.0</MaxDistance>
      <MaxNumberOfJunctions>1</MaxNumberOfJunctions>
   </Parameters>
   <Parameters Type1="Stalk" Type2="Vascular">
      <Lambda>150.0</Lambda>
      <ActivationEnergy>100.0</ActivationEnergy>
      <TargetDistance>4.0</TargetDistance>
      <MaxDistance>8.0</MaxDistance>
      <MaxNumberOfJunctions>2</MaxNumberOfJunctions>
   </Parameters>
   <Parameters Type1="Stalk" Type2="BrM">
      <Lambda>25.0</Lambda>
      <ActivationEnergy>-5.0</ActivationEnergy>
      <TargetDistance>2.5</TargetDistance>
      <MaxDistance>5.0</MaxDistance>
      <MaxNumberOfJunctions>2</MaxNumberOfJunctions>
   </Parameters>
   <Parameters Type1="Tip" Type2="BrM">
      <Lambda>25.0</Lambda>
      <ActivationEnergy>-5.0</ActivationEnergy>
      <TargetDistance>2.5</TargetDistance>
      <MaxDistance>5.0</MaxDistance>
      <MaxNumberOfJunctions>2</MaxNumberOfJunctions>
   </Parameters>

   <Parameters Type1="POS" Type2="POS">
      <Lambda>20.0</Lambda>
      <ActivationEnergy>-100.0</ActivationEnergy>
      <TargetDistance>10.0</TargetDistance>
      <MaxDistance>20.0</MaxDistance>
      <MaxNumberOfJunctions>6</MaxNumberOfJunctions>
   </Parameters>
   <Parameters Type1="Drusen" Type2="BrM">
      <Lambda>30.0</Lambda>
      <ActivationEnergy>-100.0</ActivationEnergy>
      <TargetDistance>2.0</TargetDistance>
      <MaxDistance>4.0</MaxDistance>
      <MaxNumberOfJunctions>1</MaxNumberOfJunctions>
   </Parameters>
   <Parameters Type1="PIS" Type2="PIS">
      <Lambda>20.0</Lambda>
      <ActivationEnergy>-100.0</ActivationEnergy>
      <TargetDistance>8.0</TargetDistance>
      <MaxDistance>16.0</MaxDistance>
      <MaxNumberOfJunctions>6</MaxNumberOfJunctions>
   </Parameters>
   <NeighborOrder>1</NeighborOrder>
</Plugin>

 <Plugin Name="ConnectivityGlobal">
<Penalty Type="Tip">1000000</Penalty>
<Penalty Type="Stalk">1000000</Penalty>
```

```
   <Penalty Type="Vascular">1000000</Penalty>
 </Plugin>

   <Steppable Type="PIFInitializer">
      <PIFName>40x40-OuterRetina-BrM-CC.txt</PIFName>
   </Steppable>

   <Steppable Type="UniformInitializer">

      <Region>
         <BoxMin x="18" y="12" z="2"/>
         <BoxMax x="21" y="15" z="4"/>
         <Gap>0</Gap>
         <Width>3</Width>
         <Types>Tip</Types>
      </Region>
      <Region>
         <BoxMin x="0" y="0" z="4"/>
         <BoxMax x="40" y="40" z="6"/>
         <Gap>0</Gap>
         <Width>1</Width>
         <Types>BrM</Types>
      </Region>
      <Region>
         <BoxMin x="0" y="0" z="34"/>
         <BoxMax x="40" y="40" z="35"/>
         <Gap>0</Gap>
         <Width>1</Width>
         <Types>NonStick</Types>
      </Region>

</Steppable>

<Steppable Type="SteadyStateDiffusionSolver" Frequency="1">
      <DiffusionField>
         <DiffusionData>
            <FieldName>Oxygen</FieldName>
            <DiffusionConstant>1.0</DiffusionConstant>     <!--diffusion
constant    is    rescaled    in    the    stationary    equation.    see
SteadyStateDiffusionSolver.cpp for parameter rescaling-->
             <DecayConstant>0.000000000005</DecayConstant>    <!--oxygen
does not decay but SteadyStateDiffusionSolver requires a non-zero decay
constant -->
         </DiffusionData>
         <OxygenSecretion>
            <Parameters    CellType="Vascular"    Hb="0.0"    Khem="0.0"
alpha="0.0" beta="0.01" bf="4.0" delta="0.0616" n="1" pblood="80.0"/>
          <Parameters  CellType="Stalk"  Hb="0.0"  Khem="0.0"  alpha="0.0"
beta="0.01" bf="0.0" delta="0.0616" n="2" pblood="65.0"/>
         </OxygenSecretion>
       <SecretionData>
            <Secretion Type="PIS">-0.43</Secretion>
         </SecretionData>
      </DiffusionField>
 </Steppable>
```

```
        <Steppable Type="FlexibleDiffusionSolverFE">
      <DiffusionField>
         <DiffusionData>
            <FieldName>VEGF1</FieldName>
            <ConcentrationFileName/>
            <DiffusionConstant>0.06</DiffusionConstant>
            <DecayConstant>0.06</DecayConstant>
            <DeltaT>1</DeltaT>
            <DeltaX>1.0</DeltaX>
            <DoNotDecayIn>Stalk</DoNotDecayIn>
          <DoNotDecayIn>Tip</DoNotDecayIn>
            <DoNotDecayIn>Vascular</DoNotDecayIn>
         </DiffusionData>
         <SecretionData>
            <Secretion Type="Stalk">0.01</Secretion>
            <Secretion Type="Tip">0.01</Secretion>
            <Secretion Type="Vascular">0.01</Secretion>
         </SecretionData>
      </DiffusionField>
      <DiffusionField>
         <DiffusionData>
            <FieldName>MMP</FieldName>
            <ConcentrationFileName/>
            <DiffusionConstant>0.0003</DiffusionConstant>
            <DecayConstant>0.06</DecayConstant>
            <DeltaT>1</DeltaT>
            <DeltaX>1.0</DeltaX>
         </DiffusionData>
         <SecretionData>
            <Secretion Type="Tip">1.0</Secretion>
         </SecretionData>
      </DiffusionField>

      <DiffusionField>
         <DiffusionData>
            <FieldName>VEGF2</FieldName>
            <DiffusionConstant>0.12</DiffusionConstant>
            <ExtraTimesPerMCS>12</ExtraTimesPerMCS>
            <DecayConstant>0.006</DecayConstant>
         </DiffusionData>
       <SecretionData>
            <Secretion Type="HRPE">0.01</Secretion>
            <Secretion Type="RPE">0.005</Secretion>
          <Uptake       Type="Vascular"                MaxUptake="0.28"
RelativeUptakeRate="0.28"/>
          <Uptake        Type="Stalk"                  MaxUptake="0.56"
RelativeUptakeRate="0.56"/>
          <Uptake         Type="Tip"                   MaxUptake="0.56"
RelativeUptakeRate="0.56"/>
         </SecretionData>

</DiffusionField>
```

```
   </Steppable>

</CompuCell3D>
```

angio_growth_19112010_11_16_47.py:

```
import sys
from os import environ
import string
sys.path.append(environ["PYTHON_MODULE_PATH"])

#

import CompuCellSetup

sim,simthread = CompuCellSetup.getCoreSimulationObjects()

#Create extra player fields here or add attributes

pyAttributeAdder,listAdder=CompuCellSetup.attachListToCells(sim)

CompuCellSetup.initializeSimulationObjects(sim,simthread)

#
##################
##########  PLUGINS
##################
#

import CompuCell

from angio_growth_plugins_19112010_11_16_47 import *

changeWatcherRegistry=CompuCellSetup.getChangeWatcherRegistry(sim)

stepperRegistry=CompuCellSetup.getStepperRegistry(sim)


mitPy=MitosisPyPlugin(sim,changeWatcherRegistry,stepperRegistry)
doublingVolumeDict = {6:64,5:64}
mitPy.setCellDoublingVolume(doublingVolumeDict)

#
##################
##########  STEPPABLES
##################
#


from PySteppables import SteppableRegistry
```

```
steppableRegistry=SteppableRegistry()

from angio_growth_steppables_19112010_11_16_47 import *
volumeParamSteppable=VolumeParamSteppable(sim,1)
steppableRegistry.registerSteppable(volumeParamSteppable)

#from          angio_growth_steppables_19112010_11_16_47          import
ExtraAttributeClock
#cell_attrib=ExtraAttributeClock(_simulator=sim,_frequency=1)
#steppableRegistry.registerSteppable(cell_attrib)



#
##################
##########  COMPUCELL3D LOOPS
##################
#

CompuCellSetup.mainLoop(sim,simthread,steppableRegistry)
```

angio_growth_plugins_19112010_11_16_47.py:

```
from CompuCell import MitosisSimplePlugin
from PyPlugins import *
from PySteppables import CellList
from CompuCell import NeighborFinderParams
import time,sys

class MitosisPyPluginBase(StepperPy,Field3DChangeWatcherPy):
   def
__init__(self,_simulator,_changeWatcherRegistry,_stepperRegistry):


      Field3DChangeWatcherPy.__init__(self,_changeWatcherRegistry)
      self.simulator=_simulator
      self.mitosisPlugin=MitosisSimplePlugin()
      self.mitosisPlugin.setPotts(self.simulator.getPotts())
      self.mitosisPlugin.turnOn()
      self.mitosisPlugin.init(self.changeWatcher.sim)
      self.counter=0
      self.mitosisFlag=0
      self.doublingVolumeDict=0
      _changeWatcherRegistry.registerPyChangeWatcher(self)
      _stepperRegistry.registerPyStepper(self)




   def setPotts(self,potts):
      self.mitosisPlugin.setPotts(potts)

   def setDoublingVolume(self,_doublingVolume):
```

```
      self.doublingVolume=_doublingVolume;
      self.mitosisPlugin.setDoublingVolume(self.doublingVolume)

   def setCellDoublingVolume(self,_doublingVolumeDict):
      self.doublingVolumeDict=_doublingVolumeDict;
      for i in self.doublingVolumeDict.keys():
         print self.doublingVolumeDict[i]

   def field3DChange(self):
      cell = self.changeWatcher.newCell
      if cell and self.doublingVolumeDict.has_key(cell.type) and
cell.volume>self.doublingVolumeDict[cell.type]:
         print "Type: ", cell.type, " Doubling Volume: ",
self.doublingVolumeDict[cell.type], " Current Volume: ", cell.volume
         self.setDoublingVolume(self.doublingVolumeDict[cell.type])

self.mitosisPlugin.field3DChange(self.changeWatcher.changePoint,self.ch
angeWatcher.newCell,self.changeWatcher.newCell)
         self.mitosisFlag=1

   def step(self):
      if self.mitosisFlag:
         print "ABOUT TO DO MITOSIS"
         self.mitosisFlag=self.mitosisPlugin.doMitosis()
         self.childCell=self.mitosisPlugin.getChildCell()
         self.parentCell=self.mitosisPlugin.getParentCell()
         self.updateAttributes()
         self.mitosisFlag=0

   def updateAttributes(self):
      self.childCell.targetVolume=self.parentCell.targetVolume
      self.childCell.lambdaVolume=self.parentCell.lambdaVolume
      self.childCell.type=self.parentCell.type


class MitosisPyPlugin(MitosisPyPluginBase):
   def __init__(self , _simulator , _changeWatcherRegistry ,
_stepperRegistry):

MitosisPyPluginBase.__init__(self,_simulator,_changeWatcherRegistry,_st
epperRegistry)


   def updateAttributes(self):


      if self.parentCell.type==6 or self.parentCell.type==5:
         self.childCell.type=6
       self.childCell.targetVolume=35
         self.childCell.lambdaVolume=12
         self.parentCell.targetVolume=35
         self.parentCell.lambdaVolume=12
       self.childCell.targetSurface=70
         self.childCell.lambdaSurface=10
         self.parentCell.targetSurface=70
```

```
         self.childCell.lambdaSurface=10


      if self.parentCell.type==4 :
         self.childCell.type=4
       self.childCell.targetVolume=30
         self.childCell.lambdaVolume=15
         self.parentCell.targetVolume=30
         self.parentCell.lambdaVolume=15
```

angio_growth_steppables_19112010_11_16_47.py:

```
from PySteppables import *
import CompuCell
import sys
import time
from math import *
from XMLUtils import dictionaryToMapStrStr as d2mss
from XMLUtils import CC3DXMLListPy

class VolumeParamSteppable(SteppablePy):
   def __init__(self,_simulator,_frequency=1):
      SteppablePy.__init__(self,_frequency)
      self.simulator=_simulator
      self.inventory=self.simulator.getPotts().getCellInventory()
      self.cellList=CellList(self.inventory)
      self.nTrackerPlugin=CompuCell.getNeighborTrackerPlugin()
      self.cellFieldG=self.simulator.getPotts().getCellFieldG()

self.focalPointPlasticityPlugin=CompuCell.getFocalPointPlasticityPlugin
()
      self.dim=self.cellFieldG.getDim()
      self.fieldNameNeoVascular = 'VEGF2'
      self.fieldNameRPE = 'Oxygen'
      self.fieldNameBM = 'MMP'
      self.output_file           =           open("902-JRB-28JRR-40JRP-
16LRB60LRR300.txt",'w')


   def start(self):
      import CompuCellSetup
      for cell in self.cellList:


         if cell.type== 1 or cell.type== 2:
          cell.targetVolume=67.0
            cell.lambdaVolume=25.0
          cell.targetSurface=120.0
            cell.lambdaSurface=25.0
          list_attrib=CompuCell.getPyAttrib(cell)
          list_attrib[0:2]=[0,801]
       if cell.type== 7:
          cell.targetVolume=42.0
```

```
            cell.lambdaVolume=12.0
          cell.targetSurface=70.0
            cell.lambdaSurface=10.0
       if cell.type== 5:
          cell.targetVolume=35.0
            cell.lambdaVolume=12.0
          cell.targetSurface=70.0
            cell.lambdaSurface=10.0
       if cell.type==3:
          cell.targetVolume=1
            cell.lambdaVolume=1000000000000.0
          cell.targetSurface=6
            cell.lambdaSurface=1000000000.0
       if cell.type==4:
          cell.targetVolume=36
            cell.lambdaVolume=10.0
          #cell.targetSurface=6
            #cell.lambdaSurface=1000000000.0
       if cell.type==8:
          cell.targetVolume=1000
            cell.lambdaVolume=25.0
          cell.targetSurface=900.0
            cell.lambdaSurface=25.0
       if cell.type==9:
          cell.targetVolume=512
            cell.lambdaVolume=12.0
          cell.targetSurface=600.0
            cell.lambdaSurface=10.0
       if cell.type == 5:
          list_attrib=CompuCell.getPyAttrib(cell)
          list_attrib[0:1]=[0]

   def step(self,mcs):

fieldNeoVasc=CompuCell.getConcentrationField(self.simulator,self.fieldN
ameNeoVascular)

fieldOXY=CompuCell.getConcentrationField(self.simulator,self.fieldNameR
PE)

fieldMMP=CompuCell.getConcentrationField(self.simulator,self.fieldNameB
M)
      self.Potts=self.simulator.getPotts()
      StalkTotalVolume=1.0
      POS_BRM_contact_total=0
      POS_CNV_contact_total=0
      CNV_BRM_contact_total=0
      totalVEGF2=0
      StalkTotal=0.01
      RPETotal=0
      HRPETotal=0
      pressure = 0
      RPE_BRM_totalArea = 0
```

```
    for cell in self.cellList:
       #print "lambda Volume: ", cell.lambdaVolume , "  TargetVolume:
" , cell.targetVolume,
     list_attrib=CompuCell.getPyAttrib(cell)
     POS_BRM_contact=0
     POS_CNV_contact=0
     CNV_BRM_contact=0
     Stalk_NEI=0


       ### Vascular
       if cell.type == 7:
         totalArea = 0
       Tip_Neighbor=0


cellNeighborList=CellNeighborListAuto(self.nTrackerPlugin,cell)
         for neighborSurfaceData in cellNeighborList:
           #Check to ensure cell neighbor is not medium
           if neighborSurfaceData.neighborAddress:


             if  neighborSurfaceData.neighborAddress.type  ==  5  or
neighborSurfaceData.neighborAddress.type         ==         6         or
neighborSurfaceData.neighborAddress.type == 7:

               #sum  up  common  surface  area  of  cell  with  its
neighbors
               totalArea+=neighborSurfaceData.commonSurfaceArea
               #print    "concentration:    ",    concentration,"
commonSurfaceArea:",neighborSurfaceData.commonSurfaceArea



       pt=CompuCell.Point3D()
         pt.x=int(floor(cell.xCM/max(float(cell.volume),0.001)))
         pt.y=int(floor(cell.yCM/max(float(cell.volume),0.001)))
         pt.z=int(floor(cell.zCM/max(float(cell.volume),0.001)))
         concentration=fieldNeoVasc.get(pt)
         if concentration < 0.00001 and mcs>1000:
          cell.targetVolume=0.0
          cell.targetSurface=0.0
     # Stalk
     if cell.type == 6:

         totalArea = 0
       StalkTotalVolume+=cell.volume
       StalkTotal+=1
       pt=CompuCell.Point3D()
       pt.x=int(floor(cell.xCM/max(float(cell.volume),0.001)))
         pt.y=int(floor(cell.yCM/max(float(cell.volume),0.001)))
         pt.z=int(floor(cell.zCM/max(float(cell.volume),0.001)))
         concentration=fieldNeoVasc.get(pt)
```

```
cellNeighborList=CellNeighborListAuto(self.nTrackerPlugin,cell)
            for neighborSurfaceData in cellNeighborList:
               #Check to ensure cell neighbor is not medium
               if neighborSurfaceData.neighborAddress:
                  if neighborSurfaceData.neighborAddress.type == 5 or
neighborSurfaceData.neighborAddress.type == 6 or
neighborSurfaceData.neighborAddress.type == 7:

                     #sum up common surface area of cell with its
endothelial neighbors
                     totalArea+=neighborSurfaceData.commonSurfaceArea
                  if neighborSurfaceData.neighborAddress.type == 3:
                      #sum up common surface area of cell with Bruch's
membrane
                 CNV_BRM_contact+=neighborSurfaceData.commonSurfaceArea
          CNV_BRM_contact_total+= CNV_BRM_contact
            if totalArea < 17 and (cell.targetVolume-cell.volume)<=2: #
a stalk cell grow when its contact area and internal pressure is less
than the two corresponding thresholds

               #Growth rate equation

             cell.targetVolume+=0.426 * concentration/(0.005 +
concentration)
             cell.targetSurface+= 0.852 * concentration/(0.005 +
concentration)
             # elongate the equilibrium lengths of plastic links with
other ECs when stalk cells grow

plasticityList=FocalPointPlasticityDataList(self.focalPointPlasticityPl
ugin,cell)
               for plasticityData in plasticityList:
              if plasticityData.neighborAddress.type==7 or
plasticityData.neighborAddress.type==6:
                ave_targetDistance= (cell.volume +
plasticityData.neighborAddress.volume)/15.0
                vol = plasticityData.neighborAddress.volume
                xmid=float(plasticityData.neighborAddress.xCM) /
(vol+0.001)
                ymid=float(plasticityData.neighborAddress.yCM) /
(vol+0.001)
                zmid=float(plasticityData.neighborAddress.zCM) /
(vol+0.001)
                xdiff = xmid-pt.x
                ydiff = ymid-pt.y
                zdiff = zmid-pt.z
                if abs(xdiff) > (self.dim.x/2):
                  xdiff=(abs(xdiff)-self.dim.x)
                if abs(ydiff) > (self.dim.y/2):
                  ydiff=(abs(ydiff)-self.dim.y)

                actualDist =
((xdiff*xdiff)+(ydiff*ydiff)+(zdiff*zdiff))**(0.5)
```

```
                print     "plasticityData.neighborAddress.type        ",
plasticityData.neighborAddress.type,"plasticityData.targetDistance",pla
sticityData.targetDistance, "actual dist ", actualDist

self.focalPointPlasticityPlugin.setFocalPointPlasticityParameters(cell,
plasticityData.neighborAddress,plasticityData.lambdaDistance,actualDist
,actualDist*2)
            if  (concentration  <  0.00001  and  mcs>1000):  #  kill  stalk
cells  when  RPE-derived  VEGF  is  too  low,  initial  concentration  of  is  0
so  we  wait  1000mcs  for  the  RPE-derived  VEGF  to  reach  its  stationary
concentration
             cell.targetVolume=0.0
             cell.targetSurface=0.0


        #### Tip
         if cell.type == 5 and mcs==400: #tip cells are capable of MMP
secretion for the first 24 hours
          cell.type = 6



         ###RPE Cells
         if cell.type == 1 or cell.type == 2:
            totalArea=0
          RPETotal+=1
            pt=CompuCell.Point3D()
            pt.x=int(floor(cell.xCM/max(float(cell.volume),0.001)))
            pt.y=int(floor(cell.yCM/max(float(cell.volume),0.001)))
            pt.z=int(floor(cell.zCM/max(float(cell.volume),0.001)))
            if pt.x==40:
            pt.x=0
          if pt.y==40:
            pt.y=0
          concentration2=fieldOXY.get(pt)

cellNeighborList=CellNeighborListAuto(self.nTrackerPlugin,cell)
            for neighborSurfaceData in cellNeighborList:
               #Check to ensure cell neighbor is not medium
               if neighborSurfaceData.neighborAddress:
                  if neighborSurfaceData.neighborAddress.type == 3:

RPE_BRM_totalArea+=neighborSurfaceData.commonSurfaceArea
                  if  neighborSurfaceData.neighborAddress.type  ==  3  or
neighborSurfaceData.neighborAddress.type        ==        1        or
neighborSurfaceData.neighborAddress.type == 2:
                     #sum  up  common  surface  area  of  cell  with  its
neighbors
                     totalArea+=neighborSurfaceData.commonSurfaceArea


          if  ( totalArea == 0   and mcs>10): # RPE cells die when lose
contact with their other RPEs and Bruch's membrane
             cell.targetVolume-=0.5
               cell.targetSurface-=0.5
```

```
             if cell.targetVolume<0 or cell.targetSurface<0:
            cell.targetVolume=0.0
            cell.targetSurface=0.0


          if cell.type==1 and concentration2 < 49 and list_attrib[1] >
800: #switch to HRPE cell type when PO2 is less than 49mmHg

             cell.type=2
             HRPETotal+=1
             RPETotal-=1
             list_attrib[0] = 1
          if cell.type==1:
             list_attrib[1] += 1

          if cell.type==2 and (concentration2 > 49 or list_attrib[0] >
800): #hypoxic RPE cells stop VEGF overexpression after 48 hours
               #aveox = aveox+concentration2;
             #print "concentration2", concentration2
             cell.type=1
             list_attrib[0] = 0
             list_attrib[1] = 1
          if cell.type==2 and (concentration2 < 49 or list_attrib[0] <
800):
             list_attrib[0] += 1
             #print "HRPE  ", list_attrib[0]
             HRPETotal+=1
             RPETotal-=1




         ##BM Cells
         if cell.type == 3 and mcs<500:
            pt=CompuCell.Point3D()


pt.x=int(floor(cell.xCM/max(float(cell.volume),0.000000001)))

pt.y=int(floor(cell.yCM/max(float(cell.volume),0.000000001)))

pt.z=int(floor(cell.zCM/max(float(cell.volume),0.000000001)))
          concentration2=fieldMMP.get(pt)
            cell.targetVolume-=0.075*concentration2  #  reducing  Bruch's
membrane  target  volume  proportional  to  MMP  concentration  and  removing
the voxel when target volume becomes zero

       if cell.type == 8 or cell.type == 9: # calculating total common
contact area between POS and Bruch's membrane and POS and CNV


cellNeighborList=CellNeighborListAuto(self.nTrackerPlugin,cell)
          for neighborSurfaceData in cellNeighborList:
               #Check to ensure cell neighbor is not medium
               if neighborSurfaceData.neighborAddress:
                  if neighborSurfaceData.neighborAddress.type == 3:
```

```
                 POS_BRM_contact+=neighborSurfaceData.commonSurfaceArea
                  if neighborSurfaceData.neighborAddress.type == 5 or
neighborSurfaceData.neighborAddress.type == 6:
                 POS_CNV_contact+=neighborSurfaceData.commonSurfaceArea
          POS_BRM_contact_total+= POS_BRM_contact
          POS_CNV_contact_total+= POS_CNV_contact


      if int(mcs/100.0)==mcs/100.0: #writing cell counts and contact
areas to a file every 100mcs

       self.output_file = open("902-JRB-28JRR-40JRP-
16LRB60LRR300.txt",'a')
       self.output_file.write("%d %d %d %d %d %d %d" %( StalkTotal,
RPETotal, HRPETotal ,
POS_BRM_contact_total,POS_CNV_contact_total,CNV_BRM_contact_total,RPE_B
RM_totalArea))
       self.output_file.write("\n")
       self.output_file.close()




from CompuCell import MitosisSimplePlugin
from PyPlugins import *
from PySteppables import CellList
from CompuCell import NeighborFinderParams
import time,sys

class MitosisPyPluginBase(StepperPy,Field3DChangeWatcherPy):
   def
__init__(self,_simulator,_changeWatcherRegistry,_stepperRegistry):


      Field3DChangeWatcherPy.__init__(self,_changeWatcherRegistry)
      self.simulator=_simulator
      self.mitosisPlugin=MitosisSimplePlugin()
      self.mitosisPlugin.setPotts(self.simulator.getPotts())
      self.mitosisPlugin.turnOn()
      self.mitosisPlugin.init(self.changeWatcher.sim)
      self.counter=0
      self.mitosisFlag=0
      self.doublingVolumeDict=0
      _changeWatcherRegistry.registerPyChangeWatcher(self)
      _stepperRegistry.registerPyStepper(self)




   def setPotts(self,potts):
      self.mitosisPlugin.setPotts(potts)

   def setDoublingVolume(self,_doublingVolume):
      self.doublingVolume=_doublingVolume;
      self.mitosisPlugin.setDoublingVolume(self.doublingVolume)
```

```
   def setCellDoublingVolume(self,_doublingVolumeDict):
      self.doublingVolumeDict=_doublingVolumeDict;
      for i in self.doublingVolumeDict.keys():
         print self.doublingVolumeDict[i]

   def field3DChange(self):
      cell = self.changeWatcher.newCell
      if cell and self.doublingVolumeDict.has_key(cell.type) and
cell.volume>self.doublingVolumeDict[cell.type]:
         print "Type: ", cell.type, " Doubling Volume: ",
self.doublingVolumeDict[cell.type], " Current Volume: ", cell.volume
         self.setDoublingVolume(self.doublingVolumeDict[cell.type])

self.mitosisPlugin.field3DChange(self.changeWatcher.changePoint,self.ch
angeWatcher.newCell,self.changeWatcher.newCell)
         self.mitosisFlag=1

   def step(self):
      if self.mitosisFlag:
         print "ABOUT TO DO MITOSIS"
         self.mitosisFlag=self.mitosisPlugin.doMitosis()
         self.childCell=self.mitosisPlugin.getChildCell()
         self.parentCell=self.mitosisPlugin.getParentCell()
         self.updateAttributes()
         self.mitosisFlag=0

   def updateAttributes(self):
      self.childCell.targetVolume=self.parentCell.targetVolume
      self.childCell.lambdaVolume=self.parentCell.lambdaVolume
      self.childCell.type=self.parentCell.type


class MitosisPyPlugin(MitosisPyPluginBase):
   def __init__(self , _simulator , _changeWatcherRegistry ,
_stepperRegistry):

MitosisPyPluginBase.__init__(self,_simulator,_changeWatcherRegistry,_st
epperRegistry)


   def updateAttributes(self):


      if self.parentCell.type==6 or self.parentCell.type==5:
         self.childCell.type=6
       self.childCell.targetVolume=35
         self.childCell.lambdaVolume=12
         self.parentCell.targetVolume=35
         self.parentCell.lambdaVolume=12
       self.childCell.targetSurface=70
         self.childCell.lambdaSurface=10
         self.parentCell.targetSurface=70
         self.childCell.lambdaSurface=10
```

```
    if self.parentCell.type==4 :
       self.childCell.type=4
     self.childCell.targetVolume=30
       self.childCell.lambdaVolume=15
       self.parentCell.targetVolume=30
       self.parentCell.lambdaVolume=15
```

References

1. Merks RM, Perryn ED, Shirinifard A, Glazier JA (2008) Contact-inhibited chemotaxis in de novo and sprouting blood-vessel growth. PLoS Comput Biol 4: e1000163.
2. Carmeliet P (2005) Angiogenesis in life, disease and medicine. Nature 438: 932-936.
3. Hellström M, Phng LK, Hofmann JJ, Wallgard E, Coultas L, et al. (2007) Dll4 signalling through Notch1 regulates formation of tip cells during angiogenesis. Nature 445: 776-780.
4. Carmeliet P (2000) Mechanisms of angiogenesis and arteriogenesis. Nature Medicine 6: 389-395.
5. Helmlinger G, Endo M, Ferrara N, Hlatky L, Jain RK (2000) Growth factors: formation of endothelial cell networks. Nature 405: 139-141.
6. Coultas L, Chawengsaksophak K, Rossant J (2005) Endothelial cells and VEGF in vascular development. NATURE-LONDON- 438: 937.
7. Salvucci O, Yao L, Villalba S, Sajewicz A, Pittaluga S, et al. (2002) Regulation of endothelial cell branching morphogenesis by endogenous chemokine stromal-derived factor-1. Blood 99: 2703.
8. Salvucci O, de la Luz Sierra M, Martina JA, McCormick PJ, Tosato G (2006) EphB2 and EphB4 receptors forward signaling promotes SDF-1-induced endothelial cell chemotaxis and branching remodeling. Blood 108: 2914-2922.
9. Seghezzi G, Patel S, Ren CJ, Gualandris A, Pintucci G, et al. (1998) Fibroblast growth factor-2 (FGF-2) induces vascular endothelial growth factor (VEGF) expression in the endothelial cells of forming capillaries: an autocrine mechanism contributing to angiogenesis. The Journal of cell biology 141: 1659-1673.
10. Autiero M, De Smet F, Claes F, Carmeliet P (2005) Role of neural guidance signals in blood vessel navigation. Cardiovascular research 65: 629-638.
11. Serini G, Ambrosi D, Giraudo E, Gamba A, Preziosi L, et al. (2003) Modeling the early stages of vascular network assembly. The EMBO journal 22: 1771-1779.
12. Gamba A, Ambrosi D, Coniglio A, de Candia A, Di Talia S, et al. (2003) Percolation, morphogenesis, and burgers dynamics in blood vessels formation. Physical review letters 90: 118101.
13. Lee S, Chen TT, Barber CL, Jordan MC, Murdock J, et al. (2007) Autocrine VEGF signaling is required for vascular homeostasis. Cell 130: 691-703.
14. Vernon RB, Sage EH (1995) Between molecules and morphology. Extracellular matrix and creation of vascular form. The American journal of pathology 147: 873-883.
15. Manoussaki D, Lubkin SR, Vernon RB, Murray JD (1996) A mechanical model for the formation of vascular networks in vitro. Acta biotheoretica 44: 271-282.
16. Namy P, Ohayon J, Tracqui P (2004) Critical conditions for pattern formation and in vitro tubulogenesis driven by cellular traction fields. Journal of theoretical biology 227: 103-120.
17. Szabo A, Perryn ED, Czirok A (2007) Network formation of tissue cells via preferential attraction to elongated structures. Physical review letters 98: 038102.

18. Gory-Faure S, Prandini MH, Pointu H, Roullot V, Pignot-Paintrand I, et al. (1999) Role of vascular endothelial-cadherin in vascular morphogenesis. Development 126: 2093-2102.
19. Perryn ED, Czirok A, Little CD (2008) Vascular sprout formation entails tissue deformations and VE-cadherin-dependent cell-autonomous motility. Developmental biology 313: 545-555.
20. Dejana E (2004) Endothelial cell-cell junctions: happy together. Nature reviews Molecular cell biology 5: 261-270.
21. Merks RMH, Brodsky SV, Goligorksy MS, Newman SA, Glazier JA (2006) Cell elongation is key to in silico replication of in vitro vasculogenesis and subsequent remodeling. Developmental biology 289: 44-54.
22. Merks RMH, Glazier JA (2006) Dynamic mechanisms of blood vessel growth. Nonlinearity 19: 1-10.
23. Gerhardt H, Golding M, Fruttiger M, Ruhrberg C, Lundkvist A, et al. (2003) VEGF guides angiogenic sprouting utilizing endothelial tip cell filopodia. The Journal of cell biology 161: 1163-1177.
24. Ambrosi D, Gamba A, Serini G (2004) Cell directional persistence [corrected] and chemotaxis in vascular morphogenesis. Bulletin of mathematical biology 66: 1851-1873.
25. Tosin A, Ambrosi D, Preziosi L (2006) Mechanics and chemotaxis in the morphogenesis of vascular networks. Bulletin of mathematical biology 68: 1819-1836.
26. Walker GM, Sai J, Richmond A, Stremler M, Chung CY, et al. (2005) Effects of flow and diffusion on chemotaxis studies in a microfabricated gradient generator. Lab on a chip 5: 611-618.
27. Merks RMH, Newman SA, Glazier JA (2004) Cell-oriented modeling of in vitro capillary development. Cellular Automata: 425-434.
28. Anderson AR, Chaplain. MA (1998) Continuous and discrete mathematical models of tumor-induced angiogenesis. Bull Math Biol 60: 857-899.
29. Tong S, Yuan F (2001) Numerical simulations of angiogenesis in the cornea. Microvascular research 61: 14-27.
30. Levine HA, Sleeman BD, Nilsen-Hamilton M (2001) Mathematical modeling of the onset of capillary formation initiating angiogenesis. Journal of mathematical biology 42: 195-238.
31. Bauer AL, Jackson TL, Jiang Y (2007) A cell-based model exhibiting branching and anastomosis during tumor-induced angiogenesis. Biophysical journal 92: 3105-3121.
32. Manoussaki D (2003) A mechanochemical model of angiogenesis and vasculogenesis. ESAIM: Mathematical Modelling and Numerical Analysis 37: 581-599.
33. Merks RMH, Glazier JA (2006) Dynamic mechanisms of blood vessel growth. Nonlinearity 19: C1.
34. Graner F, Glazier J (1992) Simulation of biological cell sorting using a two-dimensional extended Potts model. Physical Review Letters 69: 2013-2016.

35. Glazier JA, Graner F (1993) Simulation of the differential adhesion driven rearrangement of biological cells. Physical Review E 47: 2128-2154.
36. Savill NJ, Hogeweg P (1996) Modelling morphogenesis: from single cells to crawling slugs. J theor Biol 184: 229-235.
37. Merks RMH, Glazier JA (2005) A cell-centered approach to developmental biology. Physica A: Statistical Mechanics and its Applications 352: 113-130.
38. Lin F, Butcher EC (2006) T cell chemotaxis in a simple microfluidic device. Lab on a chip 6: 1462-1469.
39. Savill NJ, Hogeweg P (1997) Modelling morphogenesis: from single cells to crawling slugs. J Theor Biol 184: 229.
40. Homsy G (1987) Viscous fingering in porous media. Annual Review of Fluid Mechanics 19: 271-311.
41. Holm EA, Glazier JA, Srolovitz DJ, Grest GS (1991) Effects of lattice anisotropy and temperature on domain growth in the two-dimensional Potts model. Physical Review A 43: 2662-2668.
42. Vailhe B, Vittet D, Feige JJ (2001) In vitro models of vasculogenesis and angiogenesis. Lab Invest 81: 439-452.
43. Shiba Y, Takahashi M, Ikeda U (2008) Models for the study of angiogenesis. Curr Pharm Des 14: 371-377.
44. Ucuzian AA, Greisler HP (2007) In vitro models of angiogenesis. World J Surg 31: 654-663.
45. Staton CA, Reed MW, Brown NJ (2009) A critical analysis of current in vitro and in vivo angiogenesis assays. Int J Exp Pathol 90: 195-221.
46. Bordenave L, Fernandez P, Remy-Zolghadri M, Villars S, Daculsi R, et al. (2005) In vitro endothelialized ePTFE prostheses: clinical update 20 years after the first realization. Clin Hemorheol Microcirc 33: 227-234.
47. Alobaid N, Salacinski HJ, Sales KM, Hamilton G, Seifalian AM (2005) Single stage cell seeding of small diameter prosthetic cardiovascular grafts. Clin Hemorheol Microcirc 33: 209-226.
48. Ingber DE, Folkman J (1989) How does extracellular matrix control capillary morphogenesis? Cell 58: 803-805.
49. Ingber DE, Folkman J (1989) Mechanochemical switching between growth and differentiation during fibroblast growth factor-stimulated angiogenesis in vitro: role of extracellular matrix. The Journal of cell biology 109: 317-330.
50. Kubota Y, Kleinman HK, Martin GR, Lawley TJ (1988) Role of laminin and basement membrane in the morphological differentiation of human endothelial cells into capillary-like structures. The Journal of cell biology 107: 1589-1598.
51. Madri JA, Williams SK (1983) Capillary endothelial cell cultures: phenotypic modulation by matrix components. The Journal of cell biology 97: 153-165.
52. Vailhé B, Ronot X, Tracqui P, Usson Y, Tranqui L (1997) In vitro angiogenesis is modulated by the mechanical properties of fibrin gels and is related to v 3 integrin localization. In Vitro Cellular & Developmental Biology-Animal 33: 763-773.
53. Feder J, Marasa JC, Olander JV (1983) The formation of capillary-like tubes by calf aortic endothelial cells grown in vitro. Journal of cellular physiology 116: 1-6.
54. Folkman J, Haudenschild C (1980) Angiogenesis in vitro.

55. Maciag T, Kadish J, Wilkins L, Stemerman MB, Weinstein R (1982) Organizational behavior of human umbilical vein endothelial cells. The Journal of cell biology 94: 511-520.
56. Pelletier L, Regnard J, Fellmann D, Charbord P (2000) An in vitro model for the study of human bone marrow angiogenesis: role of hematopoietic cytokines. Laboratory investigation; a journal of technical methods and pathology 80: 501-511.
57. Nicosia RF, Tchao R, Leighton J (1982) Histotypic angiogenesis in vitro: light microscopic, ultrastructural, and radioautographic studies. In Vitro 18: 538-549.
58. Gagnon E, Cattaruzzi P, Griffith M, Muzakare L, LeFlao K, et al. (2002) Human vascular endothelial cells with extended life spans: in vitro cell response, protein expression, and angiogenesis. Angiogenesis 5: 21-33.
59. Sun XT, Ding YT, Yan XG, Wu LY, Li Q, et al. (2004) Angiogenic synergistic effect of basic fibroblast growth factor and vascular endothelial growth factor in an in vitro quantitative microcarrier-based three-dimensional fibrin angiogenesis system. World journal of gastroenterology : WJG 10: 2524-2528.
60. Arnaoutova I, Kleinman HK (2010) In vitro angiogenesis: endothelial cell tube formation on gelled basement membrane extract. Nat Protoc 5: 628-635.
61. Staton CA, Stribbling SM, Tazzyman S, Hughes R, Brown NJ, et al. (2004) Current methods for assaying angiogenesis in vitro and in vivo. Int J Exp Pathol 85: 233-248.
62. Auerbach R, Akhtar N, Lewis RL, Shinners BL (2000) Angiogenesis assays: problems and pitfalls. Cancer Metastasis Rev 19: 167-172.
63. Deroanne CF, Lapiere CM, Nusgens BV (2001) In vitro tubulogenesis of endothelial cells by relaxation of the coupling extracellular matrix-cytoskeleton. Cardiovascular research 49: 647.
64. Mancuso MR, Davis R, Norberg SM, O'Brien S, Sennino B, et al. (2006) Rapid vascular regrowth in tumors after reversal of VEGF inhibition. The Journal of clinical investigation 116: 2610-2621.
65. deWaal RMW, Leenders. WPJ (2005) Sprouting angiogenesis versus co-option in tumor angiogenesis.: 65-76.
66. Friedl P, Wolf K (2003) Tumour-cell invasion and migration: diversity and escape mechanisms. Nat Rev Cancer 3: 362-374.
67. Shima DT, Adamis, Ferrara N, Yeo KT, Yeo T, et al. (1995) Hypoxic induction of endothelial growth factors in retinal cells: identification of vascular endothelial growth factor (\textitVEGF) as the mitogen. Molecular Medicine 1: 182-193.
68. Carmeliet P (2001) Cardiovascular biology. Creating unique blood vessels. Nature 412: 868-869.
69. Marti HH (2005) Angiogenesis - a self adapting principle in hypoxia.: 163-180.
70. Folkman J (1995) Angiogenesis in cancer, vascular, rheumatoid and other disease. Nature Med 1: 27-31.
71. Folkman J, D'Amore. PA (1996) Blood vessel formation: what is its molecular basis? Cell 87: 1153-1155.

72. Jiang B-H, Semenza GL, Bauer C, Marti. HH (1996) Hypoxia-inducible factor 1 levels vary exponentially over a physiologically relevant range of O$_2$ tension. Am J Physiol 271: C1172-C1180.
73. Jewell UR, Kvietikova I, Scheid A, Bauer C, Wenger RH, et al. (2001) Induction of HIF-1α in response to hypoxia is instantaneous. . FASEB J 15: 1312-1314.
74. Wenger. RH (2002) Cellular adaptation to hypoxia: O$_2$-sensing protein hydroxylases, hypoxia-inducible transcription factors, and O2-regulated gene expression. FASEB J 16: 1151-1162.
75. Robinson CJ, Stringer. SE (2001) The splice variants of vascular endothelial growth factor (\textitVEGF) and their receptors. J Cell Sci 114: 853-865.
76. Kusters B, de Waal RM, Wesseling P, Verrijp K, Maass C, et al. (2003) Differential effects of vascular endothelial growth factor \textrmA isoforms in a mouse brain metastasis model of human melanoma. Cancer Res 63: 5408-5413.
77. Gerhardt H (2008) VEGF and endothelial guidance in angiogenic sprouting. Organogenesis 4: 241-246.
78. Phng LK, Gerhardt H (2009) Angiogenesis: a team effort coordinated by notch. Dev Cell 16: 196-208.
79. Jurasz P, Alonso D, Castro-Blanco S, Murad F, Radomski. MW (2003) Generation and role of angiostatin in human platelets. Blood 102: 3217-3223.
80. Wallez Y, Huber. P (2008) Endothelial adherens and tight junctions in vascular homeostasis, inflammation and angiogenesis. Biochim Biophys Acta 1778: 794-809.
81. Dejana E, Corada M, Lampugnani MG (1995) Endothelial cell-to-cell junctions. FASEB J 9: 910-918.
82. Perryn ED, Czir\'ok A, Little. CD (2003) Vascular sprout formation entails tissue deformations and \textrmVE-cadherin-dependent cell-autonomous motility. Dev Biol 2008: 545-555.
83. Lampugnani MG, Zanetti A, Corada M, Takahashi T, Balconi G, et al. (2003) Contact inhibition of \textrmVEGF-induced proliferation requires vascular endothelial cadherin, β-catenin, and the phosphatase \textrmDEP-1/CD148. J Cell Biol 161: 793-804.
84. Carmeliet. P (2003) Angiogenesis in health and disease. . Nat Med 9: 653-660.
85. Dor Y, Djonov V, Keshet. E (2003) Making vascular networks in the adult: branching morphogenesis without a roadmap. Trends Cell Biol 13: 131-136.
86. Carmeliet P, Jain RK (2000) Angiogenesis in cancer and other diseases. NATURE-LONDON-: 249-257.
87. Sanga S, Frieboes HB, Zheng X, Gatenby R, Bearer EL, et al. (2007) Predictive oncology: a review of multidisciplinary, multiscale in silico modeling linking phenotype, morphology and growth. Neuroimage 37: 120-134.
88. Anderson ARA, Chaplain MAJ (1998) Continuous and discrete mathematical models of tumor-induced angiogenesis. Bulletin of mathematical biology 60: 857-899.
89. Alarcon T, Byrne HM, Maini PK (2004) Towards whole-organ modelling of tumour growth. Progress in biophysics and molecular biology 85: 451-472.

90. Macklin P, McDougall S, Anderson AR, Chaplain MA, Cristini V, et al. (2009) Multiscale modelling and nonlinear simulation of vascular tumour growth. J Math Biol 58: 765-798.
91. Mantzaris NV, Webb S, Othmer HG (2004) Mathematical modeling of tumor-induced angiogenesis. J Math Biol 49: 111-187.
92. Zheng X, Wise SM, Cristini V (2005) Nonlinear simulation of tumor necrosis, neo-vascularization and tissue invasion via an adaptive finite-element/level-set method. Bull Math Biol 67: 211-259.
93. Frieboes HB, Lowengrub JS, Wise S, Zheng X, Macklin P, et al. (2007) Computer simulation of glioma growt and morphology. Neuroimage 37: 59-70.
94. Plank MJ, Sleeman BD (2004) Lattice and non-lattice models of tumour angiogenesis. Bull Math Biol 66: 1785-1819.
95. Cristini V, Li X, Lowengrub JS, Wise SM (2009) Nonlinear simulations of solid tumor growth using a mixture model: invasion and branching. J Math Biol 58: 723-763.
96. Owen MR, Alarcon T, Maini PK, Byrne HM (2009) Angiogenesis and vascular remodelling in normal and cancerous tissues. Math Biol 58: 689-721.
97. Bartha K, Rieger H (2006) Vascular network remodeling via vessel cooption, regression and growth in tumors. J Theor Biol 241: 903-918.
98. Welter M, Bartha K, Rieger H (2008) Emergent vascular network inhomogeneities and resulting blood flow patterns in a growing tumor. J Theor Biol 250: 257-280.
99. McDougall SR, Anderson AR, Chaplain MA (2006) Mathematical modelling of dynamic adaptive tumour-induced angiogenesis: clinical implications and therapeutic targeting strategies. J Theor Biol 241: 564-589.
100. Stephanou A, McDougall SR, Anderson ARA (2005) Mathematical Modelling of Flow in 2D and 3D Vascular Networks: Applications to Anti-Angiogenic and Chemotherapeutic Drug Strategies. Math Comput Model 41: 1137-1156.
101. Stephanou A, McDougall SR, Anderson ARA (2006) Mathematical modelling of the influence of blood rheological properties upon adaptative tumour-induced angiogenesis. Math Comput Model 44: 96-123.
102. Pries AR, Secomb TW, Gaehtgens P (1996) Biophysical aspects of blood flow in the microvasculature. Cardiovasc Res 32: 654-667.
103. Pries AR, Secomb TW (2005) Control of blood vessel structure: insights from theoretical models. Am J Physiol Heart Circ Physiol 288: 1010-1015.
104. Pries AR, Secomb TW (2008) Modeling structural adaptation of microcirculation. Microcirculation 15: 753-764.
105. Ramis-Conde I, Chaplain MA, Anderson AR, Drasdo. D (2009) Multi-scale modelling of cancer cell intravasation: the role of cadherins in metastasis. Phys Biol 6: 16008.
106. Glazier JA, Balter A, Pop\lawski NJ (2007) Magnetization to morphogenesis: a brief history of the Glazier-Graner-Hogeweg model. 79-106.
107. Poplawski NJ, Agero U, Gens JS, Swat M, Glazier JA, et al. (2009) Front instabilities and invasiveness of simulated avascular tumors. Bulletin of mathematical biology 71: 1189-1227.

108. Anderson ARA (2005) A hybrid mathematical model of solid tumour invasion: the importance of cell adhesion. Math Med Biol 22: 163.
109. Rubenstein BM, Kaufman LJ (2008) The role of extracellular matrix in glioma invasion: a cellular Potts model approach. Biophys J 95: 5661-5680.
110. Vaupel P, Kallinowski F, Okunieff. P (1989) Blood flow, oxygen and nutrient supply, and metabolic microenvironment of human tumors: a review. Cancer Res 49: 6449-6465.
111. Fischer I, Gagner JP, Law M, Newcomb EW, Zagzag D (2005) Angiogenesis in gliomas: biology and molecular pathophysiology. Brain Pathol 15: 297-310.
112. Chen N, Glazier JA, Izaguirre JA, Alber MS (2007) A parallel implementation of the Cellular Potts model for simulation of cell-based morphogenesis. Comput Phys Commun 176: 670-681.
113. Helmlinger G, Yuan F, Dellian M, Jain. RK (1997) Interstitial pH and pO$_2$ gradients in solid tumors \textitin vivo: high-resolution measurements reveal a lack of correlation. Nature Med 3: 177-182.
114. Popławski NJ, Agero U, Gens JS, Swat M, Glazier JA, et al. (2009) Front instabilities and invasiveness of simulated avascular tumors. Bull Math Biol 71: 1189-1227.
115. Chaplain MA, McDougall SR, Anderson AR (2006) Mathematical modeling of tumor-induced angiogenesis. Annu Rev Biomed Eng 8: 233-257.
116. Popel AS (1989) Theory of oxygen transport to tissue. Crit Rev Biomed Eng 17: 257-321.
117. Swat MH, Hester SD, Balter AI, Heiland RW, Zaitlen BL, et al. (2009) Multicell simulations of development and disease using the CompuCell3D simulation environment. Methods Mol Biol 500: 361-428.
118. Fotos JS, Patel VP, Karin NJ, Temburni MK, Koh JT, et al. (2006) Automated time-lapse microscopy and high-resolution tracking of cell migration. Cytotechnology 51: 7-19.
119. Bray D (1992) Cell Movements.
120. Sander LM, Deisboeck TS (2002) Growth patterns of microscopic brain tumors. Phys Rev E 66: 051901.
121. Burgess PK, Kulesa PM, Murray JD, Alvord EC (1997) The interaction of growth rates and diffusion coefficients in a three-dimensional mathematical model of gliomas. J Neuropathol Exp Neurol 56: 704-713.
122. Graner F, Glazier JA (1992) Simulation of biological cell sorting using a two-dimensional extended Potts model. Phys Rev Lett 69: 2013-2016.
123. Smith W, Assink J, Klein R, Mitchell P, Klaver CC, et al. (2001) Risk factors for age-related macular degeneration: Pooled findings from three continents. Ophthalmology 108: 697-704.
124. Grossniklaus HE, Green WR (2004) Choroidal neovascularization. Am J Ophthalmol 137: 496-503.
125. Liakopoulos S, Ongchin S, Bansal A, Msutta S, Walsh AC, et al. (2008) Quantitative optical coherence tomography findings in various subtypes of neovascular age-related macular degeneration. Invest Ophthalmol Vis Sci 49: 5048-5054.

126. Group MPS (1996) Occult choroidal neovascularization. Influence on visual outcome in patients with age-related macular degeneration. Macular Photocoagulation Study Group. Arch Ophthalmol 114: 400-412.
127. Lim JI, Tsong JW (2007) Exudative (neovascular) age-related macular degeneration. In: Lim JI, editor. Age-related macular degeneration: Informa Healthcare. pp. 125-157.
128. Bunt-Milam AH, Saari JC, Klock IB, Garwin GG (1985) *Zonulae adherentes* pore size in the external limiting membrane of the rabbit retina. Invest Ophthalmol Vis Sci 26: 1377-1380.
129. Cheng H, Nair G, Walker TA, Kim MK, Pardue MT, et al. (2006) Structural and functional MRI reveals multiple retinal layers. Proc Natl Acad Sci USA 103: 17525-17530.
130. Bagci AM, Shahidi M, Ansari R, Blair M, Blair NP, et al. (2008) Thickness profiles of retinal layers by optical coherence tomography image segmentation. Am J Ophthalmol 146: 679-687.
131. Ramrattan RS, van der Schaft TL, Mooy CM, de Bruijn WC, Mulder PG, et al. (1994) Morphometric analysis of Bruch's membrane, the choriocapillaris, and the choroid in aging. Invest Ophthalmol Vis Sci 35: 2857-2864.
132. Booij JC, Baas DC, Beisekeeva J, Gorgels TG, Bergen AA (2010) The dynamic nature of Bruch's membrane. Prog Retin Eye Res 29: 1-18.
133. Sarks SH, Arnold JJ, Killingsworth MC, Sarks JP (1999) Early drusen formation in the normal and aging eye and their relation to age related maculopathy: a clinicopathological study. Br J Ophthalmol 83: 358-368.
134. Slakter JS, Yannuzzi LA, Schneider U, Sorenson JA, Ciardella A, et al. (2000) Retinal choroidal anastomoses and occult choroidal neovascularization in age-related macular degeneration. Ophthalmology 107: 742-753; discussion 753-744.
135. Wangsa-Wirawan ND, Linsenmeier RA (2003) Retinal oxygen: fundamental and clinical aspects. Arch Ophthalmol 121: 547-557.
136. Linsenmeier RA (1986) Effects of light and darkness on oxygen distribution and consumption in the cat retina. J Gen Physiol 88: 521-542.
137. Simo R, Villarroel M, Corraliza L, Hernandez C, Garcia-Ramirez M (2010) The retinal pigment epithelium: something more than a constituent of the blood-retinal barrier. J Biomed Biotechnol 2010: 190724.
138. Marmor MF (1999) Mechanisms of fluid accumulation in retinal edema. Doc Ophthalmol 97: 239-249.
139. Kaur C, Foulds WS, Ling EA (2008) Blood-retinal barrier in hypoxic ischaemic conditions: basic concepts, clinical features and management. Prog Retin Eye Res 27: 622-647.
140. Burke JM (2008) Epithelial phenotype and the RPE: is the answer blowing in the Wnt? Prog Retin Eye Res 27: 579-595.
141. McKay BS, Irving PE, Skumatz CM, Burke JM (1997) Cell-cell adhesion molecules and the development of an epithelial phenotype in cultured human retinal pigment epithelial cells. Exp Eye Res 65: 661-671.
142. Goldbaum MH, Madden K (1982) A new perspective on Bruch's membrane and the retinal pigment epithelium. Br J Ophthalmol 66: 17-25.

143. Essner E, Gordon SR (1984) Demonstration of microfibrils in Bruch's membrane of the eye. Tissue Cell 16: 779-788.
144. Sarks JP, Sarks SH, Killingsworth MC (1994) Evolution of soft drusen in age-related macular degeneration. Eye (Lond) 8: 269-283.
145. Sarks SH, Van Driel D, Maxwell L, Killingsworth M (1980) Softening of drusen and subretinal neovascularization. Trans Ophthalmol Soc UK 100: 414-422.
146. Spraul CW, Grossniklaus HE (1997) Characteristics of drusen and Bruch's membrane in postmortem eyes with age-related macular degeneration. Arch Ophthalmol 115: 267-273.
147. Gullapalli VK, Sugino IK, Van Patten Y, Shah S, Zarbin MA (2005) Impaired RPE survival on aged submacular human Bruch's membrane. Exp Eye Res 80: 235-248.
148. Tezel TH, Del Priore LV, Kaplan HJ (2004) Reengineering of aged Bruch's membrane to enhance retinal pigment epithelium repopulation. Invest Ophthalmol Vis Sci 45: 3337-3348.
149. Defoe DM, Matsumoto B, Besharse JC (1992) Reconstitution of the photoreceptor-pigment epithelium interface: L-glutamate stimulation of adhesive interactions and rod disc shedding after recombination of dissociated *Xenopus laevis* eyecups. Exp Eye Res 54: 903-911.
150. Matsumoto B, Defoe DM, Besharse JC (1987) Membrane turnover in rod photoreceptors: ensheathment and phagocytosis of outer segment distal tips by pseudopodia of the retinal pigment epithelium. Proc R Soc Lond B Biol Sci 230: 339-354.
151. Gundersen D, Powell SK, Rodriguez-Boulan E (1993) Apical polarization of N-CAM in retinal pigment epithelium is dependent on contact with the neural retina. J Cell Biol 121: 335-343.
152. Johnson NF, Foulds WS (1977) Observations on the retinal pigment epithelium and retinal macrophages in experimental retinal detachment. Br J Ophthalmol 61: 564-572.
153. Anderson DH, Stern WH, Fisher SK, Erickson PA, Borgula GA (1983) Retinal detachment in the cat: the pigment epithelial-photoreceptor interface. Invest Ophthalmol Vis Sci 24: 906-926.
154. Anderson DH, Stern WH, Fisher SK, Erickson PA, Borgula GA (1981) The onset of pigment epithelial proliferation after retinal detachment. Invest Ophthalmol Vis Sci 21: 10-16.
155. Saint-Geniez M, Maldonado AE, D'Amore PA (2006) VEGF expression and receptor activation in the choroid during development and in the adult. Invest Ophthalmol Vis Sci 47: 3135-3142.
156. Saint-Geniez M, Kurihara T, Sekiyama E, Maldonado AE, D'Amore PA (2009) An essential role for RPE-derived soluble VEGF in the maintenance of the choriocapillaris. Proc Natl Acad Sci U S A 106: 18751-18756.
157. Shirinifard A, Gens JS, Zaitlen BL, Poplawski NJ, Swat M, et al. (2009) 3D multi-cell simulation of tumor growth and angiogenesis. PLoS One 4: e7190.
158. Bhutto IA, McLeod DS, Hasegawa T, Kim SY, Merges C, et al. (2006) Pigment epithelium-derived factor (PEDF) and vascular endothelial growth factor (VEGF)

in aged human choroid and eyes with age-related macular degeneration. Exp Eye Res 82: 99-110.

159. Martin G, Schlunck G, Hansen LL, Agostini HT (2004) Differential expression of angioregulatory factors in normal and CNV-derived human retinal pigment epithelium. Graefes Arch Clin Exp Ophthalmol 242: 321-326.
160. Kliffen M, Sharma HS, Mooy CM, Kerkvliet S, de Jong PT (1997) Increased expression of angiogenic growth factors in age-related maculopathy. Br J Ophthalmol 81: 154-162.
161. De Smet F, Segura I, De Bock K, Hohensinner PJ, Carmeliet P (2009) Mechanisms of vessel branching: filopodia on endothelial tip cells lead the way. Arterioscler Thromb Vasc Biol 29: 639-649.
162. Holderfield MT, Hughes CC (2008) Crosstalk between vascular endothelial growth factor, notch, and transforming growth factor-beta in vascular morphogenesis. Circ Res 102: 637-652.
163. Jakobsson L, Franco CA, Bentley K, Collins RT, Ponsioen B, et al. (2010) Endothelial cells dynamically compete for the tip cell position during angiogenic sprouting. Nat Cell Biol 12: 943-953.
164. Heriot WJ, Henkind P, Bellhorn RW, Burns MS (1984) Choroidal neovascularization can digest Bruch's membrane. A prior break is not essential. Ophthalmology 91: 1603-1608.
165. Killingsworth MC, Sarks JP, Sarks SH (1990) Macrophages related to Bruch's membrane in age-related macular degeneration. Eye (Lond) 4: 613-621.
166. Chen H, Liu B, Lukas TJ, Neufeld AH (2008) The aged retinal pigment epithelium/choroid: a potential substratum for the pathogenesis of age-related macular degeneration. PLoS One 3: e2339.
167. Cousins SW, Espinosa-Heidmann DG, Alexandridou A, Sall J, Dubovy S, et al. (2002) The role of aging, high fat diet and blue light exposure in an experimental mouse model for basal laminar deposit formation. Exp Eye Res 75: 543-553.
168. Penfold P, Killingsworth M, Sarks S (1984) An ultrastructural study of the role of leucocytes and fibroblasts in the breakdown of Bruch's membrane. Aust J Ophthalmol 12: 23-31.
169. Guo L, Hussain AA, Limb GA, Marshall J (1999) Age-dependent variation in metalloproteinase activity of isolated human Bruch's membrane and choroid. Invest Ophthalmol Vis Sci 40: 2676-2682.
170. Hoffmann S, He S, Ehren M, Ryan SJ, Wiedemann P, et al. (2006) MMP-2 and MMP-9 secretion by RPE is stimulated by angiogenic molecules found in choroidal neovascular membranes. Retina 26: 454-461.
171. Kvanta A, Shen WY, Sarman S, Seregard S, Steen B, et al. (2000) Matrix metalloproteinase (MMP) expression in experimental choroidal neovascularization. Curr Eye Res 21: 684-690.
172. Lambert V, Wielockx B, Munaut C, Galopin C, Jost M, et al. (2003) MMP-2 and MMP-9 synergize in promoting choroidal neovascularization. FASEB J 17: 2290-2292.
173. Ottino P, Finley J, Rojo E, Ottlecz A, Lambrou GN, et al. (2004) Hypoxia activates matrix metalloproteinase expression and the VEGF system in monkey choroid-

retinal endothelial cells: Involvement of cytosolic phospholipase A2 activity. Mol Vis 10: 341-350.

174. Karagiannis ED, Popel AS (2006) Distinct modes of collagen type I proteolysis by matrix metalloproteinase (MMP) 2 and membrane type I MMP during the migration of a tip endothelial cell: insights from a computational model. J Theor Biol 238: 124-145.
175. Sato H, Takino T (2010) Coordinate action of membrane-type matrix metalloproteinase-1 (MT1-MMP) and MMP-2 enhances pericellular proteolysis and invasion. Cancer Sci 101: 843-847.
176. van Hinsbergh VW, Koolwijk P (2008) Endothelial sprouting and angiogenesis: matrix metalloproteinases in the lead. Cardiovasc Res 78: 203-212.
177. Xiong W, Knispel R, MacTaggart J, Greiner TC, Weiss SJ, et al. (2009) Membrane-type 1 matrix metalloproteinase regulates macrophage-dependent elastolytic activity and aneurysm formation *in vivo*. J Biol Chem 284: 1765-1771.
178. Yana I, Sagara H, Takaki S, Takatsu K, Nakamura K, et al. (2007) Crosstalk between neovessels and mural cells directs the site-specific expression of MT1-MMP to endothelial tip cells. J Cell Sci 120: 1607-1614.
179. Cherepanoff S, McMenamin P, Gillies MC, Kettle E, Sarks SH (2010) Bruch's membrane and choroidal macrophages in early and advanced age-related macular degeneration. Br J Ophthalmol 94: 918-925.
180. Anderson DH, Mullins RF, Hageman GS, Johnson LV (2002) A role for local inflammation in the formation of drusen in the aging eye. Am J Ophthalmol 134: 411-431.
181. Hageman GS, Luthert PJ, Victor Chong NH, Johnson LV, Anderson DH, et al. (2001) An integrated hypothesis that considers drusen as biomarkers of immune-mediated processes at the RPE-Bruch's membrane interface in aging and age-related macular degeneration. Prog Retin Eye Res 20: 705-732.
182. Tsigkos S, Koutsilieris M, Papapetropoulos A (2003) Angiopoietins in angiogenesis and beyond. Expert Opin Investig Drugs 12: 933-941.
183. Zech JC, Pouvreau I, Cotinet A, Goureau O, Le Varlet B, et al. (1998) Effect of cytokines and nitric oxide on tight junctions in cultured rat retinal pigment epithelium. Invest Ophthalmol Vis Sci 39: 1600-1608.
184. Luna JD, Chan CC, Derevjanik NL, Mahlow J, Chiu C, et al. (1997) Blood-retinal barrier (BRB) breakdown in experimental autoimmune uveoretinitis: comparison with vascular endothelial growth factor, tumor necrosis factor α, and interleukin-1β-mediated breakdown. J Neurosci Res 49: 268-280.
185. Elner VM, Strieter RM, Elner SG, Baggiolini M, Lindley I, et al. (1990) Neutrophil chemotactic factor (IL-8) gene expression by cytokine-treated retinal pigment epithelial cells. Am J Pathol 136: 745-750.
186. Harhaj NS, Antonetti DA (2004) Regulation of tight junctions and loss of barrier function in pathophysiology. Int J Biochem Cell Biol 36: 1206-1237.
187. Sainson RC, Johnston DA, Chu HC, Holderfield MT, Nakatsu MN, et al. (2008) TNF primes endothelial cells for angiogenic sprouting by inducing a tip cell phenotype. Blood 111: 4997-5007.

188. Spaide R, Armstrong D, Browne R (2003) Choroidal neovascularization in age-related macular degeneration--what is the cause? Retina 23: 595-614.
189. Zarbin MA (2004) Current concepts in the pathogenesis of age-related macular degeneration. Arch Ophthalmol 122: 598-614.
190. Tamai K, Spaide RF, Ellis EA, Iwabuchi S, Ogura Y, et al. (2002) Lipid hydroperoxide stimulates subretinal choroidal neovascularization in the rabbit. Exp Eye Res 74: 301-308.
191. Baffi J, Byrnes G, Chan CC, Csaky KG (2000) Choroidal neovascularization in the rat induced by adenovirus mediated expression of vascular endothelial growth factor. Invest Ophthalmol Vis Sci 41: 3582-3589.
192. Oshima Y, Oshima S, Nambu H, Kachi S, Hackett SF, et al. (2004) Increased expression of VEGF in retinal pigmented epithelial cells is not sufficient to cause choroidal neovascularization. J Cell Physiol 201: 393-400.
193. Schwesinger C, Yee C, Rohan RM, Joussen AM, Fernandez A, et al. (2001) Intrachoroidal neovascularization in transgenic mice overexpressing vascular endothelial growth factor in the retinal pigment epithelium. Am J Pathol 158: 1161-1172.
194. Bhutto IA, Uno K, Merges C, Zhang L, McLeod DS, et al. (2008) Reduction of endogenous angiogenesis inhibitors in Bruch's membrane of the submacular region in eyes with age-related macular degeneration. Arch Ophthalmol 126: 670-678.
195. An E, Lu X, Flippin J, Devaney JM, Halligan B, et al. (2006) Secreted proteome profiling in human RPE cell cultures derived from donors with age related macular degeneration and age matched healthy donors. J Proteome Res 5: 2599-2610.
196. Research on Microbial Biofilms; 2002. NIH, National Heart, Lung, and Blood Institute.
197. Yanjun Z, Guangyu L, Bin F, Qing W, Ving J, et al. (2007) Study of hypoxia-induced expression of HIF-1alpha in retina pigment epithelium. Bull Exp Biol Med 143: 323-327.
198. Aiello LP, Northrup JM, Keyt BA, Takagi H, Iwamoto MA (1995) Hypoxic regulation of vascular endothelial growth factor in retinal cells. Arch Ophthalmol 113: 1538-1544.
199. Spraul CW, Lang GE, Grossniklaus HE, Lang GK (1999) Histologic and morphometric analysis of the choroid, Bruch's membrane, and retinal pigment epithelium in postmortem eyes with age-related macular degeneration and histologic examination of surgically excised choroidal neovascular membranes. Surv Ophthalmol 44: 10-32.
200. Hussain AA, Starita C, Marshall J (2004) Transport characteristics of aging human Bruch's membrane: implications for age-related macular degeneration. In: Ioseliani O, editor. Focus on Macular Degeneration Research (AMD): Nova Biomedical Books. pp. 59-113.
201. Chong NH, Keonin J, Luthert PJ, Frennesson CI, Weingeist DM, et al. (2005) Decreased thickness and integrity of the macular elastic layer of Bruch's

membrane correspond to the distribution of lesions associated with age-related macular degeneration. Am J Pathol 166: 241-251.

202. Crane IJ, Liversidge J (2008) Mechanisms of leukocyte migration across the blood-retina barrier. Semin Immunopathol 30: 165-177.
203. Shaw SK, Bamba PS, Perkins BN, Luscinskas FW (2001) Real-time imaging of vascular endothelial-cadherin during leukocyte transmigration across endothelium. J Immunol 167: 2323-2330.
204. Ryan SJ (1979) The development of an experimental model of subretinal neovascularization in disciform macular degeneration. Trans Am Ophthalmol Soc 77: 707-745.
205. Korte GE, Pua F (1988) Choriocapillaris regeneration in the rabbit: a study with vascular casts. Acta Anat (Basel) 133: 224-228.
206. Marmor MF (1990) Control of subretinal fluid: experimental and clinical studies. Eye (Lond) 4: 340-344.
207. Putting BJ, Zweypfenning RC, Vrensen GF, Oosterhuis JA, van Best JA (1992) Blood-retinal barrier dysfunction at the pigment epithelium induced by blue light. Invest Ophthalmol Vis Sci 33: 3385-3393.
208. Imamura Y, Noda S, Hashizume K, Shinoda K, Yamaguchi M, et al. (2006) Drusen, choroidal neovascularization, and retinal pigment epithelium dysfunction in SOD1-deficient mice: a model of age-related macular degeneration. Proc Natl Acad Sci USA 103: 11282-11287.
209. Rudolf M, Malek G, Messinger JD, Clark ME, Wang L, et al. (2008) Sub-retinal drusenoid deposits in human retina: organization and composition. Exp Eye Res 87: 402-408.
210. Zweifel SA, Imamura Y, Spaide TC, Fujiwara T, Spaide RF (2010) Prevalence and significance of subretinal drusenoid deposits (reticular pseudodrusen) in age-related macular degeneration. Ophthalmology 117: 1775-1781.
211. Arnold JJ, Sarks SH, Killingsworth MC, Sarks JP (1995) Reticular pseudodrusen. A risk factor in age-related maculopathy. Retina 15: 183-191.
212. Grossniklaus HE, Kang SJ, Berglin L (2010) Animal models of choroidal and retinal neovascularization. Prog Retin Eye Res 29: 500-519.
213. Cohen SY, Dubois L, Tadayoni R, Delahaye-Mazza C, Debibie C, et al. (2007) Prevalence of reticular pseudodrusen in age-related macular degeneration with newly diagnosed choroidal neovascularisation. Br J Ophthalmol 91: 354-359.
214. Spaide RF (1999) Choroidal neovascularization in younger patients. Curr Opin Ophthalmol 10: 177-181.
215. Orzalesi N, Migliavacca L, Miglior S (1994) Subretinal neovascularization after naphthalene damage to the rabbit retina. Invest Ophthalmol Vis Sci 35: 696-705.
216. Baba T, Bhutto IA, Merges C, Grebe R, Emmert D, et al. (2010) A rat model for choroidal neovascularization using subretinal lipid hydroperoxide injection. Am J Pathol 176: 3085-3097.
217. Kimura H, Sakamoto T, Hinton DR, Spee C, Ogura Y, et al. (1995) A new model of subretinal neovascularization in the rabbit. Invest Ophthalmol Vis Sci 36: 2110-2119.

218. Qiu G, Stewart JM, Sadda S, Freda R, Lee S, et al. (2006) A new model of experimental subretinal neovascularization in the rabbit. Exp Eye Res 83: 141-152.
219. Ni M, Holland M, Jarstadmarken H, De Vries G (2005) Time-course of experimental choroidal neovascularization in Dutch-Belted rabbit: clinical and histological evaluation. Exp Eye Res 81: 286-297.
220. Haugh LM, Linsenmeier RA, Goldstick TK (1990) Mathematical models of the spatial distribution of retinal oxygen tension and consumption, including changes upon illumination. Ann Biomed Eng 18: 19-36.
221. Roos MW (2004) Theoretical estimation of retinal oxygenation during retinal artery occlusion. Physiol Meas 25: 1523-1532.
222. Szczerba D, Szekely G (2005) Computational model of flow-tissue interactions in intussusceptive angiogenesis. J Theor Biol 234: 87-97.
223. Perfahl H, Byrne HM, Chen T, Estrella V, Alarcon T, et al. (2011) Multiscale modelling of vascular tumour growth in 3D: the roles of domain size and boundary conditions. PLoS One 6: e14790.
224. Welter M, Bartha K, Rieger H (2009) Vascular remodelling of an arterio-venous blood vessel network during solid tumour growth. Journal of theoretical biology 259: 405-422.
225. Pries AR, Hopfner M, le Noble F, Dewhirst MW, Secomb TW (2010) The shunt problem: control of functional shunting in normal and tumour vasculature. Nat Rev Cancer 10: 587-593.
226. Bauer AL, Jackson TL, Jiang Y (2007) A cell-based model exhibiting branching and anastomosis during tumor-induced angiogenesis. Biophys J 92: 3105-3121.
227. Zhang SX, Ma JX (2007) Ocular neovascularization: implication of endogenous angiogenic inhibitors and potential therapy. Prog Retin Eye Res 26: 1-37.
228. Qutub AA, Mac Gabhann F, Karagiannis ED, Vempati P, Popel AS (2009) Multiscale models of angiogenesis. IEEE Eng Med Biol Mag 28: 14-31.
229. Klein R, Klein BE, Tomany SC, Meuer SM, Huang GH (2002) Ten-year incidence and progression of age-related maculopathy: The Beaver Dam eye study. Ophthalmology 109: 1767-1779.
230. Stevens TS, Bressler NM, Maguire MG, Bressler SB, Fine SL, et al. (1997) Occult choroidal neovascularization in age-related macular degeneration. A natural history study. Arch Ophthalmol 115: 345-350.
231. Wong TY, Chakravarthy U, Klein R, Mitchell P, Zlateva G, et al. (2008) The natural history and prognosis of neovascular age-related macular degeneration: a systematic review of the literature and meta-analysis. Ophthalmology 115: 116-126.
232. Polito A, Isola M, Lanzetta P, Gregori D, Bandello F (2006) The natural history of occult choroidal neovascularisation associated with age-related macular degeneration. A systematic review. Ann Acad Med Singapore 35: 145-150.
233. Grossniklaus HE, Gass JD (1998) Clinicopathologic correlations of surgically excised type 1 and type 2 submacular choroidal neovascular membranes. Am J Ophthalmol 126: 59-69.
234. Lim JI (1999) Iatrogenic choroidal neovascularization. Surv Ophthalmol 44: 95-111.

235. Zweifel SA, Spaide RF, Curcio CA, Malek G, Imamura Y (2010) Reticular pseudodrusen are subretinal drusenoid deposits. Ophthalmology 117: 303-312 e301.
236. Yoder MC (2010) Is endothelium the origin of endothelial progenitor cells? Arterioscler Thromb Vasc Biol 30: 1094-1103.
237. Yoder MC, Mead LE, Prater D, Krier TR, Mroueh KN, et al. (2007) Redefining endothelial progenitor cells via clonal analysis and hematopoietic stem/progenitor cell principals. Blood 109: 1801-1809.
238. Popławski NJ, Shirinifard A, Swat M, Glazier JA (2008) Simulation of single-species bacterial-biofilm growth using the Glazier-Graner-Hogeweg model and the CompuCell3D modeling environment. Math Biosci Eng 5: 355-388.
239. Popławski NJ, Swat M, Gens JS, Glazier JA (2007) Adhesion between cells, diffusion of growth factors, and elasticity of the AER produce the paddle shape of the chick limb. Physica A 373: 521-532.
240. Glazier JA, Zhang Y, Swat M, Zaitlen B, Schnell S (2008) Coordinated action of N-CAM, N-cadherin, EphA4, and ephrinB2 translates genetic prepatterns into structure during somitogenesis in chick. Curr Top Dev Biol 81: 205-247.
241. Xu Z, Chen N, Shadden SC, Marsden JE, Kamocka MM, et al. (2009) Study of blood flow impact on growth of thrombi using a multiscale model. Soft Matter 5: 769-779.
242. Merks RMH, Brodsky SV, Goligorksy MS, Newman SA, Glazier JA (2006) Cell elongation is key to *in silico* replication of *in vitro* vasculogenesis and subsequent remodeling. Dev Biol 289: 44-54.
243. Roorda A, Zhang Y, Duncan JL (2007) High-resolution in vivo imaging of the RPE mosaic in eyes with retinal disease. Invest Ophthalmol Vis Sci 48: 2297-2303.
244. Linsenmeier RA, Braun RD (1992) Oxygen distribution and consumption in the cat retina during normoxia and hypoxemia. J Gen Physiol 99: 177-197.
245. Roos MW (2007) Theoretical estimation of retinal oxygenation during retinal detachment. Comput Biol Med 37: 890-896.
246. Lehman A (2005) JMP for basic univariate and multivariate statistics: a step-by-step guide: SAS Publishing.
247. Pogue BW, Paulsen KD, O'Hara JA, Wilmot CM, Swartz HM (2001) Estimation of oxygen distribution in RIF-1 tumors by diffusion model-based interpretation of pimonidazole hypoxia and Eppendorf measurements. Radiat Res 155: 15-25.
248. Shahidi M, Wanek J, Blair NP, Mori M (2009) Three-dimensional mapping of chorioretinal vascular oxygen tension in the rat. Invest Ophthalmol Vis Sci 50: 820-825.
249. Serini G, Ambrosi D, Giraudo E, Gamba A, Preziosi L, et al. (2003) Modeling the early stages of vascular network assembly. EMBO J 22: 1771-1779.
250. Chen R, Silva E, Yuen W, Brock A, Fischbach C, et al. (2007) Integrated approach to designing growth factor delivery systems. FASEB J 21: 3896-3903.
251. Leith JT, Michelson S (1995) Secretion rates and levels of vascular endothelial growth factor in clone A or HCT-8 human colon tumour cells as a function of oxygen concentration. Cell Prolif 28: 415-430.

252. Mac Gabhann F, Ji JW, Popel AS (2006) Computational model of vascular endothelial growth factor spatial distribution in muscle and pro-angiogenic cell therapy. PLoS Comput Biol 2: e127.
253. Padera TP, Stoll BR, Tooredman JB, Capen D, Di Tomaso E, et al. (2004) Pathology: cancer cells compress intratumour vessels. Nature 427: 695-695.
254. Holash J, Maisonpierre P, Compton D, Boland P, Alexander C, et al. (1999) Vessel cooption, regression, and growth in tumors mediated by angiopoietins and VEGF. Science 284: 1994.
255. Ellertsdottir E, Lenard A, Blum Y, Krudewig A, Herwig L, et al. (2010) Vascular morphogenesis in the zebrafish embryo. Developmental biology 341: 56-65.
256. Lencinas A, Broka DM, Konieczka JH, Klewer SE, Antin PB, et al. (2010) Arsenic Exposure Perturbs Epithelial-Mesenchymal Cell Transition and Gene Expression In a Collagen Gel Assay. Toxicological Sciences 116: 273-285.

Abbas Shirinifard
The Biocomplexity Institute
Swain Hall
212 S Hawthorne Dr,
Bloomington, IN 47405-7003
Email: ashirini@indiana.edu
Tel: 812-855-1304

Education:

Physics (B.A.), Shiraz University, Shiraz, Iran (2002)
Physics (M.S.), Sharif University of Technology, Tehran, Iran (2005)
Physics (Ph.D.), Indiana University, Bloomington, IN (2005-2012)

Research Interest:

My research interests are multi-cell simulation of biological and disease processes. In my research, I use the laws of physics to understand underlying biological processes and their representations. I have extensively analyzed patterning instabilities in angiogenesis using analytical and numerical calculations. These studies have led to a multi-cell three-dimensional simulation of neoangiogenesis and vascular tumor growth in three dimensions. I have developed a multi-cell simulation of the retina which is capable of predicting a range of cellular and morphometric changes and defects due to aging that can initiate choroidal neovascularization and recapitulating the histopathology of wet age-related macular degeneration. Currently, in collaboration with the Texas-Indiana Virtual Start Center, I am extending my angiogenesis computational framework to predict the effects of toxins on angiogenesis during embryonic development.

In parallel to developing multi-scale simulations, I have experience in running *in vitro* and *ex ovo* experiments and successfully developed a novel *in vitr*o angiogenesis assay capable of producing high-quality functional blood vessels (US Patent Application PCT/US2011/028492).

Positions and Employment

2002-2005	Teaching Assistant, Department of Physics, Sharif University Of Technology, Tehran, Iran
2005-2006	Teaching Assistant, Department of Physics, Indiana University, Bloomington, IN
2006-2011	Research Assistant, The Biocomplexity Institute, Indiana University, Bloomington, IN
2011-	Research Associate, The Biocomplexity Institute, Indiana University, Bloomington, IN

Professional Society Membership:

American Physical Society, Association for Research in Vision and Opthalmology, American Mathematical Society, Society for Industrial and Applied Mathematics.

Patent Application:

US Patent Application PCT/US2011/028492, "Engineered Lumenized Vascular Networks and Support Matrix", filed 03/15/2011

Peer-reviewed Publications

1. **Shirinifard A.**, Gens J.S., Zaitlen B.L., Popławski N.J., Swat M., Glazier J.A (2009). 3D multi-cell simulation of tumor growth and angiogenesis. PLoS One. 4(10):e7190.
2. **Shirinifard A.**, Glazier J.A., Swat M., Gens J.S., Family F., Jiang Y., Grossniklaus H.E. (2012) Adhesion Failures in the Bruch's Membrane-Retinal Pigment Epithelium-

Photoreceptor Outer Segment Complex Determine the Pattern of Choroidal Neovascularization: A Computer Simulation Study. PLoS Comput Biol., in press

3. Popławski N.J., **Shirinifard A.**, Ubirajara A., Gens J.S., Swat M., Glazier J.A. (2010). Front Instabilities and Invasiveness of Simulated 3D Avascular Tumors. PLoS ONE 5(5): e10641.
4. Merks R.M., Perryn E.D., **Shirinifard A.**, Glazier J.A. (2008). Contact-inhibited chemotaxis in de novo and sprouting blood-vessel growth. PLoS Comput Biol. 4(9):e1000163.
5. Popławski N.J., **Shirinifard A.**, Swat M., Glazier J.A. (2008). Simulation of single-species bacterial-biofilm growth using the Glazier-Graner-Hogeweg model and the CompuCell3D modeling environment. Math Biosci Eng. Apr; 5(2):355-88.
6. Thomas G.T., Zhang Y., Swat M., **Shirinifard A.**, Glazier J.A. (2011). Computer simulations of cell sorting due to differential adhesion. PLoS ONE 6(10): e24999.
7. Swat M., Thomas G.L., Belmonte J.M., **Shirinifard A.**, Hmeljak M., Glazier J.A. (2012). Multi-Scale Modeling of Tissues Using CompuCell3D. Methods in Cell Biology, Volume 110.

Invited Talks

1. Association for Research in Vision and Opthalmology Meeting, Fort Lauderdale, FL, 2011
2. American Physical Society March Meeting, Dallas, TX, 2011
3. American Mathematical Society Special Sessions, Notre Dame, IN, 2010
4. University of Illinois at Urbana-Champaign, Understanding Complex Systems conference, 2008
5. Indiana University Cyclotron Facility, Bloomington, IN, 2009
6. American Mathematical Society Spring Central Section Meeting, Bloomington, IN, 2008